UNIVERSITY OF CALIFORNIA
SANTA CRUZ

THE AUTOMATED PLANET FINDER TELESCOPE'S AUTOMATION AND FIRST THREE YEARS OF PLANET DETECTIONS

A dissertation submitted in partial satisfaction of the
requirements for the degree of

Doctor of Philosophy

in

ASTRONOMY & ASTROPHYSICS

by

Jennifer Burt

June 2016

The Dissertation of Jennifer Burt
is approved:

Professor Gregory Laughlin, Chair

Professor Steven Vogt

Dr. R. Paul Butler

Dean Tyrus Miller
Vice Provost and Dean of Graduate Studies

Table of Contents

List of Figures

List of Tables

Abstract

The Automated Planet Finder telescope's automation and first three years of planet detections

by

Jennifer Burt

The Automated Planet Finder (APF) is a 2.4m, f/15 telescope located at the UCO's Lick Observatory, atop Mt. Hamilton. The telescope has been specifically optimized to detect and characterize extrasolar planets via high precision, radial velocity (RV) observations using the high-resolution Levy echelle spectrograph. The telescope has demonstrated world-class internal precision levels of 1 m/s when observing bright, RV standard stars. Observing time on the telescope is divided such that $\sim$80% is spent on exoplanet related research and the remaining $\sim$80% is made available to the University of California consortium for other science goals. The telescope achieved first light in 2013, and this work describes the APF's early science achievements and its transition from a traditional observing approach to a fully autonomous facility.

First we provide a characteristic look at the APF telescope and the Levy spectrograph, focusing on the stability of the instrument and its performance on RV standard stars. Second, we describe the design and implementation of the dynamic scheduling software which has been running our team's nightly observations on the APF for the past year. Third, we discuss the detection of a Neptune-mass planet orbiting the nearby, low-mass star GL687 by the APF in collaboration with the HIRES instrument on Keck I. Fourth, we summarize the APF's detection

of two multi-planet systems: the four planet system orbiting HD 141399 and the 6 planet system orbiting HD 219134. Fifth, we expand our science focus to assess the impact that the APF - with the addition of a new, time-varying prioritization scheme to the telescope's dynamic scheduling software - can have on filling out the exoplanet Mass-Radius diagram when pursuing RV follow-up of transiting planets detected by NASA's TESS satellite. Finally, we outline some likely next science goals for the telescope as it continues its world-class, RV performance.

To my parents, for instilling in me the dedication and love of learning necessary to follow the long road towards attaining my dreams.

Acknowledgments

The work presented in this thesis, and the many learning processes that led to it, are due in large part to the excellent mentorship provided by Greg Laughlin over the course of my graduate career. His ability to look at problems in ways I would never have considered, and to somehow seamlessly incorporate a large number of seemingly random pop culture references while doing so, has served as both inspiration and comic relief in many a science meeting. The past six years have been an excellent scientific adventure, and I look forward to many more collaborative projects moving forward.

Additional and emphatic thanks are due to to Steve Vogt, for showing me how to shoot straight when searching for planets; to Paul Butler, for teaching me to always trust the data; and to Brad Holden, for countless conversations that have helped me grow both as a scientist and as a person over the past few years. And only some of which were about cats and twitter.

In addition to the insight gained from my mentors, I have been privileged to share innumerable life experiences (some of them relevant to science, but most of them not) with my fellow graduate students. Katie has been the world's best housemate over the past five years, and life in Boston will be much too quiet and well-behaved without her. Jill's sage advice on all things wine-, cheese-, and life-related has come to bear on more important moments in my life than I think either of us ever anticipated. And no office will ever compare to the one shared with Caroline, Elizabeth, Emily and Justin. You four have made long work days not only bearable, but something to look forward to with the guarantee of good conversation and the occasional crafting of ridiculous charts on the white board.

None of this would have been possible without the love and support of my family. My parents started me on this journey over two decades ago when they pulled out that telescope, and have been by my side every step of the way since. (Even when they weren't sure if being an astronomer would ever pay the bills.) Their belief in me and my ability to handle whatever life throws my way has been a true source of inspiration, without which I wouldn't be nearly as fearless as I am today. And to my siblings (those related by blood and otherwise), thank you for always keeping me grounded, for picking up the phone when I call at ridiculous hours of the day and night, and for reminding me that even overly educated scientists should occasionally take the time to laugh over stupid text messages. To my extended family - thank you for not disowning me when I missed one too many Thanksgivings while living on the west coast. I promise to make up for it now that I'm headed back east. Finally, thank you to Inara for being the ultimate late night science companion and for always lending a paw (or four) when I was in need of a break from the laptop.

The author of this thesis was a primary investigator of all of the research presented on the following pages. Chapters 3 and 4 are first author works by her, originally published in the Journal of Astronomical Telescopes, Instruments and Systems, and the Astrophysical Journal, respectively. Chapter 5 contains segments of papers previously published by the Astrophysical Journal, reproduced here with permission from the co-authors - of whom the author is one.

Chapter 1

Introduction

1.1 The radial velocity method

1.1.1 Concept

Over the past two decades, advances in the field of exoplanet detection have proven that exoplanets are ubiquitous in our own galaxy. Recent surveys suggest that stars like the sun host 1.6 planets on average (Cassan *et al.*, 2012). One of the key planet detection methods to date is the Doppler Spectroscopy method, also known as the Radial Velocity (RV) method. As a planet orbits around its host star, the planet exerts a gravitation pull on the star, causing the star to move on its own (albeit much smaller) orbit around the system's center-of-mass. If this orbit moves the star towards/away from the Earth (in the *radial* direction) then it will cause the star's spectral absorption lines to systematically Doppler shift around their rest wavelength (Equation 1.1.1).

$$z = \frac{\lambda - \lambda_o}{\lambda_o} = \frac{1 + V_r/c}{\sqrt{1 - V_T^2/c^2}} - 1 \tag{1.1}$$

where z is the redshift, λ and λ_o are the observed and rest wavelengths, respectively, V_r is the star's radial velocity, and V_T is the star's total velocity relative to the observer. In log λ space, the wavelength shift $\lambda - \lambda_o$ is independent of the rest wavelength, and provides a direct measurement of the relative velocity between the source and the observer.

Using ground-based telescopes, we can monitor a star's spectral absorption lines and look for periodic shifts in their positions that suggest a planet on a Keplerian orbit around the star (Figure 1.1). The shifts induced by planetary companions are small though, with measurements of a 1 m s^{-1} signal corresponding to $\Delta\lambda/\lambda_o = 3 \times 10^{-9}$. On the detector of a typical mid- to high-resolution spectrograph (R $\sim$ 100,000), this translates into a linear displacement of about 3×10^{-4} resolution elements (or $\sim$ 10^{-4} line widths). In order to successfully extract these shifts it is crucial to have both an instrument capable of high-resolution spectroscopy, in order to discern the star's individual lines in the first place, and a simultaneous wavelength calibration source, so that the lines' movements can be determined to within fractions of an angstrom. In instruments like the Levy spectrograph, we use a cell of gaseous, molecular iodine (I_2) which the starlight passes through on its way to the CCD, thus super imposing the I_2 absorption lines on the stellar spectrum. These lines then work as a fiducial wavelength scale that experiences the same instrumental shifts and distortions as the stellar spectrum.

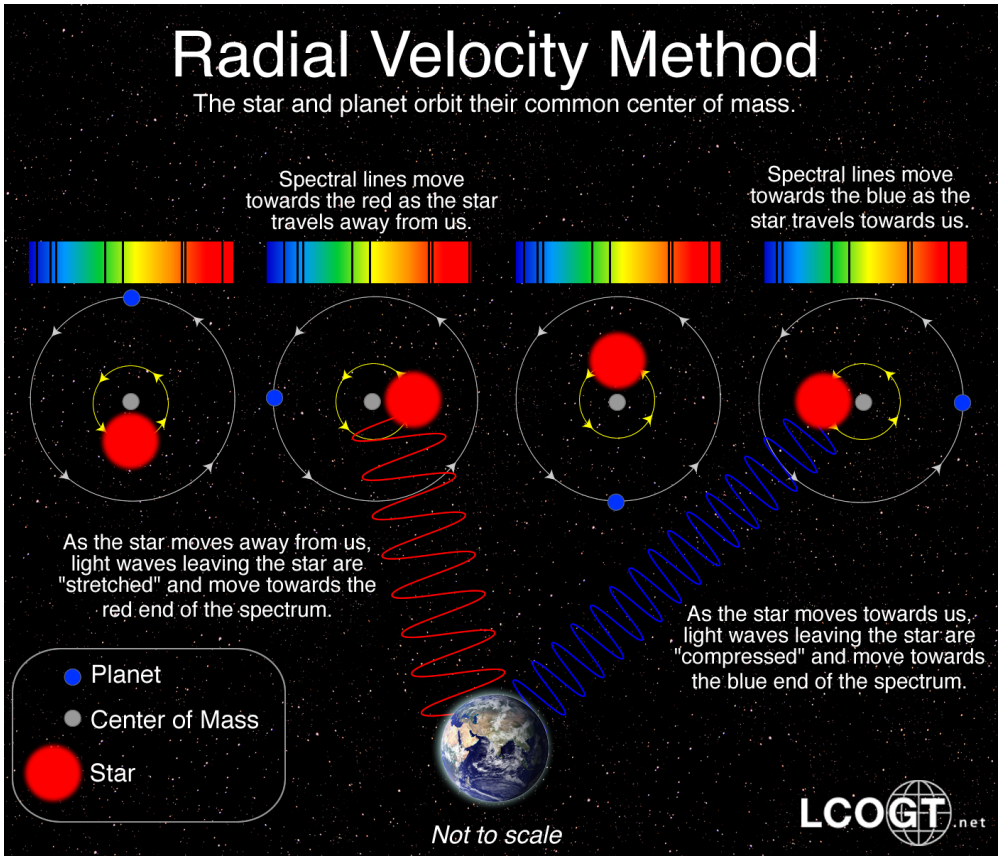

Figure 1.1: A schematic of the Radial Velocity method for detecting exoplanets produced by the Las Cumbres Observatory Global Telescope (LCOGT) Network [https://lcogt.net/spacebook/radial-velocity-method/]

1.1.2 RV signals

A planet in orbit around a star induces a perturbation on its host of the form:

$$V_r(t) = K\ [\cos(\nu(t)\ +\ \omega) +\ e\ \cos\omega]\ +\ \gamma \tag{1.2}$$

where $\nu(t)$ is the true anomaly, ω is the longitude of periastron, e is the planet's orbital eccentricity, γ is the velocity of the system's barycenter, and K is the radial velocity semi-amplitude:

$$K = \left(\frac{2\pi G}{P}\right)^{1/3} \frac{m_{pl}\sin i}{(M_* + m_{pl})^{2/3}} \frac{1}{\sqrt{1-e^2}} \tag{1.3}$$

where G is the gravitational constant, P is the planet's orbital period, M_* is the mass of the host star, and m_{pl} is the mass of the planet.

When plotted over time, the relative radial velocity values of a star orbited by a single planet will form a sinusoidal curve where the height corresponds to the semi-amplitude of the planet's RV signal, K, and the curve's period corresponds to the periodicity of the Doppler shifts observed in the stellar spectrum (Figure 1.2).

For cases where the mass of the host star can be determined using other means, a Keplerian fit to the RV data produces the semi-major axis of the planet's orbit and a lower limit on the planetary mass ($m\sin i$). Although the true mass of the planet can be significantly

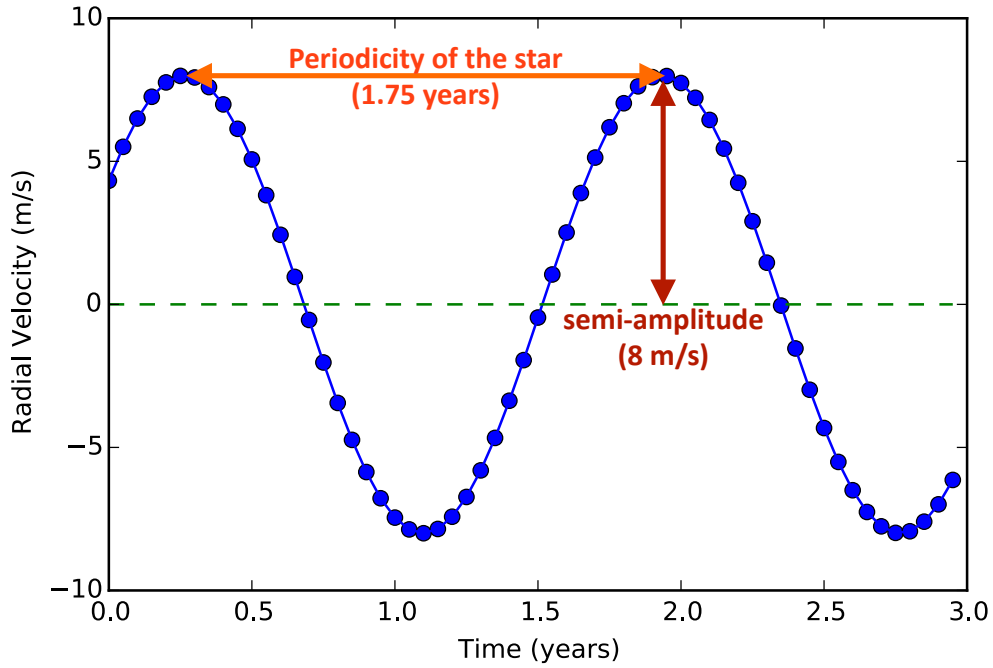

Figure 1.2: A schematic of the Radial Velocity signal a planet imparts on its host star

different from the minimum mass based on the planet's inclination, the probability that the orbital inclination is between two randomly chosen values $i_1 < i < i_2$ is given by:

$$\text{Prob}(i) = |\cos i_2 - \cos i_1| \tag{1.4}$$

Thus the minimum and absolute mass values agree within a factor of 2 ($m_{pl} \leq 2\, m_{pl} \sin i$) as long as the planet's inclination is between 30 and 90° which, according to Equation 1.4, occurs in roughly 87% of cases (Eggenberger and Udry, 2010).

1.2 Current state of the field

The radial velocity method has been used to measure masses for over 700 exoplanets (Akeson *et al.*, 2013). RV science lead to the detection of the first multi-planet system, three planets orbiting Upsilon Andromeda published in Butler *et al.* (1999), produced the timing estimates needed to observe the first transiting planet, HD 209458b (Charbonneau *et al.*, 2000; Henry *et al.*, 2000), and provided the first hints that super-Neptunes existed via the Rossiter-McLaughlin effect (Sato *et al.*, 2005).

Early detections were biased towards massive planets on short period orbits (e.g. Mayor and Quelos, 1996; Marcy and Butler, 1996; Butler *et al.*, 1996a) because of the resulting large semi-amplitude (many 10s - 100s of m s^{-1}) these planets impart on their host stars, and the $\sim$ 10 m s^{-1} precision floor that existed for optical spectrographs at that time. Doppler precision improved to 3 m s^{-1} for the first time in 1996 (Butler *et al.*, 1996a) and reached down to 1 m s^{-1} for the first time with the commissioning of the High Accuracy Radial velocity Planet Searcher (HARPS) spectrograph in 2004 (Rupprecht *et al.*, 2004).

Over the past decade, new, purpose-built instruments including the Planet Finder Spectrograph on the Magellan Clay telescope, HARPS-N on the Telescopio Nazionale Galileo and the Levy Spectrograph on the APF have been installed specifically to address the need for high quality RV observations that will expand the semi-amplitude parameter space to which we are sensitive (Crane *et al.*, 2006; Cosentino *et al.*, 2012; Vogt *et al.*, 2014b). These instruments, each of which represents a significant step forward in RV precision capabilities, enabled the detection of smaller, less massive bodies such as the two super Earths orbiting Kapteyn's star

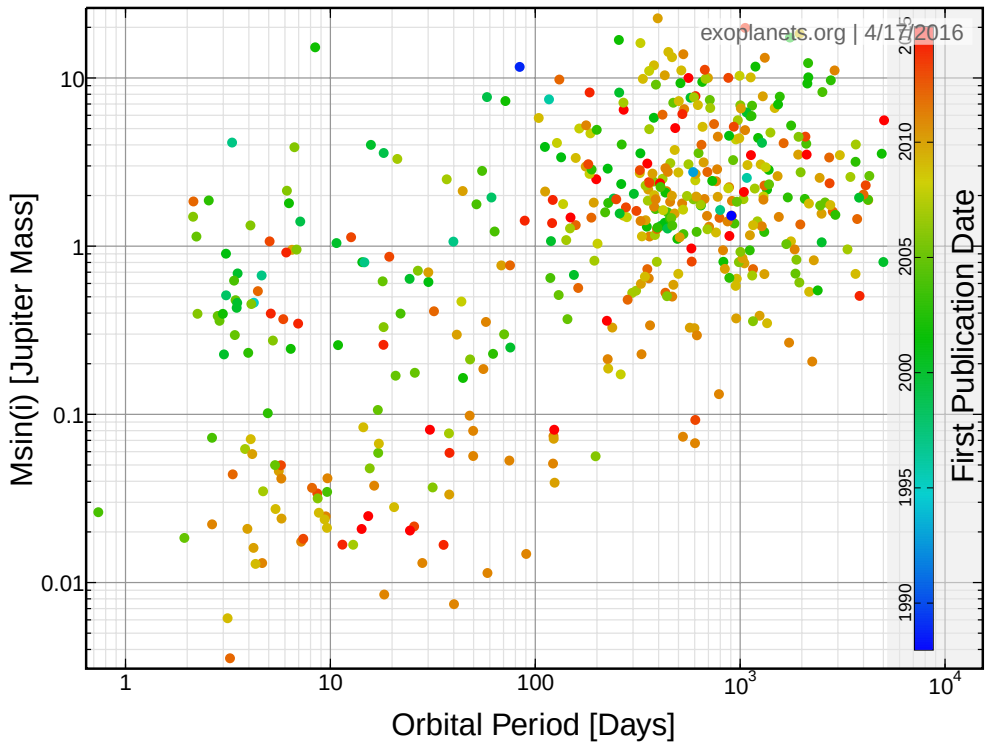

Figure 1.3: Orbital periods and minimum masses of planets detected using the RV method, data and plot created with exoplanets.org (Han *et al.*, 2014).

(4.8 and 7.0 $M_\oplus$, Anglada-Escudé *et al.* (2014)) and HD 219134b (3.4 $M_\oplus$, Vogt *et al.* (2015)), among many others (Figure 1.3).

With the advancement to precision levels of a few m s^{-1} RV science began detecting the signatures of close-in, low-mass systems of planets, something that defied conventional theories of planet formation as our own solar system contains no such objects. The first such discovery was the triple-Neptune system orbiting HD 69830, where all of the planets have semi-major axes less than 0.62AU. For this system, the dispersion among the RV measurements before fitting any of the planetary signatures amounted to only 3.7 m s^{-1}. while the RMS dispersion of the post-fit residuals was just 0.8 m s^{-1} (Lovis *et al.*, 2006). More recently, a

system made up entirely of short-period super Earths was discovered around the nearby star HD 7924 (Fulton *et al.*, 2015) and another containing a broad range of planets (six total planets, ranging from a short period super-Earth to a Saturn mass planet on a 6 year orbit) was detected around the nearby K dwarf star HD 219134 (Vogt *et al.*, 2015).

With the continued instrumental improvements to RV precision and the allocation of more time on large telescopes (Magellan, Keck, etc) the number of planets detected using the RV method grew steadily from 1997 and 2011, but after 2011 the discovery rate experienced a dramatic downturn (Figure 1.4). This is due in part to the fact that significant telescope time has been dedicated to transit follow-up after the success of missions like NASA's *Kepler* (Coughlin *et al.*, 2015). But is also because observers are working to detect ever smaller planetary signals, which require increasing RV precision, exponentially more RV observations over a longer timeline and fighting against a number of noise sources that become delimiting factors at the sub-m s^{-1} level. For reference, one of the most precise RV planet detections yet published was a 0.77 m s^{-1} signal from a $3.6M_{\oplus}$ planet in a 58.43 day orbit around HD 85512, achieved using data from the ESO's HARPS spectrograph (Pepe *et al.*, 2011). This detection, made using 185 observations (with an average single-measurement of 0.67 m s^{-1}) over 7.5 years, showcases the difficulty of detecting a low mass, terrestrial planets.

1.2.1 Challenges in precision RV planet detection

Real planetary signals are never as clean and well defined as the schematic shown in Figure 1.2. The radial velocity (RV) precision obtainable for any star is a quadrature sum of noise contributions from Poisson photon statistics, stellar jitter, and instrumental errors, $\sigma_{tot}^2 =$

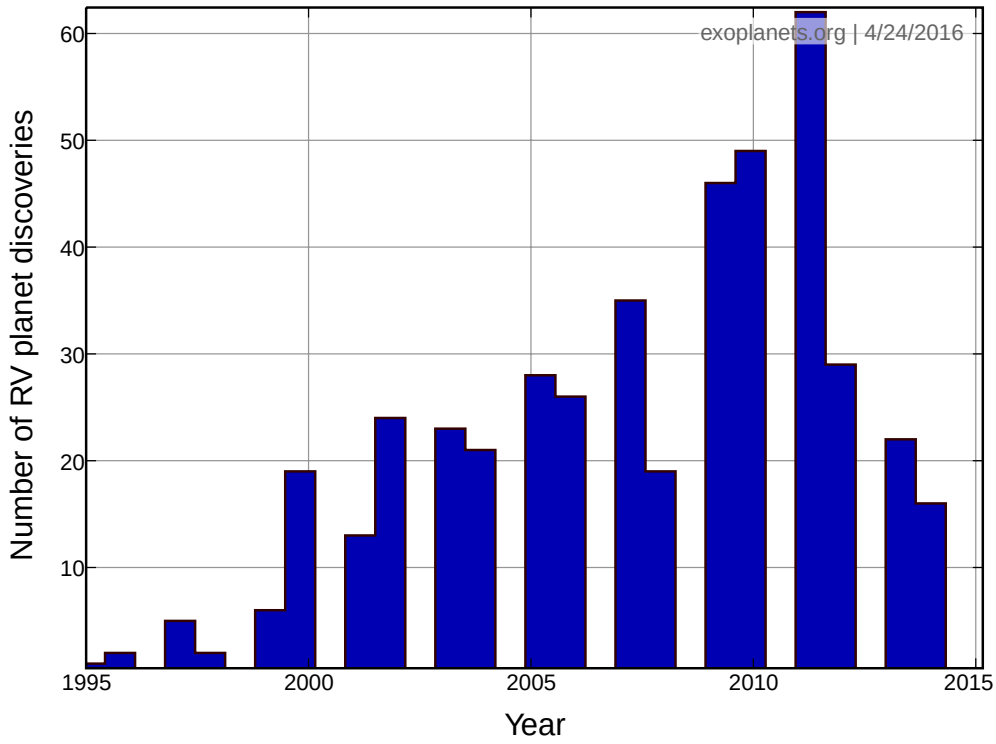

Figure 1.4: Discovery timeline for planets detected using the RV method, data and plot created with exoplanets.org (Han *et al.*, 2014).

$\sigma^2_{poisson} + \sigma^2_{jit} + \sigma^2_{inst}$. Because of how these noise sources add, it is necessary to address all of them simultaneously in order to decrease the uncertainty in RV detections.

As an example, imagine that a nearby, bright, late G dwarf such as Sigma Draconis (HD 185144), with V = 4.7, $M_* \sim 0.87\ M_\odot$ and $L_* \sim 0.43 L_\odot$ generates normally distributed stellar jitter with σ = 0.7 ms^{-1}, and that long-term instrumental precision and Poisson errors amount to σ = 0.7 ms^{-1}. These figures are in excellent concordance with the σ =1.1 ms^{-1} total RMS scatter of the APF velocity measurements obtained for this star during Q2-4 2013 (Vogt *et al.*, 2014b). A hypothetical $3M_\oplus$ planet orbiting at a = 0.65 AU from Sigma Draconis receives the same energy flux that Earth receives from the Sun, and induces a radial velocity half-amplitude K = 0.4 ms^{-1} in its P = 200 day orbital period. If stellar and instrumental errors are uncorrelated and normally distributed, the detection of such a planet would not be difficult, as suggested by the periodogram in Figure 1.5, where the three horizontal lines represent False Alarm Probabilities of 0.1%, 1%, and 10% respectively from top to bottom.

Looking at this example, it is clear that a careful and thorough characterization of both the activity exhibited by a star and the noise contributed by the telescope/instrument being used to take the observations (σ_{jit} and σ_{inst}, both of which are larger in individual observations than the signal created by the theoretical planet itself) is key to detecting any low amplitude signals in an RV dataset.

1.2.1.1 Instrumental noise

As RV precision approaches the 1 m s^{-1} level, the noise contributed by the instrument itself can become a delimiting factor in attaining the level of data needed for cutting edge sci-

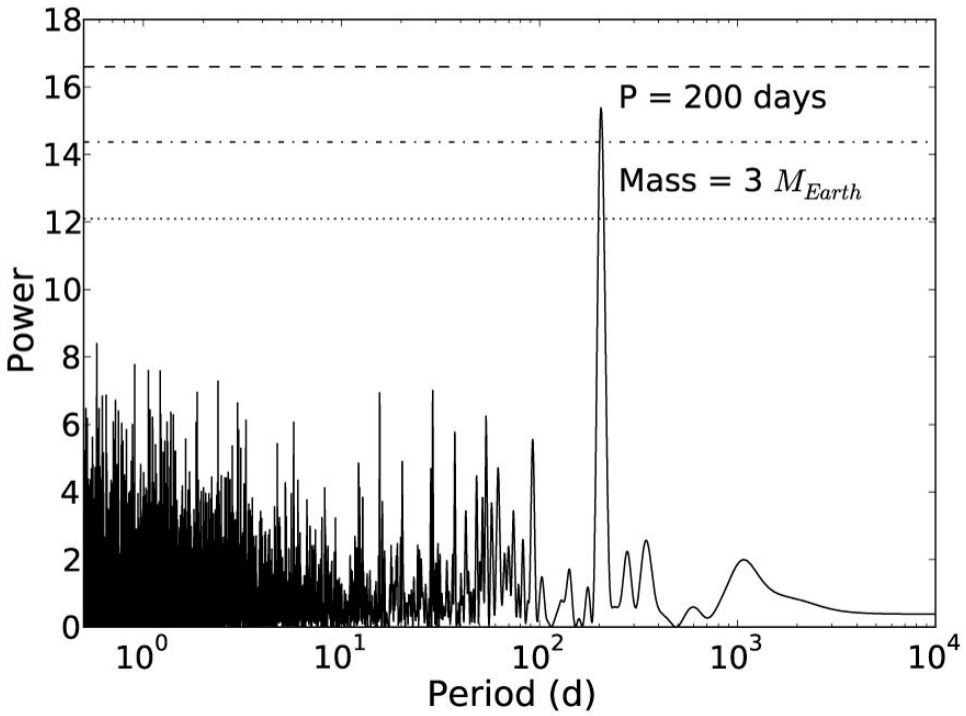

Figure 1.5: Periodogram of 500 randomly chosen synthetic velocities obtained over a 5-year period assuming 1 m s^{-1} all-in Doppler precision and the presence of a 3 $M_\oplus$ planet in a 200-day orbit about a 0.87 $M_\odot$, V = 4.7 K0V primary.

ence. This noise can be due to the spectrograph itself moving as a result of vibrations; changes in the temperature and/or air pressure which can shift the spectra and affect focus; motion of the photocenter of the spectrographic slit due to guiding errors, focus, seeing fluctuations, or atmospheric refraction; or uneven illumination of the spectrograph slit and/or the optical train (Podgorski *et al.*, 2014). What makes the instrumental noise especially tricky to address is the difficulty that comes with trying to disentangle it from the stellar signal. Even the highest quality RV data products contain both astrophysical noise from the stars themselves and instrumental noise from the telescope and instrument used to obtain the observations. Further, when working with only one telescope/instrument there is no way to separate the effects of these two sources of noise.

Because it is so difficult to properly quantify and characterize a given instrument's noise signature, RV spectrographs have been built to be increasingly stable over the past decade. Approaches to this include passive athermalization of the struts that hold the instrument's camera (Vogt *et al.*, 2014b), putting the echelle grating inside a vacuum controlled chamber (Crane *et al.*, 2006), or putting the entire instrument inside a temperature and vacuum controlled enclosure (Cosentino *et al.*, 2012). Yet even HARPS-N, the most stable spectrograph currently in operation, adds a 1.0 m s^{-1} σ_{inst} term into their error budget when fitting planetary signals (Motalebi *et al.*, 2015).

1.2.1.2 Stellar noise

Radial-velocity perturbations related to stellar activity are referred to as "stellar jitter". Stellar jitter is caused by magnetic phenomena at the surface of stars (spots, plages, etc)

which induce radial-velocity variations as they evolve both temporally and spatially (Saar and Donahue, 1997; Saar *et al.*, 1998). The level of a star's jitter depends on its effective temperature, stellar activity, and projected rotational velocity (Saar *et al.*, 1998; Wright, 2005; Isaacson and Fischer, 2010a), but these dependencies have not been modeled in detail yet. Typical values of stellar jitter are $\sim$ 5 m s^{-1} for slowly rotating, chromospherically quiet G-K dwarfs (Santos *et al.*, 2000; Wright, 2005) and up to 50 m s^{-1} for young, active, mid-F5 to early-M (Paulson *et al.*, 2004). Because of these significant signals, precision Doppler planet searches tend to focus on old, quiet, slowly rotating stars - qualities assessed using metrics like the R'$_{HK}$ parameter which represents the fraction of a star's bolometric flux emitted by the chromosphere in the Ca II H and K lines (Noyes *et al.*, 1984).

Yet even inactive stars often present signals on the order of a few m s^{-1} , which can drown out evidence of a small planet. The low K signals associated with star spots can be especially dangerous, as long-lived spot patterns will cause variations in the star's absorption lines which are then modulated by the rotational period of the star and can mimic a planetary signal (Queloz *et al.*, 2001; Bonfils *et al.*, 2007). This had lead to a number of published planet detections that were later refuted/retracted when it was realized that the star's activity signature lined up with the published planetary signal (e.g. Robertson and Mahadevan, 2014; Rajpaul *et al.*, 2015). When the star is instead observed for much longer than the typical lifetime of a single star spot, the spot signals becomes incoherent and are incorporated into the star's RV signal as noise (Eggenberger and Udry, 2010). While the stellar activity is less prone to being falsely characterized as Keplerian in this case, it will still increase the difficulty of detecting actual planetary signals in the data.

1.3 A dedicated, automated telescope with a stable, high-resolution optical spectrograph

The Automated Planet Finder (APF) telescope at Lick Observatory was designed specifically for the detection and characterization of exoplanets around bright stars (V < 12) at the 1-2 m s^{-1} level. When striving for the detection of small planetary signals, it is crucial that the overall precision of the RV data be well below the semi-amplitude that the planet induces on its host star. Obtaining a high overall precision requires the minimization of a variety of variables. The design of the APF and the accompanying data reduction pipeline used by our team directly addresses the four largest effects, as detailed below.

1.3.1 High Resolution

Increased resolution (at the R >$\sim$100,000 level) provides two key advantages for RV planet detection efforts. The first is that it enables a more detailed modeling of the star's absorption lines in all RV exposures, increasing the information content of a given spectrum and allowing for a more precise determination of the relative shift of the star's lines between spectra taken at different times. This result is most apparent in planets that have numerous, narrow, spectral lines; namely small, cool, M-dwarfs (Burt *et al.*, 2015).

Secondly, high resolution spectra have the potential to be used as an indicator of stellar activity to help weed out false positive planet detections. In spectra where individual absorption lines are spanned by a relatively high number of resolution elements, line bisectors, which trace the shape of stellar absorption lines and identify variations due to star spots and other activity

induced phenomena, can be constructed for each individual observation. When comparing the bisector velocity span and radial velocity values of active stars, a clear anti-correlation is often seen. In some cases, this allows observers to approximately correct the RV measurements for the influence of the spots (Queloz *et al.*, 2001).

The APF telescope is paired with the cross-dispersed Levy echelle spectrograph which is capable of resolutions up to 140,000 using the 0.5" slit, and produces normal RV observations (taken through the 1" slit) with typical resolutions of 90,000-100,000.

1.3.2 High Cadence

High cadence observations can be used to help extract planetary signatures from RV data if the planet's signal is not significantly higher than the dispersion observed in its observations, as is often the case with small planets or planets orbiting noisy stars. A large number of observations that thoroughly cover the planet's RV phase curve is also critical for ruling out false positives, especially given the relatively high number of free parameters in the orbital solution for multi-planet systems. One promising result suggests that stable spectrometers may be able to average over stellar noise and reach precisions below 0.5 m s^{-1} , at least for some stars. After removing the signals of three super-Earth planets orbiting HD 20794, Pepe *et al.* (2011) found that the RMS of their residual velocities decreased from 0.8 m s^{-1} to 0.2 m s^{-1} when the data was binned in 1 - 40 night intervals.

In addition to beating down the photon noise and correlated stellar jitter, high cadence observations can also be used to characterize the stellar noise signatures of a star's magnetic activity. Preliminary results indicate that a sufficiently dense sampling properly covering the typi-

cal timescales of the different noise sources (star spots, plages, and convective inhomogeneities) lead to significant improvements in planet detection limits (Dumusque *et al.*, 2011).

With 80% of its time dedicated to the detection and characterization of extrasolar planets, the APF's observing approach is designed to obtain high cadence observations of interesting RV targets. In addition, the telescope's high overall efficiency (see §2.3.4) helps to lower the exposure time necessary on individual targets so that, if necessary, the same star can be visited multiple times throughout the night to help average over noise that happens on the timescale of a few hours.

1.3.3 Instrument Stability

High resolution and high cadence observations are only useful if they are spread out onto a stable spectrograph. As noted above, instrumental errors are one of the main noise terms in determining the overall error budget for a given RV observation. These errors come from a variety of sources, including 1) changes in temperature in the spectrograph which cause thermoelastic distortions of the spectrograph optical train that in turn shifts the spectra on the detector and changes the focus; 2) changes in atmospheric pressure which cause structural deformation of the spectrograph; 3) the motion of the spectrograph itself due to vibrations of the facility as a whole or of the instrument itself 4) stresses induced upon the spectrometer structure that cause strains and bending in the mechanical structure or 5) changes in air temperature, pressure, and even humidity inside the instrument which change the index of refraction of the air. All of these events can result in lateral shifts of the spectra and focus errors (Podgorski *et al.*, 2014).

The Levy spectrograph sits inside a temperature stabilized chamber which we can

control to a precision of 0.1°C. This keeps the yearly and daily temperature swings on Mt. Hamilton (spanning 90°between seasons, and often 20°or more just over the course of one night) from influencing the instrument. The Levy is not pressure controlled, however, and shifts in the spectrograph's position that correlate with changes in the atmospheric pressure are noticeable over hourly-daily timespans. Fortunately our RV reduction software is capable of noticing and removing these shifts, which are of the same order as planetary signals, through the use of wavelength calibrating I_2 absorption lines, so the lack of vacuum control does not affect our science at the 1m s^{-1} level (Vogt *et al.*, 2015). The telescope itself is operated mainly in a "wind-shielding" mode, which keeps the shutters open just enough to track the target star through each exposure and thus helps to limit the amount of wind-shake inside the dome which would otherwise lead to vibrational instabilities (Lanclos *et al.*, 2014).

1.3.4 Internal Uncertainty

Radial Velocity internal uncertainty is defined as the RMS about the mean of the velocity values of the 700+ individual 2Å chunks that make up a single stellar spectrum, divided by the square root of the number of chunks. Thus, the internal uncertainty represents errors in the fitting process, which are dominated by the photon noise. The internal uncertainty does not include potential systematic errors associated with the instrument (σ_{inst}), nor does it account for astrophysical noise (σ_{jit}) associated with the star and therefore represents only a lower limit to the accuracy of the data for finding companions (Burt *et al.*, 2015).

Without the ability to extract RV values from stellar spectra with sub-m s^{-1} precision, there is little a telescope facility (even one that addresses the resolution, cadence and stability

criteria discussed above) can do to detect small semi-amplitude signals. In addition to being the only way to detect subtle planetary signatures, being able to produce data with a small internal uncertainty also provides the clearest picture of what the target star's activity looks like and allows for potential characterization and removal of correlated activity signatures. Since the APF's commissioning, we have been using the RV reduction pipeline first presented in Butler *et al.* (1996a). This pipeline has continued to evolve over the past two decades, and has demonstrated the ability to produce sub-m s^{-1} signals on a variety of recent publications (see e.g. Burt *et al.*, 2015; Vogt *et al.*, 2015).

1.4 Thesis outline

Taken together, the APF telescope, Levy echelle spectrograph and the Butler reduction pipeline form a specialized and competitive approach to RV exoplanet science. In the following pages, I present my work using and improving the APF telescope and the Levy spectrograph, from the facility's commissioning in 2012 through Spring of 2016. In Chapter 2 I present an overview of the telescope and instrument themselves, making particular note of the various ways in which they meet the high resolution, high precision and longterm stability criteria outlined above. Then in Chapter 3 I describe the development and implementation of the dynamic scheduler that autonomously operates the APF each night, making minute-to-minute decisions about the best stars to observe based on both atmospheric conditions (seeing, cloud cover, etc) and the science goals of my team. Chapter 4 describes the detection of one of the APF's first planets, GL 687, a Neptune mass planet orbiting a nearby M-dwarf star. The APF's

two multi-planet system detections are then discussed in part in Chapter 5. Next I describe the next generation scheduler that I am currently designing/testing in order to optimize the APF's collaboration with NASA's upcoming TESS mission in Chapter 6, and predict what contributions the APF will be able to make to the planetary mass-radius diagram. Finally, I conclude in Chapter 7 with a summary of current and upcoming plans for the APF, emphasizing the role it can play as we transition from planet detection to planet characterization with TESS and the James Webb Space Telescope coming on line later this decade.

Chapter 2

Overview of the Automated Planet Finder

2.1 Introduction

The Automated Planet Finder (APF) is a 2.4m, f/15 telescope located at the UCO's Lick Observatory, atop Mt. Hamilton. The telescope has been specifically optimized to detect and characterize extrasolar planets via high precision, radial velocity observations using the Levy spectrometer. Observing time on the telescope is divided such that $\sim$80% is spent on exoplanet related research and the remaining $\sim$20% is made available to the University of California consortium for other science goals.

The APF achieved first light in Winter 2012/2013 and began producing science quality observations in Summer 2013. The exoplanet time on the telescope is currently operated under a shared-time policy in which two teams (one based at UC Santa Cruz and one based at UC Berkeley) each get 40% of the observing time each quarter after programs that help to finance the telescope are taken off the top. This procedure was implemented in Winter 2013/14

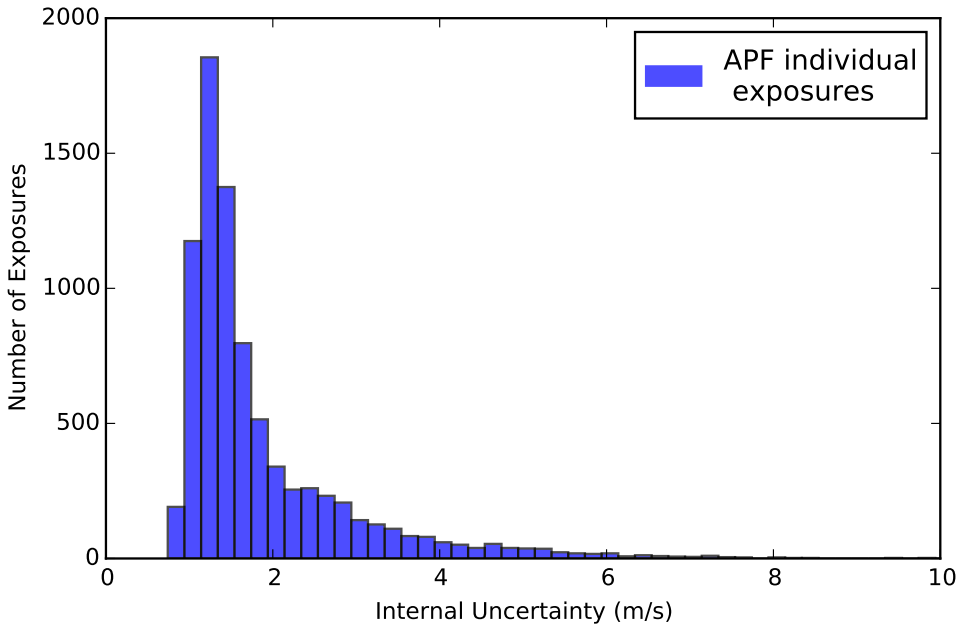

Figure 2.1: Internal uncertainty values for the UCSC APF team's RV exposures between July 1, 2013 and March 1, 2016.

and works on a whole-night allocation system.

Between July 1, 2013 and March 1, 2016 our team at UCSC has obtained $\sim$ 8300 individual RV exposures (meaning that no binning has occurred) spanning some 1100 hours of open shutter exposure time. The internal uncertainties (see §3.2.2 for a detailed explanation of this parameter) of the individual exposures are shown in Figure 2.1. The prominent spike of exposures at $\sim$ 1 m s^{-1} precision showcases the APF's performance abilities and establishes its position as a world-class RV facility.

2.2 Technical Specifications of the APF

2.2.1 Telescope Characteristics

The telescope has an Alt-Az mount and two Nasmyth foci. At one of these foci sits the Levy Spectrometer, a high-resolution prism cross-dispersed echelle optimized for high precision radial velocity research. The other focus is currently vacant but offers a well-corrected 2 arc-minute diameter FOV. The diameter of M2 is kept small to minimize central obstruction losses, and mirrors M2 and M3 are coated with enhanced silver for higher efficiency in the visible. M3 is also on a motorized rotation stage that provides rapid (30-second) switchover between the two Nasmyth foci.

The telescope is housed in an Ice-Storm dome that is slaved to the telescope and co-rotates with it. The dome has dual shutters that can be used either in a split- shutter mode for best wind protection, or with both shutters over the top to enable access to targets at elevation angles below 43 degrees. Both telescope and dome can slew at 3 degrees/sec in azimuth and 2 degrees/sec in elevation. The telescope can point all the way down to the horizon, can work down to about 15 degrees elevation without vignetting, and up to within 3 degrees of the zenith. There are no other limitations on sky coverage. The dome includes AC units to keep the internal temperature close to the expected nightly average and large vent doors to allow rapid temperature equalization.

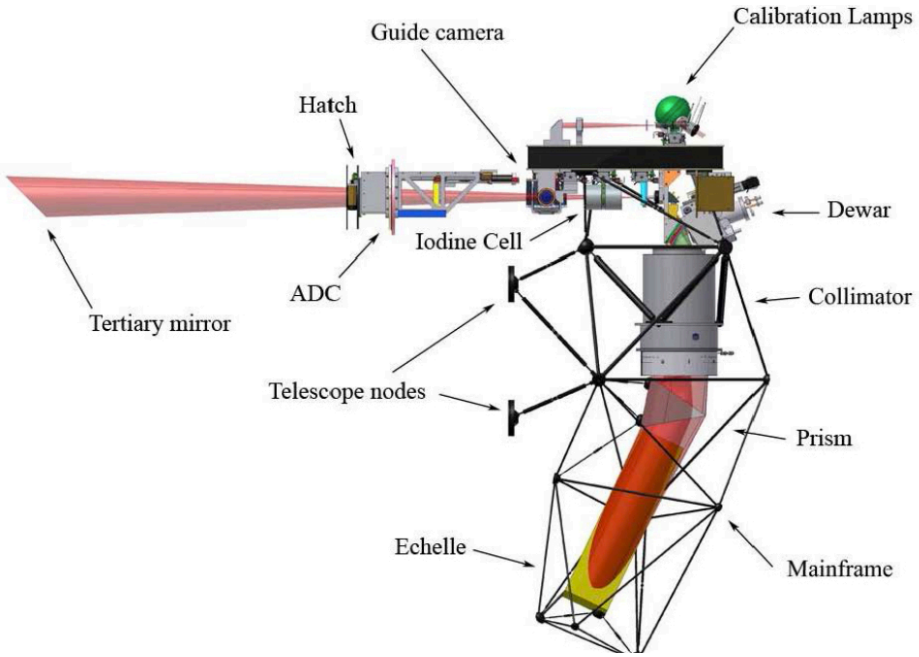

Figure 2.2: A schematic of the APF's optical train, starting with the beam from the tertiary mirror.

2.2.2 Levy Spectrometer Characteristics

The Levy spectrometer is a prism cross-dispersed echelle. It features a 200mm diameter collimated beam and achieves a throughput (resolution x slit width product) of 114,000 arcseconds. The optical train (2.2) is supported within a determinate structure Invar space-frame that has been optimized to provide a high degree of passive athermalization to hold constant focus, image scale and image position. An all-dioptric f/3.17 lens group, used in double-pass, serves as both the collimator and camera. Cross-dispersion is done by a prism, also used in double pass. Further characteristics of the spectrometer can be found in Table 2.1.

Table 2.1: Levy spectrometer characteristics

Parameter	Characteristics
Collimator/camera	EFL 483.4 mm; f/3.17
Grating	41 gr/mm R-4 Echelle (214x840mm)
Detector	E2V CCD42-90
Detector dimensions	2048x4608
Pixel size	13.5 μm
Dispersion at 5500Å	1.46 Å/mm or 0.0197 Å/pixel
Spectral coverage	3743–9800Å(small gaps above 7500Å)
Order separation	8" at 7800Å, increasing to 13" at 3700Å
Max spectral resolution	∼150,000 at 5500Å
Thermal control	passive athermalization, insulated housing, temperature control at 0.1C
Slit dimensions (w x l)	0.5x8", 0.75x8", 1x8", 2x8", 8x8", 1x3", 2x3", 1x12" , 2x12"
Maximum slit length	7.5" (without order overlap)
Filters	none
CCD readout time	∼40s
CCD readout noise	3–4 electrons

Table 2.1 (cont'd): Levy spectrometer characteristics

Parameter	Characteristics
Arc lamps	Thorium-Argon, 50W incandescent
Wavelength calibrations	Iodine absorption cell
Fringing	Some visible redward of $\sim$6500Å

2.2.3 Atmospheric Dispersion Corrector

Light incoming from the tertiary mirror (M3) first enters an input hatch that is used to help keep out dirt and dust and then encounters a trombone-style atmospheric dispersion corrector (ADC). The ADC removes, to very high degree, the dispersion caused by atmospheric refraction that spreads the stellar seeing disk at the slit into a spectrum. If not removed, such dispersion causes image motion, light loss at the slit, and variable (elevation dependent) echelle order separation. Uncompensated atmospheric dispersion at 15° elevation, together with the 3740-9500Å spectral range of the Levy's echelle format, produces a widening of the stellar seeing disk into a spectrum that is over 7 arc-seconds long at the slit. Such dispersion generally would not be aligned with the slit, producing significant spectrally-dependent light loss and image motion, both of which would also be elevation dependent. This style of ADC works extremely effectively, and produces essentially perfect atmospheric dispersion compensation all the way down to 15° elevation.

2.2.4 Guide Camera

The APF relies on having a telescope with very tight closed-loop guiding specifications, and uses a rather different scheme for the guider camera optics. Instead of guiding on

light spilled off of reflective slit jaws, or off of a reflective slit aperture, as is often done, the APF guider system uses a beamsplitter to pick off 4% of the light, presenting a fully symmetric and un-vignetted stellar seeing disk to the guide camera. We originally used a pellicle beamsplitter, uncoated on one side, and antireflection-coated on the other side as the beamsplitter. However, the pellicle was sensitive to mechanical vibrations in the telescope structure and was thus replaced by a 3-mm thick fused silica plate, uncoated on the front side and AR-coated on the back side.

2.2.5 Target Acquisition

Targets are acquired using a Princeton Instruments PhotonMax camera. This guide camera uses a thermo-electrically cooled frame-transfer CCD with 16 μum pixels in a 512x512 format (8.2mm x 8.2mm). It has both a conventional and a charge-multiplying readout amplifier; the former enables acquisition of targets as faint as Vmag=15 while the latter can access target as faint as Vmag=18. The image scale is 0.107 arc-sec/pixel, yielding a 55”x55” FOV. All-sky pointing of the telescope is excellent at about 3–4" RMS down to 15° elevation, so targets always end up in the guider FOV. There is no image rotator. The guider is fed by a beam-splitter that directs 4% of the incident light to the guider camera. Guiding is thus done directly on a small fraction of the image, rather than on light spilled off of slit jaws. The entrance slit is not viewable during guiding. Instead, a guide box is superimposed on the CCDTV image that marks the location of the slit. An exposure meter function keeps track of photons falling within the slit box, and can be set to terminate the exposure at some desired exposure value. More importantly, the exposure meter also calculates the photon-weighted time centroid

of each observation that is required for computing accurate barycentric corrections.

- Magnitude limits of guider: V$\sim 4-15$ (in safe mode); down to V=18.5 with charge multiplication mode, though this will require further software effort to provide safeguards for the camera.

- Guider FOV: 55" x 55" at 0.108"/pixel

- Telescope pointing accuracy (absolute): < 3 - 4" RMS (for elevations 15-88°)

2.3 Observing Performance

2.3.1 Spectrograph Stability

To ensure an optimal observing set up, we periodically asses the stability of the determinate magnesium invar structure to which the Levy spectrograph is attached. Monitoring the spectrograph's movement over weeks or months allows us to identify thermal shorts with the outside of the instrument enclosure, and to characterize the Levy's response to changes in atmospheric pressure as the enclosure is not pressure controlled.

The stability analysis is based on a series of ThAr lamp exposures taken through the pinhole decker of the instrument. We take one pinhole exposure at the beginning of each night's observing to create a long-term baseline, in addition to occasional all night series of exposures to track the instrument's short term response to environmental conditions. These exposures create a 'map' of spectral lines which are then fed into a Fourier shift analysis algorithm that can determine shifts in both the echelle dispersion and cross-dispersion directions.

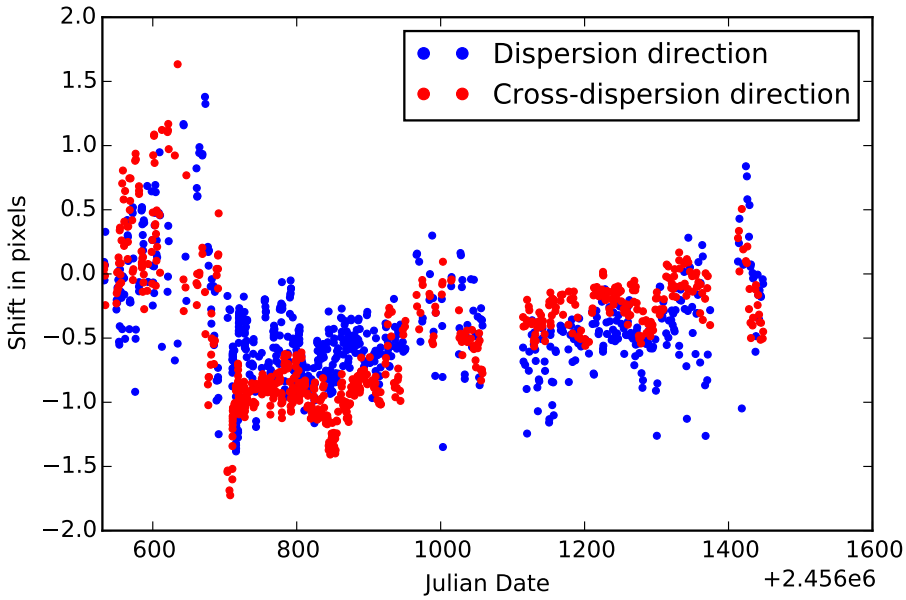

Figure 2.3: A time series of shifts observed in the Levy spectrograph via ThAr exposures taken through the pinhole decker. Blue points are the shifts in the dispersion dimension and red points are shifts in the cross-dispersion direction. The two shifts rarely span more that 0.5 pixels over a single night, and stay within $\sim$ 2 pixels of their respective mean values over the 3 year time span depicted in this plot.

All pinhole ThAr images have their shifts calculated with respect to a zero point image taken in Fall 2013. The directional shifts rarely span more that 0.5 pixels over a single night, and stay within $\sim$ 2 pixels of their respective mean values over the 3 year time span depicted Figure 2.3. The dispersion and cross-dispersion direction shifts correlate strongly with one another, producing a Pearson Product-Moment Correlation value of r = 0.511, which suggests that whatever is causing the individual shifts is affecting both directions. Further examination of the cross-correlation function of the two shift series showed no notable lag between the two series, so the shifts happen simultaneously and one direction is not pulled along by the other.

The movement of the spectrograph over time is mostly decoupled from the average

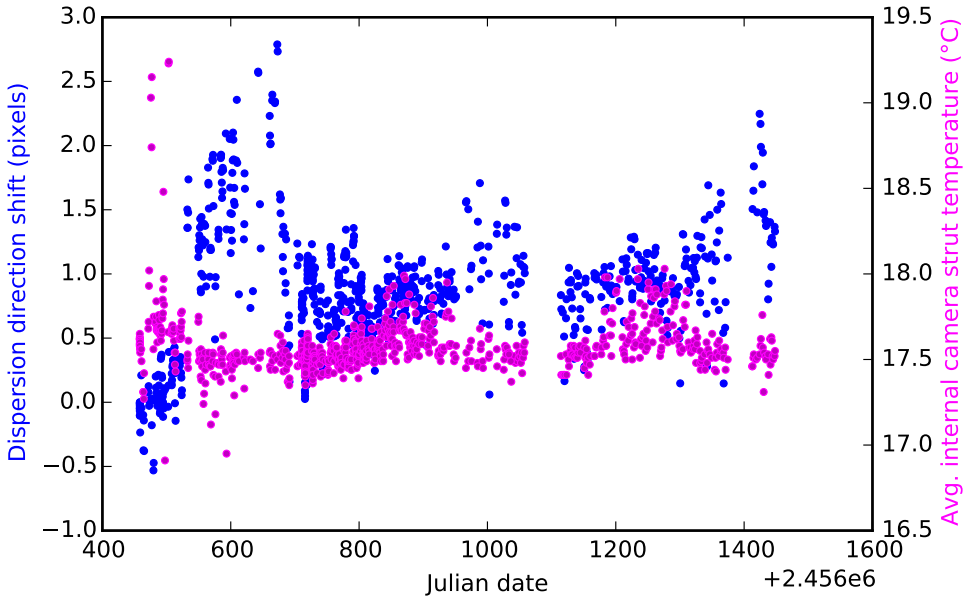

Figure 2.4: The dispersion direction shifts of the Levy spectrograph compared to the average temperature of the internal struts that support the instrument's camera. The struts are controlled to $\sim$ 0.1 °C and the spectrograph's motion is mostly decoupled from the small temperature swings that do exist.

temperature of the internal struts that hold the camera in place, which we have been controlling to $\pm$ 0.1°C since November of 2013 (Figure 2.4). The internal camera struts do show some correlation with the outside dome temperature, however, especially when the outside temperature exceeds 17°C (Figure 2.5). During the hottest parts of the year (generally August-Sept), the internal strut temperature can be increased by up to 0.5°C from its nominal value of 17.5°C, as seen in the pink data of Figure 2.4 at $\sim$ 900 and 1300 days. This cross-talk shows that our internal strut control loop is better at heating than it is at cooling, and emphasizes why the instrument's athermalization design is key.

The spectrograph's movement in the dispersion direction does, however, clearly cor-

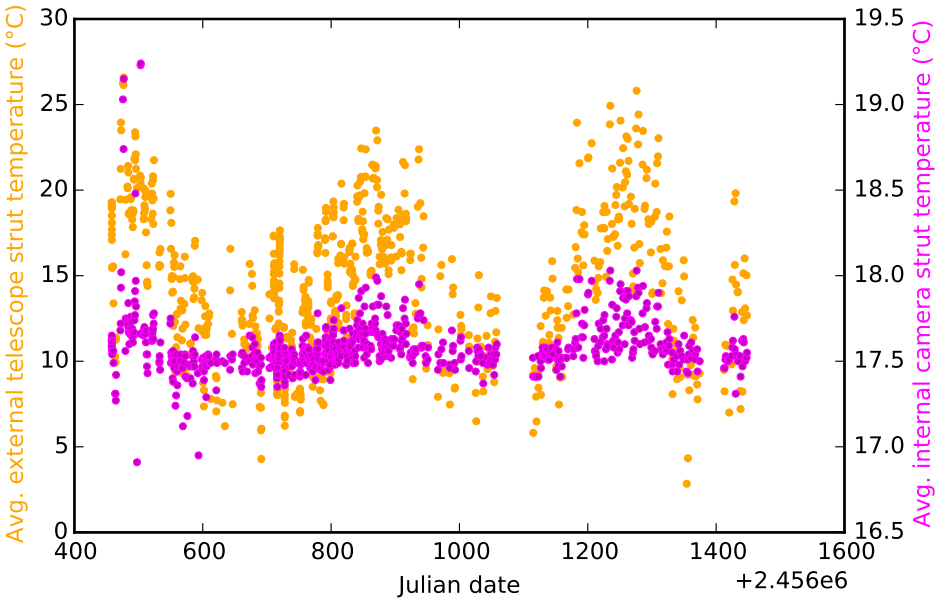

Figure 2.5: The external dome temperature (averaged from the 4 telescope struts) plotted against the average temperature of the internal camera struts. There is some correlation over the seasons, especially in the summer with the dome temperatures reach >17°C. Even though we actively control the internal strut temperatures to $\pm$ 0.1°C, they still feel the effects of the outside temperatures when the cooling control loop can't produce enough flow.

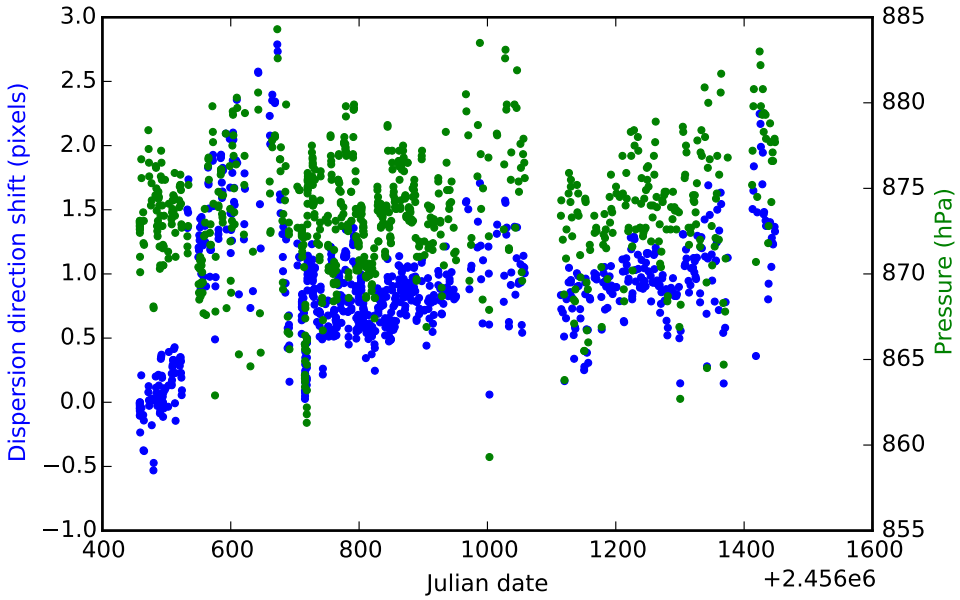

Figure 2.6: The Levy spectrograph's movement in the dispersion direction correlates with the outside atmospheric pressure. This is not surprising as the Levy is not pressure controlled, and further investigations reveal no evidence of systematic errors in our RV data due to the pressure-driven shifts.

relate with the atmospheric pressure (Figure 2.6). As noted above, the Levy is not pressure controlled, nor is it in a vacuum sealed enclosure, so this correlation is not surprising. A pressure shift of 20 hPa, which is not an unreasonable range to cover over the course of 24 hours, can move the spectrograph roughly 1 pixel in the dispersion direction. So over an 8-10 hour night of observing, we can see spectrograph shifts of up to 0.5 pixels (which explains much of the variation in Figure 2.3). Upon realizing the magnitude of this effect, we carried out a series of experiments looking for systematic errors in our RV standard stars' data due to these pressure-driven shifts, but found no evidence of errors or reason for concern (see §2.3.2 for more detail).

2.3.2 Environmental parameters

Fulton *et al.* (2015) report use of radial velocity data obtained using the APF telescope to characterize a multiple-planet system orbiting HD 7924. In the course of their analysis, they investigated correlations with environmental parameters such as air pressure and CCD temperature, and find improvements up to a factor of two in the RMS of APF velocities when the data is de-trended against these factors.

In light of these results, we initiated a similar set of experiments. We compared the velocity values for the RV standard stars HD 185144, HD 9407 and HD 10700 against all of the environmental parameters stored for each observation. We detect no notable correlation between the Doppler velocity measurements and any of these factors. When fitting linear trends to the velocities as a function of air pressure, we see the RMS change from 1.84 ms^{-1} to 1.81 ms^{-1} for HD185144, 2.13 ms^{-1} to 2.11 ms^{-1} for HD 10700 and 2.46 ms^{-1} to 2.33 ms^{-1} for HD 9407. Similarly, when fitting against the CCD temperature we see changes in the RMS of 1.84 ms^{-1} to 1.71 ms^{-1}, 2.13 ms^{-1} to 2.13 ms^{-1} and 2.46 ms^{-1} to 2.42 ms^{-1} for HD 185144, HD 10700 and HD 9407, respectively.

In our view, it is likely that the difference in correlation strengths stems from the different instrument focusing procedures and data reduction pipelines used in the separate analyses of the HD 7924 and HD 219134 spectra. Due to the lack of evident trends, we have elected not to decorrelate our data set against environmental variables.

2.3.3 Resolution

Figure 2.7 shows a representative plot of the Levy's spectral resolving power at 5120 Å, which is in the center of one of the bluest orders in the Iodine region. The resolutions are derived from spectra of the B2V star HR 496 taken through the telescope's 0.5, 0.75, 1 and 2 arcsecond slits with the iodine cell in the path. With the 0.5" slit, which we use for taking the template observations that are key to our RV science, resolutions at or above 100,000 are achieved across the entire Iodine region, in some cases reaching as high as 150,000. All of the curves in Figure 2.7 were taken at a single, best-focus position for the instrument. If instead we were to focus the instrument anew when using different slits or when studying different regions of the echelle format, we would see further improvements in the spectra's peak resolution. Our standard, non-template, RV observations are all taken through the 1 arc-second slit, which produces resolutions of 90,000 - 120,000 throughout the iodine region.

2.3.4 Telescope efficiency

The APF optical path exposes incoming light to a total of 47 surfaces including the telescope mirrors and the CCD. A thorough understanding of the telescope's total efficiency is key to developing accurate exposure time calculators and for monitoring the condition of the primary, secondary and tertiary mirrors over month to year timescales. In order to quantify the telescope's efficiency, we target spectrophotometric standard stars presented in Massey *et al.* (1988) and/or Stone (1996) and observe them on the APF using the "wide-open" 8"x8" slit.

After the spectral orders of each observation are extracted, we smooth the spectra, remove cosmic rays and clip off 200 pixels at the beginning and end of each order to help

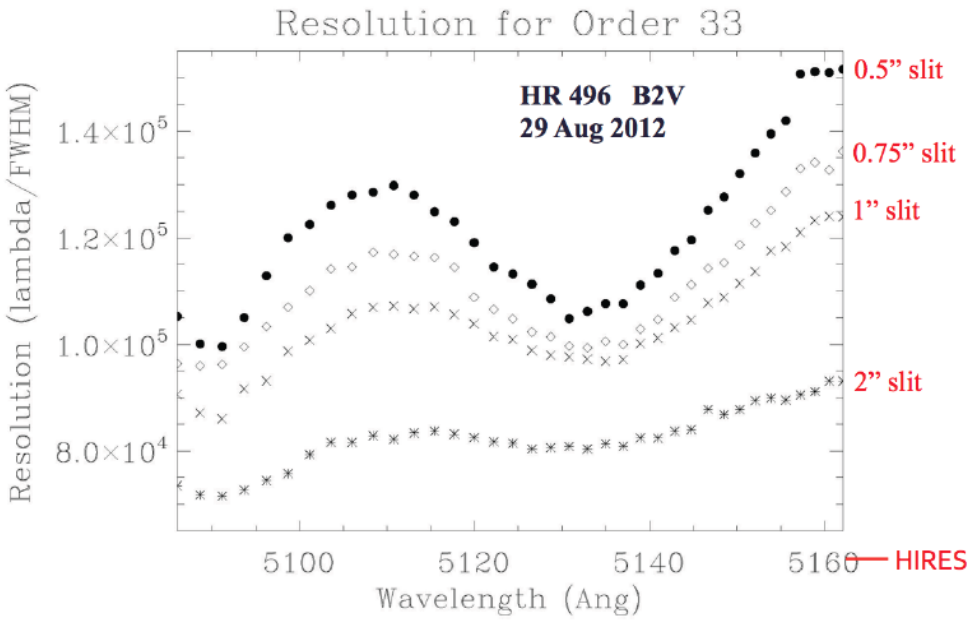

Figure 2.7: Spectral resolving power of the Levy at 5120 Å through a variety of slits.

reduce edge effects. We fit a 4th order polynomial to each order's smoothed spectrum, and use the fit and the observation's exposure time to determine the incident rate of photons/second/pixel in each pixel of that order. We then determine the "expected" number of counts based on the procedure outlined in Massey *et al.* (1988), where we estimate the atmospheric extinction for each observation using Hayes and Latham (1975) which is based upon work done in-part at Lick Observatory. By comparing the expected and actual photon/second rates at the wavelengths tabulated in the spectrophotometric standard reference papers listed above, we can calculate the total efficiency of the entire optical train of the APF - from the primary mirror all the way through to the CCD.

The most recent efficiency estimates (performed in September of 2015) predict a peak efficiency of $\sim$ 14% at 5700 Å. Figure 2.8 depicts efficiency curves for a variety of photometric

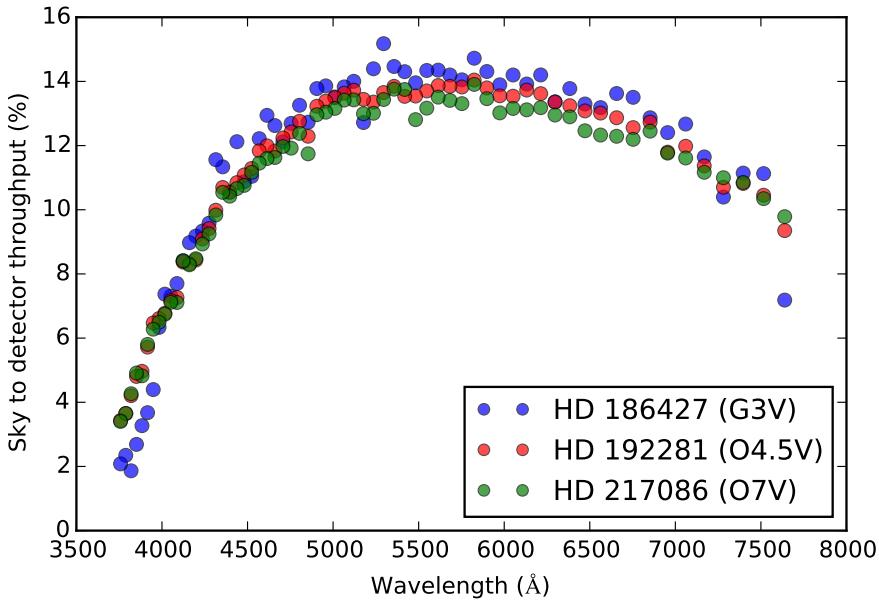

Figure 2.8: APF efficiency values for photometric standard stars, derived from observations taken through the 8”x8” slit on September 7th, 2015.

standard stars.

Chapter 3

The capabilities and performance of the Automated Planet Finder telescope with the implementation of a dynamic scheduler

3.1 Introduction

The Doppler Velocity technique now has two decades of success in enabling extrasolar planetary detections. It has produced candidates with masses approaching that of Earth, and has been especially successful in detecting long period planets. In recent years, Doppler Velocity confirmations have proven vital to gaining an understanding of the planetary candidates discovered by photometric space missions, especially Kepler. Doppler Velocity campaigns are responsible for 31% of the 1854 confirmed planetary discoveries in the past three decades, but they account for 87% of the 330 confirmed planets with periods longer than 1 year (Zolotuhkin, 1995). Ground-based facilities, furthermore, are amenable to the operation of long-term sur-

veys due to their relativity low construction and operational costs along with their ability to be upgraded as instrumentation improves.

In order to find analogs of our own solar system, we need to extend the catalog of successful radial velocity (RV) planet detections to encompass longer-period planets (particularly true Jupiter analogs) and smaller mass, short-period planets. This means observing efforts must increase their temporal baselines and cadence of observation to more effectively populate each planet's RV phase curve.

The Automated Planet Finder, located at the Mt. Hamilton station of UCO/Lick Observatory, combines a 2.4-m telescope with a purpose-built, high-resolution echelle spectrograph, and is capable of 1 m s^{-1} Doppler Velocity precision(Vogt *et al.*, 2014b). Eighty percent of the telescope's observing time is specifically dedicated to the detection of extrasolar planets. This time is shared evenly between two exoplanet research groups, one at UC Santa Cruz and one at UC Berkeley. Time is allocated in whole night segments, with a schedule developed quarterly by the telescope manager. Target lists and operational software are developed separately as the two exoplanet groups are focused on different types of planet detection/follow up. For a description of the UC Berkeley planet detection efforts, see Fulton *et al.* (2015). The remaining 20% of telescope time is dedicated to at-large use by the University of California community. All users are allowed to request specific nights if it is beneficial to their science goals (for example: to obtain RV values while a planet transits its star), and such requests are taken into account by the telescope manager when setting the schedule.

The APF leverages a number of inherent advantages to improve efficiency. For example, its Levy spectrometer, a high-resolution prism cross-dispersed echelle spectrograph with a

maximum spectral resolving power of R$\sim$ 150,000, is optimized for high precision RV planet detection (Radovan *et al.*, 2010; Vogt *et al.*, 2014b). A full description of the design and the individual components of the APF is available in Vogt *et al.* (2014b).

To support long-running surveys, we have developed a dynamic scheduler capable of making real-time observing decisions and running the telescope without human interaction. Through automation and optimization, we increase observing efficiency, decrease operating costs and minimize the potential for human error. The scheduler's target selection is driven by balancing scientific goals (what we *want* to observe based on scientific interest, required data quality, and desired cadences) and engineering constraints (what we *can* observe based on current atmospheric conditions and physical limitations of the telescope). To address these criteria, we need to know how the velocity precision extracted from a given stellar spectrum depends on inputs that can be monitored before and during each observation. We have assessed the influences of the various inputs by analyzing 16 months of data taken on the APF between June 2013 & October 2014.

The plan of this paper is as follows: in § 3.2 we describe the current APF radial velocity catalog, paying special attention to the variety of spectral types and the frequency of observations. In § 3.3 we evaluate the relations between velocity precision and parameters including stellar color and V band magnitude, airmass, seeing, date of observation and atmospheric transparency and we explain how these relations inform the nightly decision-making process executed by the observing software. In § 3.4 we outline the parameters that were assumed to be important prior to on-sky observations, but that have since been determined to have little relevance. In § 3.5 we describe how the relevant relations are integrated into the schedul-

ing software, and we discuss its structure, its dependencies, and its capabilities. In § 3.6 we discuss other automated and semi-automated observatories and highlight both the similarities and differences between those systems and that employed by the APF. Finally we conclude in § 3.7 by reviewing the application of the APF's automated observing strategy to the telescope's current and upcoming observing scientific campaigns.

3.2 Data set description

3.2.1 Description of observing terminology

This paper differs from most publications discussing precision radial velocity work in that all of the plots, equations and discussions presented are based on individual, un-binned exposures of stars. It is well known that pulsation modes (p-modes) in stars cause oscillations on the stellar surface, adding noise to the RV signal. It has also been well documented that the noise imparted by these p-modes in late-type stars can be averaged over by requiring total observation times longer than the $\sim 5-15$ minute periods typical of the pulsation cycles (Santos *et al.*, 2004; Dumusque *et al.*, 2011). Thus the majority of radial velocity publications, especially those dealing with exoplanet detections, present *binned* velocities and error values. That is, they take multiple, individual *exposures* of a star during the night and then combine (bin) them to create one final *observation* with its own velocity and internal error estimate (Dumusque *et al.*, 2011; Burt *et al.*, 2014; Fulton *et al.*, 2015). The binned observations therefore contain more photons than any individual exposure, but, more importantly, average over the pulsation modes on the star, and therefore exhibit a measurably smaller scatter (Figure 3.1).

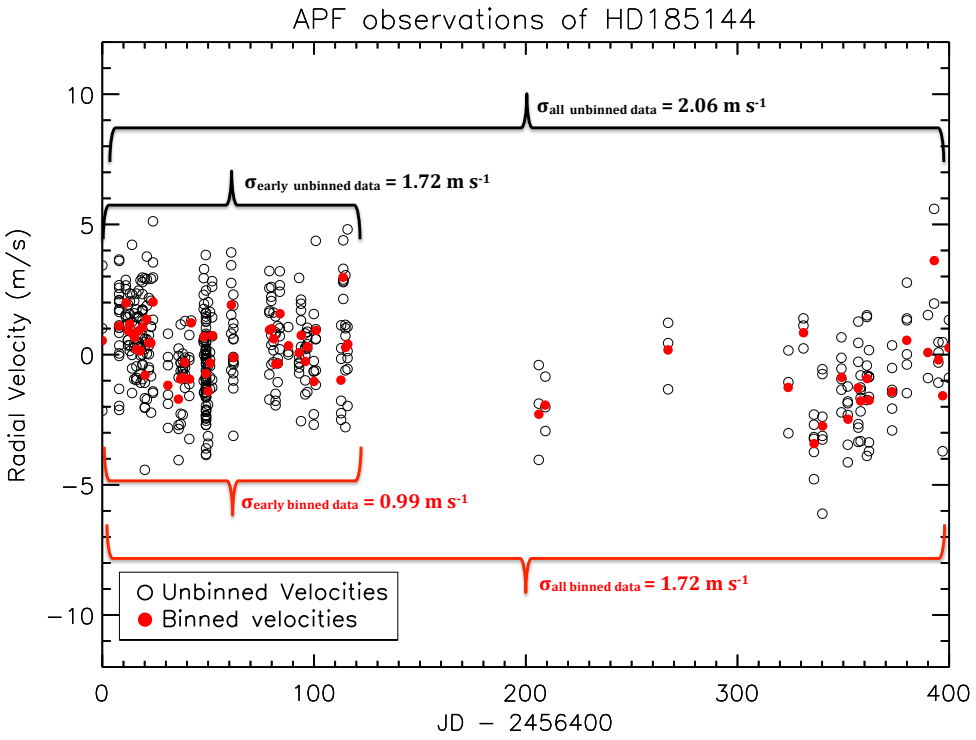

Figure 3.1: Our radial velocity dataset for the RV standard star HD 185144 showing the individual exposures (open circles in black) and the resulting binned velocities (solid circles in red). The binned velocities have a much smaller RMS value (0.99 m s^{-1} for the first 120 days and 1.72 m s^{-1} over the entire 400 day span, compared to the 1.72 m s^{-1} and 2.06 m s^{-1} exhibited by the un-binned data over the same respective time spans) due to their increased signal-to-noise. Additionally the individual exposures are each ∼60 seconds long while the binned velocities span at least ∼5min, so they average over the p-modes of the star. This paper uses the individual exposure data when carrying out all further analyses and calibrations. The change in the RMS values between the first 120 days and the full data set is largely due to a change in observing strategy. After the first 4 months we started observing HD 185144 less frequently and with fewer exposures in each observation to allow for more targets to be observed each night.

These terms, exposure and observation, will be used specifically throughout this paper to help make clear to the reader whether we are talking about an exposure - a single instance of the shutter being open and collecting photons from the star, or an observation - the combination of all exposures taken of a star over the course of a night. Similarly, exposure time will refer to the open shutter time during one exposure and observation time will refer to the total open shutter time spent on a target between all exposures. In the case of the star's observation consisting of only one exposure, then the observation time is equivalent to the exposure time.

3.2.2 The APF data set

The APF's star list is made up of legacy targets first observed as part of the Lick-Carnegie exoplanet campaign using the HIRES spectrograph on the Keck I telescope. Stars for the Lick-Carnegie survey were selected based on three main criteria:

- Spectral type between F5 and M : stars with spectral types earlier than F5 exhibit oscillations that can produce pseudo-Keplerian signals, and are fast rotators with few spectral lines so they are avoided

- Single stars : no stars with companions closer than 5", as this can lead to scattered light from the nearby companion making its way into the spectrograph slit and contaminating the target star's signal

- Quiet stars : Only stars without large amounts of emission in the Ca II H & K line cores are permitted, as core emission in these lines is an indicator of stellar chromospheric activity (Noyes *et al.*, 1984) which means increased stellar jitter, making the planet signals

harder to detect.

The resulting Lick-Carnegie target list is comprised of ∼1800 stars, which have been monitored using Keck/HIRES over the past two decades. When creating the initial target list for the APF, the Lick-Carnegie star list was culled for targets with V magnitudes brighter than 12 and declinations above -20°. In order to efficiently prove the APF's capabilities, we selected stars with suspected short-period planets (P <100 days) that required only 1-2 more rounds of phase coverage to verify. The presence and the false-alarm probabilities of these short-period, Keplerian signals were determined by analyzing the existing Keck/HIRES RV datasets using the publicly available Systemic Console (Meschiari *et al.*, 2009a). Systemic allows users to fit planetary signals to RV data and derive the orbital properties, while also providing tools to handle error estimation and assess orbital stability. This selection process resulted in a list of 127 stars.

The calibrations described in this paper are based on data taken with the APF between June 2013 and October 2014. The data set includes precision Doppler observations of 80 of the 127 stars selected from the Lick-Carnegie survey and this is before the development/inclusion of the dynamic scheduler, thus all data in this paper were obtained using fixed star lists. Our precision Doppler observations encompass spectra of 80 stars and incorporate 600 hours of open shutter time. The stars span spectral types from early G to mid M, have 3.5 <V <12, and are all located within 160 pc (Figure 3.2).

Every APF star has a set of observations containing between one and seven hundred exposures. Individual exposures are restricted to a maximum length of fifteen minutes to avoid cosmic ray accumulation and to minimize uncertainty when calculating the photon-weighted

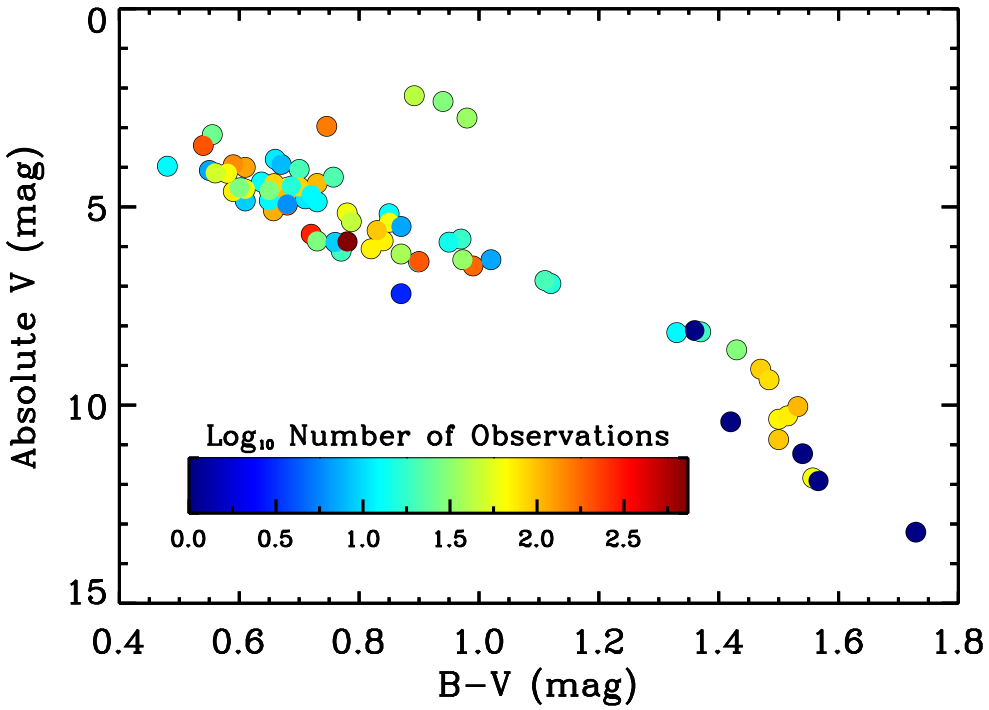

Figure 3.2: Color-Magnitude diagram for stars observed with APF and used in the analysis described herein. Color coding represents the number of exposures that have been obtained for each star. Our dataset spans a wide range in color and magnitude and contains stars with spectral types from F6 to M4.

midpoint times. Additionally, we enforce a total observing time limit of one hour per target per night to ensure that telescope time is not wasted on observing faint objects when conditions are poor.

For each individual exposure, the $\overline{\text{FWHM}}$ (the average FWHM of the star over the integration time) of the guide camera's seeing disk is logged in the FITS image header, along with the total number of photons from the exposure meter and the total exposure time. Colors, magnitudes and distances for the stars are obtained from SIMBAD (Wenger *et al.*, 2000).

All spectra are analyzed using the data reduction techniques described in detail by Butler *et al.* (1996a), which produces a measurement of the stellar RVs and associated internal uncertainties. The reduction pipeline analyzes each exposure's extracted spectrum in 2Å chunks and determines the radial velocity shift for each chunk individually. The final reported velocity is the average over all the chunks, while the internal uncertainty is defined as the RMS of the individual chunk velocity values about the mean, divided by the square root of the number of chunks. Thus the internal uncertainty represents errors in the fitting process, which are dominated by the photon noise. The internal uncertainty does not include potential systematic errors associated with the instrument, nor does it account for astrophysical noise (or "jitter") associated with the star and, therefore, represents only a lower limit to the accuracy of the data for finding companions.

3.2.3 Determining additional systematic errors

We use the APF's 737 individual exposures of HD 185144 (Sigma Draconis, HR 7462), a bright RV standard star, to estimate the precision with which we can measure radial

velocities. It should be noted that the radial velocity values produced by our analysis pipeline are all relative velocities and thus have a mean value set for convenience to zero. We examine the unbinned, or individual, exposures, finding that star's mean internal uncertainty is μ_{int} = 1.0 m s^{-1} and that the mean of the absolute values of its velocity measurements is μ_{abs} = 1.8 m s^{-1}. Because μ_{abs} includes effects from the internal uncertainty *in addition* to other sources of error such as the stellar jitter and the instrument systematics, its value is always higher than the internal uncertainty value for a given exposure.

The difference between these two parameters implies an additional quadrature offset of 1.5 m s^{-1}, which we then generalize as σ_s = 1.5 m s^{-1} (Figure 3.3). We take this offset value to represent the additional error contributions from all other systematics, including the known 5-15 minute pulsation modes of the star that the binned data averages over and the systematics from the instrument. If, instead, we compared the mean internal uncertainty to the standard deviation of the velocity measurements (σ_{vel} = 2.3 m s^{-1}) we would require a larger additional offset term (σ_s = 2.0 m s^{-1})[1]. We note, however, that the data are strongly affected by the velocities of exposures that fall in the outlying, non-Gaussian tail. We thus choose to determine our error estimate using the mean of the absolute values of the velocity measurements (instead of the standard deviation of the velocities) as it mitigates the influence of the outliers.

We use the relations of Wright (2005), which presents radial velocity jitter estimates at the 20th percentile, median and 80th percentile levels to assess the expected stellar activity for

[1] As stated, the internal uncertainties and velocities used in this analysis are extracted from the individual spectra obtained by the telescope. Our normal operational mode determines the internal uncertainties from data binned on a two hour time scale, which is the approach used by Vogt *et al.* (2014b) and yields a standard deviation of σ_{bin} = 1.05 m s^{-1} for HD 185144. This value is notably smaller than the standard deviation of the individual velocities, σ_{vel} = 2.3 m s^{-1}, because we deliberately acquired 6 observations of HD 185144 in order to both average over the pulsation modes and achieve a high precision for the final binned observations.

HD 185144. We find an estimated median jitter of $\sigma'_{rv} = 3.5$ m s^{-1}, and a 20^{th} percentile value of 2.3 m s^{-1}. Noting that the 20^{th} percentile value matches the σ_{vel} for our exposures, obtained over a timespan of 400 days, suggests that the star is in fact intrinsically quiet. That is to say, we expect only 20% of stars with the same evolution metric, activity metric (both described by Wright 2005) and B-V color as HD 185144 to have activity levels less than 2.3 m s^{-1}. Given that we measure $\mu_{abs} = 1.8$ m s^{-1}, HD 185144 is, at a minimum, much quieter than expected based on its color, activity and evolution. Even so, it is reasonable to expect that some fraction of the observed uncertainty is due to the star itself (astrophysical noise) or currently unknown planets rather than instrumental effects, thus indicating that the instrument is performing very well.

To verify that the size of the offset between μ_{int} and μ_{abs} is not specific to the HD 185144 data set, we compare the mean values of these parameters for every star observed by the APF during the time span of Figure 3.3. That is, we apply the same procedure detailed above for HD 185144 to all stars observed during the same date range, and then compute and compare the mean values of μ_{int} and μ_{abs} for each star's set of exposures (Figure 3.4). As expected, the values for the mean of the absolute radial velocity values are always higher than the mean internal uncertainty values because μ_{abs} includes the effects of the internal uncertainty combined with additional sources of error such as the stellar jitter and instrument systematics. Additionally some of these stars are planet hosts, and thus display even higher μ_{abs} values because of the planet's influence. However the quietest, non-planet hosting stars are able to reach μ_{abs} values of slightly less than 2 m s^{-1}, suggesting that the additional error offset value determined using HD 185144 ($\sigma_s = 1.5$ m s^{-1}) is appropriate.

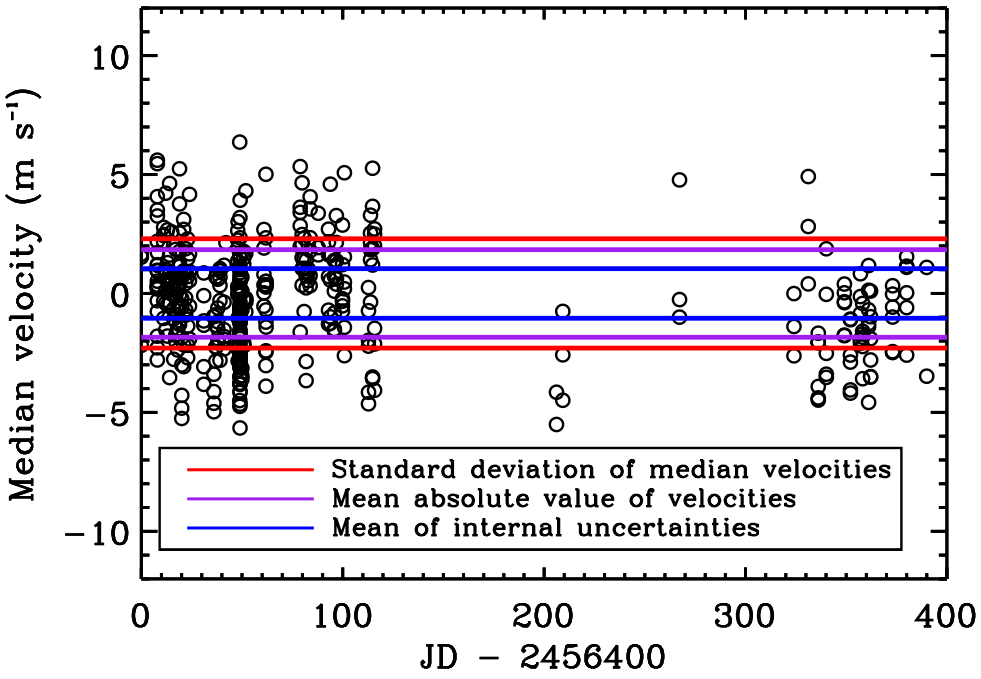

Figure 3.3: Radial velocities from APF exposures on the star HD 185144 [G9V, m_v = 4.68], 737 points in total. The internal uncertainty estimates produced by the data reduction pipeline are noticeably smaller than the actual spread in the data. The internal error does not account for telescope systematic errors or sources of astrophysical noise in the star. Our average internal uncertainty is μ_{int} = 1.0 m s^{-1} (blue line) but we find the mean absolute value of the HD185144 velocity measurements to be μ_{abs} = 1.8 m s^{-1} (purple line). We adopt an estimate that the additional systematic uncertainty in our velocity precision is σ = 1.5 m s^{-1}.

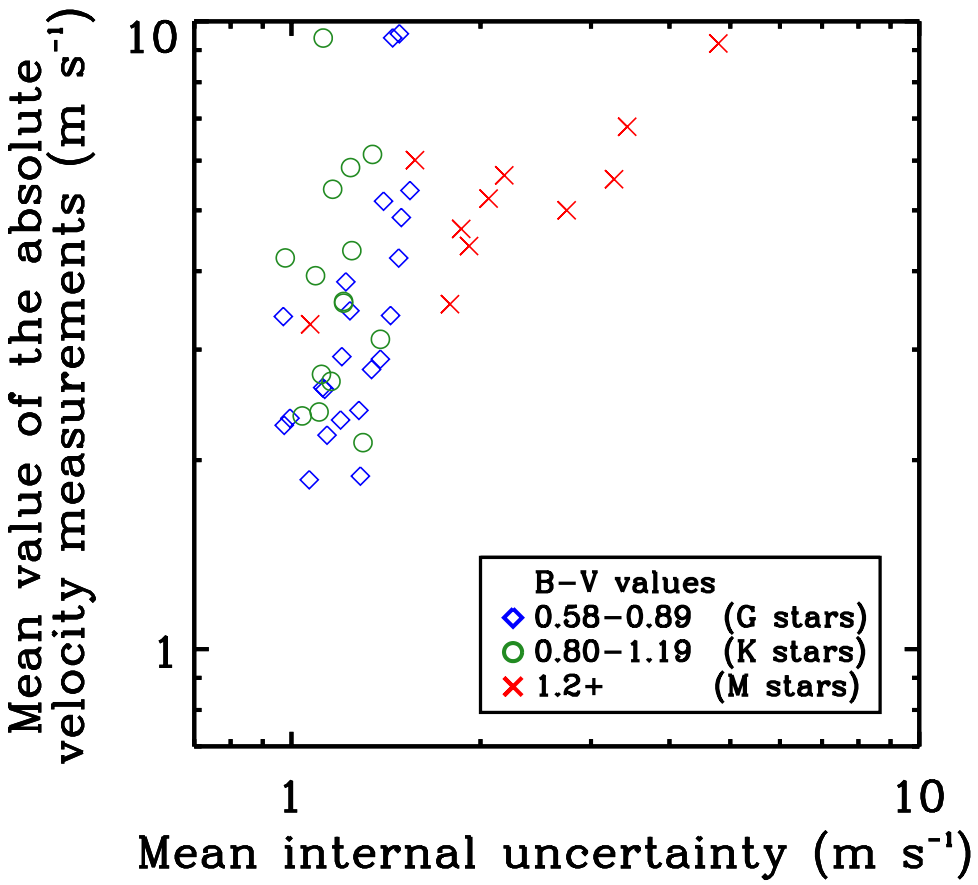

Figure 3.4: Mean values of μ_{int} and μ_{abs} for each star observed during the same time span as the HD 185144 analysis presented in Figure 3.3. The μ_{abs} values are always larger because they include the internal uncertainty *in addition* to other effects such as stellar jitter and instrument systematics. For bright, quiet stars it is possible to reach μ_{abs} values of 1.8 m s^{-1}.

3.3 Observing inputs

To create an efficient and scientifically informative exoplanet survey we must balance scientific interest in a range of target stars with the observing limitations presented by the weather and the telescope's physical constraints.

3.3.1 Parameters of scientific interest

There are a number of criteria of astronomical importance. For each star, the following parameters are utilized by the scheduling software to determine whether the star is given a high rating for observation:

- Observing priority - a numerical rating that reflects the observers' assessment of potential Keplerian signals in the RV data.
- Desired cadence - dictates the desired wait time between observations of a specific target.
- Desired precision - the average allowable internal velocity uncertainty for measurements of a specific target.

Both observing priority and cadence are determined via the observers' examination of the star's existing data set. As mentioned in Section 3.2, we use the publicly available Systemic Console to analyze our RV data sets. The console produces a Lomb-Scargle periodogram from the selected RV data set, which displays peaks corresponding to periodic signals in the data. When a peak surpasses the analytic *false alarm probability* (FAP) threshold defined by this method, the observers note the period and the half-amplitude of the signal and use those values

to decide upon an observing cadence and desired level of precision that will fill out the signal's phase curve quickly and with data points of the appropriate SNR. The desired precision is further refined if the observers have some knowledge of the star's stellar activity, as this sets a lower limit to the attainable precision. Details on the fitting procedures and the statistical capabilities of the Systemic Console are described in detail in Meschiari et. al, 2009.

For each star, this information (along with other characteristics such as right ascension, declination, the V magnitude and the B-V color) is stored in an on-line Google spreadsheet accessible to team members and the telescope software. This database of target stars drives the survey design and target selection while also being easily accessed, understood and updated by observers.

3.3.2 Relating iodine region photons to the internal uncertainty of RV values

In perfect conditions (no clouds, no loss of light due to seeing) all stars that are physically available and deemed in need of a new observation (based on their cadence) are simply ranked by observing priority and position in the night sky and then observed one after another, until dawn. Cloud cover and atmospheric turbulence, however, make such conditions rare. Furthermore, stars with low declinations spend only short periods at low air mass. Consequently there are a substantial number of constraints that affect the quality of an exposure. In order to maximize the scientific impact of each night's exposures, the conditions must be evaluated dynamically, and data taken only when the desired precision listed in the database is likely to be attainable.

To identify the targets that can be expected to attain their desired precision within

the one hour observing time limit, the observing program must link the night-time conditions and the physical characteristics of each star with the resulting internal uncertainty over a given exposure time. To this end, we first relate the internal uncertainty of a given exposure to the number of photons that fall in the iodine (I_2) line-dense region of the spectrum (i.e. the $\lambda \sim 5000-6200$Å bandpass) where our radial velocity analysis is performed.

We fit the relation between internal uncertainty and photons in the iodine region separately for the G and K star data set (comprised of 2790 G star exposures and 957 K star exposures) and the M star data set (comprised of 837 M star exposures). Because information on a star's RV value comes from the location of its spectral lines, we expect the M stars - which contain many more spectral lines - to achieve better precision for the same number of photons. This expectation is validated by Figure 3.5 where a vertical offset between the G/K star best-fit line and the M star best-fit line is evident. Comparing the zero points for the best-fit lines (Table 1), we find a factor of 2 difference between the stellar groups. Thus the M stars reach the same level of internal uncertainty with half the number of photons required by the G and K star population. Additionally, the slopes of both best-fit lines are close to the m= -2 expected for shot-noise limited observations with m= -1.58 and -1.73 for the G/K and M stars, respectively. The fact that the slopes are shallower than m= -2, indicating performance better than shot-noise limited, is reasonable as the internal uncertainty only accounts for the errors resulting from the extraction of the spectrum from the original FITS files. We emphasize that this is just a piece of the error budget, and does not include other random or systematic errors.

The functional form of these best-fit lines is given by Equation 3.1. Note that the numeric values for each variable (in the case of Eq 3.1, A and B) are listed in Table 1. This

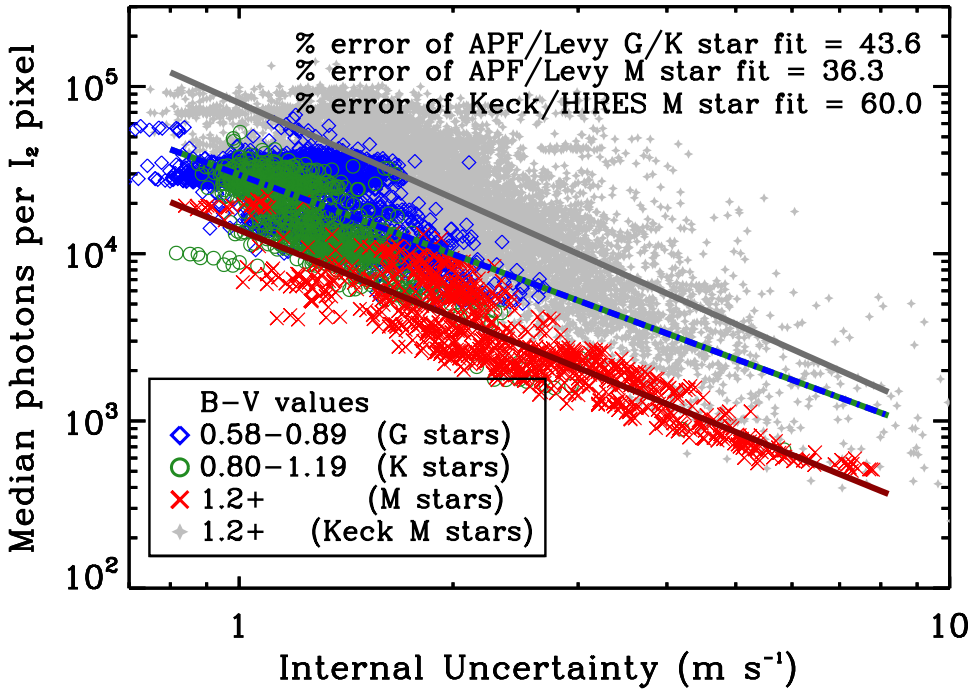

Figure 3.5: Observations of G (blue), K (green) and M (red) type stars during the 1.5 years of APF/Levy observations. We plot the individual 2,790 G star exposures, 957 K star exposures and 837 M star exposures. The gray diamonds represent M star data obtained using Keck/HIRES as part of the Lick-Carnegie planet survey where the Keck/HIRES pixels have been scaled to match the same Å /pixel scale as the APF/Levy (0.0183 /pixel). We find that the G and K stars have the same zero point and the same slope, so we combine these two data sets for this analysis. The green and blue dashed line represents the best-fit to the APF/Levy's combined G and K star dataset, while the red line shows the best-fit to the APF/Levy M star data set which is fit separately due to the increase of spectral lines in later spectral types. As expected, the APF/Levy M stars show higher data precision for the same number of photons in the I_2 region of the spectrum. The percent errors quoted on the figure are calculated using the scatter in the difference between the observed I_2 photons and the I_2 photons from the best-fit lines, so they represent the scatter of the sample and not the error on the mean. The dark gray line is the best-fit to the Keck/HIRES M star data set. Comparing this to the red line reveals that the APF requires 5.75x fewer photons in the I_2 region to achieve velocity precision comparable to Keck/HIRES on M stars down to at least M_v=10.

format will be used for all relations presented in § 3.3.

Functional form of the fits applied in Figure 3.5 :

$$\log_{10}(N_{med}) = A + B \cdot \log_{10}(\sigma_{int}), \tag{3.1}$$

Where N_{med} is the median number of photons per pixel in the I_2 region for a given exposure, and σ_{int} is the estimated internal uncertainty for the resulting radial velocity value.

The gray points in Figure 3.5 correspond to spectra of M stars obtained with Keck/HIRES since November 2002 as part of the Lick-Carnegie planet search. There are 168 stars represented, all with B-V $>$ 1.2, resulting in 8872 individual exposures. In order to compare these individual velocities to those obtained on the APF in a meaningful way, we rescale the Keck/HIRES pixels so that they represent the same range of Å per pixel as those on the the APF/Levy. This involves two different scaling factors as the HIRES instrument underwent a detector upgrade in 2004 that changed its pixel size from 24μm to 15μm, resulting in different sampling values. Applying these factors means that all of the data shown in Figure 3.5 represents the median number of e^- per pixel, where each pixel covers 0.0183 - the native value for the APF/Levy in the I_2 region.

The figure shows that for M stars, the APF requires ∼5.75x fewer photons in the I_2 region to achieve velocity precision comparable to Keck[2] Speed estimates for the APF/Levy,

[2]Based on the work of Bouchy *et al.* (2001), we expect that for K dwarfs the relative speed should scale as the "information content" Q(Connes, 1985), which is proportional to the ratio of the resolutions, $Q \propto (R_{APF}/R_{HIRES})$. For HIRES, the "throughput" (the resolving power times the angular size of the slit) is 39,000" (Vogt *et al.*, 1994a) and for the APF it is 114,000"(Vogt *et al.*, 2014b). Normally HIRES was used with the 0.861" slit giving a filled aperture resolution of 45k while for the Levy a 1" slit is used, so the ratio of the resolutions is 2.5. The Levy demonstrates a larger than expected improvement over HIRES which could be explained by the increased number of lines in the iodine region for M dwarfs. Further investigation is beyond the scope of the current paper but we plan to include such analysis in a future publication. We note that the excellent seeing at MK means that some data were observed

carried out last year (Vogt *et al.*, 2014b), show that the telescope and instrument together are approximately 6x slower than Keck/HIRES. Combining these two effects indicates that the APF has essentially the same speed-on-sky as Keck/HIRES for precision RVs of M stars. This is not altogether unexpected, as HIRES was never specifically optimized for precision RV work. The APF's Levy spectrograph was purpose-built for high-precision, RV science and therefore features much higher spectral resolution and finer wavelength sampling than HIRES. Both of these factors, as well as the significantly higher system efficiency of the APF/Levy optical train over that of Keck/HIRES (Vogt *et al.*, 2014b), combine to make APF as fast as Keck/HIRES for precision RV work on M dwarfs, at least down to M_v=10.

To assess whether the exposures of these stars represent a Gaussian distribution, we compare the standard RMS and the scatter calculated using a Tukey's biweight method around each fit. The Tukey's biweight scatter provides a more robust statistic for data drawn from a non-Gaussian distribution as it less heavily weights the outliers, which are assumed not to be part of a normal distribution (Beers *et al.*, 1990). For the G and K star fit, the standard RMS is 0.182 while the biweight scatter is 0.186. Similarly, for the M stars, the standard RMS is 0.151 while the biweight scatter comes out to 0.155.

In the limit of a true Gaussian distribution, these two metrics would produce the same result. Employing a bootstrap analysis of each method, we find the standard deviation of both the RMS and the biweight scatter of the G and K star sample to be 0.002. Similarly, the standard deviation of both the RMS and the biweight scatter of the M star sample is 0.003. Noting the similarity of these standard deviations with the actual offsets found between the RMS and

with a much higher effective R, up to 90k, which may explain the large scatter we see in Figure 5.

biweight scatter, we determine that the observations for both sets of stars are drawn from a mostly Gaussian distribution.

3.3.3 Real-time effects

3.3.3.1 Data selection

Knowing the median number of photons per pixel in the iodine region required to achieve a given level of RV precision enables us to determine the expected exposure time for a star *if* we know how quickly those photons accumulate. To determine this rate and the relation between the final exposure meter value and the number of photons in the I_2 region (used to set upper bounds on observing time) we study a subset of the year of APF data described in Section 3.2.

Cuts are applied to the main data set to select only those observations taken on clear nights and in photometric conditions, as non-photometric data will induce skew in the results. First, we select only exposures with seeing $\overline{\text{FWHM}} < 2$", which results in 935 individual observations. We then perform separate, multi-variate linear regressions on the photon accumulation rate in the I_2 region of the spectrum and the photon accumulation rate for the exposure meter (Eq 3.2, Eq 3.4) on all remaining data points. In each case, we calculate the variance of deviations from the best-fitting relation for all of the data. We also calculate the variance for all of the points on a given night. We then reject nights using the F-ratio test. Namely, if the standard deviation of a given night is more than twice the standard deviation of the population as measured by the Tukey's biweight then all observations from that night are rejected. This results in data sets of 865 exposures used in the I_2 photon accumulation rate regression and 816 exposures in

the exposure meter photon accumulation rate regression. Points that fall significantly below the regression line are most likely due to clouds while those falling above the line are likely due to erroneous readings from the exposure meter.

Once the nights with large variance have been removed, we repeat the regressions on the remaining points to determine the actual fits described in Section 3.3.3.2. In Figures 3.6 and 3.7 the points in color are those used to perform the linear regressions, while the points in gray are those we rejected after they were deemed non-photometric. Figure 3.8 uses the same set of data as Figure 3.7 in order to keep only the normally distributed exposure meter readings.

3.3.3.2 Linear regressions

To determine the predicted observation time of a star, we perform a multi-variate linear regression using the trimmed dataset resulting from the procedure described in the previous section. The regression estimates the rate at which photons accumulate in the pixels of the iodine region of the spectrum, and accounts for [1] the star's V magnitude, [2] its B-V color, [3] slit loss due to the current seeing conditions, [4] the airmass based on the star's location and [5] the modified date of the observation (Figure 3.6). The modified date is calculated by subtracting the maximum date from each observation following the selection process described above. This makes the zero point of the relationship the value at the time of the last photometric observation. We use the modified date parameter to address the degradation of the telescope's mirror coatings over time. When the mirrors are recoated it will introduce a discontinuity in this parameter, and we will then adjust the zero point of all regression fits based on the new throughput estimates and watch for any changes that develop in the slope of the regressions.

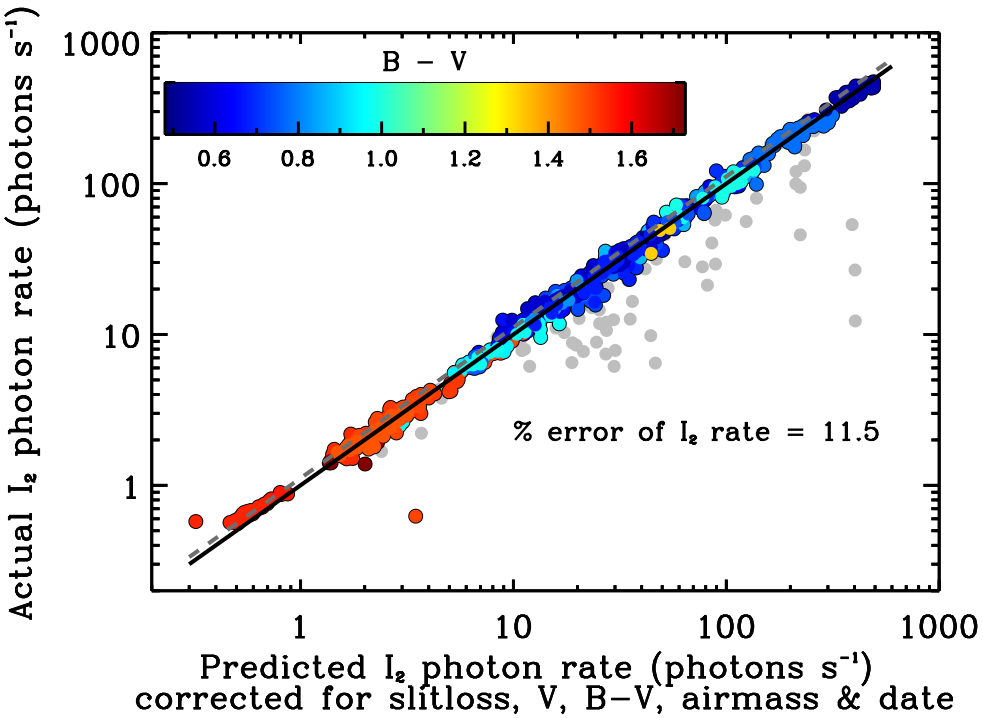

Figure 3.6: Multi-variate linear regression of the iodine pixel photon accumulation rate which incorporates stellar color, stellar magnitude, atmospheric seeing and airmass. Colored points are used in calculating the regression, while gray points have been rejected as non-photometric data as described in Section 3.3.3.1. The black line is a 1:1 relationship, and the grey dashed line shows the relation offset by one standard deviation, which is the limit we use operationally. The strong correlation between the data and the regression line enables prediction of the rate of photon accumulation in the spectrum's iodine region (a value not calculated until the data reduction process) using the stellar properties and ambient conditions. We can thus estimate the observation time required to meet a specific median I2 photon value, and, in conjunction with Figure 3.5, a radial velocity precision.

The multi-parameter fit over these five variables results in a best-fit plane, of which we present a projection in Figure 3.6. To help visualize the goodness of fit, we plot the data on one axis, the linear regression combination on the other and place a 1:1 line on top. This approach is also used when plotting the linear regression in Figure 3.7.

The regression gives :

$$\log_{10}(r_{I_2}) = -\frac{1}{2.5}\left(V_c + \alpha_I(B-V) + \beta_I(\sec(z)) + \gamma_I(\text{MJD}) + C_I\right), \tag{3.2}$$

with

$$V_c = V_m - 2.5 \cdot \log_{10}(f_t), \tag{3.3}$$

where r_{I_2} is the photon accumulation rate in the iodine region, z is the angle of the star relative to zenith, MJD is a modified Julian date and f_t is the fraction of the starlight that traverses the spectrograph slit.

By dividing the number of I_2 region photons necessary to meet our desired RV precision (derived from Eqn 3.1) with the photon accumulation rate in the I_2 region calculated using Eqn 3.2, we can determine the predicted observation time for a star for a specified internal uncertainty in a given set of conditions. These predicted observation times account for atmospheric conditions such as seeing and airmass, but do not address the issue of atmospheric transparency. The APF lacks an all-sky camera with sufficient sensitivity to assess the brightness of individual stars, meaning that we cannot evaluate the relative instantaneous transparency of different regions of the sky. Instead we must determine the transparency during each individual observa-

tion by comparing the rate of photon accumulation we observe with what is expected for ideal transparency. Although the I_2 region photons provide a straightforward way to determine the predicted exposure times, the number of iodine region photons is available only after the final FITS file for an observation has been reduced to yield a radial velocity measurement. Thus we cannot monitor in real time the rate at which they are registered by the detector to assess the cloud cover.

Instead, we compute a transparency estimate during each exposure using the telescope's exposure meter. The exposure meter is created by using series of 2D images from the guider camera that are updated every 1-30 seconds depending on the brightness of the target. Rather than guiding on light reflected off a mirrored slit aperture, as is traditionally done, the APF uses a beamsplitter to provide 4% of incoming light to the guider camera as a fully symmetric, unvignetted seeing disk. This allows a straightforward way to monitor how well the telescope is tracking its target and provide realtime corrections to both under and over guiding - both of which smear out the telescope's point spread function on the CCD and result in broader full width at half maximum values for spectral lines. Guide cameras that utilize the reflected light off of a mirrored slit aperture are significantly more sensitive to these problems in good seeing, as the majority of the light falls through the spectrograph slit. In our experience, the loss of 4% of the star's light is acceptable if it ensures that the telescope's guiding is steady throughout the night and across the different regions of the sky.

After each guiding exposure is completed, the guide camera then passes the 2D FITS images it creates to the SourceExtractor software (Bertin and Arnouts, 1996) which analyzes each image and provides statistics on parameters such as the flux and full-width at half-

maximum (FWHM), which are in turn used to evaluate the current atmospheric seeing. These guide camera images are also used to meter the exposures. Each image is integrated over the rectangular aperture corresponding to the utilized spectrograph slit, with background photons (determined using adjacent, background-estimating rectangles) subtracted off to determine the number of star-generated photons accumulated by the guide camera.

Analysis of the existing APF data suggests that the exposure meter rate (much like the iodine photon accumulation rate) depends on the star's color, its V magnitude, the atmospheric seeing (in the form of slit losses), the airmass and the date of observation. A multi-variate linear regression to the exposure meter rate over these five terms results in the correlation displayed in Figure 3.7.

Because the exposure meter is rapidly updated, we can monitor photon accumulation in real-time during an observation. Atmospheric seeing is already incorporated into the V_c term in the linear regression (Eqns 3.3, 3.4), so any decrease from the expected exposure meter rate likely stems from an increase in clouds and corresponding decrease in atmospheric transparency. The ratio of expected exposure meter rate to observed exposure meter rate provides a "slowdown" factor that the scheduler tracks throughout the night and multiplies by the predicted 'clear night' observation times calculated using Eqn 3.2 to determine a best guess exposure duration.

The regression in Figure 3.7 gives :

$$\log_{10}(r_E) = -\frac{1}{2.5}\left(V_c + \alpha_E(B-V) + \beta_E(\sec(z)) + \gamma_E(\mathrm{MJD}) + C_E\right), \tag{3.4}$$

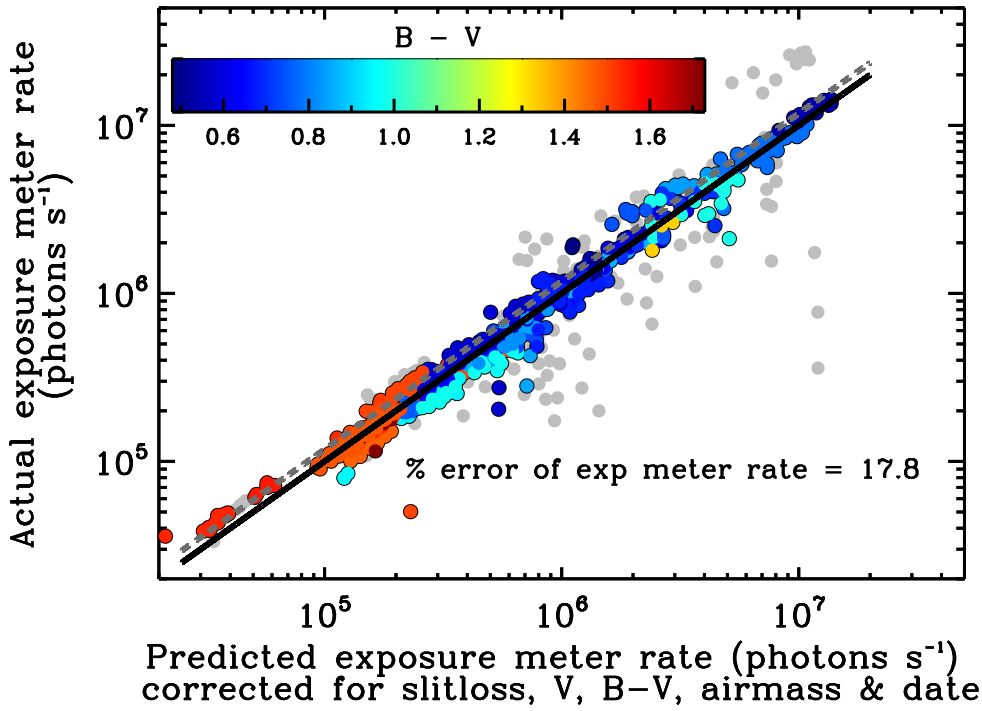

Figure 3.7: Multi-variate linear regression to the exposure meter photon accumulation rate, as measured on the APF guider, which incorporates stellar color, stellar magnitude, atmospheric seeing and airmass. Colored points are used in calculating the regression, while gray points have been rejected as described in Section 3.3.3.1. The black line is a 1:1 relation, and the grey dashed line shows the relation offset by one standard deviation, which is the limit we use operationally. The strong correlation permits prediction of the expected exposure photon accumulation rate for a given star in photometric conditions, and thus provides a measure of the transparency. Any decrease in exposure photon accumulation rate from what is predicted is presumed to arise from decreases in atmospheric transparency brought about by cloud cover.

where r_E is the photon accumulation rate on the exposure meter, α_E, β_E, γ_E and C_E have the same meanings as in Eqn 3.2 but for the exposure meter photon accumulation rate instead of the Iodine photon accumulation rate, z is the star's zenith angle, and V_c is defined in Eqn 3.3.

3.3.4 Setting upper bounds on exposure time

Finally, because of the scatter seen in Figures 3.6 and 3.7, we must ensure that exposures end when photons sufficient to achieve the desired RV precision have accumulated instead of continuing on for extra seconds or minutes. Photons in the I_2 region can't be monitored during the observation. However the APF data set shows a strong relationship between the number of photons obtained in the I_2 region of the spectrum and the photons registered by the exposure meter, which is monitored in realtime.

The telescope's guide camera, which is used for the exposure meter, has a broad bandpass and is unfiltered. This generates a strong color-dependent bias when comparing the guider photons to those that fall in the much narrower I_2 region. We apply a quadratic B-V color correction term to produce the relation shown in Figure 3.8. Combining this with the equations identified in Figure 3.5, we obtain relations that allow us to relate the desired internal precision to the corresponding number of photons in the iodine region of the spectrum, and then to the number of photons required on the exposure meter. The resulting exposure meter threshold is used to place an upper limit on the exposure. This is particularly useful on nights with patchy clouds, where the cloud cover estimate calculated during the previous observation can be significantly higher than the cloud cover in other parts of the sky - resulting in artificially high

predicted observation times. In this case, the exposure meter can be used to stop an observation if the desired photon count is reached early, improving efficiency.

Fit applied in Figure 3.8 :

$$\log_{10}(R) = \delta + \epsilon(\mathrm{B}-\mathrm{V}) + \zeta(\mathrm{B}-\mathrm{V})^2, \tag{3.5}$$

where R is the ratio of photons on the exposure meter to photons in the iodine region of the spectrum.

3.3.5 Combining the fits

The above relations are combined to enable the scheduling algorithm to select scientifically optimal targets. The following list summarizes the combination scheme.

Steps to determining an object's predicted observation time and exposure meter cut-off

1. Query spreadsheet for stellar attributes (V, B-V, required precision, RA, Dec, observing priority).

2. Use Equation 3.1 to determine the desired number of photons in the I_2 region of the spectrum.

3. Use Equation 3.2 to calculate the observation time required to obtain the desired total number of I_2 region photons in ideal transparency conditions.

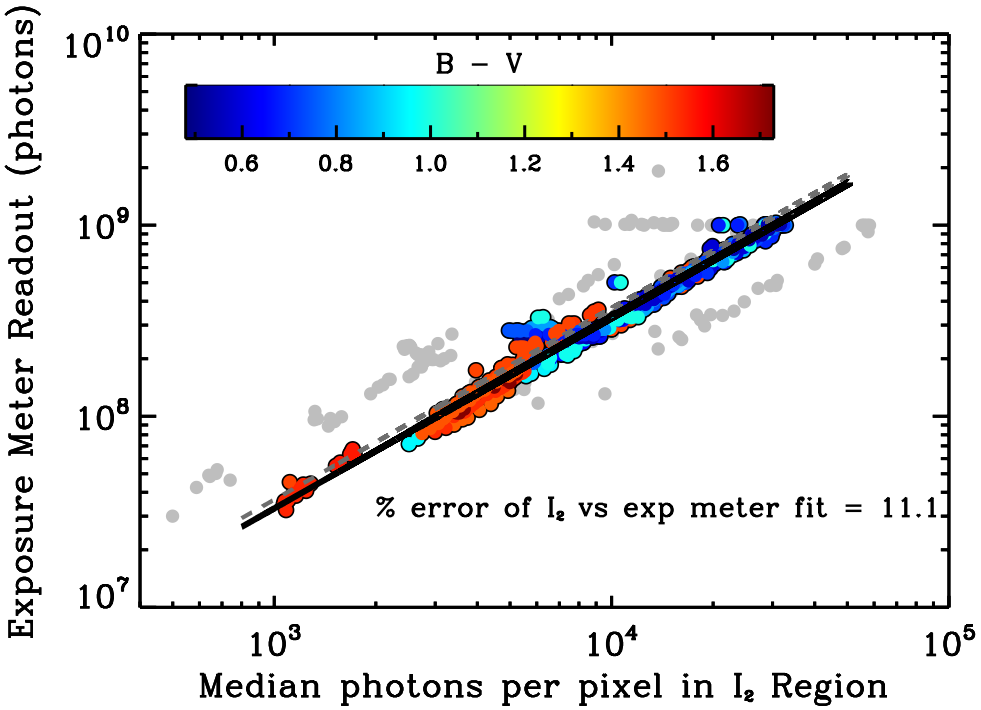

Figure 3.8: Color-corrected relationship between the photons in the I_2 region of the spectrum and the photons registered by the exposure meter. The black line shows the best-fit, and the grey dashed line shows the relation offset by one standard deviation, which is the limit we use operationally. To increase telescope efficiency, we require a way to ensure observations don't continue when the number of iodine region photons necessary to achieve the desired internal uncertainty has already been achieved. As described in Section 3.3.3.2 there is no way to measure the I_2 region photon accumulation in real time. However, the tight correlation between I_2 photons and photons on the exposure meter (which does update in real time) displayed here allows us to set a maximum exposure meter value based on our desired precision level. Thus the observation software will end the exposure when the specified exposure meter value is met, even if the open shutter time falls short of the predicted observation time. This is particularly useful for cases where the cloud cover used in calculating the predicted observation time is actually more than the cloud cover on the target, which would result in an erroneously long observation.

4. Multiply the slowdown factor, calculated during the previous observation using Eqn 3.4, with the ideal transparency observation time estimates to get the predicted observation time in current conditions.

5. Calculate the exposure meter threshold based on the required number of I_2 region photons using Eqn 3.5.

We find scatters of 11.5% and 11.1% in Figures 3.6 and 3.8 respectively (Table 1). This means that, even on a photometric night, we may not accumulate the number of photons in the I_2 region necessary for the desired precision as the photon arrival rate could be too low. To increase the likelihood of getting enough photons to reach the desired number of photons in the I_2 region, we increase the observation time estimate and the exposure meter threshold by 11.5% and 11.1%, or one standard deviation. By implementing this padding factor we ensure that 84% of the time we observe a target, we will obtain the desired number of I_2 photons. However, this does not necessarily guarantee that we will achieve the desired internal uncertainty, due to the scatter in the relation between the I_2 region photons and the uncertainty estimates seen in Figure 3.5 and quantified in Table 1.

Using these predicted observation times, the scheduler can evaluate whether any potential target can be observed at its desired precision within the one-hour observation time limit. Combining the predicted observation times with the targets' coordinates determines whether it will remain within the allowed $20-85^\circ$ elevation range during the exposure. Stars that satisfy all these criteria are then ranked based on their observing priority, time past cadence requirement, and distance from the moon, with the highest scoring star being selected for observation. The

scheduler then transmits the necessary information for the selected star, including its expected observation time and exposure meter threshold, to the observing software, breaking up the total observation time into a number of individual exposures if necessary.

Table 3.1: Values for fit variables in Section 3.3

Variable	Equation	Description	Value(s)
$A_{G/K}$, A_M	Eqn 3.1	constant terms for APF G/K and M stars	4.47, 4.14
$B_{G/K}$, B_M	Eqn 3.1	linear terms for APF G/K and M stars	-1.58, -1.73
A_{Keck}	Eqn 3.1	constant term for Keck M stars	5.03
B_{Keck}	Eqn 3.1	linear terms for Keck M stars	-1.83
$\sigma_{G/K}$	Eqn 3.1	RMS for fit to APF G/K stars	0.182 dex, 43.5%
σ_M	Eqn 3.1	RMS for fit to APF M stars	0.151 dex, 36.2%
σ_{Keck}	Eqn 3.1	RMS for fit to Keck M stars	0.252 dex, 60.0%
α_I	Eqn 3.2	B-V term in I_2 photon rate (LR)	-0.0311
β_I	Eqn 3.2	airmass term in I_2 photon rate LR	0.158
γ_I	Eqn 3.2	date term in I_2 photon rate LR	0.00136
C_I	Eqn 3.2	constant term in I_2 photon rate LR	-11.2
σ_{I_2}	Eqn 3.2	RMS value of $r_{I_2} - r_{I_{2obs}}$	0.0499 dex, 11.5%
α_E	Eqn 3.4	B-V term in exp meter photon rate LR	-0.908
β_E	Eqn 3.4	airmass term in exp meter photon rate LR	0.0852
γ_E	Eqn 3.4	date term in exp meter photon rate LR	0.00118
C_E	Eqn 3.4	constant term in exp meter photon rate LR	-21.8
σ_E	Eqn 3.4	RMS value of $r_E - r_{Eobs}$	0.0742 dex, 17.8%
δ	Eqn 3.5	constant B-V term in I_2 vs exp meter	4.52
ϵ	Eqn 3.5	linear B-V term in I_2 vs exp meter	-0.196
ζ	Eqn 3.5	quadratic B-V term in I_2 vs exp meter	0.262
σ_{I_2Exp}	Eqn 3.5	RMS for fit to I_2 vs exp meter	0.0463 dex, 11.1%

3.4 Dismissed factors

Exposures obtained during 2013 and 2014 indicate that some factors initially suspected to be important need not impact target selection considerations. For example, the original observing protocol avoided targets within 45° of the direction of any wind above 5 mph to avoid wind shake in the telescope. We find, however, no discernible increase in the internal uncertainty (indicated by the color scale in Figure 3.9) as a function of wind speed or direction. This resilience likely stems from an effective wind shielding mode for the dome shutters, which opens them just enough to ensure that there is no vignetting of the target star (Vogt *et al.*, 2014b). In addition, substantial effort has been put into tuning the telescope's servo motors in order to "stiffen" the telescope and thus mitigate the effect of wind gusts that do manage to enter the dome (Lanclos *et al.*, 2014).

We also previously assigned higher priority to targets with elevation in the 60-70° range, removing scientifically interesting targets that were closer to the horizon from consideration. As shown in Figure 3.10, however, there is no significant loss in velocity precision as a function of elevation from 90° down to 20° thanks to the telescope's atmospheric dispersion corrector (ADC) which works down to 15°. The telescope has a hard observing limit of 15° because of the ADC's range and because working at lower elevations leads to vignetting by the dome shutters. We still enforce an elevation range of $20-85°$ to avoid mechanical problems in telescope tracking at the high elevations.. Working at elevations approaching our lower limit does result in longer predicted observation times (due to the airmass term) which can result in stars being skipped over in favor of other, higher elevation targets.

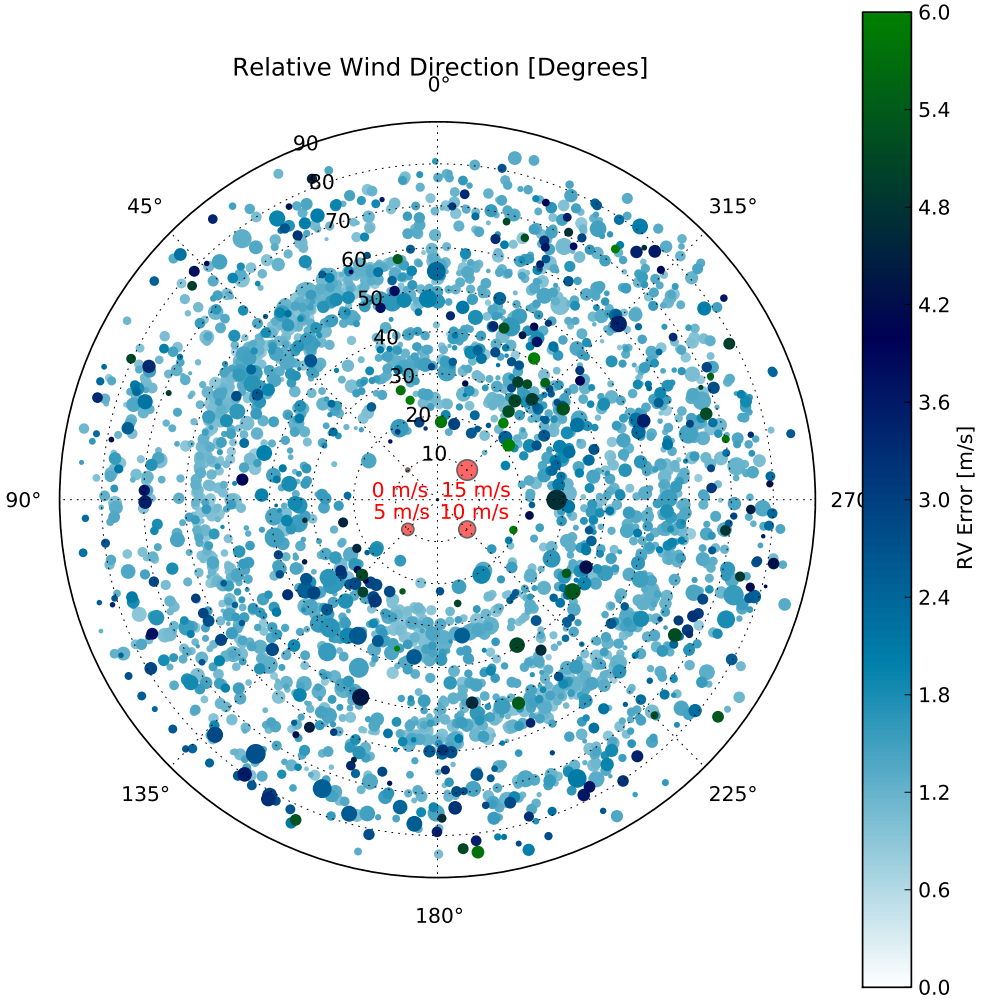

Figure 3.9: Windspeed (point size) and direction (azimuthal position) plotted for 3155 individual exposures reveals no strong correlation between pointing near/into the wind and the estimated internal uncertainty displayed in the color bar. The exposures represented in this figure were obtained before we had the means to determine condition-based exposure times. Thus all exposures were run until the reached their exposure meter threshold, or up to a static maximum exposure time of 900s and then terminated, regardless of the number of photons collected by the exposure meter. This means the wind based effects are not being mitigated by longer exposure times, and wind direction can thus be ignored when deciding which stars are considered viable targets for the next observation.

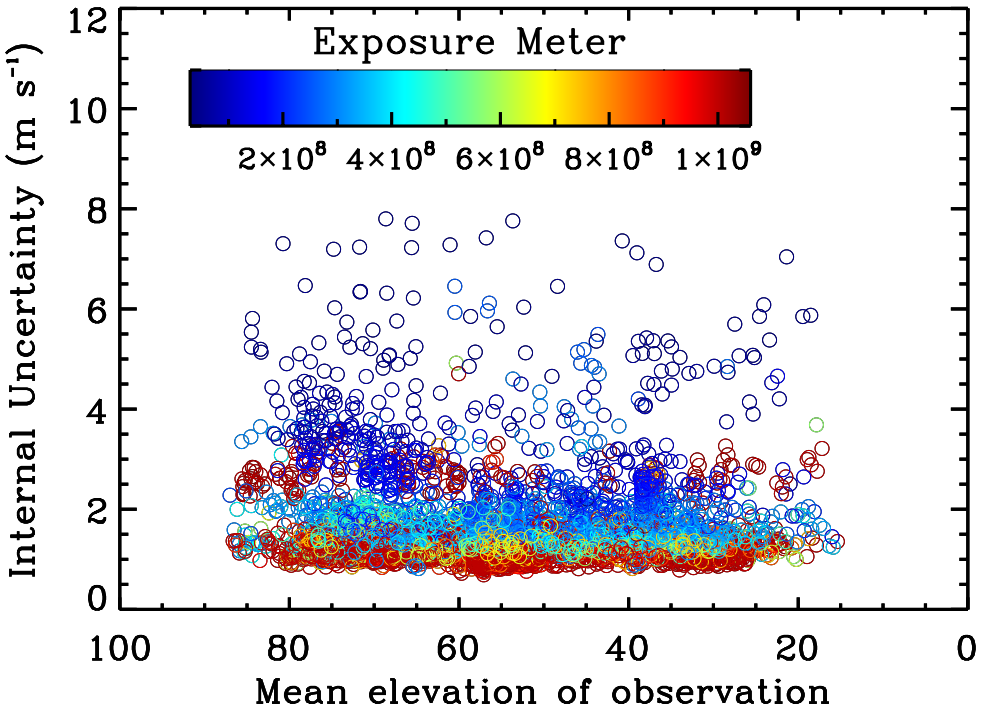

Figure 3.10: The radial velocity precision as a function of the elevation shows no strong correlation, once we compare observations with a fixed exposure meter value. As our linear regressions in Figure 4 and 5 account for the decline in the photon accumulation rate with decreasing elevation, we do not need to add an additional term to account for other elevation effects such as increased seeing. Similar to the Figure 3.9, the observations presented here were taken before the adaptive exposure time software was in use. Thus every exposure has a static maximum exposure time of 900s and the low elevation effects are not being mitigated by allowing for longer exposures. The telescope's ADC only functions down to 15°, the same elevation at which the telescope begins to vignette on the dome shutter, thus providing the lower limit for our observations.

Finally, we no longer assign a weighting value to the slew time necessary to move between targets. The APF is capable of moving at 3° s^{-1} in azimuth and 2° s^{-1} in elevation, which means that a direct slew to a target across the sky would take only one minute. Because the CCD takes approximately 40 seconds to read out each observation, this slew time factor is small enough to be considered unimportant. Furthermore, with the introduction of the wind shielding mode, the telescope's movement was altered so that it must first drop to a "safe elevation" of 15° before rotating to the target azimuth and then moving upwards to the appropriate elevation. This is done to protect the primary mirror from falling debris while the dome shutters are reconfigured to minimize wind-effects for the next observation during the slew. An additional result is that all slews take approximately the same amount of time, which provides justification for discounting slew time as an input to target selection.

3.5 Dynamic scheduler overview

In Section 3.3, we described a method to predict observation times for targets given their precision requirements and the current atmospheric conditions. To automate the determination of these observation times and the selection of the optimal target at any time throughout the night we have implemented a dynamic scheduler (written in Python) called `Heimdallr`.

`Heimdallr` runs all of the APF's target selection efforts and interfaces with pre-existing telescope control software so that, once it submits an observation request, it waits until that set of exposures is completed before reactivating. Telescope safety, system integrity, and alerts about current weather conditions are monitored by two services called `apfmon` and

checkapf. Each of these software sets has the ability to override Heimdallr if they detect conditions that pose a threat to, or represent a problem with, the telescope. This ensures that the facility's safety is always given priority.

Additionally, while directing the night's operations, Heimdallr uses other pre-existing utilities including openatnight, prep-obs and closeup which, as their names suggest, open the facility prior to nightfall (or when night time conditions warrant), prepare the instrument and optical train for observing, and close the facility, securing the telescope when conditions warrant. The setting of the guider camera, the configuration of dome shutters and the control of telescope movement to avoid interference with the cables wrapped around the telescope base is handled by yet another utility called scriptobs.

3.5.1 Observing description

Typically, Heimdallr initiates in the afternoon and prompts the instrument control software to focus the instrument by obtaining a dewar focus cube (series of exposures of the quartz halogen lamp taken through the Iodine cell) using the standard observation slit. Once the software determines a satisfactory value for the instrument's dewar position (via a simple linear least squares parabolic fit to the focus values), it proceeds to take all of the calibration exposures that are required by the data reduction pipeline. Upon completing these tasks, Heimdallr then waits until dusk, at which point it consults checkapf to ensure that there are no problematic conditions in the weather and then apfmon to ensure facility readiness. If both systems report safe conditions, it then opens the dome, allowing the telescope to thermalize with the outside air.

`Heimdallr` runs a main loop that continuously monitors a variety of keywords supplied by the telescope. At 6° twilight, the telescope is prepped for observing and begins by choosing a rapidly rotating B star from a pre-determined list. The B star has no significant spectral lines in the I_2 region and serves as a focus source for the telescope's secondary mirror while also allowing the software to determine the current atmospheric conditions (as described in Section 3.3.3.2).

At 9° twilight, `Heimdallr` accesses the online database of potential targets and parses it to obtain all the static parameters described in Section 3.1. It then checks the current date and time and eliminates from consideration those stars not physically available. The scheduler then employs the stars' coordinates, B-V colors and V magnitudes, combined with the seeing and atmospheric transparency determined during the previous observation, to calculate the predicted observation time for each target given their desired precision levels. Stars unable to reach the desired precision within the one hour maximum observation time are eliminated from the potential target list.

The remaining stars are ranked based on scientific priority and time past observing cadence. The star with the highest score is passed to `scriptobs` to initiate the exposure(s). When the exposures finish, `Heimdallr` updates the star's date of last observation in the database with the photon-weighted midpoint of the last exposure and begins the selection process anew.

When the time to 9° morning twilight becomes short enough that no star will achieve its desired level of precision before the telescope must close, `Heimdallr` shuts the telescope using `closeup` and initiates a series of post-observing calibration exposures. Once the cali-

brations finish, `Heimdallr` exits.

3.5.2 Other operational modes

In addition to making dynamic selections from the target database during the night, `Heimdallr` can also be initiated in a fixed list or ranked fixed list operational mode. The fixed list mode allows observers to design a traditional starlist that `Heimdallr` will move through, sending one line at a time to `scriptobs`. Any observations that are not possible (due to elevation constraints) will be skipped and the scheduler will simply move to the next line.

The ranked fixed list option allows users to provide a target list that `Heimdallr` parses to determine the optimal order of observations. That is, after finishing one observation from the list, the scheduler will then perform a weighting algorithm similar to what is employed by the dynamic use mode to determine which line of the target list is best observed next. `Heimdallr` keeps track of all the lines it has already selected, so that they do not get initiated twice, and will re-analyze the remaining lines after each observation to select the optimal target. This option is especially useful for observing programs that have a large number of possible targets but don't place a strong emphasis on which ones are observed during a given night.

3.6 Comparing with other facilities

There are a number of automated and semi-automated facilities that perform similar observations. Examples include HARPS-N, CARMENES, the Robo-AO facility at Palomar and the Las Cumbres Observatory Global Telescope (LCOGT) network. In order to place the

APF's operations in context relative to these other observatories, we will briefly discuss the approaches of these other dedicated radial velocity facilities (CARMENES, HARPS-N, and the NRES addition to LCOGT) and of the more general facility with queue scheduling (Robo-AO). We will then highlight the common approaches along with discussing what is simpler for our facility as it is dedicated to a single-use.

3.6.1 RV surveys

Radial Velocity surveys generally require tens or hundreds of observations of the same star to detect planetary companions. Traditionally, high-precision velocities were obtained on shared-use facilities and observing time was limited. More recently, however, purpose built systems (such as HARPS) have presented the opportunity to obtain weeks or months of contiguous nights.

The HARPS-N instrument, installed on the Telescopio Nazionale Galileo at Roque de los Muchachos Observatory in the Canary Islands, is a premier system for generating high-precision velocities. At present, it is primarily devoted to Kepler planet candidate follow up and confirmation. The system allows users to access XML standard format files that define target objects using the Short-Term-Scheduler GUI (STS) to guide the process and then assemble the objects into an observing block. When an observer initiates an observation, these blocks and their associated observing preferences are passed to the HARPS-N Sequencer software, which places all of the telescope subsystems into the appropriate states, performs the observation, and then triggers the data reduction process (Cosentino *et al.*, 2012). Thus, while the building of target lists has been streamlined, nightly observation planning still requires attention from an

astronomer or telescope technician.

The forth-coming Calar Alto CARMENES instrument is expecting first light in 2015. CARMENES will also be used to obtain high-precision stellar radial velocity measurements on low-mass stars. Its automated scheduling mechanism relies on a two-pronged approach: the off-line scheduler which plans observations on a weekly to nightly time scale based on target constraints that can be known in advance, and the on-line scheduler which is called during the evening if unexpected weather or mechanical situations arise and require adapting the previously calculated nightly target list (Garcia-Piquer *et al.*, 2014).

Finally, the LCOGT network will soon implement the Network of Robotic Echelle Spectrographs (NRES), six high resolution optical echelle spectrographs slated for operation in late 2015. Like all instruments deployed on the LCOGT network, the scheduling and observing of NRES will be autonomous. Users submit observing requests via a web interface which are then passed to an adaptive scheduler which works to balance the requests' observing windows with the hard constraints of day and night, target visibility, and any other user specified constraints (e.g. exposure time, filter, airmass). If the observation is selected by the adaptive scheduler, it creates a "block" observation tied to a specific telescope and time. This schedule is constructed 7 days out, but rescheduling can occur during the night if one or more telescopes become unavailable due to clouds, or if new observing requests arrive or existing requests are canceled. In this event, the schedule is recalculated, and observations are reassigned among the remaining available sites (Eastman *et al.*, 2014).

3.6.2 Automated queue scheduling

Robo-AO is the first fully automated laser guide star adaptive optics instrument. It employs a fully automated queue scheduling system that selects among thousands of potential targets at a time with an observation rate of ~ 20 objects hr^{-1}. Its queue scheduling system employs a set of XML format files which use keywords to determine the required settings and parameters for an observation. When requested, the queue system runs each of the targets through a selection process, which first eliminates those objects that cannot be observed, and then assigns a weight to the remaining targets to determine their priority in the queue at that time. The optimal target is chosen, and the scheduler passes all observation information to the robotic system and waits for a response that the observations were successfully executed. Once the response is received, the observations are marked as completed and the relevant XML files are updated (Riddle *et al.*, 2014).

3.6.3 Comparing our approach to other efforts

We have designed this system based on our RV observing program carried out over the past 20 years at Keck and other facilities. This experience, coupled with the preexisting software infrastructure, has guided the development of both the dynamic scheduler software itself and our observing strategy.

Comparison to these other observing facilities and the strategies they employ emphasizes some shared design decisions. For example, the APF has a similar target selection approach to that of the Robo-AO system. Both utilize a variety of user specified criteria to eliminate those targets unable to meet the requirements and then rank the remaining targets, passing

the object with the highest score to the observing software. Additionally, as is common with all of the observing efforts mentioned above, our long term strategy is driven by our science goals and is in the hands of the astronomers involved with the project.

Several differences are also notable. The first is that we lack an explicit long term scheduling component in our software. Our observing decisions are made in real time in order to address changes in the weather and observing conditions that occur on minute to hour time scales, and to maximize the science output of nights impacted by clouds or bad seeing. However, for a successful survey there must also be a longterm observing strategy for each individual target. We address this need via a desired cadence and required precision for every potential target. By incorporating the knowledge of how often each star needs to be observed and a way to assess whether the evening's conditions are amenable to achieving the desired precision level, `Heimdallr` adheres to the longterm observing strategy outlined by our observing requirements and doesn't need to generate separate multi-week observing lists.

A second difference is that the final output of the scheduler is a standard star list text file, one line in length. This format has been in use in UCO-supported facilities such as Lick and Keck Observatories for more than 20 years, and thus is familiar to the user community. The file is a simple ASCII text file with key value pairs for parameters and a set of fixed fields for the object name and coordinates. This permits ready by-eye verification of the next observation if desired and allows the user to quickly construct a custom observing line that can be inserted into the night's operations if needed. Observers can furthermore easily make a separate target list in this format for observations when not using the dynamic scheduler (see Sec 3.5.2)

Finally, we use a Google spreadsheet for storing target information and observing

requirements, as opposed to a more machine-friendly format such as XML. Although Lick Observatory employs a firewall to sharply limit access to the APF hosts, it only operates on the incoming direction. Thus it is straightforward and non-compromising from a security standpoint for our internal computers to send a request to Google and pull the relevant data back onto the mountain machines. This approach provides team members with an accessible, easy-to-read structure that is familiar and easily exportable to a number of other formats. Google's version control allows for careful monitoring of changes made to the spreadsheet and ensures that any accidental alterations can be quickly and easily undone. The use of the Google software also allows interaction with a browser, so no custom GUI development is required. Therefore, we are taking advantage of existing software to both minimize our development effort, and make it as easy as possible to have the scientists update and maintain the core data files that control the observations.

3.7 Observing campaigns on the automated planet finder

The APF has operated at high precision for over a year, and has demonstrated precision levels of $\sigma \sim 1$ m s^{-1} on bright, quiet stars such as Sigma Draconis (Vogt *et al.*, 2014b). The telescope's slew rate permits readout-limited cycling and 80-90% open shutter time, allowing for 50-100 Doppler measurements on clear nights.

3.7.1 The Lick-Carnegie survey

`Heimdallr`'s design dovetails with the need to automate the continued selective monitoring of more than 1,000 stars observed at high Doppler precision at Keck over the past 20 years (Butler, 2016). The APF achieves a superior level of RV precision and much-improved per-photon efficiency in comparison to Keck/HIRES for target stars with V <10. As a primary user, we can employ the APF on 100+ nights per year in the service of an exoplanet detection survey.

At present, 127 stars have been prioritized for survey-mode observation with the APF. This list emphasizes stars that benefit from the telescope's more northern location, and gives preference to stars that display prior evidence of planetary signals. We adopt a default cadence of 0.5 observations per night. When a star is selected, it is observed in a set of 5-15 minute exposures with the additional constraint that the total of a night's sequential exposures (the observation time) on the star is less than an hour. Additionally, information obtained at Keck has, in some cases, permitted estimates for the stellar activity of specific target stars. In these cases, observation times can be adjusted to conform to a less stringent desired precision.

With its ability to predict observation times, `Heimdallr` readily achieves efficiencies that surpass the use of fixed lists, and indeed, its performance is comparable to that of a human observer monitoring conditions throughout the night.

3.7.2 TESS pre-covery survey

`Heimdallr` is readily adopted to oversee a range of observational programs, and a particularly attractive usage mode for APF arises in connection with NASA's Transiting Exo-

planet Survey Satellite (TESS) mission. TESS is scheduled for launch in 2017, and is the next transit photometry planet detection mission in NASA's pipeline (Ricker *et al.*, 2014). Transit photometry observations of potential planet signatures generally require follow-up confirmation, with RV being the most common. Currently there is a dearth of high-precision RV facilities in the northern hemisphere, and HARPS-N is heavily committed to Kepler planet candidate follow up. NASA recently announced plans to develop an instrument for the 3.5m WIYN telescope at Kitt Peak Observatory capable of extreme precision Doppler spectrography to be used for follow up of TESS planet candidates (Beal, 2014). However such an instrument will require time for development and commissioning and thus is not a viable candidate for pre-launch observations of TESS target stars. The APF's year-round access to the bright stars near the north ecliptic pole, which will obtain the most observation time from TESS, makes it an optimal facility to conduct surveys in support of the satellite's planet detection mission.

At present, comparatively little is known about the majority of TESS's target stars. We have little advance knowledge of which stars host properly inclined, short-period transiting planets observable by the satellite. We will thus start with a default value for the observing cadence and be poised to adapt quickly should hints of planetary signatures start to emerge. Additionally, initial desired precisions (and the corresponding observation times) must rest on the suspected stellar jitter of the targets.

The availability of on-line databases to track all of the science-based criteria will be crucial for moving back and forth quickly between this project and further Lick-Carnegie follow up. Evaluations of the value of APF coverage are governed by three scientific criteria (priority, cadence and required precision), along with supporting physical characteristics (RA, Dec, V

and B-V) for each target. Thus when beginning RV support for TESS, `Heimdallr` can easily be instructed to reference the TESS database when determining the next stellar target (instead of the Lick-Carnegie List).

TESS observations also provide an excellent test bed for experimenting with alternate observational strategies. For example, Sinukoff (2014) stated that obtaining three 5-minute exposures of a star spaced approximately two hours apart from one another during the night results in a 10% increase in precision over taking a singe 15 minute exposure. The TESS stars that will be monitored by the APF are all located in the north ecliptic pole region, meaning that the slew times will be almost negligible. It is thus likely that an observing mode that subdivides exposures to improve precision could be very valuable. In short, the APF is extremely well matched to the TESS Mission.

Chapter 4

The Detection of GL 687b with the Automated Planet Finder

4.1 Introduction

The Copernican principle implies that the Earth, and, by extension, the solar system, do not hold a central or specifically favored position. This viewpoint is related to the so-called *mediocrity principle* (Kukla, 2010), which notes that an item drawn at random is more likely to come from a heavily populated category than one which is sparsely populated.

These principles, however, have not had particularly apparent success when applied in the context of extrasolar planets. Mayor *et al.* (2009a) used their high precision Doppler survey data to deduce that of order 50% (or more) of the chromospherically quiet main-sequence dwarf stars in the solar neighborhood are accompanied by a planet (and in many cases, by multiple planets) with $M\sin(i) \lesssim 30 M_{\oplus}$, and orbital periods of $P < 100\,\mathrm{d}$. Taken strictly at face value,

this result implies that our own solar system, which contains nothing interior to Mercury's $P = 88\,\mathrm{d}$ orbit, did not participate in the galaxy's dominant mode of planet formation. Yet the eight planets of the solar system have provided, and continue to provide, the de-facto template for most discussions of planet formation.

Indeed, where extrasolar planets are concerned, M-dwarfs and mediocrity appear to be effectively synonymous. Recent observational results suggest that low-mass planets orbiting low-mass primaries are by no means rare. Numerous examples of planets with $M_\mathrm{p} < 30\,M_\oplus$ and M-dwarf primaries have been reported by the Doppler surveys (e.g. Butler *et al.* 2004; Mayor *et al.* 2009a, and many others), and the *Kepler* Mission has indicated that small planets are frequent companions to low mass stars. For example, Dressing and Charbonneau (2013) report that among dwarf stars with $T_\mathrm{eff} < 4000\,\mathrm{K}$, the occurrence rate of $0.5\,R_\oplus < R_\mathrm{p} < 4\,R_\oplus$ planets with $P < 50\,\mathrm{d}$ is $N = 0.9^{+0.04}_{-0.03}$ planets per star. Improved statistics, however, are required for a definitive statement that is couched in planetary masses as well as in planetary radii. Figure 4.1 shows the current distribution of reported planets and planetary candidates orbiting primaries with $M_\star < 0.6 M_\odot$, which we adopt as the functional border between "M-type" stars and "K-type stars".

The census of low-mass planets orbiting low-mass primaries can be accessed using a variety of techniques. For objects near the bottom of the main sequence, it appears that transit photometry from either ground (Charbonneau, 2010) or space (Triaud *et al.*, 2013) offer the best prospects for planetary discovery and characterization. For early to mid M-type dwarfs, there is a large enough population of sufficiently bright primaries that precise Doppler detection (see, e.g. Rivera *et al.* (2010)) can play a lead role. For the past decade, we have had a sample

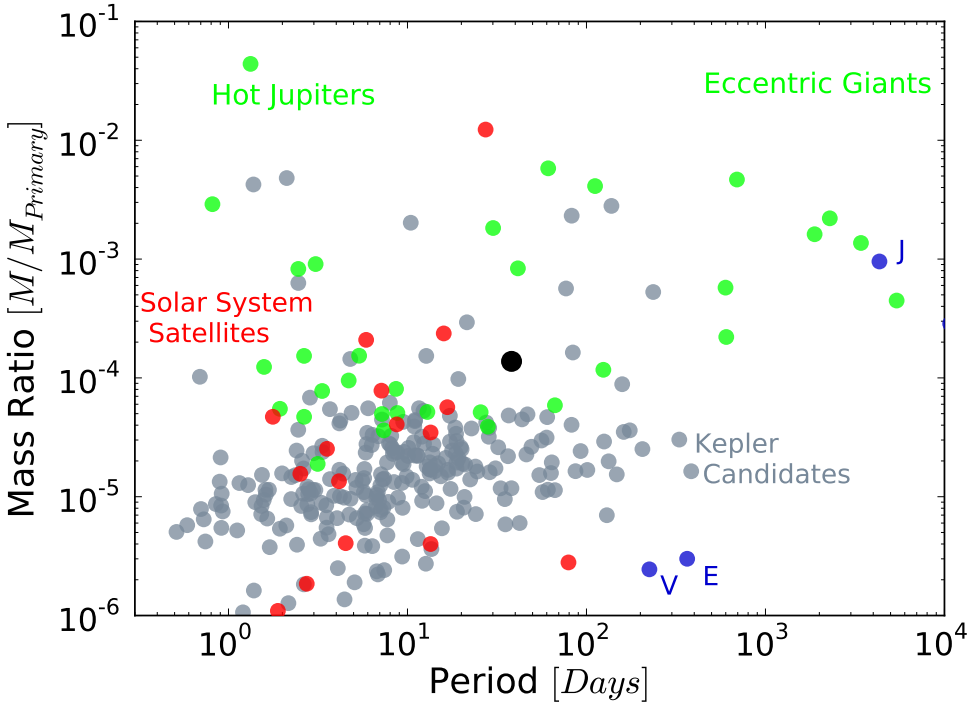

Figure 4.1: Population digram for currently known extra solar planets orbiting stars with reported masses $M_{\rm star} < 0.6 M_{\odot}$. *Green circles:* Planets securely detected by the radial velocity method (either with or without photometric transits). *Red circles:* The regular satellites of the Jovian planets in the Solar System. *Gray circles:* Kepler candidates and objects of interest. Radii for these candidate planets, as reported in Batalha *et al.* (2013a), have been converted to masses assuming $M/M_{\oplus} = (R/R_{\oplus})^{2.06}$ (Lissauer *et al.*, 2011a), which is obtained by fitting the masses and radii of the solar system planets bounded in mass by Venus and Saturn, which may be a rather naive transformation given the startling range of observed radii for planets with masses between Earth and Uranus. Venus, Earth, and Jupiter are indicated on the diagram for comparison purposes. Data are from www.exoplanets.org, accessed 01/12/2014 (Han *et al.*, 2014).

of $\sim$160 nearby, photometrically quiet M-type stars under precision radial velocity surveillance with the Keck telescope and its HIRES spectrometer. In recent months, this survey has been supplemented by data from the Automated Planet Finder Telescope (Vogt, S.S. et al., 2014). Here, we present 16.6 years of Doppler velocity measurements for the nearby M3 dwarf GJ 687 (including 122 velocity measurements from Keck, 20 velocity measurements from the APF, and 5 velocity measurements made with the Hobby-Eberly Telescope) and we report the detection of the exoplanet that they imply. We use this discovery of what is a highly archetypal representative of a planet in the Milky Way – in terms of its parent star, its planetary mass, and its orbital period – to motivate a larger discussion of the frequency of occurrence, physical properties, and detectability of low-mass planets orbiting M-type stars.

The plan for this paper is as follows. In §2, we describe the physical and spectroscopic properties of the red dwarf host star Gliese 687. In §3, we describe our radial velocity observations of this star. In §4 we describe our Keplerian model for these observations, along with an analysis that assesses our confidence in the detection. In §5, we describe our photometric time series data for the star, which aids the validation of the planet by ruling out spot-modulated interpretations of the Doppler variations. In §6, we discuss the ongoing refinement of the planet-metallicity correlation for low-mass primaries, in §7, we discuss the overall statistics that have emerged from more than 15 years of precision Doppler observations of M-dwarf stars with the Keck Telescope, and in §8 we conclude with an overview that evaluates the important future role of the APF telescope in precision velocimetry of nearby, low-mass stars.

4.2 GJ 687 Stellar Parameters

Gliese 687 (LHS 450, BD+68°946) lies at a distance, d = 4.5 pc, is the 39th-nearest known stellar system, and is the closest star north of +60° declination. Figure 4.2 indicates GJ 687's position in the color-magnitude diagram for stars in the Lick-Carnegie Survey's database of Keck observations. Due to its proximity and its brightness (V=9.15, K_s=4.548), Gliese 687 has been heavily studied, and in particular, the CHARA Array has recently been used to obtain direct interferometric angular diameter measurements for the star. Boyajian *et al.* (2012) find $R_\star/R_\odot = 0.4183 \pm 0.007$, and derive $L_\star/L_\odot = 0.02128 \pm 0.00023$, $T_{\rm eff} = 3413\,{\rm K}$, and use the mass-radius relation of Henry and McCarthy (1993) to obtain $M_\star/M_\odot = 0.413 \pm 0.041$. As illustrated in Figure 4.3, Gliese 687's mean Mt. Wilson S value and the dispersion of its S-index measurements from our spectra indicate that it has a moderate degree of chromospheric activity. This conclusion is in concordance with our long-term photometric monitoring program, which also indicates that the star is somewhat active.

4.3 Radial Velocity Observations

Doppler shifts from both the Keck and APF platforms were measured, in each case, by placing an iodine absorption cell just ahead of the spectrometer slit in the converging beam of stellar light from the telescope (Butler *et al.*, 1996b). The forest of iodine lines superimposed on the stellar spectra generates a wavelength calibration and enables measurement of each spectrometer's point spread function. The radial velocities from Keck were obtained by operating HIRES at a spectral resolving power R∼60,000 over the wavelength range of 3700-

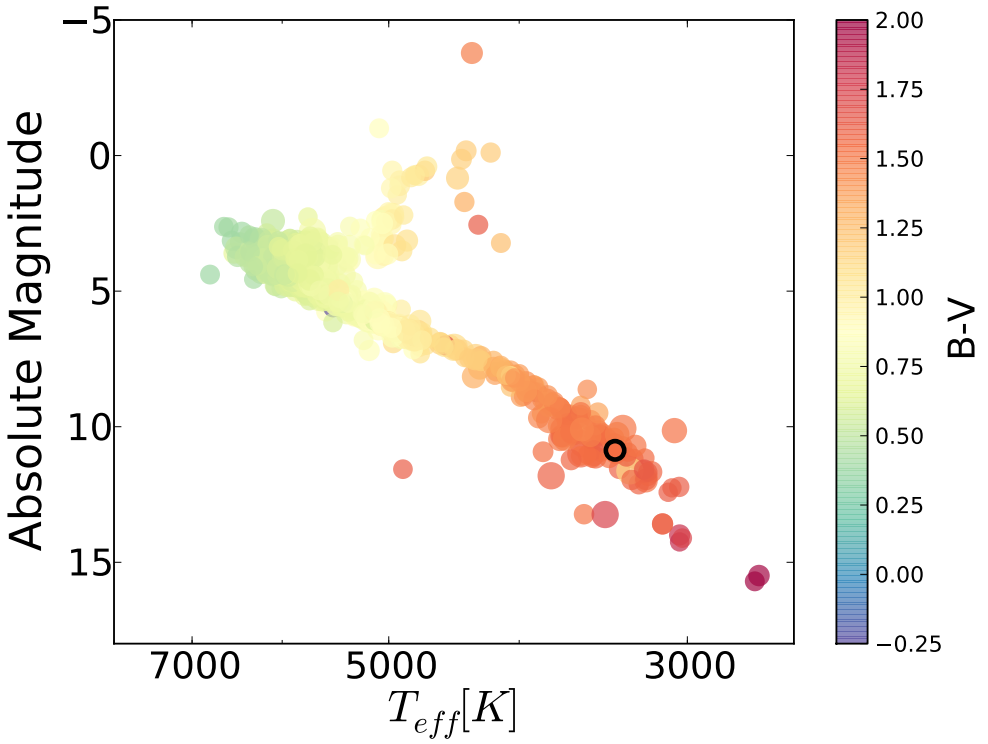

Figure 4.2: HR diagram with GJ 687's position indicated as a small open circle. Absolute magnitudes, M, are estimated from V band apparent magnitudes and Hipparcos distances using $M = V + 5\log_{10}(d/10 \text{ pc})$. All 956 stars in our catalog of radial velocity measurements (for which more than 20 Doppler measurements exist) are shown, color-coded by their B-V values, with point areas sized according to the number of observations taken.

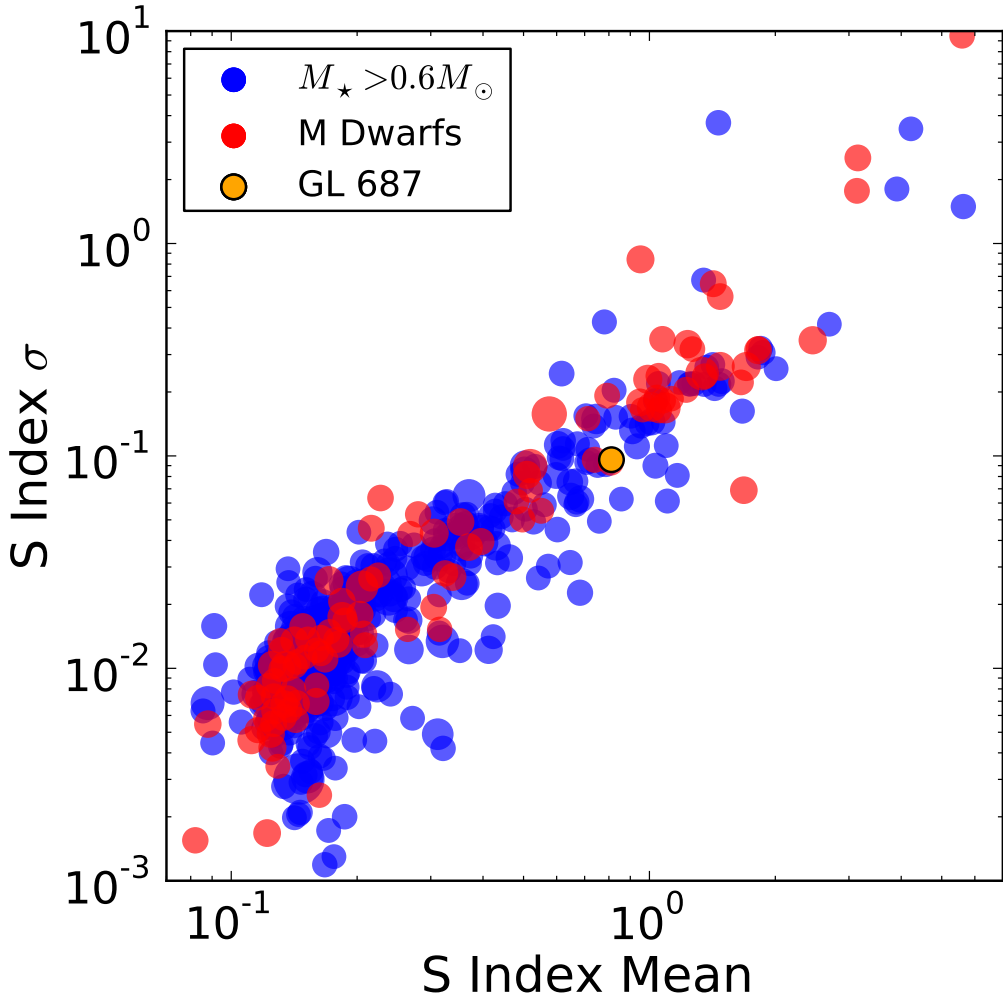

Figure 4.3: The average value of the S-index against the standard deviation of the S-index for all the stars in the Lick-Carnegie database. Stars with $M_\star < 0.6 M_\odot$ are colored red. GJ 687 is shown as an orange circle in the midst of this population, showing that it is a somewhat active star. The areas subtended by the individual points are, in all cases, proportional to the number of Doppler velocity observations that we have collected of the star (with systems above an upper bound of 250 observations receiving the same point size).

8000 , though only the region 5000-6200 containing a significant density of iodine lines was used in the present Doppler analysis (Vogt *et al.*, 1994b). The APF measurements were obtained over a similar spectral range, but at a higher spectral resolving power, R$\sim$108,000. For each spectrum that was obtained, the region containing the iodine lines was divided into $\sim$700 chunks, each of ~ 2 width. Each chunk produces an independent measure of the wavelength, PSF, and Doppler shift. The final measured velocity is the weighted mean of the velocities of the individual chunks. All radial velocities (RVs) have been corrected to the solar system barycenter, but are not tied to any absolute velocity system. As such, they are "relative" velocities, with a zero point that can float as a free parameter within an overall system model.

The internal uncertainties quoted for all the radial velocity measurements in this paper reflect only one term in the overall error budget, and result from a host of systematic errors that stem from the characterization and determination of the point spread function, detector imperfections, optical aberrations, consequences of undersampling the iodine lines, and other effects. Two additional major sources of error are photon statistics and stellar "jitter". The latter varies widely from star to star, and can be mitigated to some degree by selecting magnetically inactive older stars and by time-averaging over the star's unresolved low-degree surface *p*-modes. All observations in this paper have been binned on 2-hour timescales. In addition to the radial velocities that we have obtained at Keck and APF, we also use five Doppler measurements obtained by Endl *et al.* (2003) at the Hobby-Eberly Telescope located at McDonald Observatory. These radial velocity observations are presented in the appendix.

4.4 The Best Fit Solution

The combined radial velocity data sets show a root-mean-square (RMS) scatter of 7.58 $\mathrm{m\,s^{-1}}$ about the mean velocity. This scatter is measured after we have applied best-fit telescope offsets of 0.64 $\mathrm{m\,s^{-1}}$ for Keck, -1.71 $\mathrm{m\,s^{-1}}$ for APF, and 1.27 $\mathrm{m\,s^{-1}}$ for HET.

A Lomb-Scargle periodogram of the 149 velocity measurements of GJ 687 is shown in Figure 4.4. False alarm probabilities are calculated with the bootstrap method, as described in Efron (1979), iterating 100,000 times for a minimum probability of $\mathrm{P_{false}} < 1e-5$ as easily met by the tallest $\mathrm{P_b}$=38.14 day peak in Figure 4.4. This signal in the data is modeled as a $M_\mathrm{b}\sin(i) = 0.06\,M_J$ planet with an orbital eccentricity, $e_b = 0.04$.

Using Levenberg-Marquardt optimization, we obtained a best-fit Keplerian model for the system. This fit, which assumes $i = 90^\circ$ and $\Omega = 0^\circ$ for the planet, is listed in Table 4.2. The phased RV curve for the planet in Table 4.2 is shown in Figure 4.5. A power spectrum of the residuals to our one-planet fit is shown in Figure 4.6 and indicates no significant periodicities. Also shown in this figure is a periodogram of our Mt. Wilson S-index measurements from the spectra, which are a proxy for the degree of spot activity on the star at a given moment. None of the peaks in the periodogram of S-index values coincide with the peak that we suspect to be a planet.

The reduced chi-squared statistic for our fit is $\chi^2_{red} = 18.55$ and results in a fit with an RMS of 6.16 $\mathrm{m\,s^{-1}}$ and estimated stellar jitter of $\sigma_{\mathrm{jitter}} = 5.93$ $\mathrm{m\,s^{-1}}$ (the estimate of the stellar jitter that is required to bring the reduced chi-squared statistic of the fit down to unity). Thus, if the true stellar jitter is of order 6.0 $\mathrm{m\,s^{-1}}$, which is reasonable for a moderately active star

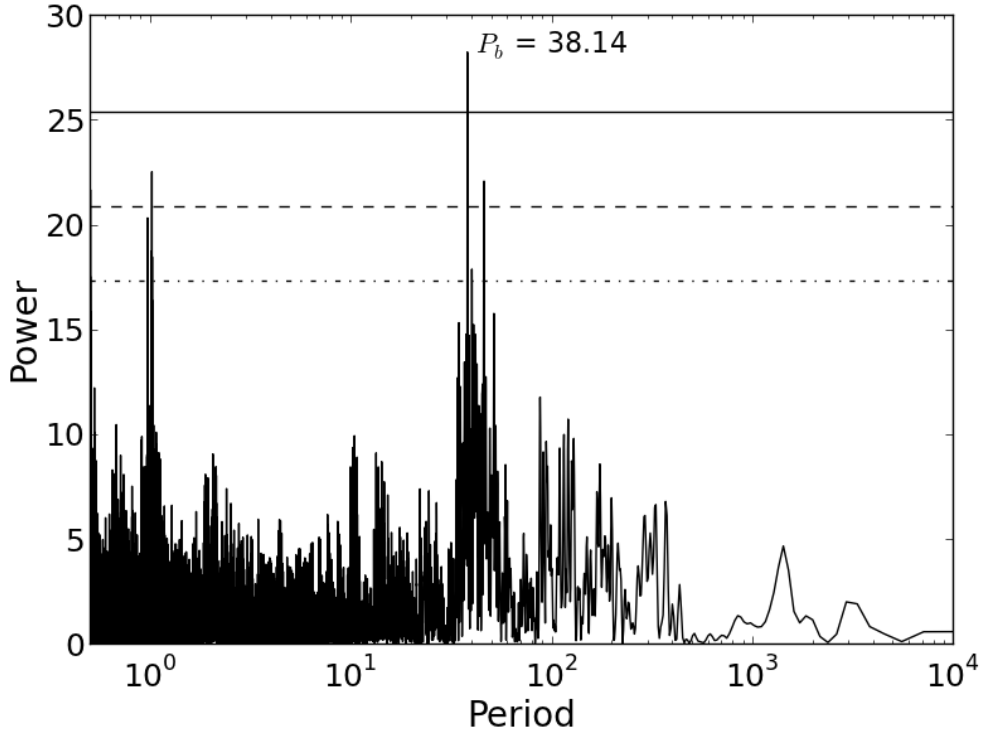

Figure 4.4: Lomb-Scargle periodograms for combined radial velocity measurements of GJ 687 from the HET, Keck and APF telescopes. The horizontal lines from top to bottom represent false alarm probabilities of 0.01%, 0.1%, and 1.0% respectively.

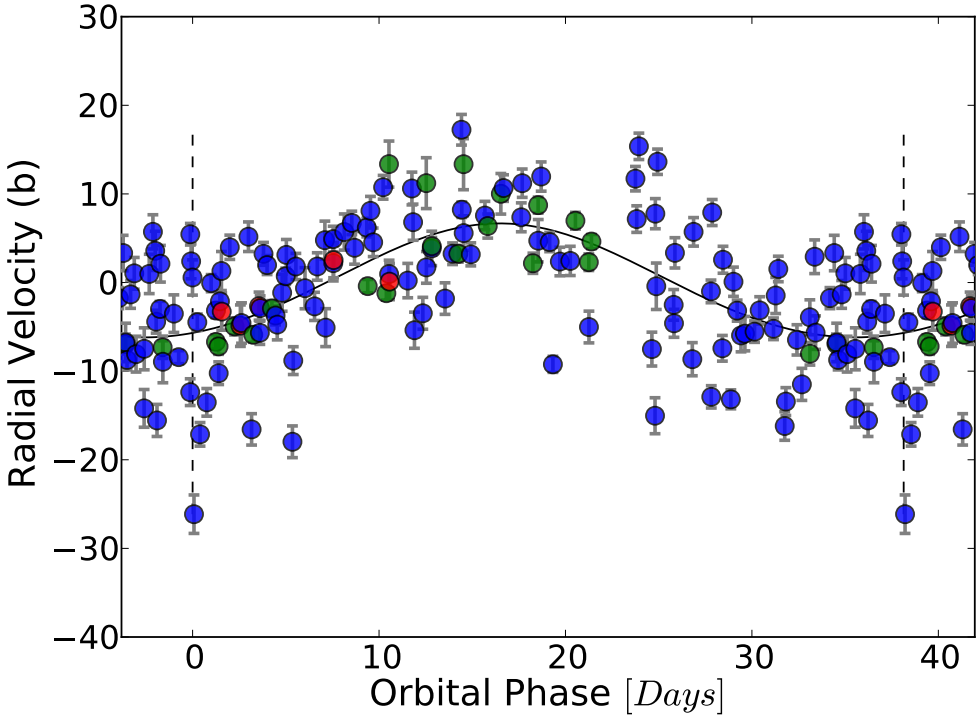

Figure 4.5: Phased radial velocity model for planet b, folded at the $P = 38.14$ d orbital period. The blue points correspond to Keck data points, green points to APF data, and the red points are HET data. The vertical dashed lines demarcate the extent of unique data.

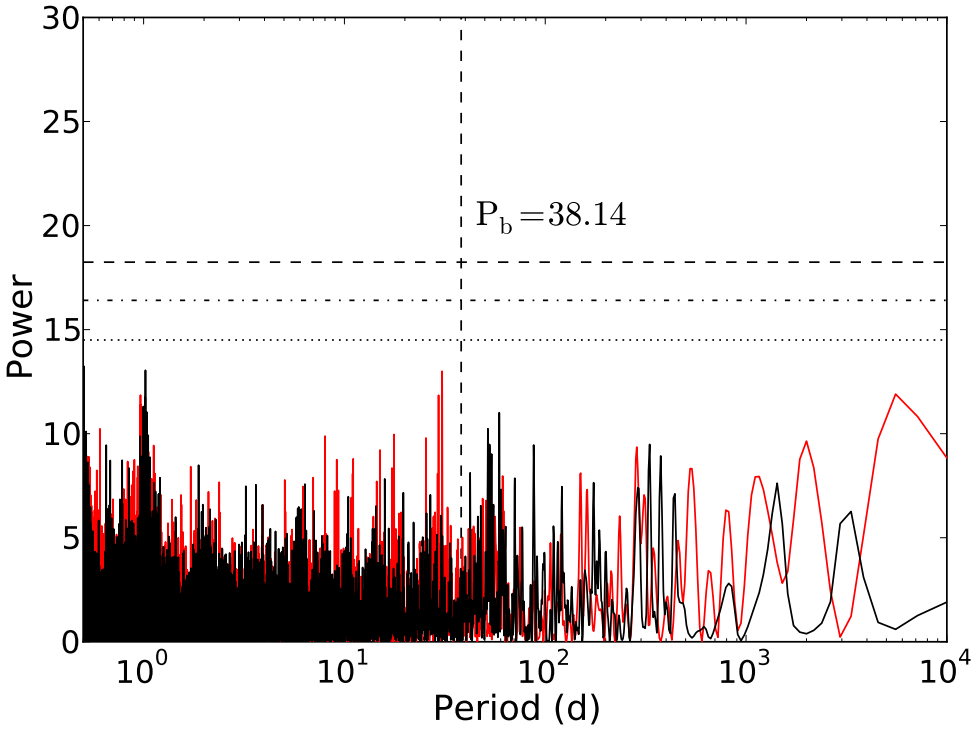

Figure 4.6: Lomb-Scargle periodogram of the radial velocity residuals to the fit given in Table 4.2 plotted in black, and the Lomb-Scargle periodogram of the Mt. Wilson S-index values plotted behind in red.

like Gliese 687, then our fit adequately explains the excess variance in the radial velocity time series.

In order to compute parameter uncertainties for our orbital fit, we implement a Markov Chain Monte Carlo algorithm (Ford, 2005, 2006; Balan and Lahav, 2009; Meschiari *et al.*, 2009b; Gregory, 2011). The MCMC algorithm returns a chain of state vectors, $\mathbf{k}_i$ (a set of coupled orbital elements, e.g. period, mass, etc. and the three velocity offset parameters). The goal of the Markov Chain calculation is to generate an equilibrium distribution proportional to $\exp[\chi^2(\mathbf{k})]$. We adopt non-informative priors on all parameters (and uniform in the log for masses and periods). The resulting error correlations are shown in Figure 4.7, and a set of 100 states drawn randomly from the converged chain are shown in the orbital diagram in Figure 4.8.

The error correlation diagram indicates that all parameters are well determined, save for the usual degeneracies between mean anomaly and ω for the low-eccentricity orbit. The distribution of the residuals relative to the best-fit model shows no evident pathologies. Indeed, a quantile-quantile plot (shown in Figure 4.9) indicates that the distribution of residuals is well described by a normal distribution. We note that the smaller scatter of points obtained with the APF telescope could be a consequence of the fact that they were all taken within a Δt = 140d period, and thus sample only one segment of the stellar activity cycle.

A potentially significant challenge to correctly identifying the orbital period of a proposed exoplanet arises from the discrete and uneven sampling inherent in radial velocity surveys. The spacing of observations leads to increased noise and the presence of aliases within the star's periodogram which can be mistaken for a true orbital signature. For a real signal occurring at a frequency f_{planet} we expect alias signatures at $f = f_{planet} \pm n f_{sampling}$ where n is an

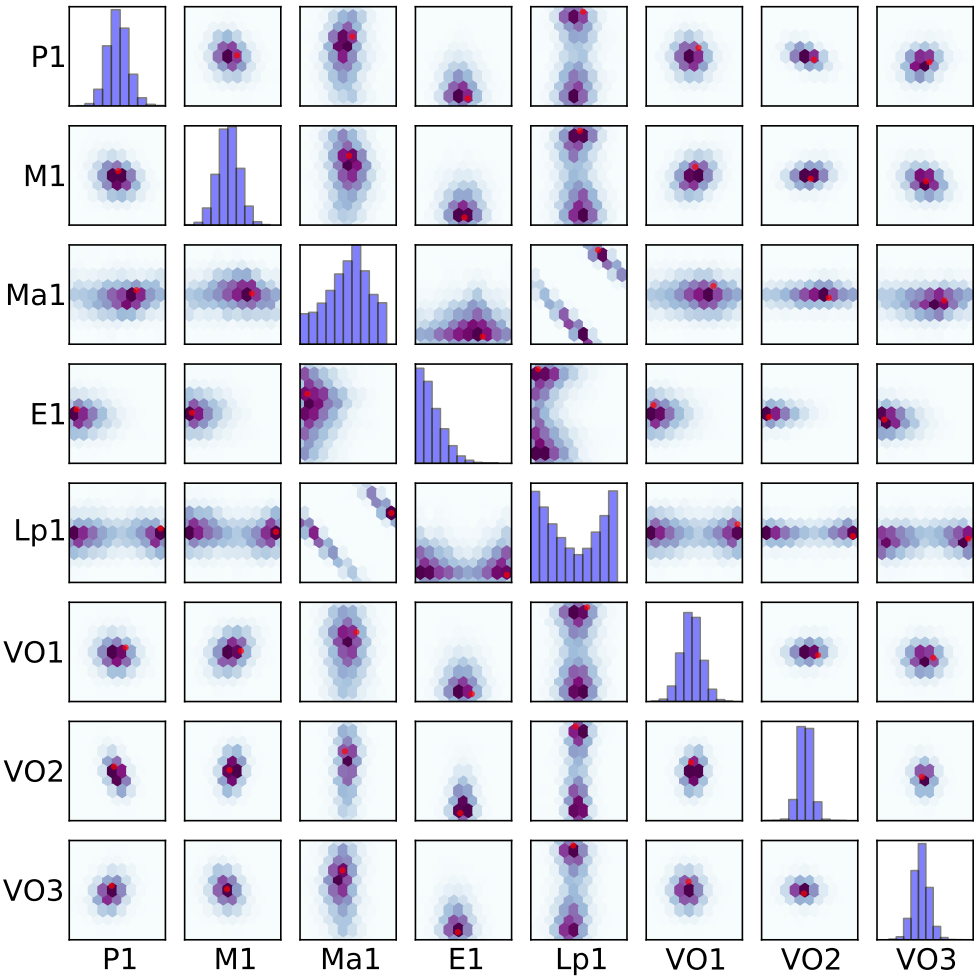

Figure 4.7: Smooth scatter plots of parameter error correlations for our Markov chain. In each case, the best-fit model is indicated with a small red dot, and the density of models within the converged portion of the chain is shown as a blue-toned probability distribution function. The diagonal line of entries shows the marginalized distribution for each parameter of the one-planet model.

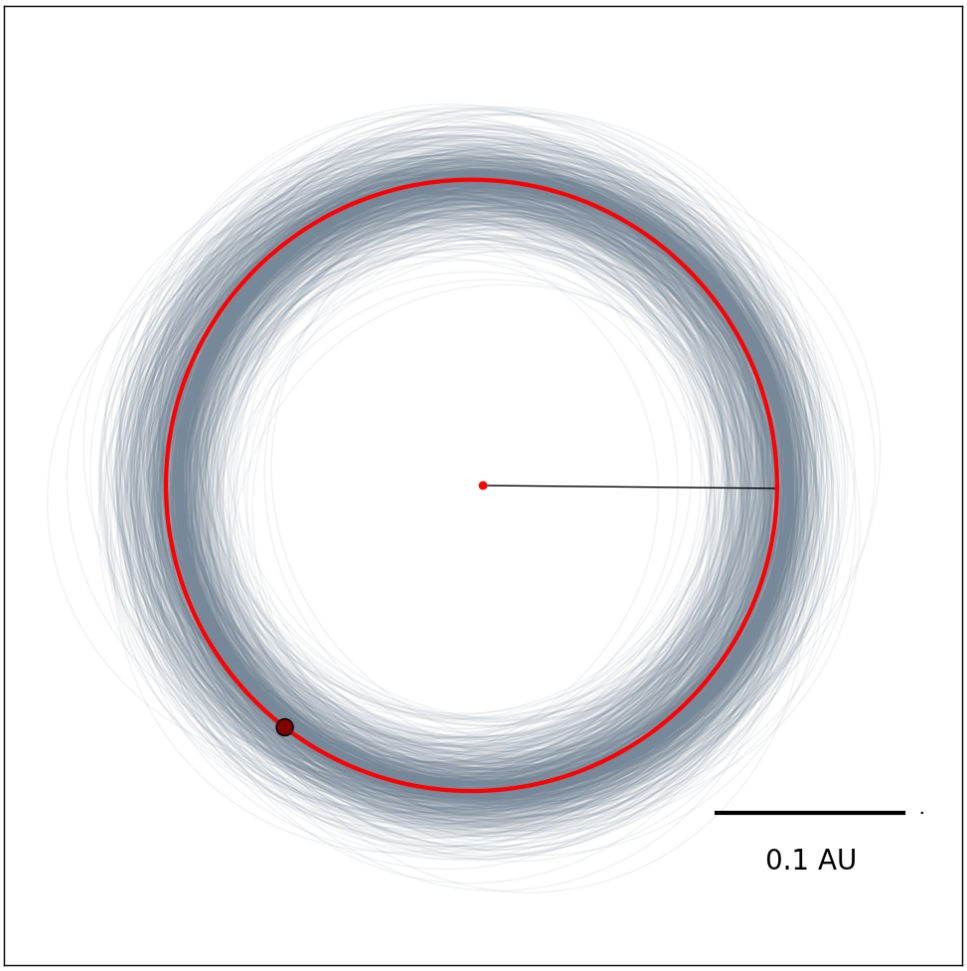

Figure 4.8: The orbit of the proposed planetary companion to GJ 687. The larger red point corresponds to the location of the planet at the initial observation epoch, HJD 2450603.97. The line from the origin corresponds to the planet's periastron. For the geometry plotted, transits, should they occur, would happend when the planet traverses the positive y-axis. The light lines are 100 orbits of the planet drawn from the converged segment of the Markov Chain. The red dot in the center of the diagram corresponds to the size of the star when drawn to scale. The small black dot next to the distance scale bar indicates the size of the planet when drawn to scale, and assuming it has $R_{\rm P} = R_{\rm Nep}$.

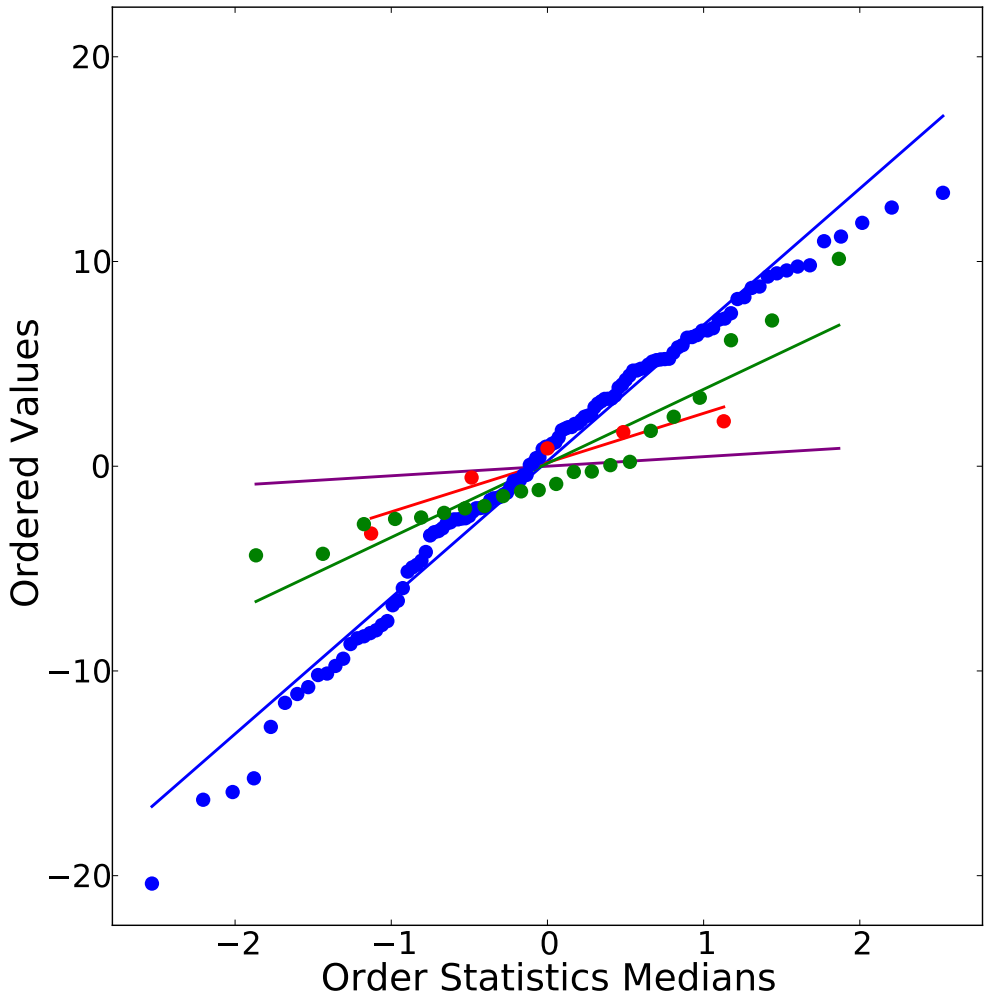

Figure 4.9: Quantile-Quantile plot for the velocity residuals to the 1-planet model fit. Adherence of the points to the lines indicate the degree to which the radial velocities from the two telescopes conform to a normal distribution. APF points are shown in green, Keck points are shown in blue, and HET points are shown in red.

integer. In order to aid confirmation that the periodic signal we observe is actually a planetary signature, we must be able to calculate where aliases due to our observing cadence will occur, and then verify that they are not the source of the signal. The aliases are determined using a spectral window function as defined by Roberts *et al.* (1987)

$$W(\nu) = \frac{1}{N} \sum_{r=0}^{N} \exp^{-2\pi i \nu t_r}, \tag{4.1}$$

where N is the total number of observations and t is the date on which they were taken. Plotting this function will result in peaks that are due solely to the sampling cadence of the data. Because our observations are constrained by when the star is visible in the night sky, and because Keck Telescope time is allocated to Doppler surveys primarily when the Moon is up, we expect aliases at periods of 1 solar day, 1 sidereal day, 1 synodic month and 1 sidereal year. Examining the window function we do see peaks resulting at these periods, but careful analysis of the periodogram for our radial velocity observations shows no evidence of strong signals occurring at the locations necessary for our $P = 38.14$day signal to be a potential alias instead of a true Keplerian signature.

With an apparent K_s-band magnitude of 4.54, Gliese 687 is brighter (in the near infrared) than *all* known hosts of transiting extrasolar planets other than 55 Cancri. As a consequence, transits by Gliese 687's planetary companion (which has an equilibrium temperature, $T_{\rm eq} \sim 260\,{\rm K}$), were they to occur, would be of substantial scientific value. In particular, transmission spectroscopy with JWST would give insights into what is likely a dynamic and chemically rich planetary atmosphere. The *a-priori* geometric transit probability for Gliese 687 b, however,

is a scant $P_{\rm tr} = 1.2\%$, and as we describe below, there is no evidence that transits occur. With $M\sin(i) = 19 M_{\oplus}$, the currently observed mass-radius range for exoplanets indicates that the planetary radius, $R_{\rm p}$ could credibly range from $R_{\rm p} \sim 0.2 R_{\rm Jup}$ to $R_{\rm p} \sim 0.6 R_{\rm Jup}$, implying potential transit depths in the $d = 0.2\%$ to $d = 2\%$ range.

4.5 Photometric Observations

During the 2009–2013 observing seasons, we acquired a total of 866 photometric observations of GJ 687 on 519 nights with the Tennessee State University (TSU) T12 0.80 m automatic photoelectric telescope (APT) at Fairborn Observatory in Arizona. The T12 APT is one of several TSU automatic telescopes operated at Fairborn (Henry, 1999a; Eaton *et al.*, 2003). It is equipped with a two-channel precision photometer that employs a dichroic filter and standard Strömgren b and y filters to separate the two passbands and two EMI 9124QB bi-alkali photomultiplier tubes to measure the b and y count rates simultaneously. We observed GJ 687, designated our program star (P), differentially with respect to three neighboring comparison stars: C1 (HD 156295, $V = 5.54$, $B-V = 0.22$, F0 IV), C2 (HD 160198, $V = 7.65$, $B-V = 0.46$, F2 V), and C3 (HD 161538, $V = 7.01$, $B-V = 0.44$, F2 V). A detailed description of the observing sequence and the data reduction and calibration procedures are given in Henry (1999a).

We computed all pairwise differential magnitudes $P-C1$, $P-C2$, $P-C3$, $C3-C2$, $C3-C1$ and $C2-C1$ in both the b and y passbands, corrected them for atmospheric extinction, and transformed them to the standard Strömgren photometric system. Observations with

internal standard deviations greater than 0.01 mag were discarded to remove data taken in non-photometric conditions. Intercomparison of the six sets of differential magnitudes demonstrated that HD 156295 (C1) is a low-amplitude variable while both HD 160198 (C2) and HD 161538 (C3) are constant to the expected measurement precision. To improve our precision, we combined the separate differential b and y observations into a single $(b+y)/2$ "passband." We also computed the differential magnitudes of GJ 687 with respect to the mean brightness of the two good comparison stars: $P-(C2+C3)/2$. The standard deviation of the $C3-C2$ comparison star differential magnitudes is 0.0020 mag, which we take to be the precision of a single measurement.

A total of 606 nightly measurements in the five observing seasons survived the cloud-filtering process. These data are plotted as $P-(C2+C3)/2$ differential magnitudes in the top panel of Figure 4.10. The five individual observing seasons are plotted in the remaining panels. The standard deviations for the yearly light curves are given in each panel. These range from 0.0049 to 0.0092 mag, compared to the measurement precision of 0.0020 mag. Gaps of 10–12 weeks in the yearly light curves for 2009 through 2012 are due to southern Arizona's July–September rainy season when good photometry is not possible.

Low-amplitude variability is seen in GJ 687 during each observing season, resembling light curves typical of modestly active stars with spot filling factors of a few percent (see, e.g., Henry *et al.*, 1995). The 2010 light curve has the largest amplitude variability (~ 0.03 mag) and reveals cyclic variation with a time scale of ~ 60 days. The other light curves have lower amplitudes and include cyclic variations of ~ 60 and also ~ 30 days. These year-to-year and cycle-to-cycle variations are also typical of modestly active stars. We interpret the 60-day vari-

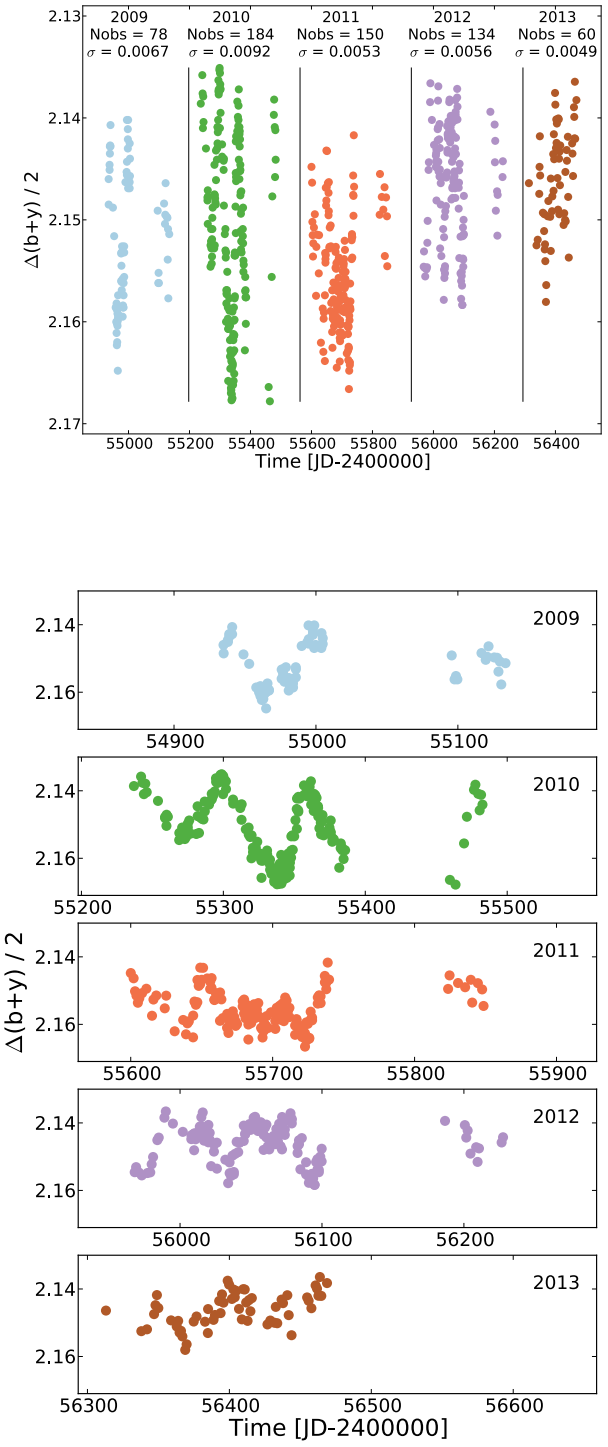

Figure 4.10: Photometric data taken of GJ 687 over 5 years. The top panel shows the total data set with information regarding observations and standard deviation for each year. The bottom panel gives a closer look at the data seperated by year.

ability as the signature of the star's rotation period and the 30-day variability as a sign of spot activity on opposite hemispheres of the star.

A frequency spectrum of the 2010 observations, based on least-squares sine fitting over a range of trial frequencies, is shown in the bottom panel of Figure 4.11. We see a strong signal at a period of 61.8 $\pm$ 1.0 d. We take this to be our best measurement of the star's rotation period. Inspection of the 2010 photometric segment of Figure 4.10 clearly shows the overall 60-day modulation that generates the periodogram peak. Departures from perfect periodicity are presumably caused by the evolution of the spot activity on the surface of the star.

Finally, we search for transits of GJ 687 b by first removing the spot variability from each of the yearly light curves. We do this by successively subtracting multiple frequencies from each yearly light curve using the method described in Henry *et al.* (2001). We removed three to six frequencies from each light curve until each set of residuals approached the precision of a single observation. The residuals from all five observing seasons are plotted in the top panel of Figure 4.12, phased with the 38.14-day best-fit planetary orbital period and a time of mid transit computed from the orbital parameters. The vertical bar represents the 0.0022 mag standard deviation of the residuals from their mean, very close to the measurement precision given above. A sine fit to the phased data gives a formal semi-amplitude of just 0.00011 $\pm$ 0.00012 mag. Since none of the frequencies removed from the yearly light curves were similar to the orbital frequency or its harmonics, this result limits any periodic brightness variability of the star on the observed radial velocity period to a very small fraction of one milli-magnitude (mmag). This rules out the possibility that the 38.14-day radial velocity variations in GJ 687 are induced by stellar activity, as has been documented in somewhat more active stars, for instance, by Queloz

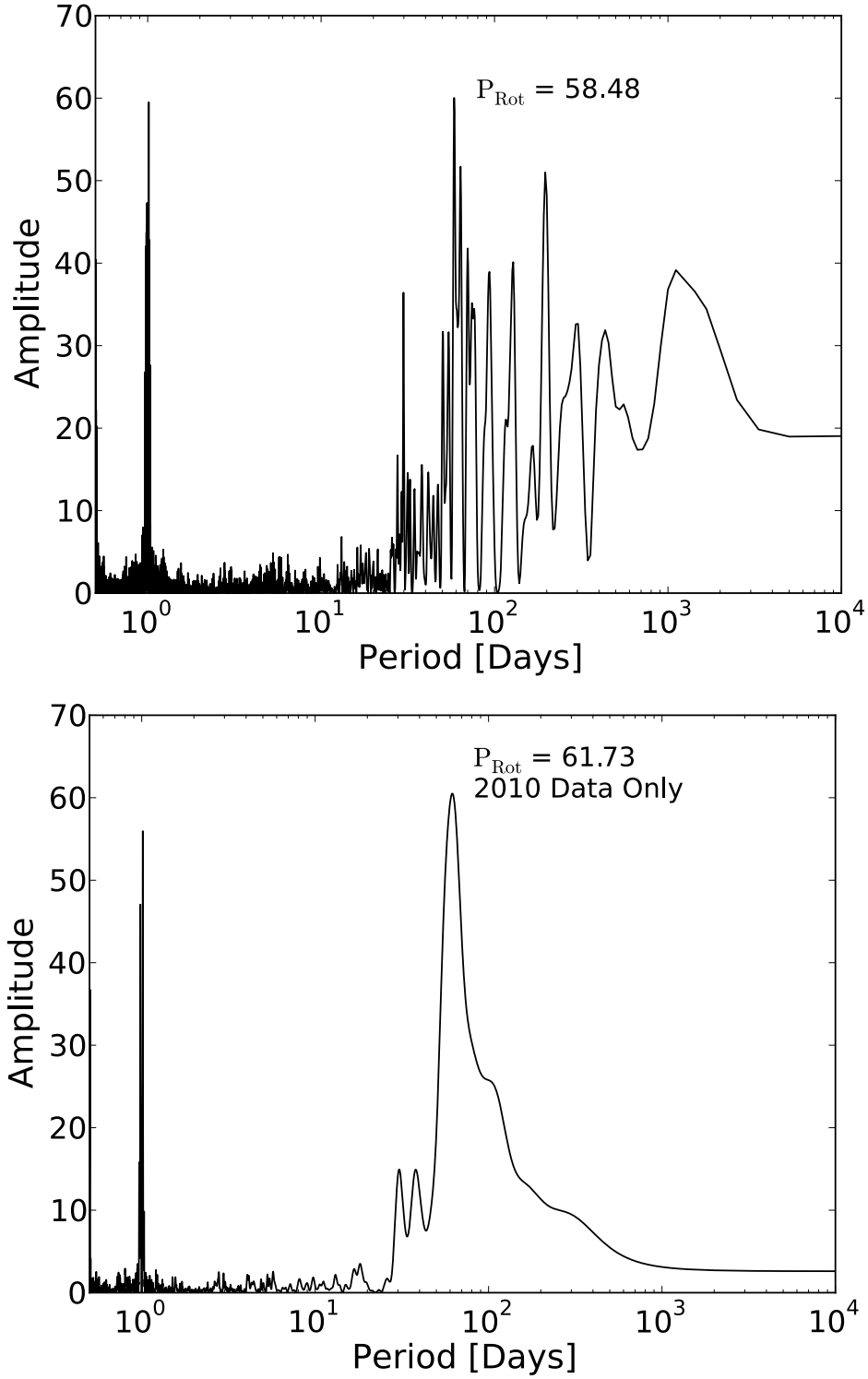

Figure 4.11: Lomb-Scargle periodogram of the photometric observations of GJ 687. In the combined data set, the maximum observed power occurs at 58.48 days (top panel). However when we consider only data obtained in 2010, where the rotational modulation is most clearly exhibited, we find that maximum power occurs at P = 61.73 days (bottom panel). We identify this periodicity with the rotational period of the star.

et al. (2001), Paulson *et al.* (2004), and Boisse *et al.* (2012). Instead, this lack of photometric variability confirms that the radial velocity variations in GJ 687 result from true planetary reflex motion.

The photometric observations within $\pm$0.13P of mid-transit are replotted with an expanded scale in the bottom panel of Figure 4.12. The solid curve shows the predicted phase, depth (assuming Neptune-like density), and duration of a central transit, computed from the stellar radius in Table reftab:687stellarparams and the orbital elements in Table 4.2. The horizontal error bar under the predicted transit time gives the $\pm 1\sigma$ uncertainty in the timing of the transit. The photometric observations when filtered using the Henry *et al.* (2001) procedure described above, and when folded at the $P = 38.14$ day best-fit period for the planet, give no indication that transits occur. We note, however, that the Markov Chain models generate a five-day window for possible transits, and so a more conservative approach is also warranted. In Figure 4.13, we plot the unfiltered photometric data, indicating the range of photometric points that potentially could have been affected by transits were they to occur. Because of uncertainties in the orbit, the potential transit duration, the potential size of the planet, and the error in the photometric filtering, we recommend that continued photometric monitoring be carried out to confirm that transits do not occur.

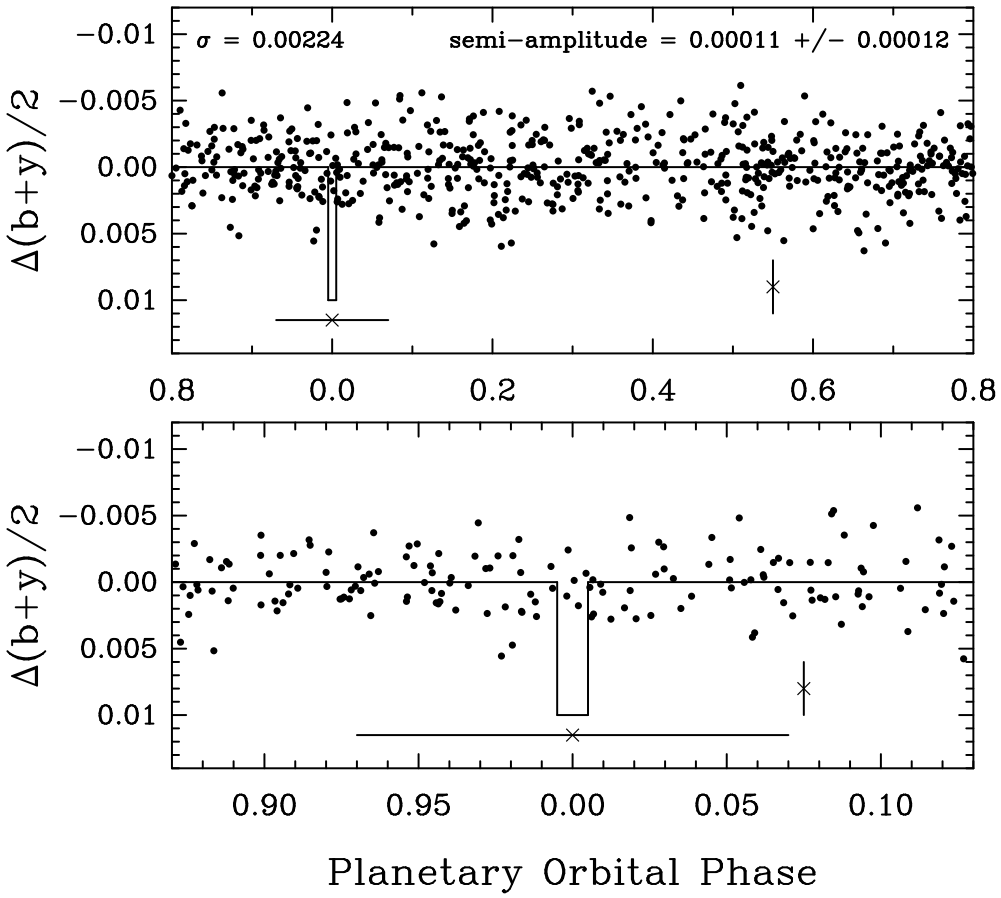

Figure 4.12: *Top panel* Filtered differential photometric measurements for Gliese 687 folded at the best-fit planetary period, P = 38.14 days. A light curve model for a centrally transiting Neptune-sized planet is shown. The vertical error bar indicates the 0.002 magnitude photometric precision. The horizontal error bar shows the 1-σ uncertainty on the time of a central transit. *Bottom panel* shows a magnified view of the folded photometric data in the vicinity of the predicted time of central transit.

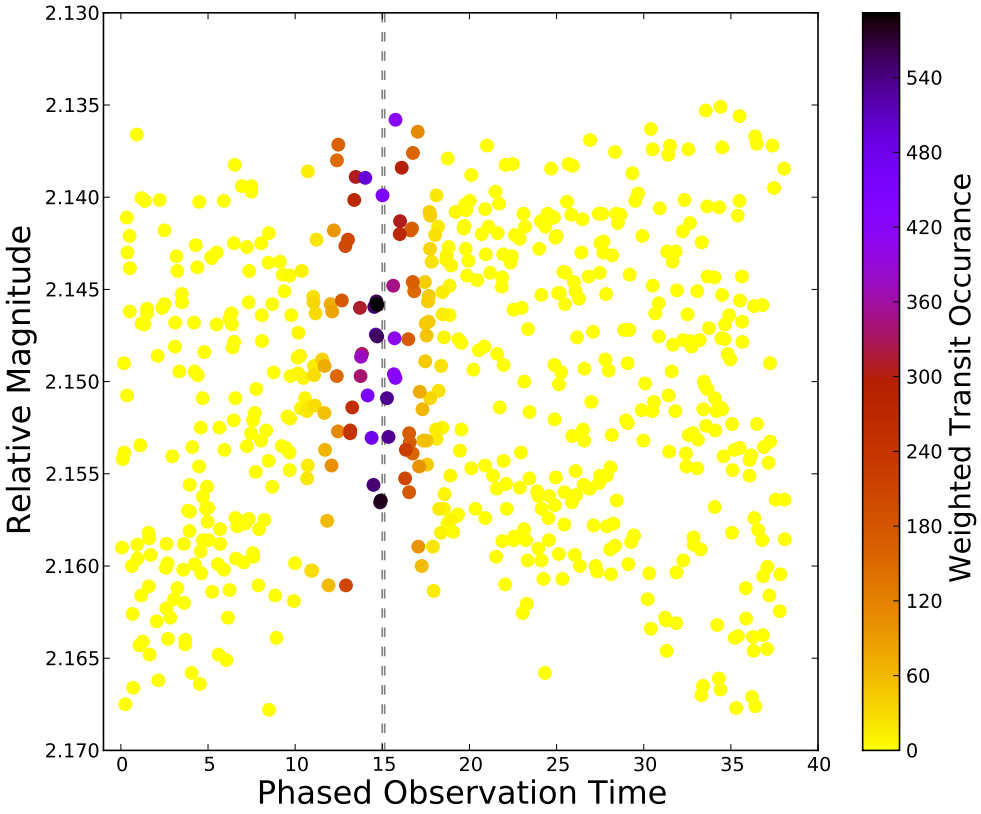

Figure 4.13: For each of the 10,402 potential systems in our Markov chain, we check the predicted transit times against our photometric observations. If a photometric data point lies within the transit window of a particular member of the Markov chain, we assign a value to that point which is cosine-weighted by its distance from the predicted time of central transit. The sum of these values is mapped onto the color of the points in the diagram. The phase of the points, as well as the vertical gray bar spanning the predicted 3-hour central transit duration are for our best fit model given in Table 4.2.

Table 4.1: Stellar Parameters for Gliese 687

Parameter	Value	Reference
Spectral Type	M3 V	(Rojas-Ayala *et al.*, 2012)
Mass ($M_\odot$)	0.413 ± 0.041	(Boyajian *et al.*, 2012)
Radius ($R_\odot$)	0.4183 ± 0.0070	(Boyajian *et al.*, 2012)
Luminosity ($L_\odot$)	0.0213 ± 0.00023	(Boyajian *et al.*, 2012)
Distance (pc)	4.5 ± 0.115	(Rojas-Ayala *et al.*, 2012)
$B-V$	1.5	Simbad
V Mag.	9.15	(Rojas-Ayala *et al.*, 2012)
J Mag.	5.335	(Cutri *et al.*, 2003)
H Mag.	4.77	(Cutri *et al.*, 2003)
K Mag.	4.548	(Cutri *et al.*, 2003)
Avg. S-index	0.811	This work
$\sigma_{\text{S–index}}$	0.096	This work
P_{rot} (days)	61.8 ± 1.0	This work
T_{eff} (K)	3413 ± 28	(Boyajian *et al.*, 2012)

Table 4.2: 1-planet model for the GJ 687 System

Parameter	Best fit	Errors
Period (d)	38.14	(0.015)
Mass (M_J)	0.058	(0.007)
Mass ($M_\oplus$)	18.394	(2.167)
Mean Anomaly (deg)	234.62	(87.962)
Eccentricity	0.04	(0.076)
Longitude of periastron (deg)	359.43	(120.543)
Semi-major Axis (AU)	0.16353	(0.000043)
Time of Periastron (JD)	2450579.11	(9.32)
RV Half Amplitude (m s^{-1})	6.43	(0.769)
First Observation Epoch (JD)	2450603.97	
Velocity Offsets		
Keck/HIRES	0.64 m s^{-1}	(0.63)
APF/Levy	-1.71 m s^{-1}	(1.68)
HET	1.27 m s^{-1}	(0.98)

Table 4.2 (cont'd): 1-planet model for the GJ 687 System

Parameter	Best fit	Errors
χ^2	18.55	
RMS	6.16 m s^{-1}	
Jitter	5.93 m s^{-1}	

Note. — All elements are defined at epoch JD = 2450603.97. Uncertainties are reported in parentheses.

4.6 Metallicity

Gliese 687 appears to have a slightly sub-solar metallicity. Rojas-Ayala *et al.* (2012) use Na I, Ca I, and H_2O-K2 calibrations to estimate [Fe/H]=-0.09 for Gliese 687, whereas the M-dwarf metallicity calibration of Schlaufman & Laughlin 2010 yields a value [Fe/H]=-0.02.

The connection between the detectable presence of a giant extrasolar planet and the metallicity of the host star was noticed soon after the first extrasolar planets were detected (Gonzalez, 1997), and has been studied in many previous works, see, e.g. Fischer and Valenti (2005a); Sousa *et al.* (2011a). For M dwarfs, recent work, such as that by Neves *et al.* (2013), suggests that the giant planet stellar metallicity correlation holds robustly for M-dwarf primaries, but that for planets with mass, $M_{\rm p} \lesssim 20 M_{\oplus}$, no correlation is found with host star metallicity, and indeed, Neves *et al.* (2013) report a hint of *anti*-correlation between the presence of a low-mass planet and host star [Fe/H]. Our detection of a Neptune-mass companion to Gliese 687, and our Lick-Carnegie database of Doppler measurements of M dwarf stars provides an opportunity to revisit this topic.

Our database of radial velocity observations taken at the Keck Telescope contains

142 M-type stars with the necessary spectral information to assess metallicity, 17 of which are known to host planets published in the peer-reviewed literature. We break the planet-hosting stars into two subgroups based on their masses - stars with $M\sin(i)$ planets less than 30 M_{Earth} are described as Neptune hosting while stars with $M\sin(i)$ planets greater than 30 M_{Earth} are listed as Jupiter hosting. We replicate the procedure of Schlaufman and Laughlin (2010) and examine how horizontal distance from a field M dwarf main sequence in a M_{K_s} vs. $(V-K_s)$ color-magnitude diagram (CMD) correlates with metallicity, as noted e.g., by Baraffe *et al.* (1998). The top panel of Figure 4.14 displays all of the Lick-Carnegie survey M dwarf stars plotted in M_{K_s} vs. $(V-K_s)$, with grey dots denoting survey stars without known planets, red dots denoting survey stars that host "Neptune-mass" planets and blue dots representing the survey stars that host "Jupiter-mass" planets. It can be seen that most planet hosting stars fall to the right of the field M dwarf main sequence presented in Johnson and Apps (2009) (black line), which is taken to be a [Fe/H]=0.017 isometallicity contour in this CMD. In order to quantify the likelihood that a star's horizontal distance from the isometallicity contour is related to its propensity to host planets, we compare the distances for our actual planet-hosting stars with randomly drawn samples from the collection of M dwarfs in the survey.

We characterize the position of each M dwarf by obtaining V-band and K_s photometry and then using them to calculate the distance statistic Σ :

$$\Sigma = \sum_{i=1}^{n} (V-K_s)_i - (V-K_s)_{iso} \tag{4.2}$$

To determine if the Σ of our known planet hosting subgroups is significant or, al-

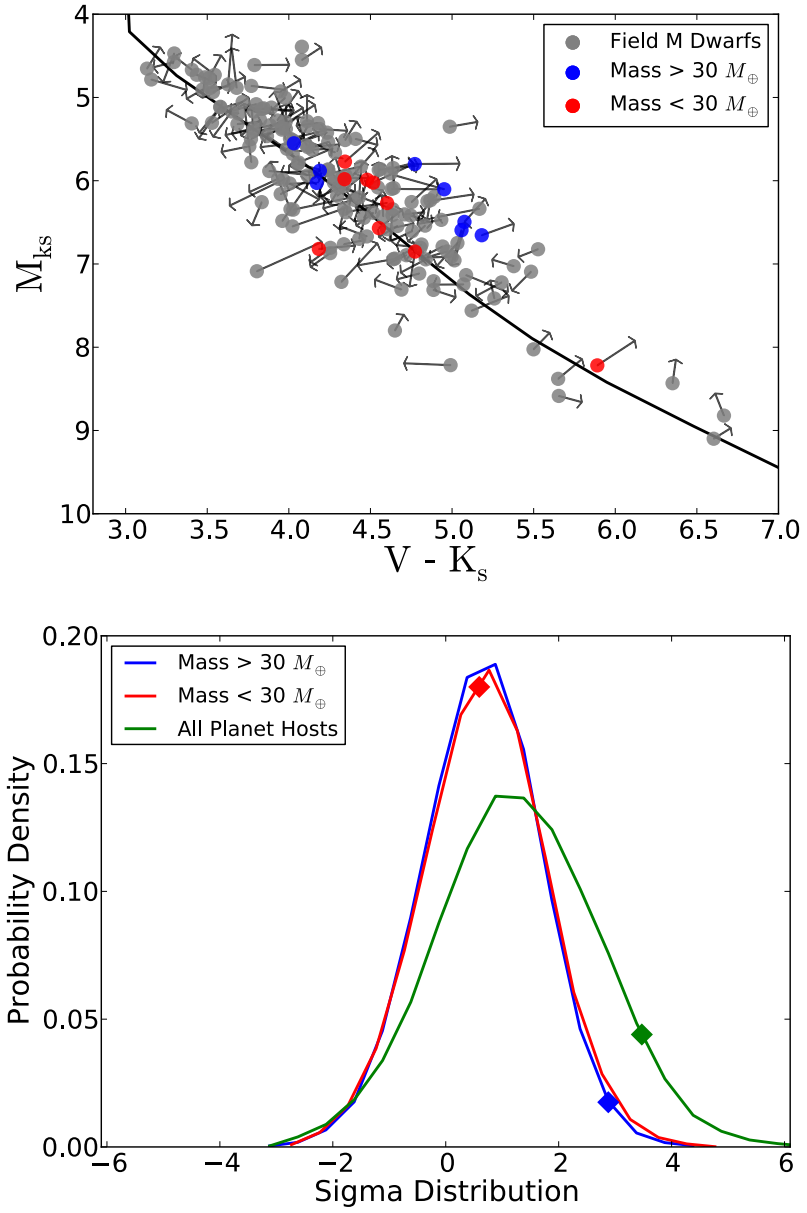

Figure 4.14: *Top panel* Location of the 142 M dwarfs from the Lick-Carnegie radial velocity survey. Stars known to host Jupiter-mass planets are plotted in blue, those known to host twice-Neptune Msin(i) (or smaller) planets are plotted in red and non-planet hosting survey M dwarfs are plotted in grey. The field M dwarf main sequence from JA09 is shown as a black line and the arrows affixed to each point represent that survey star's proper motion. *Bottom panel* Distributions generated via Monte Carlo simulations of the cumulative sample distance of field M dwarfs from the M dwarf main sequence used by Johnson and Apps 2009. The points plotted on top of each curve in the bottom panel represent the actual cumulative distance from the MS for our planet hosting and field star samples.

ternatively, if it could be produced by chance, we make use of a Monte Carlo simulation that calculates the cumulative sample distance of survey M dwarfs from the field M dwarf main sequence presented by Johnson and Apps 2009. For the simulation, we randomly select a subset of M dwarfs from the Lick-Carnegie field star list, setting the sample size equal to the number of M dwarfs known to host either Jovian or Neptune mass planets. Then we compute the cumulative horizontal distance of those stars from the field M dwarf MS, where stars to the right of the MS add their distance to the sum and stars to the left of the MS subtract their distance. We repeat this process 10,000 times to determine the distribution of cumulative horizontal distances from the MS given no correlation between whether the star hosts an exoplanet and its location in the $(V-K_s)-(M_{K_s})$ CMD.

Our results show that for Jupiter planet mass hosts, $\Sigma = 2.359$, which corresponds to a probability of $p = 0.053^{+0.13}_{-0.04}$ that the stars' cumulative distance from the isometallicity contour occurred by chance. For the Neptune hosts, we find that $\Sigma = 1.113$ leading to $p = 0.452^{+0.24}_{-0.23}$, and for the combination of all planet hosts, we obtain $\Sigma = 3.473$ or $p = 0.0775^{+0.09}_{-0.05}$. The distributions resulting from the Monte Carlo simulation and the locations of the actual planet hosting stars Σ values are displayed in the bottom panel of Figure 4.14. The points plotted on top of each curve in Figure 4.14 represent the actual cumulative distance of our planet hosting star samples from the field M dwarf MS. Our results thus indicate that the planet-metallicity correlation is robust for M-dwarf hosts of planets with $M > 30M_{\oplus}$, but that at smaller masses there is, at present, no evidence a correlation exists.

4.7 Planet Recovery

The Lick-Carnegie exoplanet survey and its predecessors have carried out a long-term monitoring program of the brightest M-dwarf stars in the sky. Our database of observations contains 159 stars that have more than 10 observations apiece, and which, additionally, have median internal uncertainty $\sigma < 10\,\mathrm{ms}^{-1}$. Within this group, there is a subset with extensive data sets. For example, 11 stars have $N > 100$ observations and median internal uncertainties $\sigma < 13\,\mathrm{ms}^{-1}$. A question of substantial interest, therefore, is the degree to which the observations taken to date have probed the true aggregate of planetary companions to the M-dwarf stars in our survey.

The effort required to obtain the existing data has been substantial. Among the M-type stars alone, our database contains a total of 5,468 velocity measurements from Keck I, totaling 2,579,862 seconds (29.86 days) of on-sky integration. Overheads, including the acquisition of high S/N spectra, CCD readout time, and weather losses, add materially to this time investment. Furthermore, the distribution of total observing time allotted to the stars on the list has been highly uneven. Targets such as Gliese 436 and Gliese 876, which harbor planetary systems of particular interest, have received much more attention than the typical red dwarf in the survey. For example, Gliese 436 has 148 observations and Gliese 876 has 204 observations obtained with the Keck Telescope. The stars themselves also exhibit a range of chromospheric activity levels. The resulting star-to-star dispersion in “stellar jitter" (tantamount to a measurement uncertainty, σ_{jit}) complicates the evaluation of threshold levels for $M\sin(i)$ as a function of orbital period to which planetary companions can be excluded.

There are a variety of approaches to the measurement of false alarm probabilities (FAP) in the context of spectral analysis of unevenly sampled data. See, e.g. Baluev (2012) for a recent discussion. A very simple approach is described by Press *et al.* (1992). For a gaussian random variable[1], the probability distribution for obtaining a peak at frequency ω of Lomb-normalized power (Scargle, 1982), $P_{\rm N}(\omega)$, is exponential with unit mean. If a data set drawn from measurements of a white noise (Gaussian) distribution supports measurement of M independent frequencies, the probability that no peak exceeds power z (the FAP) is $\mathcal{P}(P_{\rm N} > z) = 1-(1-\exp^{-z})^M$.

We adopt a FAP of 10^{-4}, calculated with the above method (and using Monte-Carlo simulations to determine M) as the generic threshold for attributing a given planetary signal to a given dataset. With this detectability threshold, we use the Systemic Console 2.0 software package (Meschiari *et al.*, 2012) to determine the number of readily detectable planets in our M-dwarf data set. A "readily detectable" planet generates a signal that can be isolated algorithmically (and automatically) by straightforward periodogram analysis and Levenberg-Marquardt minimization. The results of this exercise are shown in Figure 4.15, which locates signals corresponding to 19 previously published planets orbiting 14 separate M-dwarf primaries. Other than Gliese 667C, there are no stars on our 159-star list for which a planet has been published by another group, and for which the automated algorithm finds no planets. Regarding GJ 667C, 40 observations have been made at Keck, and these were used in a characterization of the GJ 667C system (Anglada-Escudé *et al.*, 2012), however the peak planetary signal for this set fell below

[1]Clearly, the generating function for typical radial velocity datasets has non-Gaussian (and unknown) error. False Alarm Probabilities must therefore be treated with great caution when evaluating the existence of a planet with $K \gtrsim \sigma_{\rm unc.}$.

our FAP threshold when utilizing only the Keck data. The bright planet-hosting red dwarfs Gliese 832, 3634, and 3470 all have declinations that are too far south to be observed from Mauna Kea, and HIP 79431 (RA 16h 12m 41.77s DEC -18° 52′ 31.8″) is not on the list of M-dwarfs being monitored at Keck.

The Kepler Mission's photometric data have been used to infer that small planets orbiting M-dwarfs are very common. For example, Dressing and Charbonneau (2013) find an occurrence rate of 0.9 planets per star in the range $0.5\,R_\oplus < R_\mathrm{p} < 4\,R_\oplus$ with P $<$ 50 days. Given the existence of this large number of small-radius planets, it is of interest to make a quantitative analysis of how deep into the expected population of super-Earth type planets suggested by the Kepler Mission the Keck Radial Velocity Survey has probed. To answer this question, we have created synthetic radial velocity data sets that contain test planets, and which conform with the timestamps, the internal measurement uncertainties, and the stellar properties (namely mass) for all 104 M-dwarfs under surveillance at Keck with at least 20 radial velocity observations. To address the error source arising from stellar jitter, σ_jit, we use the median value provided in Wright (2005) of 3.9 $\mathrm{m\,s^{-1}}$ as the expected level of σ_jit for our M-dwarf stars. This value is then added in quadrature with the internal uncertainty and applied to the synthetic data set to create a more accurate representation of the system.

For each of the 104 stars in the Keck survey, we have created 400 synthetic data sets. Each set contains a single planet. The planets are evenly spaced in log period from 2 to 100 days, and evenly spaced in log mass from 1 $M_\oplus$ to 1 M_Jup. We assign a circular orbit to these test planets and assume $i = 90°$ and $\Omega = 0°$ in each case. We then calculate the radial velocity each of these planets would induce on a parent star. A Gaussian distribution with $\sigma^2 = {\sigma_\mathrm{internal}}^2 + {\sigma_\mathrm{jitter}}^2$

Star Name	Planet	Source	Period(Days)	Mass(M_{Jup})	Ecc
HD 285968	GJ 176 b	Calc	8.775	0.031	0.0
HD 285968	GJ 176 b	Pub	8.7832	0.026	0.0
HIP 22627	GJ 179 b	Calc	2249.994	0.829	0.197
HIP 22627	GJ 179 b	Pub	2288	0.824	0.210
GJ 1214	GJ 1214 b	Calc	2.732	0.024	0.11
GJ 1214	GJ 1214 b	Pub	1.580	0.0204	0.0
GL 317	GL 317 b	Calc	692.965	1.164	0.0
GL 317	GL 317 b	Pub	692.9	1.18	0.193
GL 382	GL 382	Calc	36.380	0.071	0.0
GL 388	GL 388	Calc	2.226	0.143	0.06
GL 433	GL 433 b	Calc	7.3699	0.016	0.2
GL 433	GL 433 b	Pub	7.371	0.0182	0.080
GL 625	GL 625	Calc	21.316	0.032	0.33
GL 876	GJ 876 b	Calc	61.033	1.924	0.0
	GJ 876 c	Calc	30.228	0.636	0.01
	GJ 876 d	Calc	15.042	0.117	0.05
GL 876	GJ 876 b	Pub	61.117	1.95	0.032
	GJ 876 c	Pub	30.088	0.612	0.26
	GJ 876 d	Pub	1.938	0.018	0.207
	GJ 876 e	Pub	124.26	0.0392	0.055
HIP 109388	GJ 849 b	Calc	2001.096	1.049	0.0
HIP 109388	GJ 849 b	Pub	1880	0.83	0.040
HIP 57050	HIP 57050 b	Calc	41.373	0.267	0.291
HIP 57050	HIP 57050 b	Pub	41.397	0.298	0.314
HIP 57087	GJ 436 b	Calc	2.644	0.067	0.149
HIP 57087	GJ 436 b	Pub	2.644	0.0737	0.15
HIP 70890	HIP 70890	Calc	364.742	0.021	0.1
HIP 74995	GJ 581 b	Calc	5.368	0.048	0.0
	GJ 581 c	Calc	12.918	0.017	0.156
	GJ 581 d	Calc	68.689	0.017	0.4
HIP 74995	GJ 581 b	Pub	5.369	0.0499	0.031
	GJ 581 c	Pub	12.918	0.0168	0.070
	GJ 581 d	Pub	66.640	0.0191	0.250
HIP 83043	GJ 649 b	Calc	592.764	0.267	0.33
HIP 83043	GJ 649 b	Pub	598.3	0.325	0.3
HIP 85523	GJ 674 b	Calc	4.691	0.034	0.19
HIP 85523	GJ 674 b	Pub	4.694	0.035	0.2
HIP 109388	GJ 849 b	Calc	2001.099	1.049	0.14
HIP 109388	GJ 849 b	Pub	1880	0.83	0.040
HD 204961	GJ 832 b	Calc	3440.923	0.639	0.12
HD 204961	GJ 832 b	Pub	3420	0.644	0.12

Figure 4.15: A table of recovered known extra solar planets orbiting M-Dwarf stars for which Doppler velocity measurements from the Keck telescope exist in the Lick-Carnegie database of observations. Published values (indicated with "Pub") are drawn from the compilation at www.exoplanets.org, accessed 2/14/2014. Also shown are the results obtained by our planet-finding algorithm (indicated with "Calc"), when launched on a blind survey for planets.

is used to perturb the predicted radial velocity value.

Each of the 104×400 synthetic systems is passed to the planet search algorithm. Figure 4.16 shows examples of the returned planets for 4 of the 104 stars in this experiment including the star of main interest here, GJ 687. In Figure 4.16 the black lines from bottom to top represent constant $K = \left(2\pi G/P\right)^{1/3} M_{\rm P} M_{\star}^{-2/3}$ values of 1, 10, and 100 m s^{-1} respectively. As expected, the detectablity thresholds lie roughly along lines of constant K. To determine the smallest K value we could reliably detect for each star, we find the smallest value of K for which a planet was found for at least 50% of the chosen periods. This median value generates the green lines seen in the figure. The top panel of Figure 4.17 shows these minimum K values for each of the 104 stars that we tested. For clarity, the stars in this figure have been ordered by increasing minimum K, and are colored by the number of observations we have for each.

If a test planet lies in its star's habitable zone, (defined as the semi-major axis at which the flux received by the planet is the solar constant received at Earth) we can ask how large the planet needs to be to be detectable by our radial velocity survey. Figure 4.17 shows these threshold masses for each of the 104 M-dwarf stars which we analyzed. These stars maintain the ordering from the top panel, but now have been colored by the mass of the parent star. We see that while the Keck survey has probed substantially into the regime occupied by Neptune-mass planets, it has not made significant inroads into the super-Earth regime for periods that are of astrobiological interest.

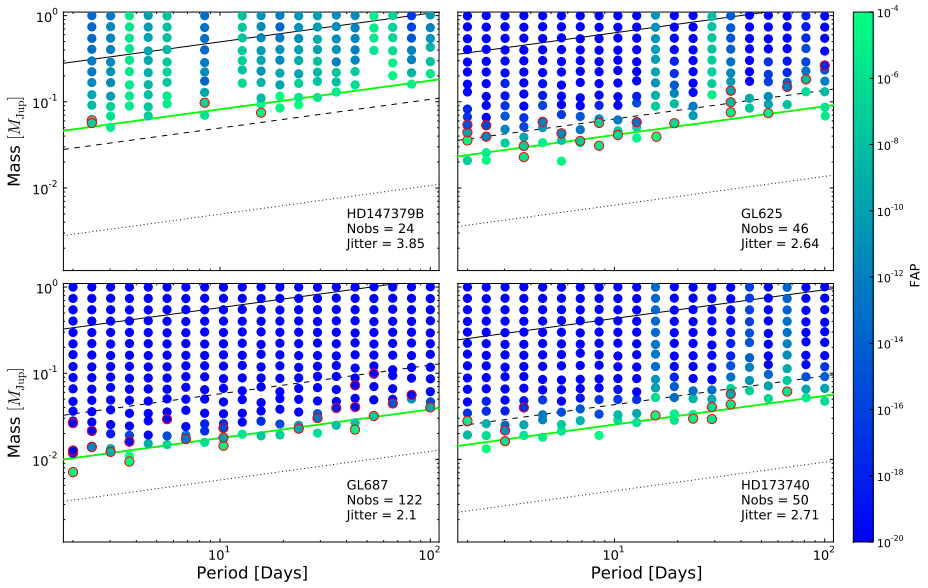

Figure 4.16: Example plots of our synthetic planet recovery around four M-dwarf stars. The points represent planets our algorithm found, colored by the false alarm probability for the initial detection. The black lines from bottom to top show radial velocity half amplitudes (K) of 1, 10, and 100 m s^{-1}. The green line is our minimum detectable K value.

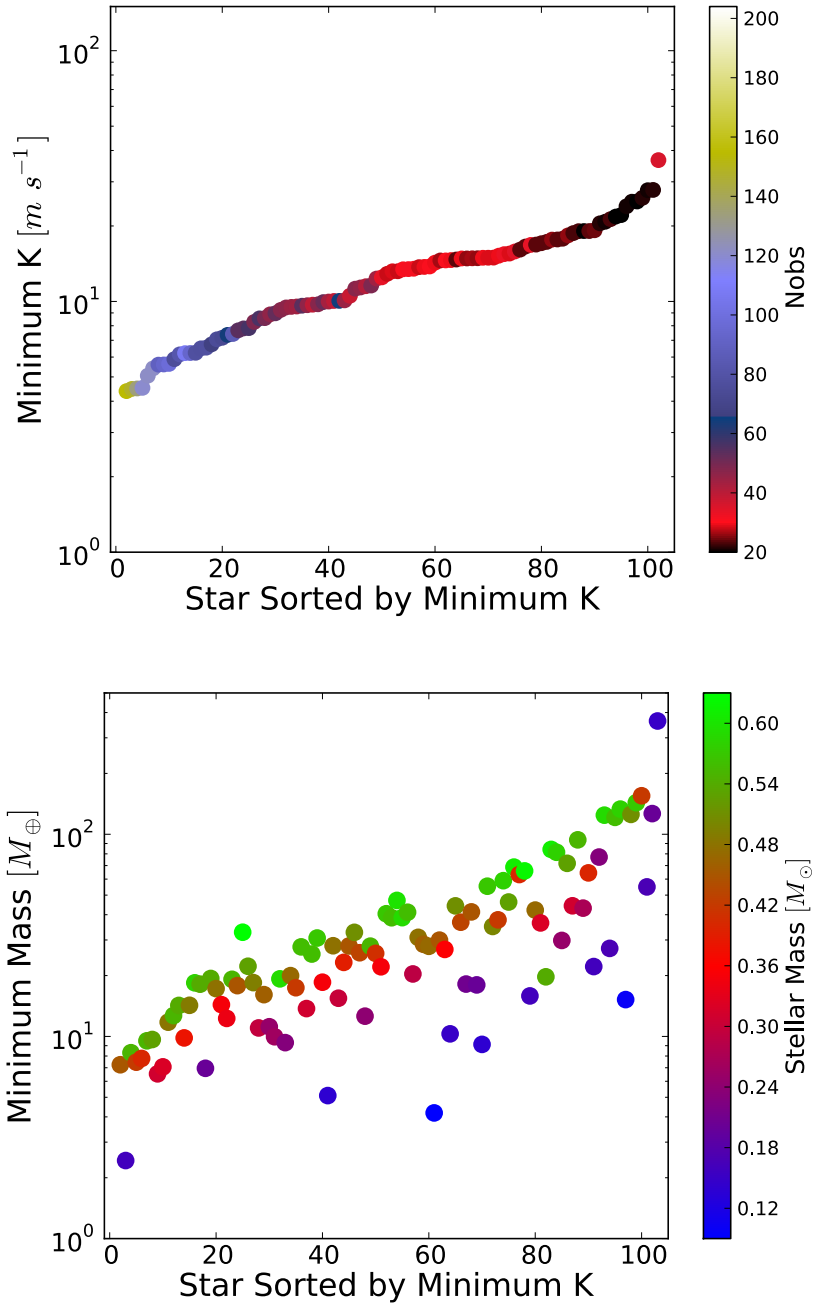

Figure 4.17: *Top panel* The minimum detectable K value for each star in our M-dwarf collection. *Bottom panel* Assuming a minimum detectable K for each M-dwarf star, if a planet was orbiting in that star's habitable zone, this is the minimum mass that planet could have and still be recovered by our method.

4.8 Discussion

GJ 687 is the second planetary system to be detected using data from the APF telescope, with the first being HD 141399 b,c,d, and e (Vogt, 2014a). APF has successfully navigated its commissioning stage, and, since Q2 2013, it has routinely acquired science-quality data that presents sub-m/s precision on known radial velocity standard stars (Vogt, 2014b). In recent months, the degree of automation for APF has increased substantially. The facility currently works autonomously through an entire night's operations, calibration, and observing program. The APF and its accompanying high-resolution Levy spectrograph together form a dedicated, cost-effective, ground-based precision radial velocity facility that is capable of detecting terrestrial-mass planets at distances from their parent stars at which surface liquid water could potentially be present.

Unlike other highly successful RV facilities, the APF uses neither image scrambling nor image slicing. With a peak efficiency of 15% and typical spectral resolutions of $R \sim 110,000$, the APF represents a critical new resource in the global quest to detect extrasolar planets. Initial speed comparisons indicate that in order to match the signal-to-noise acquired using the Keck telescope/HIRES Spectrograph combination, the APF needs only a factor of 6 increase in observing time. Since the amortized cost of a night on Keck is $\sim 77\times$ more expensive than a night on the APF, and because 80% of the APF's nights are reserved for exoplanetary work, the APF (with its sub-m/s precision and dedicated nightly cadence abilities) will likely provide key contributions to exoplanet detection and characterization in the coming years.

Gliese 687 b's radial velocity half-amplitude, $K = 6.4 \pm 0.5\,\mathrm{ms}^{-1}$, is substantially

greater than the current state-of-the-art for low mass planets. The lowest measured value for K in the catalog of Doppler-detected extrasolar planets[2] stands at $K = 0.51\,\mathrm{ms}^{-1}$ (Dumusque *et al.*, 2012). On the other hand, Gliese 687's status as one of the nearest stars to the Sun imbues it with a great deal of intrinsic interest. In our view, the relatively recent date for Gliese 687 b's detection can be attributed both to the substantial amount of stellar-generated radial velocity noise (as evidenced by Figures 4.3 and 4.5), but also to its location in Draco, high in the Northern Sky, where APF, along with HARPS North, are the only facilities that can routinely observe at sub-$1\,\mathrm{ms}^{-1}$ precision. (As evidenced by the data in this paper, Keck can observe at these high declinations, but at significantly higher expense in comparison to stars lying closer to the celestial equator.)

Indeed, Gliese 687's stellar coordinates (R.A. 17h, 36m, DEC +68°) place it very close to the north ecliptic pole, located at *RA* = 18h, Dec= +66°. This location flags it as a star of potentially great importance for the forthcoming NASA TESS Mission. As currently envisioned (and as currently funded), TESS is a two-year, all-sky photometric survey to be carried out by a spacecraft in a 27-day P/2 lunary resonant orbit. TESS will photometrically monitor $\sim 500,000$ bright stars with a $< 60\,\mathrm{ppm}$ 1-hour systematic error floor. (For reference, a central transit of the Sun by the Earth produces an 86 ppm transit depth.) The Northern Ecliptic Hemisphere will be mapped during the first year of the mission via a sequence of 13 sectors with 27 days of continuous observation per sector. These sectors overlap at the North Ecliptic Pole, and create an area of ∼1,000 square degrees (1/50th of the sky) for which photometric baselines will approach 365 days. Gliese 687 lies at the center of this TESS "overlap zone"

[2] www.exoplanets.org

(which also coincides with JWST's continuous viewing zone). Because much longer time series are produced in the overlap zone, the highest-value transiting planets found by the mission will emerge from this part of the sky (along with the sister segment covering the South Ecliptic Pole).

As mentioned above, however, the TESS overlap zone has received relatively little attention from the highest-precision Doppler surveys. About 10,000 target stars from the TESS Dwarf Star Catalog, all with V<12, are present in the overlap zone. This, of course, is far too many stars to survey with Doppler RV, but there appears to be substantial value inherent in monitoring the *brightest*, *nearest*, and *quietest* members of the cohort of TESS overlap stars. The latest estimates (Mayor *et al.*, 2009a, 2011; Batalha *et al.*, 2013a; Petigura *et al.*, 2013a) suggest that ∼50% of main sequence stars in the solar vicinity harbor $M > M_{\oplus}$ planets with $P < 100\,\mathrm{d}$. Assuming a uniform distribution in period between 5 and 100 days, the average transit probability for these planets is $\mathcal{P} \sim 2.5\%$, suggesting that of order $\mathcal{N} \sim 0.5 \times 0.025 \times 10000 \sim 125$ low mass transiting planets (and systems of transiting planets) will be detected by TESS within the overlap zone. Of these, a small handful, of order 5 systems total (and perhaps, with probability $\mathcal{P}_{\mathrm{transit}} = 1.2\%$, including Gliese 687 b) will garner by far the most attention from follow-up platforms such as JWST, due to their having optimally bright parent stars.

Our detection of Gliese 687 b suggests that by starting now, with a systematic program of Doppler observations of a target list of ∼200 carefully vetted G, K & M dwarf stars with V∼7.5 to V∼10.5 in the 1000-square degree TESS overlap zone, APF can ensure that a precise multi-year Doppler velocity time series will exist for the most important TESS planet host stars at the moment their transiting planets are discovered.

Chapter 5

Additional Planet Detections with the Automated Planet Finder

5.1 Introduction

In addition to the single planet detection around GL 687, the APF has been a major contributor to the characterization of two multi-planet systems that were published during the course of this thesis. In the following chapter, we describe the data acquisition/analysis, resulting planetary fits and important discussions that accompanied the publication of the four planets orbiting the eminently normal K dwarf HD 141399 and the six planets orbiting the extremely nearby K dwarf HD 2191344.

5.2 Four Jovian planets orbiting HD 141399

The target star considered in this section, HD 141399, is a relatively nearby (36 pc distant) slightly evolved, slightly metal-rich K-type star located high in the northern sky (46° declination). Although it is quite bright, with V=7.2, its overall mediocrity has ensured that it has remained generally obscure, even in astronomical circles. A standard Simbad search, for example, turns up only four noncommittal mentions of the star in the literature between 1850 and 2013. Yet because HD 141399 is bright, and because it is chromospherically inactive, it has been on the Keck Radial Velocity program for over a decade. Its first iodine spectrum dates to July 2003. In recent months, it has also been repeatedly observed with the new Automated Planet Finder Telescope (APF) at Lick Observatory (Vogt, S.S. et al., 2014).

Our set of 91 velocities for HD 141399 (including 77 measurements obtained at Keck and 14 new measurements obtained at the APF) indicate that the star is accompanied by an unusual subsystem of three giant planets with near-circular orbits and with periods ranging from 94.0 days to 1070.0 days. The size of the annulus around this star spanned by these planetary orbits is associated with the zone of the terrestrial planets in our own solar system. Our radial velocities, furthermore, indicate the presence of a nearly Jupiter-mass planet at a Jupiter-like distance from the star with an orbital period of roughly a decade. Our time baseline of observations does not yet allow a definitive eccentricity determination for this outer planet. HD 141399's planetary system rises above a minimal threshold of interest as a consequence both of the proximity of its inner two planets to the 2:1 mean motion resonance, as well as the fact that it may well harbor an (apparently) rare near-twin of Jupiter.

5.2.1 HD 141399 - Stellar Properties

HD 141399 (HIP 77301) is located at RA = +15:46:53.8 DEC = +46:59:10.5. As shown in Figure 5.1, which is a color-magnitude diagram of all of the stars in the current Lick-Carnegie Keck database, the star lies just at the main sequence turnoff, with a B−V magnitude of 0.77 ± 0.02 (van Leeuwen, 2007). Following Torres (2010) we derive an effective temperature $T_{\rm eff} = 5360 \pm 53$ K for this star, which, when combined with the $d = 36.17$ pc Hipparcos distance (van Leeuwen, 2007), and $V = 7.2$ magnitude imply a stellar luminosity $L = 1.59 \pm 0.39\, L_{\odot}$ and a stellar radius $R = 1.46 \pm 0.15\, R_{\odot}$. Assuming $\mathrm{M} \sim \mathrm{L}^{1/3.5}$ gives us a stellar mass estimate of $1.14 \pm 0.08\, M_{\odot}$. Using calibrations derived by Ammons *et al.* (2006), we estimate a metallicity, $\mathrm{Fe/H} = 0.18 \pm 0.16$ for HD 141399, in keeping with the presence reported herein of several giant planets. Stars with detectable giant planets similar to the ones reported here have, on average, super-solar metallicities (Fischer and Valenti, 2005a). HD 141399 has no known stellar companions, and is chromospherically quiet, with a Mt. Wilson S-index value $S_{\rm HK} = 0.16$ (Isaacson and Fischer, 2010b) which implies an expected level of stellar jitter $\sigma_{\rm jitter} \leq 2.25\,\mathrm{m\,s^{-1}}$. Indeed, as shown in Figure 5.2, HD 141399's S-index places it among the locus of lowest activity stars within the current Keck survey list.

5.2.2 Radial Velocity Observations of HD 141399

Two platforms, the HIRES spectrometer (Vogt *et al.*, 1994b) of the Keck-I telescope, and the Levy spectrometer of the new Automated Planet Finder at Lick Observatory (Vogt, S.S. et al., 2014) were used to obtain radial velocity measurements for HD 141399. Doppler shifts were measured in each case by placing an iodine absorption cell just ahead of the spectrom-

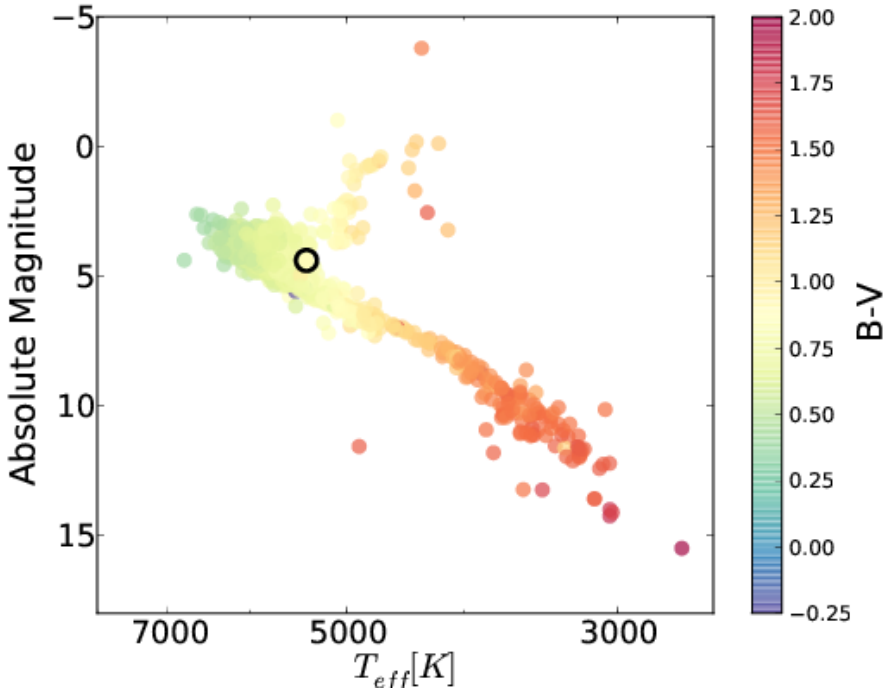

Figure 5.1: HR diagram with HD 141399's position indicated as a small open circle. Absolute magnitudes, M, are estimated from V band apparent magnitudes and Hipparcos distances using $M = V + 5\log_{10}(d/10\text{ pc})$. All 956 stars in our catalog of radial velocity measurements for which more than 20 Doppler measurements exist are shown, color-coded by their B-V values.

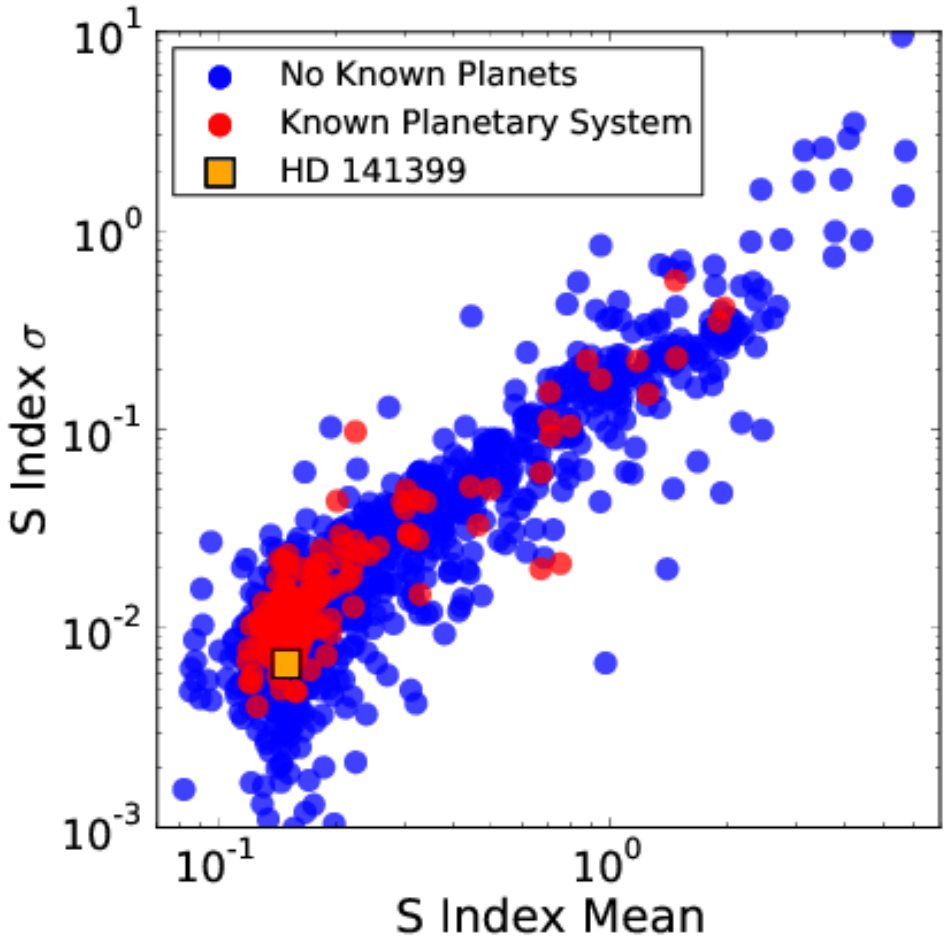

Figure 5.2: The average value of the S-Index against the standard deviation of the S-Index for all the stars in the Lick-Carnegie database. Planets with published planetary systems are colored red. HD 141399 is shown as a square near the quiet tail of the diagram.

eter slit in the converging beam of stellar light from the telescope (Butler *et al.*, 1996c). The forest of iodine lines superimposed on the stellar spectra generates a wavelength calibration and enables measurement of each spectrometer's point spread function. The radial velocities from Keck were obtained by operating HIRES at a spectral resolving power $R \sim$60,000 over the wavelength range of 3,700-8,000 , though only the region 5,000-6,200 containing a significant density of iodine lines was used in the present Doppler analysis. The APF measurements were obtained over a similar spectral range, but at a higher spectral resolving power, $R \sim$108,000. For each spectrum that was obtained, the region containing the iodine lines was divided into $\sim$700 chunks, each of ~ 2 width. Each chunk produces an independent measure of the wavelength, PSF, and Doppler shift. The final measured velocity is the weighted mean of the velocities of the individual chunks. All RVs have been corrected to the solar system barycenter, but are not tied to any absolute RV system. As such, they are "relative" RVs, with a zero point that is usually set simply to the mean of each set.

The internal uncertainties quoted for all the radial velocity measurements in this paper reflect only one term in the overall error budget, and result from a host of systematic errors from characterizing and determining the point spread function, detector imperfections, optical aberrations, effects of undersampling the iodine lines, and other effects. Two additional major sources of error are photon statistics and stellar "jitter". The latter varies widely from star to star, and can be mitigated to some degree by selecting magnetically inactive older stars and by time-averaging over the star's unresolved low-degree surface *p*-modes. The median signal to noise (S/N) of our observations from Keck/HIRES in the iodine region used to calculate the Doppler radial velocity shift is 217. The APF telescope shows a similar S/N but with less variance

owing to its state of the art precision. With a bright star such as HD 141399, the exposure time to attain this S/N is short enough that the star's *p*-mode oscillations are a real concern when determining its radial velocity. To avoid being dominated by *p*-modes, all observations in this paper have been binned on 2-hour timescales. The calculation of the binned velocity and associated timestamp take into account the internal uncertainty of each contributing spectrum.

5.2.3 Best-fit solution

The combined radial velocity data sets show a root-mean-square (RMS) scatter of 32.8 $\mathrm{m\,s^{-1}}$ about the mean velocity. This includes a "telescope" offset of $\sigma_{\mathrm{tel}} \sim -0.87\,\mathrm{m\,s^{-1}}$, between the Keck and APF velocity zero points. (The exact value of σ_{tel} is allowed to vary as a free parameter and emerges as a measured quantity in Table 5.1). HD 141399's quiet chromosphere implies a low level of expected stellar jitter, $\sigma_{\mathrm{jitt}} < 2\,\mathrm{m\,s^{-1}}$, which is consistent with a planetary explanation for the observed dispersion in radial velocities.

Table 5.1: Self-consistent 4-planet model for the HD 141399 System

		Best fit	Errors
Period (d)	b	94.35	(0.059)
	c	202.08	(0.099)
	d	1070.35	(8.178)
	e	3717.35	(555.081)
RV Half-Amplitude (ms^{-1})	b	18.8	(0.551)
	c	43.51	(0.591)
	d	22.28	(0.63)
	e	8.34	(1.239)
Mean Anomaly (deg)	b	224.63	(54.09)
	c	303.75	(15.165)
	d	273.89	(39.812)
	e	153.93	(23.889)
Eccentricity	b	0.04	(0.03)

Table 5.1 (cont'd): Self-consistent 4-planet model for the HD 141399 System

		Best fit	Errors
	c	0.05	(0.013)
	d	0.06	(0.029)
	e	0.0	(Fixed)
Longitude of Periastron (deg)	b	191.37	(55.088)
	c	214.74	(14.457)
	d	249.16	(38.966)
	e	0.0	(Fixed)
Time of Periastron (JD)	b	2452774.98	(15.371)
	c	2452663.34	(8.537)
	d	2452019.53	(119.538)
	e	2451244.36	(555.624)
Semi-Major Axis (AU)	b	0.4225	(0.00018)
	c	0.7023	(0.00023)

Table 5.1 (cont'd): Self-consistent 4-planet model for the HD 141399 System

		Best fit	Errors
	d	2.1348	(0.01086)
	e	4.8968	(0.46122)
Mass ($M_{\rm Jup}$)	b	0.46	(0.025)
	c	1.36	(0.067)
	d	1.22	(0.067)
	e	0.69	(0.164)
First Observation Epoch (JD)		2452833.85	
Velocity Offset (KECK)		0.61 m s^{-1}	(1.7)
Velocity Offset (APF)		1.48 m s^{-1}	(1.89)
χ^2		5.81	
RMS		2.36 m s^{-1}	
Jitter (KECK)		2.35 m s^{-1}	(0.281)
Jitter (APF)		2.59 m s^{-1}	(0.729)

Note. — All elements are defined at epoch JD = 2452833.85. Uncertainties are reported in parentheses.

A Lomb-Scargle periodogram of the 91 velocity measurements of HD 141399 is shown in the top panel of Figure 5.3. False alarm probabilities are calculated with the bootstrap method, as described in Efron (1979), iterating 100,000 times for a minimum probability of 1e-5 as seen on the $P_{\rm b}$, $P_{\rm c}$, and $P_{\rm d}$ peaks in the top panels of Figure 5.3. Several periodicities having vanishingly small false alarm probabilities are observed, with the strongest lying at $P_{\rm c} = 201.88$ days. This signal in the data is modeled as a $M_{\rm c}\sin(i) = 1.36 M_J$ planet with an orbital eccentricity, $e_c = 0.05$. The resulting periodogram of the residuals is shown in the second panel from the top of Figure 5.3, and indicates the presence of significant power at periods of both $P_{\rm d} = 1163$ and $P_{\rm b} = 94.52$ days. These two signals are modeled with planets of masses $M_{\rm b}\sin(i) = 0.46 M_{\rm J}$ and $M_{\rm d}\sin(i) = 1.22 M_{\rm J}$. The residuals periodogram to the three-planet fit

suggests the presence of a fourth planet in the system, with properties that are quite reminiscent of Jupiter, $P_e \sim 4000$ days, and $M_e \sin(i) \sim 1.0 M_J$.

Using Levenberg-Marquardt optimization, we generated a 4-planet best-fit Keplerian model for the system 5.4. We note that the proximity of the 94-day planet and the 201-day planet to a 2:1 mean motion resonance generates a modest dynamical interaction over the period covered by the radial velocity measurements. For our preferred model of the system, we therefore derived a Newtonian fit in which planet-planet interactions (dominated by steady orbital precession, $\dot{\omega}_b$, of the inner planet) are taken explicitly into account. This self-consistent fit (which additionally assumes $i = 90^\circ$ and $\Omega = 0^\circ$ for all four planets) is listed in Table 5.1, and the stellar reflex velocity arising from our 4-planet orbital model is compared to the radial velocity time series in the top panel of Figure 5.5. Phased RV curves for each of the four planets in Table 5.1 are shown in Figure 5.6. A power spectrum of the residuals to our four-planet fit is shown in Figure 5.7 and indicates no significant periodicities. Also shown in this figure is a periodogram of the Mt. Wilson S-Index. None of the peaks in the periodogram of S-Index values coincide with peaks that we are interpreting to arise from planets. Although there is a long term trend present in the S-Index periodogram, it does not have a well defined peak like that of planet e, shown in Figure 5.3.

It is of substantial interest to know whether planets such as the companions to HD 141399 formed *in situ*, or whether they accreted the bulk of their mass further out in the protoplanetary disk and subsequently suffered Type II migration and attendant orbital decay (Seager, 2011). In this regard, the proximity of planets b and c to the 2:1 mean motion resonance may provide an important clue. A history of quiescent inward migration would suggest that these two planets

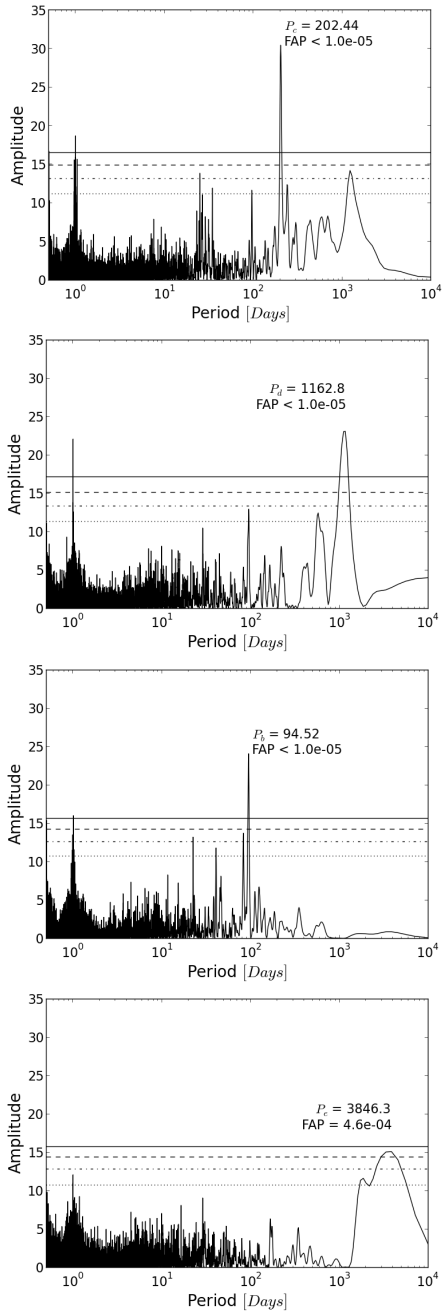

Figure 5.3: Lomb-Scargle periodograms for *top panel:* radial velocity measurements of HD 141399 from the Keck and APF telescopes, *second panel from top* residual velocities with planet c removed, *second panel from bottom* residual velocities with planets c and d removed, *bottom panel* residual velociteis with planets b, c, and d removed. The horizontal lines from top to bottom represent false alarm probabilities of 0.01%, 0.1%, 1.0% and 10.0% respectively.

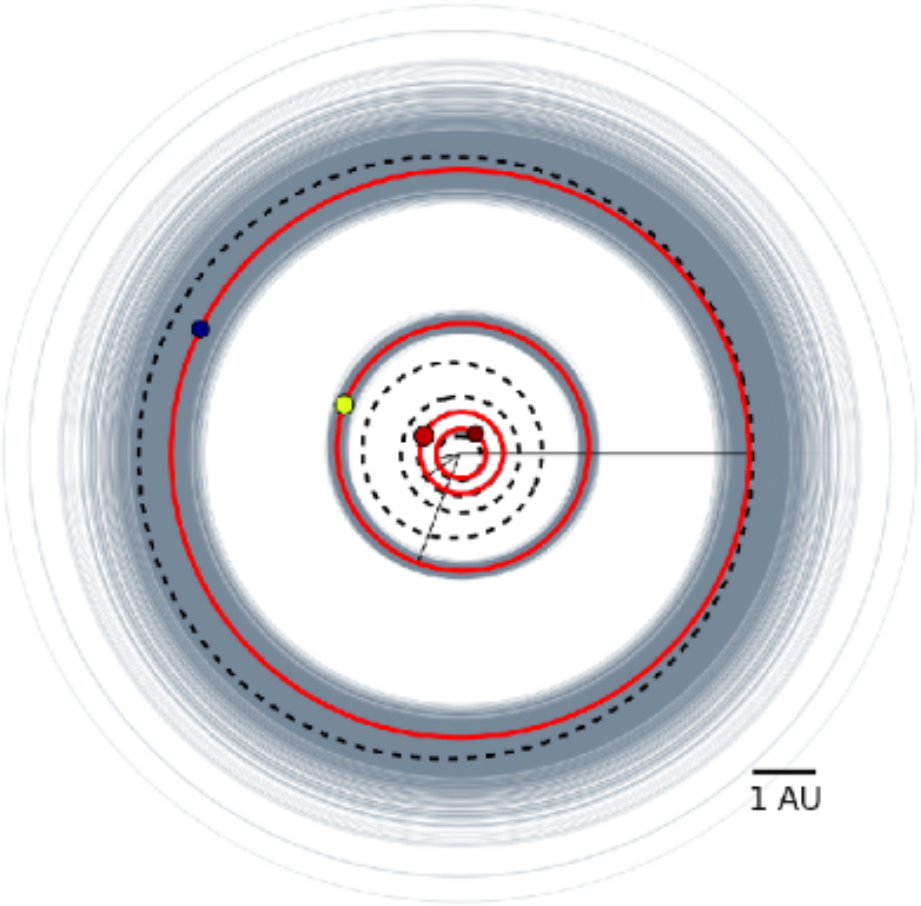

Figure 5.4: The orbits of the proposed planetary system around HD 141399. The points correspond to the location of the planets at the initial observation epoch 2452833.85. The lines from the origin correspond to each planet's perihelion. The light lines are 1000 orbits of the planets drawn from the converged segment of the Markov Chain. The dashed lines are the orbits of the solar system planets with Mercury, Venus, Earth, Mars, and Jupiter all shown here.

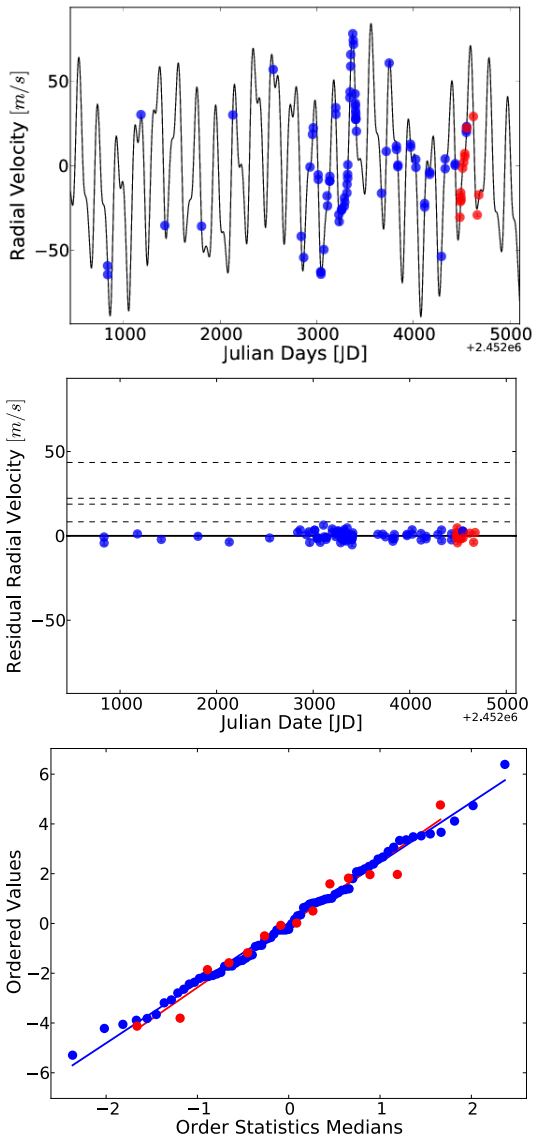

Figure 5.5: *top panel* Best-fit self-consistent integrated 4-planet model from Table 5.1, integrated and compared to the RV measurements for HD 141399. RVs obtained with Keck/HIRES are blue, RVs from the APF/Levy are shown in red. *middle panel* Velocity residuals to the best fit 4-planet model of the system. The four dashed lines indicate from top to bottom $K_c = 43.08\,m\,s^{-1}$, $K_d = 21.95\,m\,s^{-1}$, $K_b = 18.6\,m\,s^{-1}$, $K_e = 9.42\,m\,s^{-1}$, the radial velocity half-amplitudes of the detected planets in the system. *bottom panel* Quantile-Quantile plot for the velocity residuals, indicating the degree to which the errors conform to a gaussian distribution.

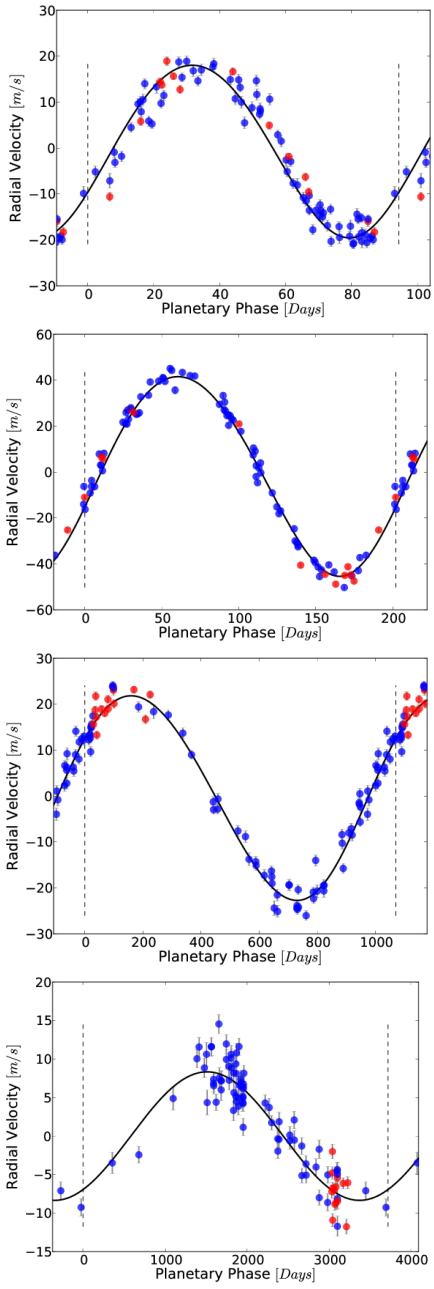

Figure 5.6: Phased RV curves for planets b, c, d, and e. The error estimate for each RV data point is also plotted, but may not be visible due to the scaling of the individual curves. The vetical dashed lines denote the extent of unique data.

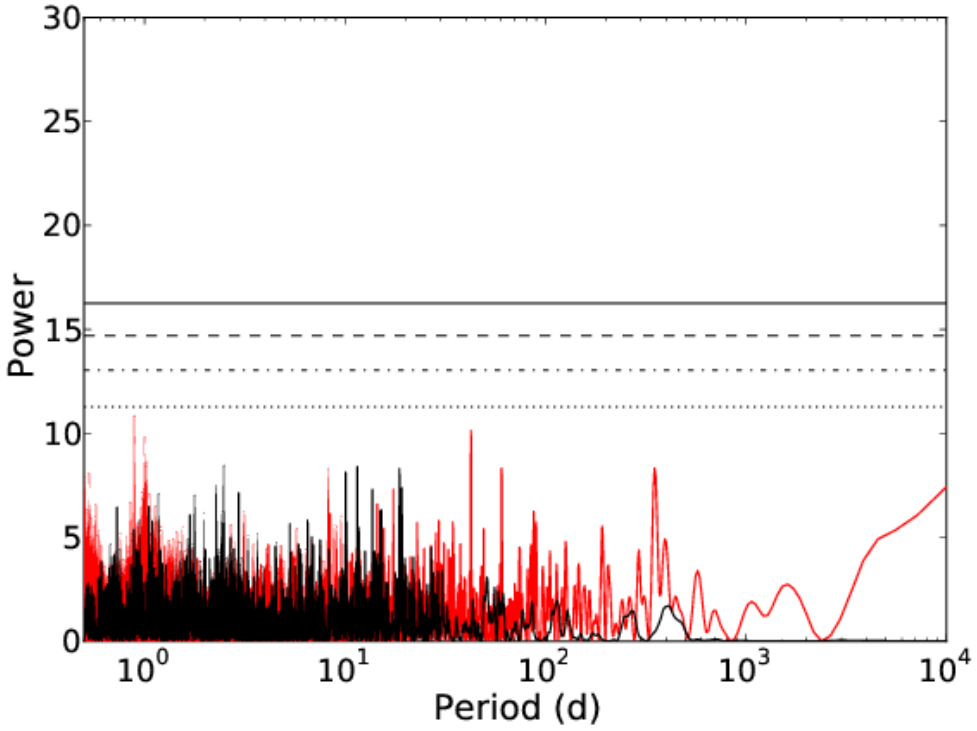

Figure 5.7: Lomb-Scargle periodogram of the radial velocity residuals to the fit given in Table 5.1 plotted in black, and the Lomb-Scargle periodogram of the Mt. Wilson S-Index values plotted behind in red.

should have been captured into resonance. Their current configuration, however, can be placed outside of the resonance with a very high degree of confidence, due to the high precision to which the orbital eccentricities have been determined.

The aggregate of candidate systems with multiple transiting planets observed by Kepler show no overall preference for configurations of planets lying in low order mean motion resonance. The Kepler systems do, however, show a mild preference for configurations in which the period ratios are a few percent larger than the nominal resonant value (Lissauer *et al.*, 2011a). The HD 141399 system conforms to this particular pattern. Recently, Batygin and Morbidelli (2013) and Lithwick and Wu (2012) have shown that when two planets in the vicinity of a low-order resonance interact gravitationally in the presence of dissipation, the initial orbital separation increases as orbital energy is converted to heat. Initially near-resonant pairs are driven toward orbits that are both more circular and separated by an increased distance that scales with the total integrated dissipation experienced. Lithwick and Wu (2012) suggest that the observed overdensity of near-resonant pairs can arise if tidal dissipation is unexpectedly efficient, with $Q \sim 10$. This explanation seems unlikely for HD 141399 b and c, which are likely gas giants, and which likely have tidal quality factors that are orders of magnitude away from the required value. Batygin and Morbidelli (2013) argue that the dissipative mechanism is provided by interaction with the surrounding protoplanetary disk. This mechanism would appear to be more viable in this case, although the hydrodynamical details are somewhat vague and remain to be worked out.

In conclusion, HD 141399 harbors a fairly unusual system in which three (and likely a fourth) Jovian-mass planets lie on low-eccentricity orbits with periods that conform to one's

naive expectation for terrestrial planets. Confirmation of this system was significantly aided by velocity measurements from the APF telescope. The quality of the measurements that the APF is obtaining show it is functioning as intended, and that it is producing Doppler measurements that conform to the current state-of-the-art.

5.3 A six-planet system orbiting the nearby star HD 219134

In this section, 276 velocities for HD 219134 (including 138 measurements with 2-hour binning obtained from long-term Keck planet surveys, 37 measurements with 2-hour binning obtained from spectra taken at Keck by the NASA Q01 Program[1], and 101 measurements with 2-hour binning made with the Automated Planet Finder (APF) telescope) reveal that this star hosts a multi-planet system.

Indeed, the radial velocities obtained at Keck have, since 2010, strongly suggested that HD 219134 is accompanied by a multiple-planet system, but the orbital architecture at periods $P < 100$ d was unclear; the observing cadence at Keck was insufficient to adequately define the orbital parameters of this rather complex multi-planet system. We find that the new APF data, however, with their high velocity precision and improved observing cadence, permit much fuller orbital characterizations for the planetary candidates. Our best model indicates that the star is accompanied by an inner configuration of five low-amplitude planets (having radial velocity half-amplitudes of K=1.9 m s^{-1}, 1.4 m s^{-1}, 2.3 m s^{-1}, 4.4 m s^{-1}, and 1.8 m s^{-1}, all with orbital periods $P < 100$ days). The system also displays a longer-period signal with $P = 2247 \pm 43$ d, and $M \sin(i) = 0.34 \pm 0.02 M_{\rm jup}$, which is similar to the mass of Saturn. The presence of this outer planet has interesting consequences for current planet formation theories.

Taken as a whole, HD 219134 presents a planetary system of substantial scientific interest. Its retinue of multiple super-Earth category planets is highly reminiscent of many of the systems discovered by Kepler, albeit in association with a star that is thousands of times

[1]NASA program: "TPF Preparatory Science: Low Mass Short-Period Companions to TPF Target Stars'; P. I.: W. Cochran'

brighter than the median star in the Kepler catalog.

5.3.1 Stellar Parameters

HD 219134 (HR 8832; GJ 892; HIP 114622) is located high in the northern sky (RA = +23:13:17, DEC +57:10:06) with stellar properties described in Table 5.2. As a bright ($V = 5.57$), nearby ($d = 6.55$ pc) K-type main sequence dwarf of naked-eye visibility, it has long been of interest as a potential planet-bearing star. It was among the original 23 UBC Precise Radial Velocity program stars observed with the CFHT starting in the early 1980s (Walker *et al.*, 1995; Walker, 2012), and it was an early target of interest at Keck. The first of our 138 Keck velocity measurements dates to JD 2450395 (November, 1996). HD 219134 is currently the 99th nearest known stellar system[2], and as a consequence, any planetary system that it harbors would rank among the ten closest known systems (a plurality of which orbit much dimmer M-dwarf primaries). Among stars known to harbor planets with masses $M_{\rm pl}\sin(i) < 10 M_{\rm jup}$, only the Sun, Alpha Cen B, 61 Virginis, and HD 20794 have brighter V magnitudes.

Figure 5.8 shows HD 219134's position on a color-magnitude diagram containing all of the stars in the current Lick-Carnegie Keck database that have accumulated more than 20 Doppler measurements, and emphasizes the star's entirely ordinary Main Sequence location. Takeda *et al.* (2007) derive mass and radius estimates of $M/M_{\odot} = 0.794$ and $R/R_{\odot} = 0.77$, along with an age, $\tau = 12.9$ Gyr. Fischer and Valenti (2005a) measure $v\sin(i) = 1.8\,{\rm kms}^{-1}$, which, if we assume equator-on geometry and a radius $R/R_{\odot} = 0.77$, implies $P_{\rm rot} \sim 20$ d. These parameters, and other known stellar characteristics, are summarized in Table 5.3.

[2] www.recons.org/TOP100.posted.htm

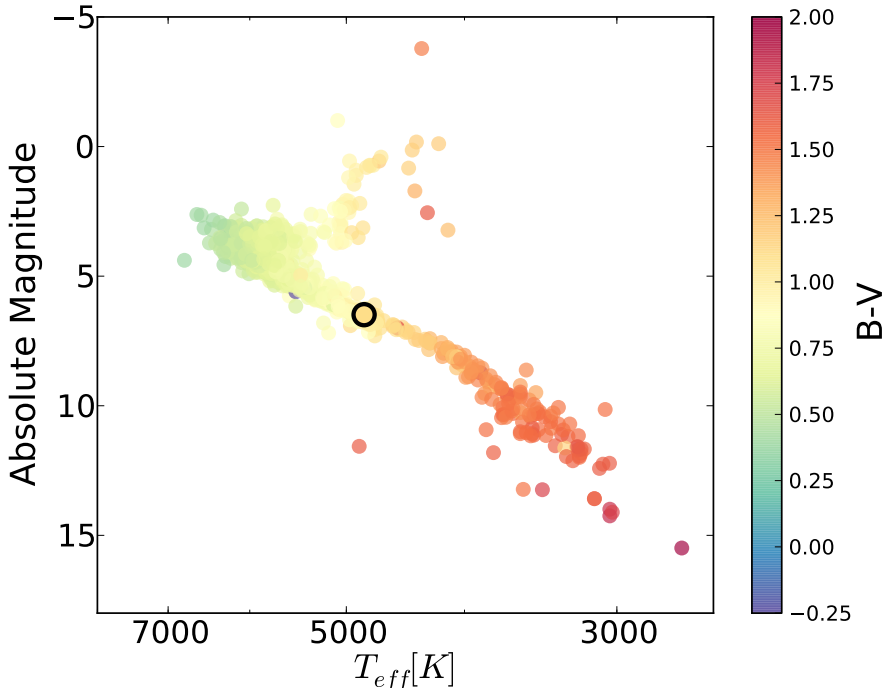

Figure 5.8: HR diagram with HD 219134's position indicated as a small open circle. Absolute magnitudes, M, are estimated from V-band apparent magnitudes and Hipparcos distances using $M = V + 5\log_{10}(d/10\text{ pc})$. All 956 stars in our catalog of radial velocity measurements for which more than 20 Doppler measurements exist are shown, color-coded by their B-V values.

Table 5.2: Stellar parameters for HD 219134

Parameter	Value	Reference
Spectral type	K3V	(Soubiran *et al.*, 2008)
M_V	6.46	(Soubiran *et al.*, 2008)
V	5.57	(Oja, 1993)
$B-V$	0.99	(Oja, 1993)
Mass ($M_\odot$)	$0.794^{+0.037}_{-0.022}$	(Takeda *et al.*, 2007)
Radius ($R_\odot$)	0.77 ± 0.02	(Takeda *et al.*, 2007)
Luminosity (L_sun)	0.31	This work
Distance (pc)	6.546 ± 0.012	(Soubiran *et al.*, 2008)
S_{hk}	0.25	This work
Age (Gyr)	12.46	(Takeda *et al.*, 2007)
[Fe/H]	0.08	(Soubiran *et al.*, 2008)
$T_{\rm eff}$ (K)	4913	(Soubiran *et al.*, 2008)
$\log(g)$ (cm s^{-2})	4.51	(Soubiran *et al.*, 2008)

In spite of its potentially great age, HD 219134 does show indications of stellar activity. It is listed as a "Flare Star" in the SIMBAD Database, and both its median S-index value and the standard deviation of its individual S-index measurements from our Keck spectra are higher than those of the main locus of stars in our Keck survey (see Figure 5.9). Isaacson and Fischer (2010a) report a stellar velocity jitter of 1.57 m s^{-1} for HD 219134, and this relatively low value is corroborated by the analysis of this paper. We do find, however, that the radial velocities for the star are potentially correlated with stellar activity over the decade-plus time baseline of our observations. A periodogram of the S-index values (including measurements at all of our Keck epochs, and at all APF epochs for which photoelectron counts in the I_2 region of the spectrum exceed $N = 25,000$) is shown in the top panel of Figure 5.10. There is a significant peak in this periodogram at $P \sim 3300$ days. This period is greater than and district from the $P \sim 2300$ day periodicity that is present in the Doppler Velocity data for this star. Figure 5.10 also shows a

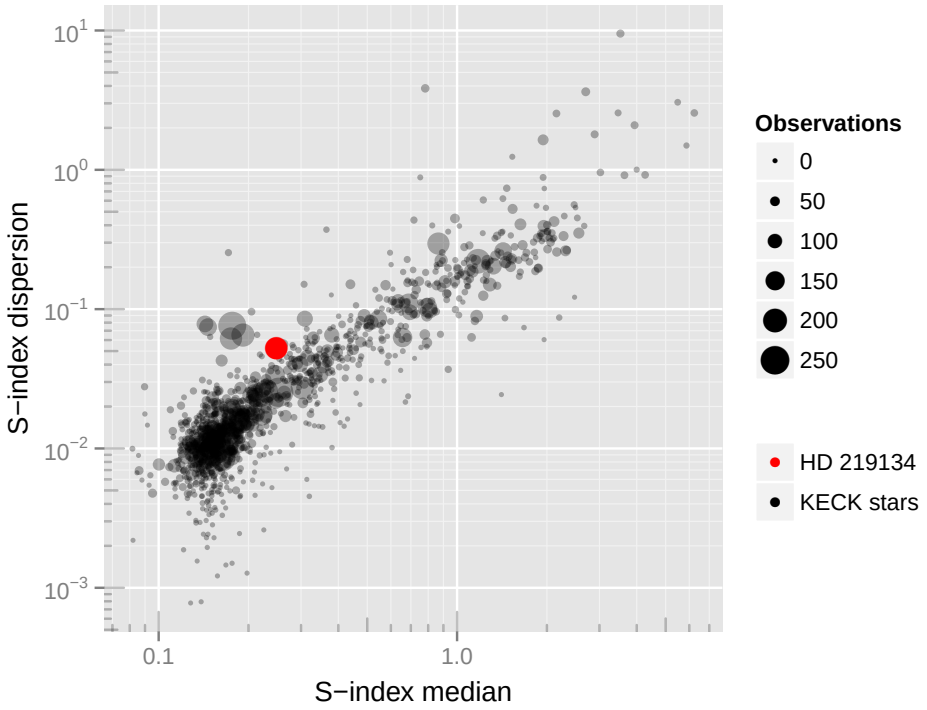

Figure 5.9: The median *S*-index values and dispersions of the *S*-index measurements for the stars in the current Keck sample. HD 219134 is shown in red. The size of the points is proportional to the number of observations.

correlation plot of the radial velocity observations and their *S*-index values. The peak at zero lag (observation record) indicates that there is correlation between the long-period signal in the radial velocities and the *S*-index values, as manifested by the long period of decline in both time series. It is therefore possible that some of the observed velocity variation can be attributed to surface activity. Caution is always warranted in interpreting long-term RV variations.

The Mt. Wilson *S*-index measures the ratio of flux from 1 bins surrounding the line centers of the Ca II H& K lines (at 3968.47 and 3933.66), as compared to two broader 25 bandpasses lying 250 to either side of the Ca II H& K line location (Duncan et al. 1991). In the standard picture, an increase in the *S*-index, whose flux emerges from above the mean photo-

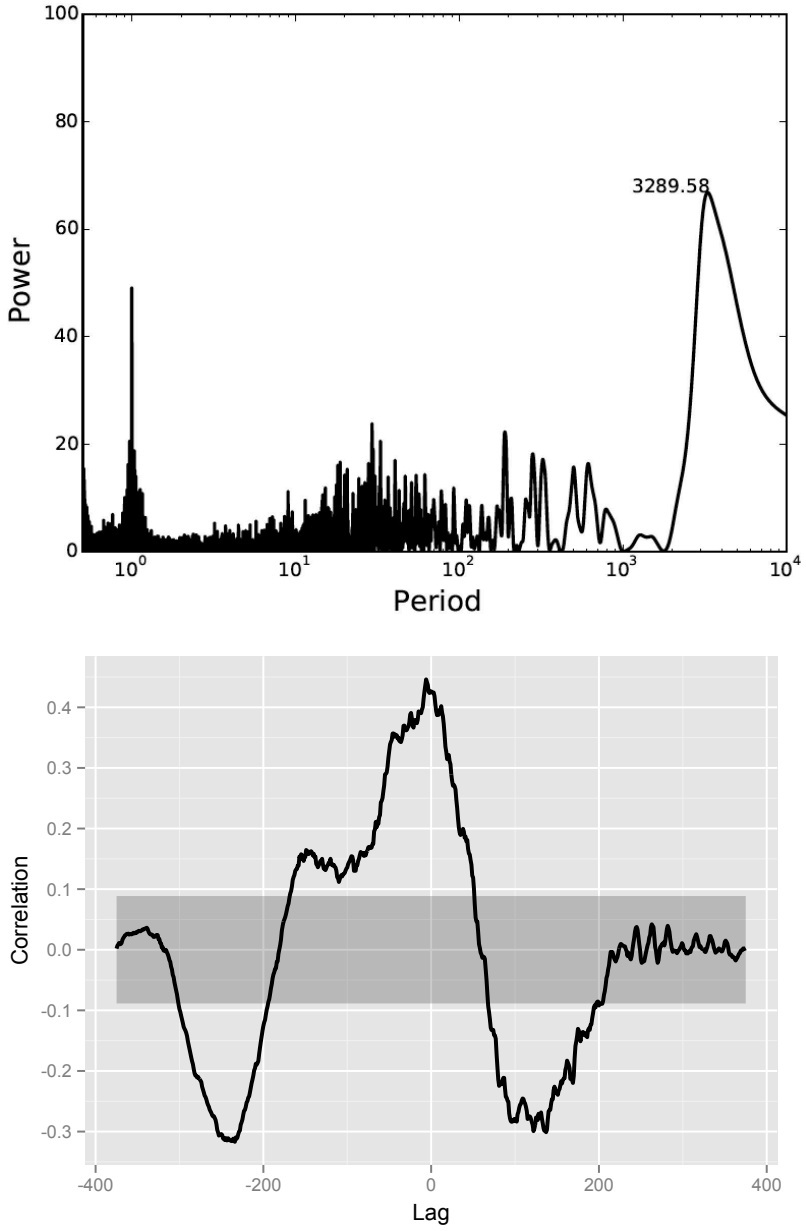

Figure 5.10: *Top Panel* shows a periodogram of the Mt. Wilson *S*-index values associated with our Keck and APF spectra of HD 219134. *Bottom Panel* shows a correlation plot for RV data points and their associated *S*-index values. The shaded area marks the 95% confidence interval for the Pearson correlation coefficient, estimated using sets of white noise data.

spheric depth of the star, corresponds with an increase in spot activity on the stellar surface. Spots, in turn, suppress convection in their vicinity, which decreases the overall convective blueshift of the star, leading to the expectation of a correlation with the Doppler velocity of the star. A star with a magnetic cycle that modulates the number of spots can therefore present a long-term Doppler trend with an amplitude and periodicity that mimics the Keplerian signal from a distant planet (Dumusque et al. 2011).

The upper panel of Figure 5.11 charts the velocity measurements taken with the Keck and the APF telescopes (with the median value for each data set subtracted) against the corresponding *S*-index measurements. While the strength of the overall positive correlation is indicated by a linear fit to the data, the color-coded time-ordering of the points indicates that the correlation was much stronger during epochs from 2000 through approximately 2010. Indeed, as is indicated by the middle panel of Figure 5.11, the correlation has reversed sign from 2012 through present, and a weak negative correlation (having less than $1\,\sigma$ significance) is present in the recent APF observations. Figure 5.12 permits comparison of the time evolution of the *S*-index values to the corresponding RV observations.

The unusual features in the time development of the RV – *S*-index correlation imply that considerable caution must be exercised in interpreting the source of the multi-year periodicity that is present in the Doppler velocity time series. Our candidate planetary signal could, for example, be produced by the superposition of the stellar magnetic activity cycle and a giant planet on a Keplerian orbit. Further monitoring, accompanied by detailed analysis, is clearly required.

Fischer and Valenti (2005a) report a number of additional spectroscopically derived

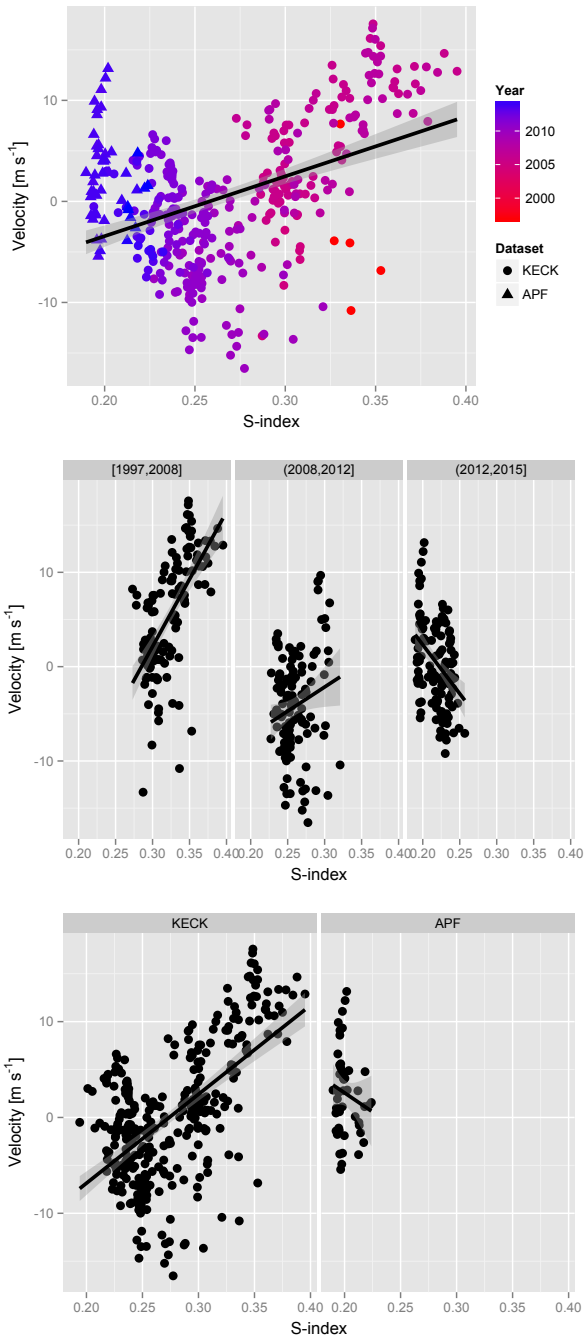

Figure 5.11: *Top Panel* shows a scatter plot of the radial velocity data for our Keck and APF observations and their associated *S*-index value. Each point is marked according to the time of observation. The best linear fit is shown as a solid line. *Middle Panel* shows the same data, faceted in time to emphasize the time-dependent correlation between the radial velocities and the S-index activity indicator. Each panel contains the same number of points. *Bottom Panel* shows the same data, faceted by dataset.

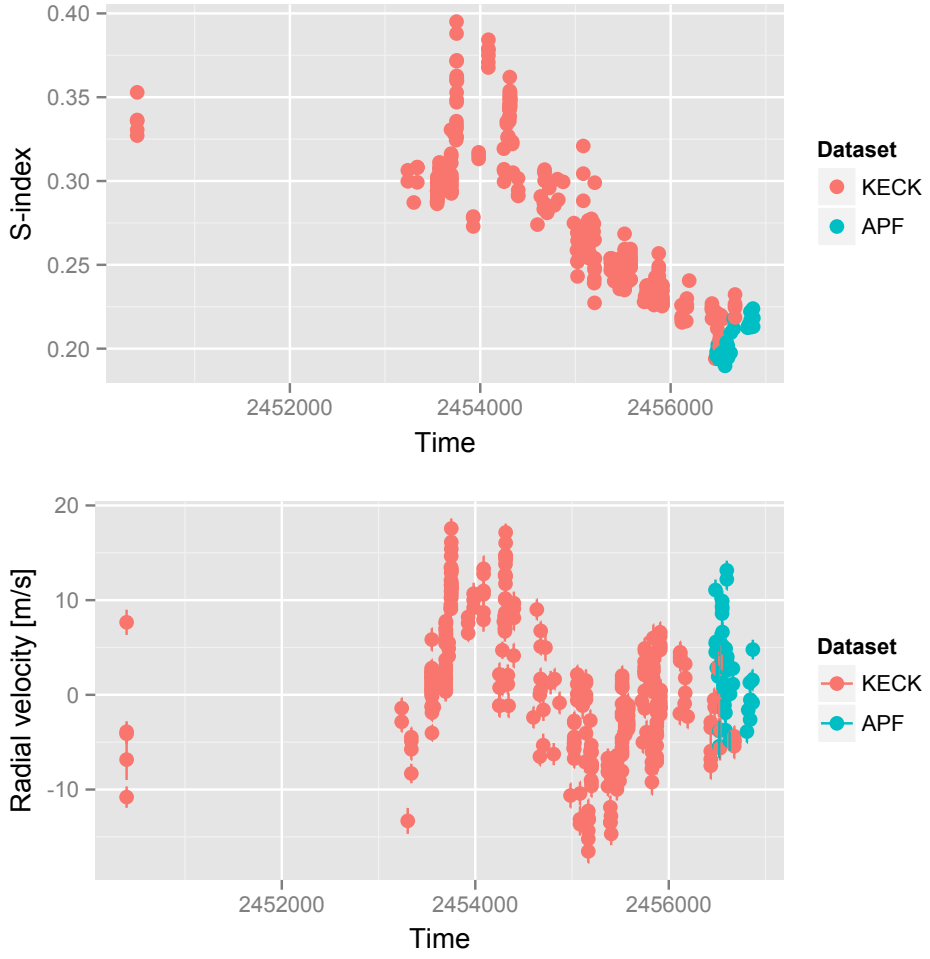

Figure 5.12: Plot of the S-index values compared to the corresponding RV observation. Velocity measurements and S-index values are shown here for each I_2 spectrum in our database for HD 219134. For purposes of RV modeling, we use 2-hour binning.

properties for HD 219134. It appears to be somewhat metal-rich in comparison to the Sun, with [M/H] = 0.09, and individual abundances that include [Na/H] = 0.13, [Si/H] = 0.02, [Ti/H] = 0.02, [Fe/H] = 0.12, and [Ni/H] = 0.09. Ramírez *et al.* (2013) report a high oxygen abundances of [O/H] = 0.23. We note that this high value seems discrepant in light of the star's other abundance measurements, as well as the value [Fe/H] = 0.04 found by (Allende Prieto *et al.*, 2004), and so must be treated with caution. One could speculate, however, that there might be a connection between the possible high abundance of iron and the apparent ease with which the system formed multiple planets having $P < 100$ days (Robinson *et al.*, 2006). Tanner *et al.* (2009) observed HD 219134 at 160 μm using the Spitzer Space Telescope's MIPS spectrometer, and found no excess emission characteristic of a remnant debris disk, in keeping with the large apparent age of the star.

5.3.2 Radial velocity observations of HD 219134

The HIRES spectrometer, located at the Keck-I telescope (Vogt *et al.*, 1994b), and the Automated Planet Finder's Levy spectrometer (Vogt *et al.*, 2014b) were employed to obtain the Doppler measurements of HD 219134 that form the basis of this section. In accordance with long-established practice, Doppler shifts at both telescopes are obtained by imprinting an iodine absorption spectrum on the collected starlight prior to its incidence on the spectrograph slit (Butler *et al.*, 1996b). The forest of added I_2 lines generates a stable wavelength calibration and permits the measurement of the spectrometer point spread function (PSF). For each spectrum so obtained, the $5000 \lesssim \lambda \lesssim 6200$ region containing a sufficient density of I_2 lines is subdivided into 700 individual segments of width 2, with each segment providing independent measures of

the wavelength, the PSF, and the Doppler shift. Our reported overall stellar velocity from a given spectrum is a weighted mean of the individual velocity measurements. The uncertainty for each velocity is the RMS of the individual segment velocity values about the mean divided by the square root of the number of segments. This “internal" uncertainty represents primarily errors in the fitting process, which are dominated by Poisson statistics. The velocities are expressed relative to the solar system barycenter, but are not referenced to any absolute fiducial point As a consequence, the velocity zero-point offset between the measurements at the two telescopes must be treated as a free parameter.

For the data set being considered here, there is an 8-year gap between the first Keck velocity measurement and the second Keck velocity measurement. The Keck HIRES CCD was upgraded during the interval between the two observations. In our reduction pipeline, we first analyze the entire Keck data set using only the spectral chunks that are present in both the pre and post-upgrade detector CCDs, thereby obviating the need for any additional internal velocity offsets. We then reanalyze the post-fix spectra, using all the spectral chunks, thereby improving the post-fix precision.

Table 5.3 presents the complete set of our RV observations for HD 219134. The RV coverage spans approximately 19 years of monitoring over 276 (two-hour binned) measurements. The median internal uncertainty for our observations is $\sigma_i \approx 0.75$ m s^{-1}, and the peak-to-peak velocity is ≈ 31.3 m s^{-1}. The velocity scatter around the average RV is ≈ 5.7 m s^{-1}. Observations marked as “Keck” are HIRES velocities from spectra obtained by the Lick-Carnegie Exoplanet team, or, in some cases, from publicly available archived spectra obtained by the California Planet Survey (Howard *et al.*, 2010). Observations marked “Q01” are

Table 5.3: Radial Velocity observations (sample)

Index	Time (JD)	RV (m s^{-1})	Uncertainty (m s^{-1})	Dataset
1	2450395.74	-4.50	0.50	KECK
2	2453239.05	-2.14	0.74	KECK
3	2453301.77	-13.31	1.37	KECK
4	2453338.71	-5.86	0.53	KECK
5	2453547.10	1.56	0.45	KECK
6	2453548.09	1.39	0.48	KECK
7	2453549.12	-0.66	0.55	KECK
8	2453550.09	2.79	0.43	KECK
9	2453551.09	0.81	0.38	KECK
10	2453552.05	-1.88	0.44	KECK
11	2453571.06	0.00	0.48	KECK
12	2453692.77	6.20	0.71	KECK
13	2453693.70	1.81	0.60	KECK
14	2453693.92	1.54	0.57	KECK
15	2453694.70	1.48	0.58	KECK

velocities computed using our pipeline from archival HIRES spectra from the 2005 NASA program: “TPF Preparatory Science: Low Mass Short-Period Companions to TPF Target Stars", to Principal Investigator W. Cochran. Observations marked “APF” are from spectra obtained with the APF telescope and Levy Spectrometer.

5.3.3 Keplerian Solution to the HD 219134 data

Figure 5.13 shows the RV measurements after binning to two-hour increments. We again note that there is a single Doppler measurement at BJD 2450395.74 (November 8th, 1996) followed by a nearly eight-year gap to the next measurement at BJD 2453239.05 (August 21, 2004). The single early epoch point is useful for cementing the lack of any apparent long-term large-scale Doppler velocity trend. The top panel of Figure 5.14 shows the error-weighted,

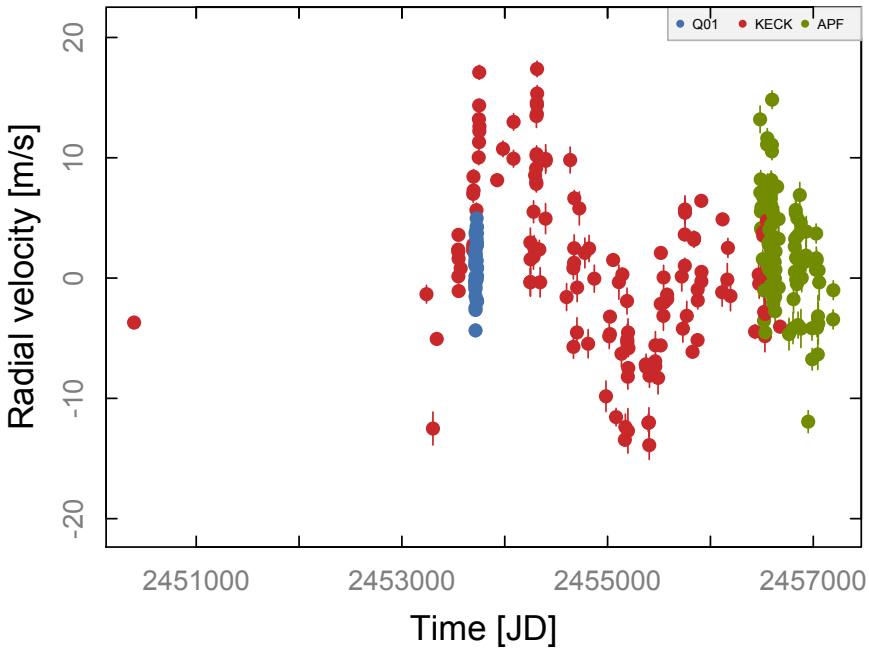

Figure 5.13: Radial velocity observations for HD 219134.

normalized Lomb-Scargle periodogram (Zechmeister and Kürster, 2009). The three horizontal lines in the plot represent different levels of false alarm probability (FAP; 10%, 1% and 0.1%, from bottom to top, respectively). The FAPs were computed by scrambling the dataset 100,000 times and sampling the periodogram at 100,000 frequencies, in order to determine the probability that the power at each frequency could be exceeded by chance (e.g. Marcy *et al.*, 2005). The bottom panel of Figure 5.14 shows the spectral window, displaying the usual peaks due to observational cadence, arising from the sidereal and solar days, and from the solar year (Dawson and Fabrycky, 2010).

We then fit the radial velocities with a Keplerian model with a vector of parameters $\bar{\theta}$, consisting of the orbital elements (period, mass, mean anomaly, eccentricity and longitude of pericenter for each planet) and vertical offsets for each dataset (to account for differences in the zero point among datasets). A simple Markov-Chain Monte Carlo algorithm (MCMC; e.g. Ford, 2005, 2006; Gregory, 2011), in conjunction with Equations 1-3 and flat priors on $\log P$, $\log \mathcal{M}$, and the other orbital parameters, was used to characterize the distribution of the parameters of the model, using the best fit the starting point. For the noise parameters, s_j, the corresponding prior is a modified Jeffrey function $p(s_j) = [(s_j + s_0)\ln(1 + s_{max}/s_0)]$; for $s_j \ll s_0$ (which we take equal to 0.3 m s^{-1}), the function is a uniform prior (which includes 0), while for $s_j \gg s_0$ the function is a regular Jeffrey prior (Gregory, 2011). The MCMC routine is run until sufficient convergence is achieved. The uncertainties in each parameter are reported in Table 5.3.3 within square brackets.

The final best-fit model is shown in Figure 5.15, with the corresponding orbital elements listed in Table 5.3.3, where we report median and mean absolute deviation for each pa-

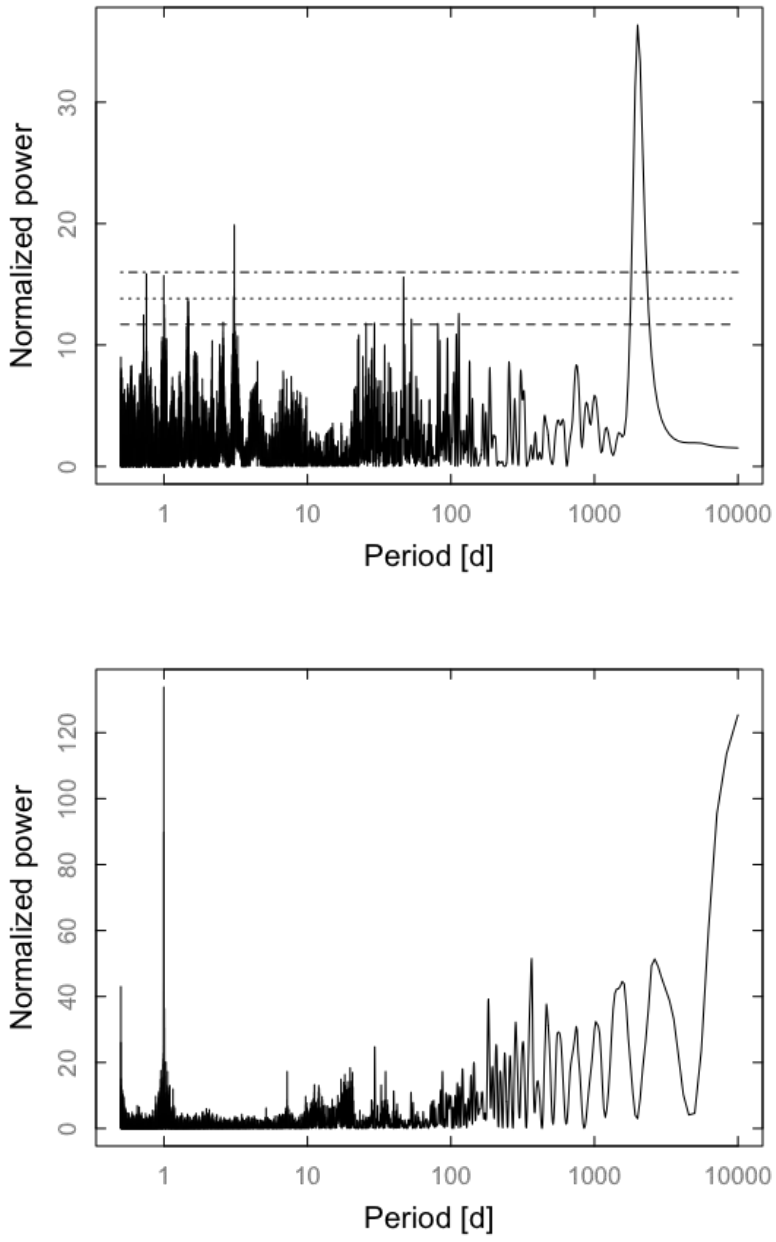

Figure 5.14: *Top panel:* Error-weighted Lomb-Scargle periodogram for HD 219134. False-alarm probability levels are shown at the 10%, 1% and 0.1% level. *Bottom panel:* Spectral window function.

rameter. The inner 5 planets are fixed on circular orbits, since the best-fit Keplerian model with eccentric orbits has crossing orbits and is therefore unstable. We also note that the gravitational (non-Keplerian) interaction between the inner 5 planets is small, but not completely negligible, since the planet pair b-c and the planet triple d-e-f lie close to mean-motion resonances (2:1 and 4:2:1 respectively).

5.3.4 Photometry of HD 219134

High-precision long-baseline photometric data have been acquired for HD 219134 with the T10 0.8m APT at Fairborn Observatory (Henry, 1999b) in the Stromgren b & y pass bands. A total of 313 observations were obtained from the 2010 through 2014 observing seasons. The two-color observations have been combined to produce a $\Delta(b+y)/2$ joint-filter time series, which improves measurement precision. The time-series is obtained using the standard quartet observing sequence that compares the target star with a set of three comparison stars (Henry, 1999b). For the observations reported here, the three comparison stars (denoted a, b, & c) are: **a** – HD 223421, (V = 6.36, B-V=0.408, F2 IV), **b** – HD 217071 (V=7.45, B-V=0.368, F1 III), **c** – HD 215588 (V=6.45, B-V=0.430, F5 V), whereas the target star HD 219134 (5.57, B-V=1.000, K3 V) is denoted star **d**.

In reducing the data, all six permutations of differential magnitudes of the four stars are evaluated. As described in Henry (1999b), only data that survive a cloud filter are retained, and the photometry is normalized so that all observing seasons have the same mean as the first season. We note, however, that there is little, if any, observable change in the mean magnitude from year to year. A 3-σ filter was applied, which removed six outlying photometric points.

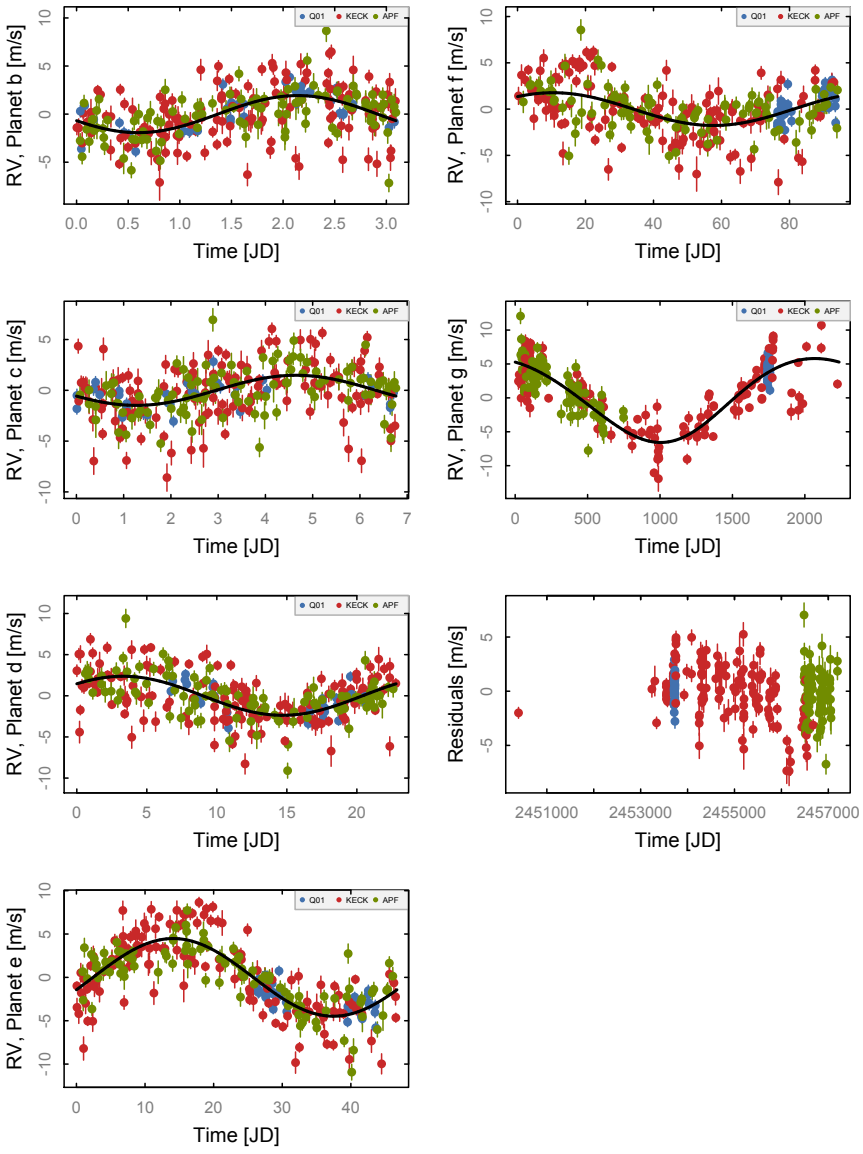

Figure 5.15: Best-fit Keplerian model for HD 219134.

In keeping with standard procedure, however, the outliers were not removed until after the data had been phased to each of the planetary periods to be sure they were not transit points.

The full photometric time series is shown in Figure 5.16 and a year-by-year breakdown is shown in Figure 5.17. The observations within each year are constant from night to night with a mean standard deviation of 0.0014 mag. This is the approximate limit of precision for a single nightly observation with the T10 APT. The yearly means are also constant to a limit of only 0.00055 mag. No significant photometric period is found in any year or across the entire data set. In addition, we have normalized the data so all yearly means are identical and fit least-squares sine curves on the candidate planetary periods with the results shown in Table 5. None of the candidate planetary periods exhibit significant photometric periodicities. Phase plots on the planetary periods show no sign of transits.

The five inner planets of the HD 219134 system have a-priori geometric probabilities of transit of 9.2%, 5.4%, 2.4%, 1.5% and 0.93% for the $P = 3.093$, 6.763, 22.81, 46.72, and 94.19 day periods, respectively. As reviewed by authors such as Wolfgang and Lopez (2015), super-Earth mass planets that are members of systems containing multiple planets with $P < 100$ d display a very large range in radii at given mass, and in expectation, often contain $\sim 1\%$ of the total planetary mass in hydrogen and helium. The presence of these light gasses, in turn, generates a substantial contribution to the overall planetary radius. If we use the solar system mass-radius relation, $M_{\rm p}/M_{\oplus} = (R_{\rm p}/R_{\oplus})^{2.06}$ (Lissauer *et al.*, 2011b), we expect that the transit depths for HD 219134 b and c will be of order $\delta_{\rm t} < 0.1\%$, which is too small a signal for phase-folded long-term ground-based photometry of the type reported here, but is within reach if platforms such as MOST, Warm Spitzer, or JWST are employed for a targeted transit check.

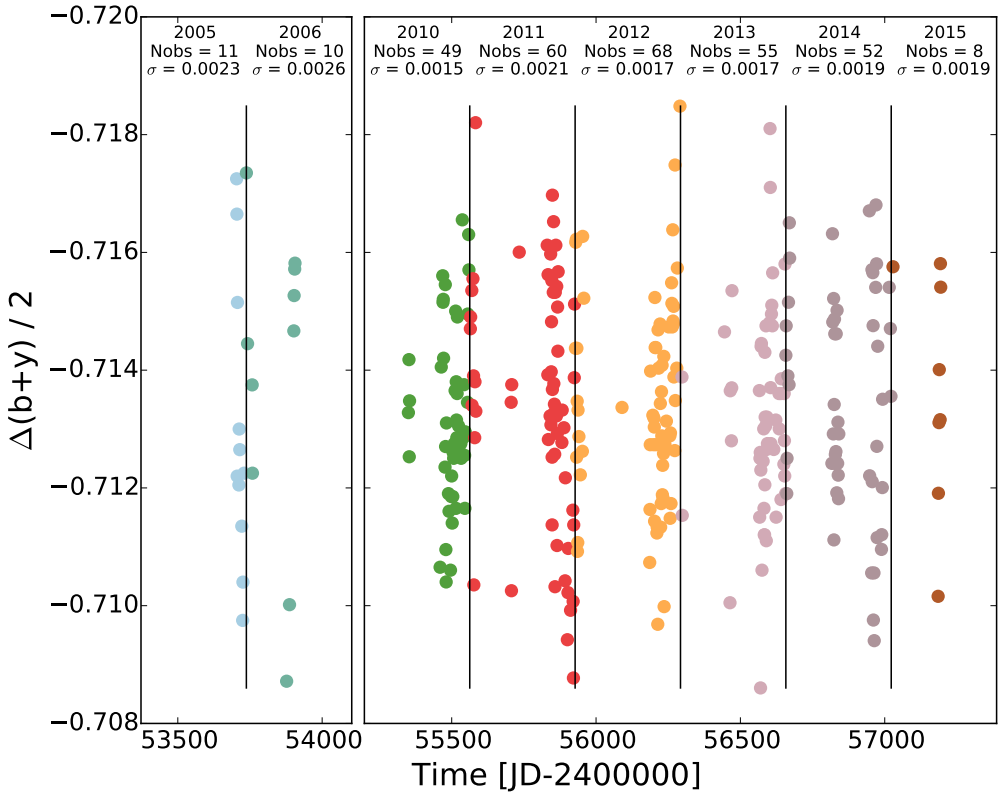

Figure 5.16: Differential photometric measurements of HD 219134 using the T10 0.8m APT at Fairborn Observatory (Henry, 1999b).

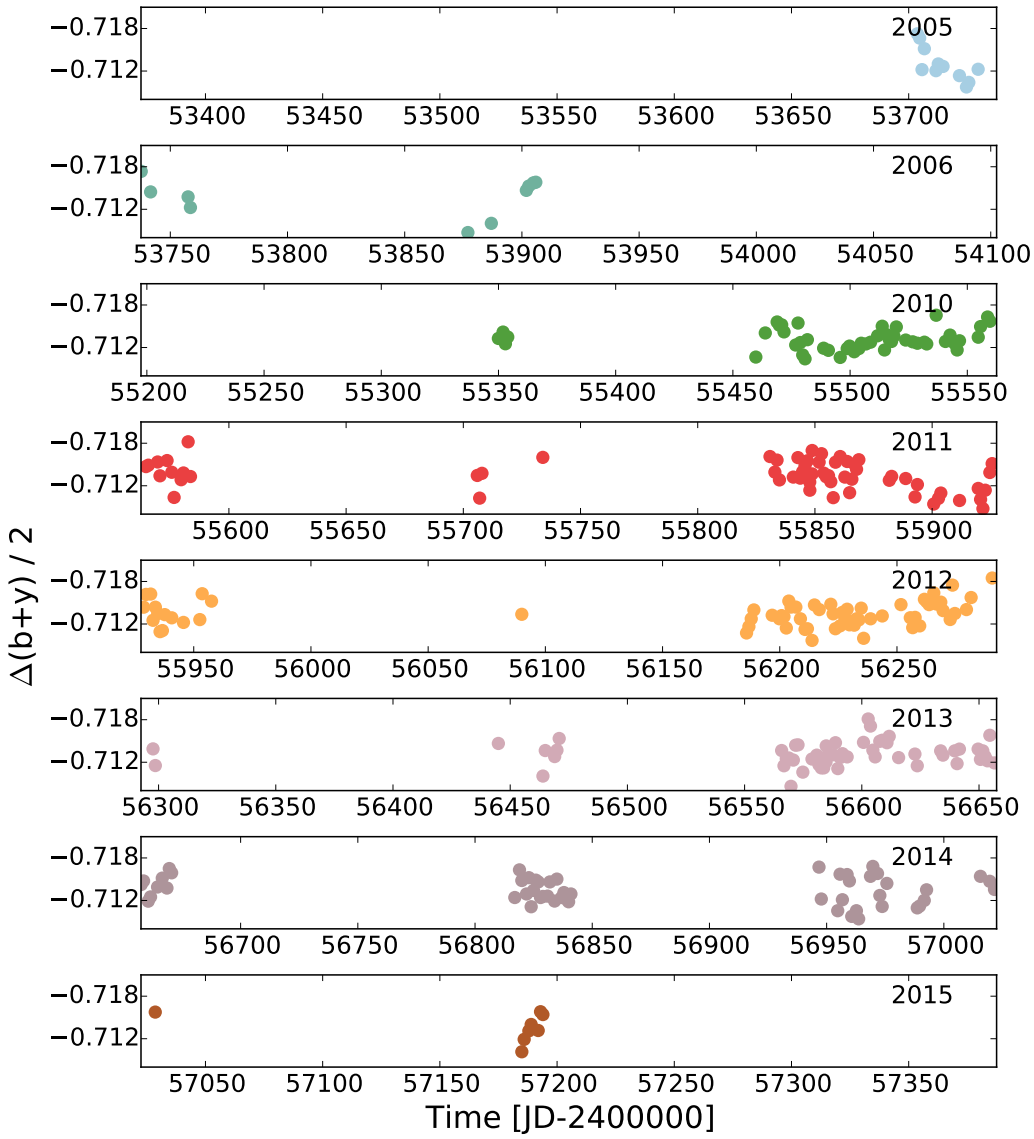

Figure 5.17: Differential photometric measurements of HD 219134 using the T10 0.8m APT at Fairborn Observatory (Henry, 1999b).

Indeed, systems such as HD 219134 form a strong basis for the scientific case of the forthcoming CHEOPS Mission, scheduled for launch in 2017.

5.3.5 Discussion

In comparison to our own Solar System, HD 219134 has an exotic architecture, with at least five super-Earth mass planets orbiting with periods of less than 100 days. Discoveries in recent years, however, have indicated that such systems are surprisingly common (Mayor *et al.*, 2009b). This result has received strong, and indeed dramatic confirmation from the Kepler Mission (Batalha *et al.*, 2013b), which revealed hundreds of candidate multiple-transiting multiple-planet systems that (at least in broad-brush strokes) call to mind HD 219134 b-f. This resemblance is underscored by Figure 5.18, in which the HD 219134 planets are shown in conjunction with Kepler's transiting planet candidates.

A question of substantial interest is whether planetary systems such as HD 219134 are assembled *in situ* (Montgomery and Laughlin, 2009; Hansen and Murray, 2012; Chiang and Laughlin, 2013), or whether the planets form at large distances and then migrate inward to their final locations. At present, it is not fully clear how to realistically distinguish between the two scenarios. Recent work by Batygin and Laughlin (2015a) has emphasized the role of outer giant planets in triggering collisional cascades among planetesimals that can potentially destroy systems of super-Earths such as those described in this paper. It will therefore be of substantial interest to understand the nature of the long-term ($P \gtrsim 2000$ day) periodicity in the radial velocity time series.

Among the thousands of planetary systems that are now known, HD 219134 stands

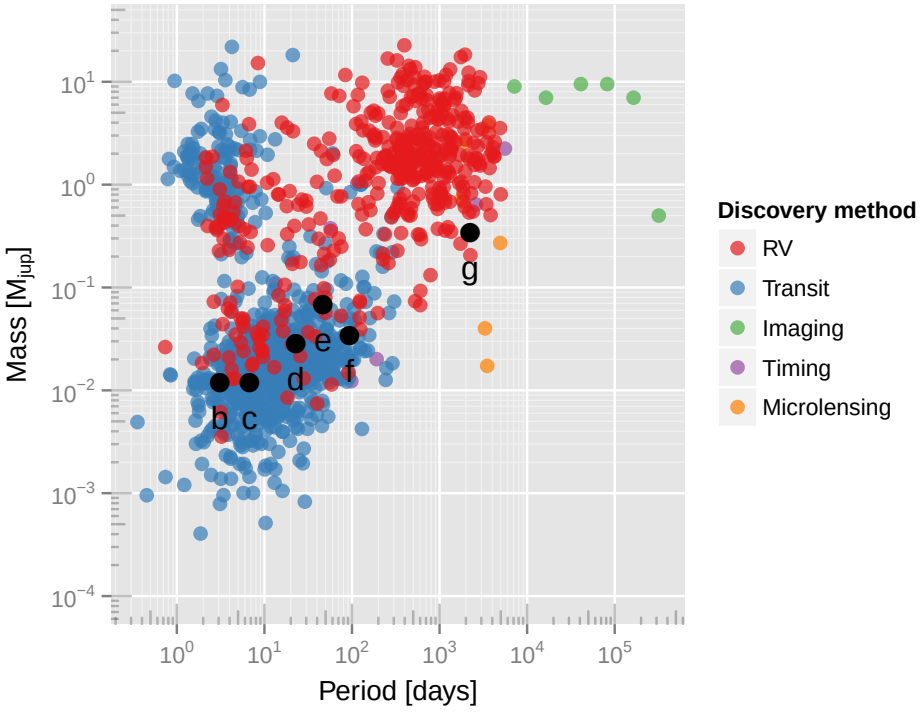

Figure 5.18: Mass-Period diagram showing planets logged by the Exoplanet Data Explorer (Wright *et al.*, 2011) (as of June 2014), and color-coded according to discovery method. The planetary candidates associated with HD 219134 (including the long-period signal that may be a signature of stellar activity) are labeled and plotted in black.

out. The bright primary star has demonstrated excellent radial velocity stability over two decades of measurement, and, given more data, there is a tantalizing possibility of finding additional low-mass planets in the system. With the parent star luminosity estimated at $0.31\,L_{\odot}$, a planet orbiting HD 219134 at 0.56 AU would receive the same energy flux that the Earth receives from the Sun. Such a planet would have an orbital period of 167 days. If it had a mass equal to that of Earth, its radial velocity half amplitude would be $K = 14\,\mathrm{cm\,s^{-1}}$. Such a signal would be challenging, but given current projections for the Doppler velocity technique, almost certainly not impossible to detect. Going forward, HD 219134 looks to be an ideal target for platforms such as APF, HARPS-N, the APTs, and other high-precision Doppler and photometric facilities with access to the far northern sky.

Table 5.4: Best-fit 6-Keplerian Model for HD 219134

	HD 219134b	HD 219134c	HD 219134d
P [days]	3.0931 [0.0001]	6.7635 [0.0006]	22.805 [0.005]
$\mathcal{M}\sin(i)$ [$\mathcal{M}_{\rm jup}$]	0.012 [0.001]	0.011 [0.002]	0.028 [0.003]
M [deg]	57 [20]	78 [27]	263 [20]
e	0	0	0
ω [deg]	0	0	0
K [ms^{-1}]	1.9 [0.2]	1.4 [0.2]	2.3 [0.2]
a [AU]	0.0384740 [8×10^{-7}]	0.064816 [4×10^{-6}]	0.14574 [2×10^{-5}]
$T_{\rm peri}$ [JD]	2449999.5 [0.2]	2449998.5 [0.5]	2449983 [1]
	HD 219134e	HD 219134f	HD 219134g
P [days]	46.71 [0.01]	94.2 [0.2]	2247 [43]
$\mathcal{M}\sin(i)$ [$\mathcal{M}_{\rm jup}$]	0.067 [0.004]	0.034 [0.004]	0.34 [0.02]
M [deg]	277 [11]	107 [35]	209 [56]
e	0	0	0.06 [0.04]
ω [deg]	0	0	215 [50]
K [ms^{-1}]	4.4 [0.2]	1.8 [0.2]	6.1 [0.3]
a [AU]	0.23508 [4×10^{-5}]	0.3753 [0.0004]	3.11 [0.04]
$T_{\rm peri}$ [JD]	2449964 [1]	2449972 [9]	2448725 [356]
Q01 $s_{\rm noise}$ [ms^{-1}]	1.1 [0.2]		
KECK $s_{\rm noise}$ [ms^{-1}]	2.5 [0.2]		
APF $s_{\rm noise}$ [ms^{-1}]	1.8 [0.2]		
Q01 Δv [ms^{-1}]	-0.9 [0.6]		
KECK Δv [ms^{-1}]	-0.8 [0.2]		
APF Δv [ms^{-1}]	-2.3 [0.6]		
$\mathcal{M}_\star$ [$\mathcal{M}_\odot$]	0.794		
χ^2	280.407		
$-\log\mathcal{L}$	593.311		
RMS [ms^{-1}]	2.223		
$\sigma_{\star,\rm Jitter}$ [ms^{-1}]	2.038		
Epoch [JD]	2450000		
Data points	276		

Chapter 6

Simulating future exoplanet contributions: An APF and TESS collaboration

6.1 Introduction

As the exoplanet census continues to grow, the super-Earth and sub-Neptune planets first detected by NASA's *Kepler* mission have asserted their position as the most common planet archetype in the galaxy (at least for planets with periods, P <100 days). These planets, with radii ranging from 1-4 $R_{\oplus}$, make up some 81% of current Kepler exoplanet candidates (Akeson *et al.*, 2013). Yet despite their ubiquity, we still do not have a clear picture of the mass–radius relation that governs these objects. They span the transition in radius space from predominantly rocky bodies to planets with the voluminous layers of volatiles seen in our own ice giants, meaning that their masses can vary widely, due to their range of possible compositions (rock, astrophysical ices and/or H/He gas).

Kepler alone has detected thousands of exoplanet candidates with radii ranging from 1-4 $R_{\oplus}$ (Coughlin *et al.*, 2015), yet providing well constrained masses for them has proven non-trivial. Many of these planets orbit faint stars and impart radial velocity (RV) signals of <1 m s^{-1}. As the most advanced RV telescopes currently in operation are only just now starting to cross the 1 m s^{-1} precision threshold - and even then only on bright, quiet, stars - follow up efforts to determine the Kepler planets' masses are both time intensive and challenging. To date, only 234 of the 1041 confirmed Kepler planet have had their masses determined via RV observations, while the other 807 planet masses remain unknown (Akeson *et al.*, 2013).

The second phase of *Kepler*, K2, is providing some improvements as it searches the ecliptic plane for evidence of transits in 80 day segments. K2 targets brighter stars than *Kepler*, and after completing 9 campaigns, 39 planet candidates (predominantly from Campaign 2) have already been confirmed and had their masses measured via RV followup (Akeson *et al.*, 2013). The super-Earth and sub-Neptune planet candidates however are still pushing towards the limits of what current telescopes can reliably measure.

While RV instrumental precision and capabilities are improving (Fischer *et al.*, 2016), perhaps the best hope for further populating the M–R diagram with small exoplanets in the near term lies with NASA's TESS mission (the Transiting Exoplanet Survey Satellite), currently scheduled to launch in late Summer 2017 (Ricker *et al.*, 2014). TESS will survey the entire night sky, looking for evidence of exoplanet transits across the brightest, nearby stars. Initial concepts for TESS suggested that almost all of the satellite's postage stamp stars would be brighter that V = 12, making them ideal targets for ground based RV follow up. More recent simulations of the survey's yields, however, show a sample that is notably skewed towards the

same magnitude ranges covered by *Kepler* (Figure 6.1) (Sullivan *et al.*, 2015).

Although many of the host stars are fainter than originally anticipated, TESS will still provide a large step forward in our efforts to understand the M–R relation in small exoplanets, providing 100+ bright stars (V < 12) with transiting planet candidates and many more faint stars (12 < V < 16) (Sullivan *et al.*, 2015). With such a plethora of targets, the follow-up efforts that are sure to dominate the RV field as TESS starts returning planet candidates need to be well thought out and (ideally) coordinated. This requires developing a detailed understanding of the potential contributions of each telescopes to the M–R diagram; specifically which areas of parameter space they can fill in and what their target coverage and error bars are likely to look like after a given amount of observing time.

In this paper, we investigate the potential contributions of Lick Observatory's Automated Planet Finder (APF) telescope to the TESS RV follow-up campaign. We begin by providing a brief overview of the telescope and its past performance in §6.2. In §6.3 we describe the creation and selection function for our simulated planet candidate database, and our use of a M-R relation (Wolfgang *et al.*, 2015) to determine likely masses and the desired RV precision in a way that incorporates the significant current uncertainties in this relation. §6.4 details the design and implementation of a new, time varying prioritization scheme that interfaces with the APF's dynamic scheduler to ensure that we are observe targets at points in their phase curve when they will provide the maximum impact on our RV analysis. Then in §6.5 we describe the observing simulator we have created for the APF and the details of our simulated, multi-year follow-up campaign, before analyzing the resulting additions to the M–R diagram in §6.6. We conclude the paper in §6.7 with a discussion of how the M–R diagram is likely to evolve with

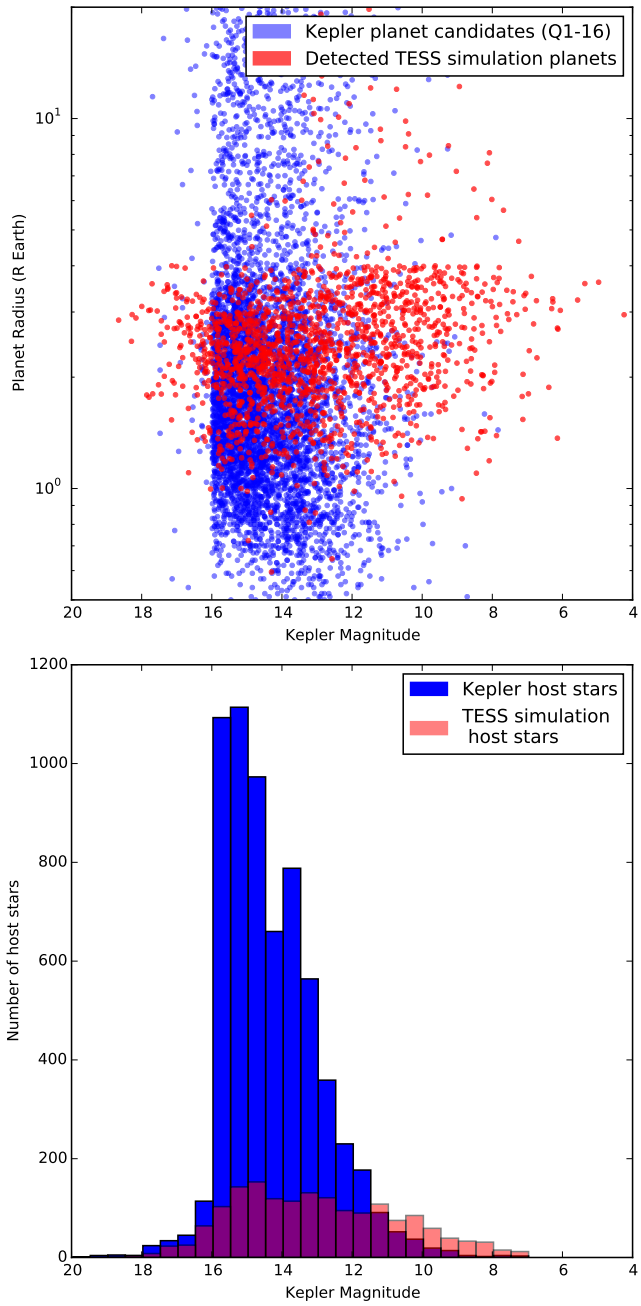

Figure 6.1: Comparison of the Kepler planet candidates and their host stars from Q1-16 against the planets and host stars from the TESS simulation utilized in this paper. While TESS does find notable more planets orbiting bright stars (top), the overall magnitude distribution of the TESS host star sample still peaks at V $\sim$ 15, making RV follow up of the fainter stars challenging.

the advent of TESS and remarks on the specific role that the APF can play in furthering our understanding of the compositions of small exoplanets.

6.2 The Automated Planet Finder

The Automated Planet Finder (APF) is a 2.4m telescope located at the Mt. Hamilton station of UCO/Lick observatory. The telescope is coupled with the high resolution ($R_{max} \sim$ 150,000), prism cross-dispersed Levy echelle spectrograph, which sits at one of the telescope's two Nasmyth ports. A full description of the design and the individual components of the APF is available in Vogt *et al.* (2014b). To support long-running surveys, we have developed a dynamic scheduler capable of making real-time observing decisions and running the telescope without human interaction. Through automation and optimization, we increase observing efficiency, decrease operating costs and minimize the potential for human error (Burt *et al.*, 2015, hereafter B15).

The APF is capable of 1 m s^{-1} Doppler Velocity precision and has contributed to the detection and characterization of 4 published planetary systems to date (Burt *et al.*, 2014; Vogt *et al.*, 2014a; Fulton *et al.*, 2015; Vogt *et al.*, 2015). Roughly seventy percent of the telescope's observing time is specifically dedicated to the detection of extrasolar planets. This time is shared evenly between two exoplanet research groups, one at UC Santa Cruz and one at UC Berkeley. Time is allocated in whole night segments, with a schedule developed quarterly by the telescope manager. Target lists and operational software are developed separately as the two exoplanet groups are focused on different types of planet detection/follow up. For a description of the

UC Berkeley planet detection efforts, see Fulton *et al.* (2015). The remaining 20% of telescope time is split between privately funded groups and at-large use by the University of California community. All UC users are allowed to request specific nights if it is beneficial to their science goals (for example: to obtain RV values while a planet transits its star), and such requests are taken into account by the telescope manager when setting the schedule.

6.3 Methodology

6.3.1 TESS Simulation & APF target selection

We make use of an updated version of the TESS planet detection simulation presented in Sullivan *et al.* (2015), hereafter S15. The most important difference from the original S15 catalog is that in this version of the simulation, each planet detected around a star has its radius and orbital period recorded. Most of the assumptions outlined in S15 still hold, including the use of planet occurrence rates derived from the Kepler mission (Fressin *et al.*, 2013) and a galactic model from TRILEGAL (Girardi *et al.*, 2005) that is modified towards the M dwarfs to match eclipsing binary radii and Interferometric radii. This simulation includes no stars with T_{eff} >15,000K and no transits with depth >0.1. It employs the same SNR threshold as outlined in S15 (detection modeled as a step function with threshold SNR set at 7.3 to correspond to one false positive in the postage stamps). The simulation also notes which planets are transiting their star, and (out of those planets that do transit) which ones are detected by TESS.

We employ a planet population from a single realization of the updated S15 code . Usually, this is a piece of software that's meant to calculate how many transits TESS will detect

for a given pointing. As such we skip tiles towards the galactic plane, because the star density is too large there for TESS pixels to resolve transits. The total yield numbers have changed slightly from the S15 results with "as-built" PSFs from Lincoln Labs now being used in the photometry model (which lowered the yield), and a bug-fix from S15 in postage stamp assignment (which raised the yield). The overall yield picture remains about the same – in this catalog (which is postage-stamp only), about 1670 planets are detected (Figure 6.2).

As in the original S15 TESS simulations, this new version allows the simulation to assign more than one planet to a given star with independent probability. The only exceptions are that (1) the periods of adjacent planetary orbits to have ratios of at least 1.2, and (2) planets around a star with a binary companion cannot have orbital periods that are within a factor of 5 of the binary orbital period. The result is that 53% of the transiting systems around FGK stars and 55% of those around M stars are multiple-planet systems.

TESS's short observing lifetime, combined with the fact that transit probability of a planet scales inversely with its semi-major axis, makes it is unlikely that the mission will observe transit events from longer period, Jovian planets that orbit TESS target stars. Such planets, however, could be readily detectable by follow-up RV surveys thanks to their large masses. Our own Jupiter, for example, produces a $\sim$10 m s^{-1} signal on the sun. To address the existence of such planets, we adopt the true Jupiter analog occurrence rate from Rowan *et al.* (2016) and insert Jupiter analogs into 3% of the stars in the TESS simulation catalog. Following the definitions presented in Rowan *et al.* (2016), these analogs have periods between 5 and 15 years, and have masses between 0.3 and 3 M_{Jup}. We draw the characteristics of our Jovian planets from a uniform distribution between the end points in each case, and pick the systems

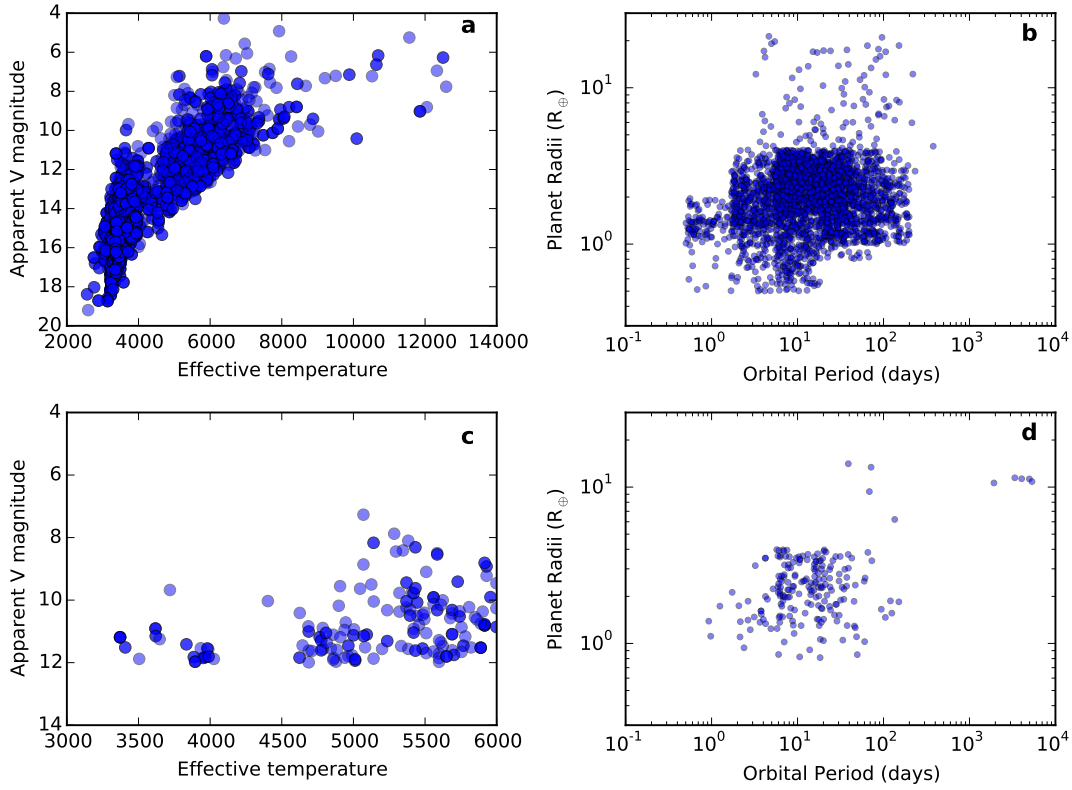

Figure 6.2: A: Effective temperature vs. apparent V magnitude for the stars in the TESS simulation. B: Orbital period vs. planetary radius for all planets in the TESS simulation, whether or not they were detected by TESS. C: Effective temperature vs. apparent V magnitude for the stars included in our APF RV follow up program (V <12, T_{eff} <6000K, and Dec >-15). D: Orbital period vs. planetary radius for planets orbiting stars meeting our selection criteria for the APF, whether or not they were detected by TESS, plus the true Jupiter analogs we add around 3% of the simulation stars.

that these giant planets are inserted into at random. Following the procedure of S15, we put these planetary additions on circular orbits around their host stars in the plane of the transiting planets.

From the resulting catalog, we cull the stars that are :

- physically visible to the APF (dec>-15)
- bright enough for the APF to perform well (V<12)
- likely F/G/K/M dwarfs (T_{eff} < 6000K)

which results in 204 planets orbiting 141 different stars that will be targeted by the APF in our observing simulation (Figure 6.2).

6.3.2 Assigning stellar noise

Stellar jitter is one of the key sources of noise in radial velocity work, and understanding its effects is important for long term RV surveys (Lovis *et al.*, 2011). We use the work of Isaacson and Fischer (2010a) (hereafter I10) to generate a jitter value for each of the simulated TESS stars in our survey, based on the stars' $B-V$ color. I10 finds that the jitter depends strongly on the color, and gives a relation for a four different color bins. In each color bin, the authors fit the jitter as a function of activity as measured by the S index. This activity index uses a differential measurement, ΔS, measured from the baseline level for quietest stars in each color bin. For our sample, we pick a median activity level for each star based on the color. In effect, we assign a jitter value to each star based on its $B-V$ color. This value is used as a seed for a random deviate. These values are then used as an additional piece of the error budget for

each velocity measurement simulated by the APF.

6.3.3 Calculating planetary masses

The updated S15 simulations provide planet radii for the generated TESS population. To simulate RV follow-up of these planets, we need a way to map these radii to masses. We use the probabilistic M-R relation of Wolfgang *et al.* (2015) (hereafter WRF16) for this purpose, as it captures the astrophysical range of densities that is emerging in the observations. In particular, we use the version of the M-R relation that was fit to planets between 1 and 8 $R_\oplus$ (the parameters of that relation are given in the 6th line of WRF16's Table 1), extrapolate this relation up to 9 $R_\oplus$, and use a lognormal distribution with $\mu(\log(M/M_{Jup})) = 0.046$ and $\sigma(\log(M/M_{Jup})) = 0.392$ for the masses of planets > 9 $R_\oplus$. This last distribution was fit via a standard maximum likelihood method to the mass distribution of all Jupiters that appeared in the Exoplanet Orbit Database (Han *et al.*, 2014) as of December 3, 2015; it therefore assumes the observed period-marginalized Jupiter mass distribution is complete and unbiased.

This M-R relation serves two purposes in our simulations (see Figure 6.3 for the resulting mass distributions). First, we need to assign "true" masses (M_{true}) to the planets in the generated TESS population in order to simulate the actual RV signal that APF would observe. To do this, we needed an M-R relation that could account for both the observed astrophysical variation in planet masses at a given radius and the uncertainty in this relation due to our data-starved, pre-TESS understanding of the underlying M-R distribution. The relation derived by WRF16 allows us to do both: its probabilistic nature accounts for the first concern, and its Bayesian formulation facilitates the second. In particular, we marginalize over the posteriors of

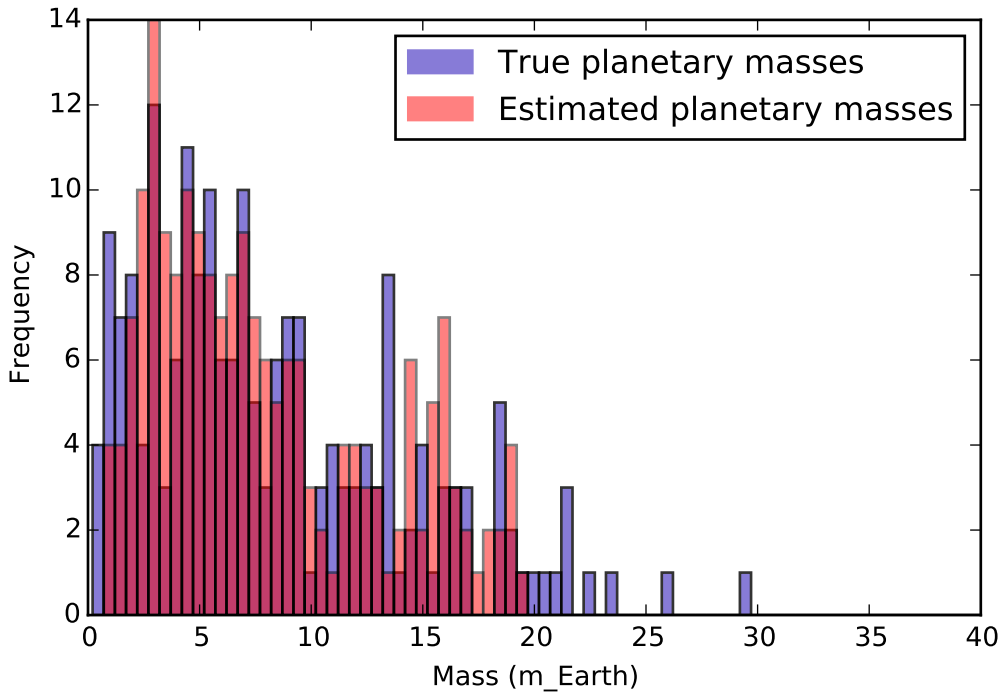

Figure 6.3: Histogram of the true and estimated mass values for each of the TESS simulation planets orbiting the culled TESS simulation stars. This excludes the true Jupiter analogs we add to the simulation, because we only have true masses for them, and no estimated masses.

the M-R relation parameters while generating each planet's M_{true} in order to include the data-driven uncertainty in the relation (see the discussion about the posterior predictive distribution in Section 6.1 of WRF16 for more details).

However, having M_{true} in-hand for these planets does not accurately represent what information we will have as we initiate RV follow-up of TESS planets. At that point we will not know M_{true} — indeed, measuring it is the entire point of the follow-up effort — yet we need an estimate of it in order to calculate what precision the APF would need to reach to measure it well. This in turn determines the prioritization of specific TESS planets each night based on the exposure times needed to meet the required precision (see Section 5.1). Since consistently high-priority planets will end up populating the observed M-R distribution and therefore constrain the inferences we make about the true underlying distribution, this estimated mass (M_{est}) plays an important role in our simulations. In the absence of any other information at the start of RV follow-up, the most likely mass value from WRF16's probabilistic M-R relation provides a good mass estimate. This is simply the "mean" relation that they report, so that $M_{est} = 1.6R^{1.8}$. Note that we will not know of the existence of the true Jupiter analogs before taking RV measurements, so there is no need for an estimated mass for them.

Because the astrophysical scatter in the probabilistic M-R relation is 2.9 $M_{\oplus}$, the average difference between M_{true} for a given planet, which contains this dispersion, and M_{est} for that same planet, which is just the mean M-R relation and thus does not, is 2.9 $M_{\oplus}$. This difference between the true and estimated masses, which we would expect in real life, drives an evolution in the target prioritization scheme as more and more data are obtained and the mass measurement converges on M_{true}. This effect is described in Section 5.2 and is one of the

observing selection effects that is uniquely captured by our simulations.

6.3.4 Setting desired RV precisions

The desired RV precision is then set by taking the planets that are marked as being detected by TESS in the simulation (the planets we would know about when setting up the APF's observing strategy), and dividing their RV amplitudes (K) in half. We calculate the RV semi-amplitude it imparts on its host star using Kepler's 3rd law (6.3.4) where M_{est} is the estimated mass of the planet.

$$K = \left(\frac{2\pi G}{P}\right)^{1/3} \left(\frac{M_{est}}{M_{star}+M_{est}}\right)^{2/3} \tag{6.1}$$

For each star we take the lowest K value out of the detected planet subset and compare it to the APF's precision floor of $\sim$1.0 m s^{-1} (B15), setting the desired precision equal to the larger of the two values (Figure 6.4). There are some stars where only one planet is detected by TESS, and its predicted and/or true K value is less than 1 m s^{-1}, making it unlikely that we will detect that planet's signature in RV data. We still include these targets, however, because planet multiplicity studies (Tremaine and Dong, 2012; Fabrycky *et al.*, 2014, e.g.) have shown that it is likely other planets (with potentially higher Ks) will exist in the system and could be detected by the APF even if they were not flagged in the original TESS data.

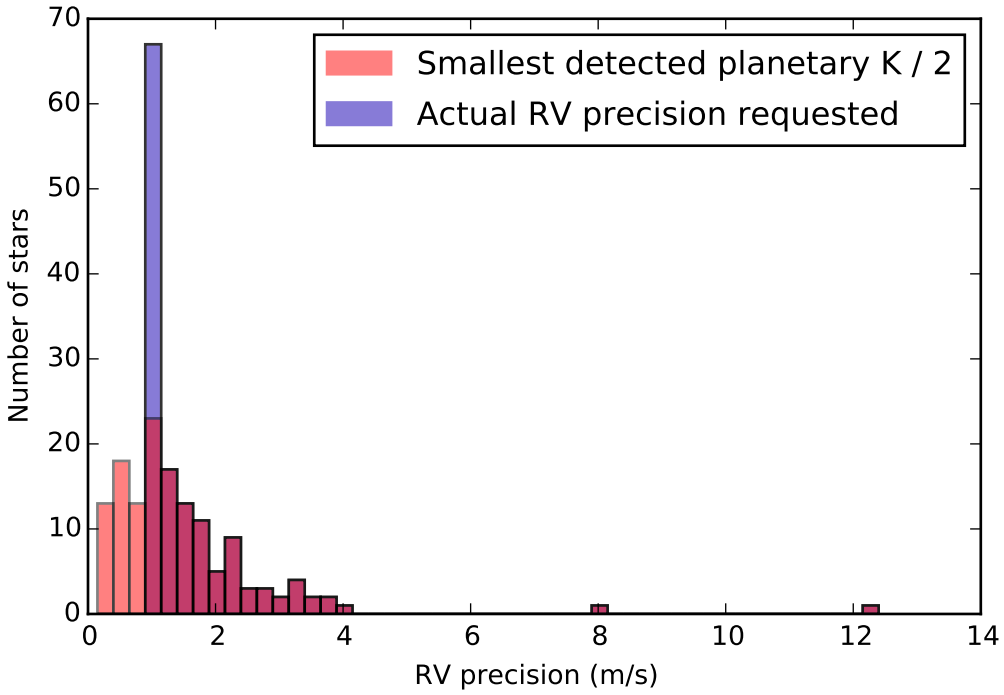

Figure 6.4: Histogram of the half-K values and resulting desired precision values set for each of the culled TESS simulation stars. These values are obtained by calculating the K values of all planets detected by TESS in the simulation and then taking the smallest semi-amplitude in each system and dividing it in half. For those stars whose result is <1 m s^{-1}, we instead set the desired precision level to 1 m s^{-1} so as not to come up against the noise floor of the APF.

6.4 Creating time-dependent observing priorities

When using RV observations to verify the Keplerian nature of a planetary signature or determine the mass of a planet, the most efficient observing method is to observe the star during its quadrature phases (when the true anomaly of the planet = $\pm$90 degrees and the amplitude of the RV induced by the orbiting planet is at a maximum). In traditional RV surveys (e.g. Vogt *et al.*, 2014b; Butler, 2016), every target star is assigned an observing priority (generally a number from 1-10) that signifies how scientifically interesting that star is, and acts as a weighting factor when deciding what stars to observe during the night. Static observing priorities, however, weight the star with the same level of observing desirableness no matter where it is in its RV phase curve. This is a sensible approach when running an RV survey without prior knowledge of the planets orbiting a star, as any observation could provide crucial insights to the star's (potentially planet-induced) movement. But now, in the era of large photometric surveys such as K2 or TESS that provide detailed periods and radii of hundreds of planet candidate targets, we can update our RV observation strategy to ensure that it optimizes the information content of each RV exposure.

6.4.1 Phase bins

The instantaneous radial velocity for a given planet at time t is given by Equation 6.4.1, where f is the true anomaly, ω is the argument of periastron, K is the RV semi-amplitude (as defined in Equation 6.3.4), and e is the planet's eccentricity.

$$V_{mod}(t) = K\left[cos(f+\omega)+ecos(\omega)\right] \tag{6.2}$$

When performing follow-up observations for missions like TESS, the RV phase curve of the planet can be calculated from the time of transit. This allows us to create RV phase "bins" that track where the planet is in its orbit around the star. We define five bins across the folded phase curve of a planet, two of which are centered at the planet's quadrature points and three more which center on the zero-crossing points (Figure 6.5).

For the case of a single planet orbiting the star, the phase bin definition is straightforward. Things get slightly more complicated, however, when the star has two or more planetary companions. In the simple case where we disregard planet-planet interactions, the total instantaneous RV of a star being orbited by N planets is then composed of a linear combination of the RV signals of each planet at the given time (Eqn 6.4.1, where R is the noise factor). In this case, we select the shortest period planet and use its period and phase location as the basis for determining which phase bin the star falls into (Figure 6.5).

$$V_{star}(t) = \sum_{i=1}^{N} V_{mod,i}(t) + R(t) \tag{6.3}$$

6.4.2 Determining the stars' current priority values

Stars currently in the light blue, quadrature sections (bins 1 and 3) are assigned higher priority than those in the zero-crossing section (bins 0, 2 and 4). The priorities are further weighted by comparing the number of observations that a star has in each of its phase bins and

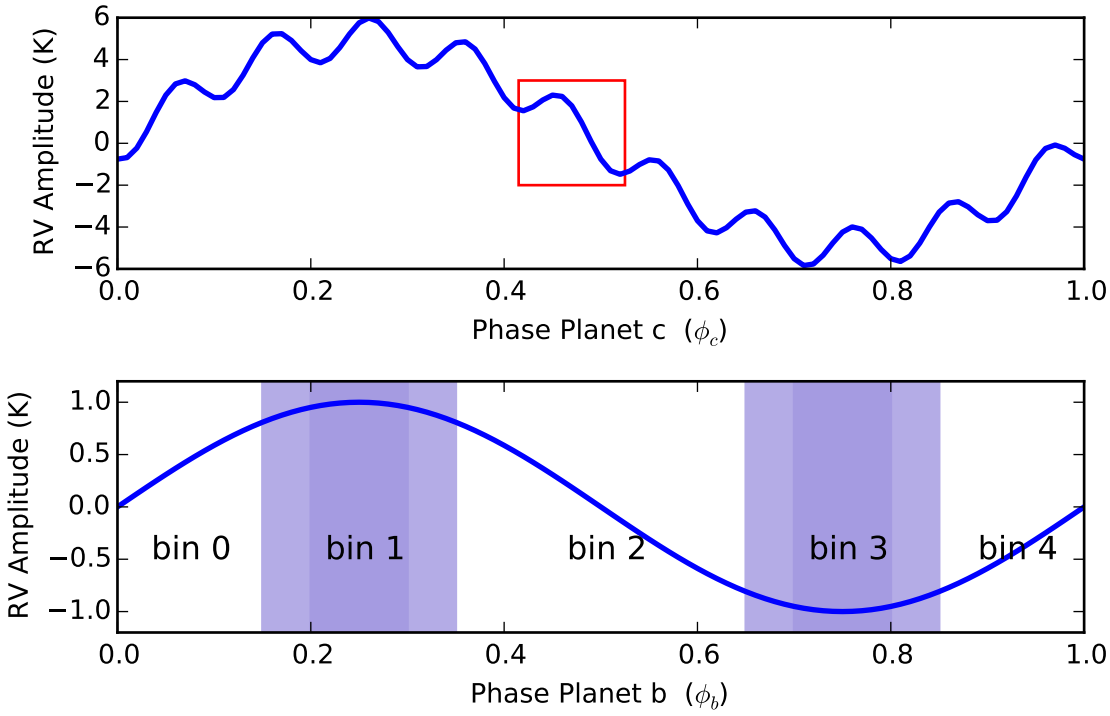

Figure 6.5: Top panel: Schematic RV phase curve of a two planet system orbiting the star, comprised of a massive long period planet and a smaller, shorter period planet. Bottom panel: In a multi-planet scenario, the prioritization system starts by folding on the shorter period planet's phase curve and defining the phase bins. The blue bins are centered on the quadrature points of the selected planet's orbit with light blue area encompassing the whole bin, and the darker region highlighting the +1 value add to priority a star gets for being right at the quadrature point.

determining which bins are "saturated", having $\geq$ 10 observations. We choose N=10 observations as the cutoff point in order to reduce the error on the average velocity (which scales inversely with $\sqrt{N-1}$) by a factor of 3. Thus when using the APF (which itself contributes an uncertainty of $\sim$ 1.5 m s^{-1}) to observe a star with a planetary signal of $\sim$2 m s^{-1} and an assumed jitter value of 1.5 m s^{-1}, obtaining N=10 observations would give an error on the mean of the velocity of :

$$\frac{\sqrt{\sigma_{jit}^2+\sigma_{inst}^2+\sigma_{ph}^2}}{\sqrt{N-1}} = 0.78 \tag{6.4}$$

The prioritization values, working on a 1-10 scale, get assigned as follows:

- If the star is currently in a quadrature bin, and that bin is not saturated, priority = 10
- If the star is currently in an un-saturated, non-quadrature bin, and both quadrature bins are already saturated, priority = 8
- If the star is currently in an un-saturated, non-quadrature bin, and one quadrature bins are already saturated, priority = 5
- If the star is currently in a quadrature bin, and that bin is already saturated, priority = 3
- If all of the star's bins are saturated, priority = 2
- If the star is currently in a saturated, non-quadrature bin, priority = 1

After the initial assignment of priorities, we specify three additional "value-added" criteria. If the star has a planet candidate with radius, R <2 $R_\oplus$ or if the star has a planet with period, P >30 days or if the planet on which the scheduler is basing its phase bins is currently

within 5% of the actual quadrature point, then we add +1 to the star's priority. This emphasizes our scientific interest in the planets that are the most likely to have rocky cores, allows us to better sample the the overall system architecture of stars with short period, inner planets and helps to obtain down a more accurate measurement of the planet's mass by sampling close to the RV quadrature inflection point.

This logic allows for the insertion of stars that have not been previously observed by missions like TESS, and thus do not have accurate RV phase information readily available. RV standard stars for example, which we use to monitor the continued performance of the APF, can be inserted into the observing database with static priorities of 9 or 7 depending on how often we want them to be observed. Stars from legacy RV surveys can be added in with static priorities if their possible planetary systems are not yet well defined, or with phase information of a suspected planet to make sure its viability is assessed in an efficient manner.

In multi-planet cases where the phase bins of the shorter planet all become saturated, we then select the planet with the second shortest orbit and begin folding on that period instead, redefining the phase bins. Because we store the JDs of all observations taken for each star, the existing observations can then be resorted into the five new phase bins so that the priority algorithm doesn't see this new period fold as starting from scratch.

6.5 Simulated APF observing

The values calculated for each star described in the sections above (true mass, estimated mass, and desired RV precision) are combined with parameters pulled directly (Vmag,

planetary radii) or derived (RA, Dec, B-V color) from our TESS simulation and placed in a new observing database for the telescope (B15). We add additional columns for the star names (TESSAPF1, TESSAPF2, etc), the planetary period on which to base the phase bins of each star, the initial phase of the selected planet at a specified JD zero point, and the number of observations in each of the five phase bins. This database is read in by the observing software at the beginning of each simulated night and guides the software's decision making process throughout the evening as it chooses what star to observe at a given time.

6.5.1 Simulating the observations

In normal operations, the APF selects its next target by picking the star with the highest priority that can be observed in a reasonable amount of time. We have written a simulator that replicates this. The details of the actual observing process, and the relations we used to compute exposure times, are described in B15. We will simply sketch out the core steps here. For a given star, we compute the desired total exposure time needed meet the required precision. The inputs for the exposure time calculation include the star's magnitude and color, but also the seeing and transparency, based on measurements from the previous observation. We then use these values to estimate the exposure time for the next observation. Because we want to ensure a certain quality of signal, the total exposure time is almost always an overestimate. We use the exposure meter to set the actual end of an exposure.

At the beginning, the simulator selects a random distribution of seeing and transparency values modeled using the history from the past three years of APF operations. The transparency is modeled as mulitplicative factor on the exposure time, so is inversely propora-

tional to the photon arrival rate. Each night uses a different mean and variance to draw random deviates from. The mean and variance of both the seeing and transparency are correlated as found in the historical data. Therefore, we have "good" nights, where the seeing and transparency are both drawn from small means with small variances, "ok" nights where the seeing or transparency is small but the other is large, and "bad" nights where the seeing is large, and the transparency can be so bad that the telescope never opens. For each observation, we draw one of the seeing and transparency pairs from the parent distributions to compute the actual photon arrival rate for a simulated observation. These random deviates are used to compute the exposure time for the next observation, and then we draw a new pair for the next observation to compute the photon arrival rate for the simulated observation. Included in this process is our empirical model for the seeing as a function of elevation.

For each observation, we record the total number of photons simulated to land in the exposure meter and in the iodine region of the spectrum, using the relations from B15. We compute the mean from those relations and then draw a random deviate using the scatter listed. The number of counts in the iodine region gives an estimate of the expected precision, from Equation 1 or Figure 5 of B15. Once again, we use that as a mean and use the measured scatter (also from Figure 5 of B15) to compute the actual precision for the simulated observation. For each measurement we compute a total error. This adds in quadrature the precision value, the expected jitter for the star (see §6.3.2), and the baseline instrumental noise we found in B15. This combination yields the total error estimate.

At the end of each exposure, the simulator appends the mid-point JD and the total uncertainty (stellar jitter and telescope effects) from the exposure onto a velocity file for that

particular star. We combine the true mass values for all planets in the system (whether or not they were originally detected by TESS) with the JD of the exposure's midpoint and the planets; initial phases at the JD zero point to calculate the star's total, instantaneous radial velocity value. We then add the noise factor for the observation and add the resulting RV value into the velocity file, which can then be opened up in the publicly available Systemic console (Meschiari *et al.*, 2009a) in order to determine the planetary masses.

The simulator starts a night at -9 degree twilight, and selects a B star off of a list. This observation is used for accounting purposes, and to set the first pair of seeing and transparency values for a given night. Each observation is ended after either the exposure meter hits the threshold or the total exposure time requested is reached. We include CCD readout for each exposure and slew times for each observation. The process continues until the sun rises at the end of the night.

The scheduling of the nights is random. The APF telescope is used for a number of programs by a variety of institutions, some of which require specific cadence or even specific nights. To simulate this, for the TESS follow up we assumed that 33% of the year was available but that the time between nights would range from one to three days, and exclude the winter break shutdown.

6.5.2 Fitting simulated RV data

We use an automated fitting process based on the publicly available Systemic console (Meschiari *et al.*, 2009a) to estimate the K and mass values for each of the transiting planets detected by TESS. The data are first binned, as is the case with real radial velocity data, though

instead of using the common 2hr binning scheme, we instead group velocities within a width of no more than 10% of a planet's orbital period.

The list of binned velocity values is then loaded into Systemic and all values known from the transit observation (such as the period, and the mean anomaly at periastron) are entered into the system fit and then frozen so that the fitting algorithm can not alter them. We freeze the orbital eccentricity and the dataset zero-point parameters to 0, to help ensure orbit stability. To provide the fitting algorithm with a sensible first guess, we use the M-R relation described in §6.3.3 to determine a starting value for the planetary mass(es). Once all of the parameters are entered for each suspected planet, we then perform a single minimization using the Simplex algorithm. To estimate the standard deviation of the best fitting K values, we implement 500 iterations of bootstraping error estimation on the binned data and its resulting fit from Systemic.

6.5.3 Making changes to the observing database

As our simulated observing program progresses through multiple months of time on sky and we learn more about the planets orbiting the target stars, it is important to allow for an evolution of the database that informs the dynamic scheduler's selection process. These changes will enable us to address three main effects. The first is the offset between the true and estimated masses of the TESS simulation planets (see Section 3.3). As described in Section 6.3.4, we use the estimated masses of the planets to set a desired precision RV level, but the actual RV values that are calculated for each simulated observation are based on the planets' true masses. The second is the presence of additional planets in the system that were not detected by TESS in the simulation, but are again included in the RV calculation process. The third effect is the change

of focus between planets in a system that occurs after the first planet has been sufficiently well fit.

To address these, we implement an“assessment" phase after every 6 months of simulated observing during which we review the Keplerian fits derived in §6.5.2 and assign observing priority offsets to each star before simulating the next season of observing. These offsets are added to the priority value calculated for each star in §6.4.2 and are used to help focus our observing time on the systems that would benefit the most from additional observations. Every star with at least 4 binned RV values has each of its planets classified as either "publish", "monitor", or "drop" based on the number of binned velocities that fall into each of its quadrature bins, N_{QBin1} and N_{QBin2}, and the ratio between the planet's semi-amplitude, K, and the errors on that semi-amplitude, σ_K, which are determined using a bootstrap approach.

- If (K / σ_K) > 5: The planet is listed as “publish”
- If 1.5 < (K / σ_K) < 5 OR N_{QBin1} < 10 OR N_{QBin2} < 10: The planet is listed as “monitor”
- If (K / σ_K) < 1.5 AND N_{QBin1} > 10 AND N_{QBin2} > 10: The planet is listed as “drop”

For each planet, we record the K and σ_K values from its fit, the number of binned velocities in each of the observing phase bins described in §6.4.1 and the planet's assessment classification. After every planet has been individually evaluated, we then assess each planetary system as a whole in order to determine whether the host star should be marked as ready for publication, needing further observations or unsuitable for further observation. We begin by looking for evidence of non-transiting and/or long period planets that weren't detected by TESS by examining the residuals to the star's Systemic fit and their resulting periodogram. Any

stars whose residuals show evidence of a significant peak in their periodogram (defined as a FAP < 1%) *or* that contain a notable linear trend (defined as the RMS of the linear fit to the planet's residuals being greater than twice the desired precision for the star listed in the observing database) are flagged as "needing review", and added to a list for us to check on before starting the next round of simulations. After examining these flagged fits by eye, we either a) add an RV offset to the fit parameters, which will account for the influence of a massive, long period companion over a relatively short observing span; b) add a new entry to our list of suspected planets, with the period and mass values suggested by the periodogram; or c) decide that the periodogram/linear fit is not convincing and do nothing. For the stars where we add either an offset or a new suspected planet to the system, we then refit the data using Systemic and put the resulting planetary fits through the "publish"/"monitor"/"drop" assessment again.

For stars where all of the planets are set to "publish", we add the star to a list of potential publications, and then set the priority offset to -5. This helps to ensure that the telescope will observe other systems, whose planets are not yet as well characterized, in the next observing season before adding more points to a star that we already have a firm grasp on. It doesn't eliminate the star from consideration though, so we will continue to get occasional data points which are necessary for detecting longer-period companions. For stars where all of the planets are set to "monitor", we set the priority offset to 0 so that the star continues to be observed normally throughout the next season. For stars where all of the planets were tagged as "drop" cases, where we do not believe that further observations will actually contribute anything to our understanding of the system, we set the priority offset to -10.

For stars that have more than one planet where at least one of the planets has been

marked as publishable, we first add the star to the list of potential publications. Then, if any of the other planets in system are listed as "monitor", we change the fold period in the observing database to the shortest period of that planet subset. This places an emphasis on observing at times when the second (or third, or fourth) planet is at its quadrature positions, helping to efficiently fill in our knowledge of the whole system. After the fold period is changed, we set the star's priority offset to 0 and move to the next target. For stars that instead have a mixture of "publish" and "drop" planets, we set the priority offset to -5 to give other, less well understood systems a chance to rise to the top of the observing selection process.

For stars that have multiple planets with a mixture of "drop" and "monitor" statuses, we start by checking whether the planet with the lowest expected semi-amplitude (which sets the desired precision in the observing database) has been marked as "drop". If so, we set the new desired precision to be the minimum of the K values from the fitted planets that are labeled as "monitor" of 1 m s^{-1} whichever is larger. If the planet on which the database is phase folding has instead been marked as "drop", then we selected the shortest period planet in the system that has a "monitor" status and change the observing database's fold period to match that planet. We then set the priority offset to 0 so that the star will continue accumulating useful data points.

A visualization of the decision tree described here can be found in Appendix A.

6.6 Results

The final dataset spans 36 months of simulated observing during which we obtained 365 nights of telescope time (3660 hours of open shutter time) on 86 different stars. Of the 91

planets orbiting these stars, we achieve 3σ mass measurements for 65 of them, and 5σ or higher mass measurements for 50 (Figure 6.6).

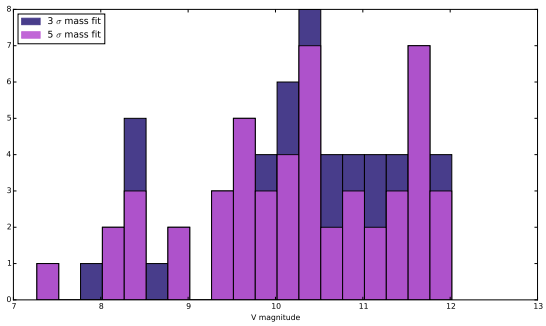

Figure 6.6: Mass measurements after 36 months of observing on the APF. When fitting for just the mass, 65 planets attain 3σ mass measurements and 50 planets attain 5σ or higher measurements.

In reviewing the data, it is clear that the scheduler is able to consistently target stars that are in/near their quadrature positions and then use the resulting RV data points to efficiently determine the planet's mass. In cases where the star is faint and the planet's signal is close to the APF's 1 m s^{-1} precision level, however, our data is not sufficient to extract a believable mass estimate even with a large number of binned velocities (Figure 6.7).

To establish context for the data points that TESS and the APF can add to the M-R diagram, we first create a current version using data from the Exoplanet Archive (Akeson *et al.*, 2013). After selecting those points that have both mass and radii measurements, along with error bars on both values, we end up with 81 planets with radii, $R < 4R_{\oplus}$ and masses, $M < 20M_{\oplus}$(Figure 6.8). There are only 9 planets whose total mass uncertainty is less than 25% of their measured mass, 19 whose total mass uncertainty is between 25-50% of their total mass, and 25 planets with total mass uncertainties ranging from 50-100%. An additional 28 planets

have mass uncertainties > 100% of their measured mass. The composition lines plotted on top of the M-R diagram are taken from Lopez *et al.* (2012), except for the "max iron" line which represents the maximum iron fraction produced by collisional stripping according to Marcus *et al.* (2010).

6.6.1 Updated M-R diagrams

We generate a new M-R diagram after each year of simulated APF observations, to visualize the contributions that the telescope can make. The number of 3σ and 5σ mass measurements increases from 36 to 56 to 65 and 24 to 42 to 50, respectively.

6.6.2 Comparison to actual planet masses

One of the most interesting checks, that cannot be performed in real life, is to see how our measured masses compare to the planets' true masses generated in §6.3.3. Figre 6.10 shows the scatter of our measured masses compared to the planet's true masses around a 1:1 line.

Overall the residuals to the 1:1 line have a median value of 1.8%, with an RMS of 31% and a median absolute deviation (MAD) of 16%. We find that the lower end of the data (for planets with true masses less than the median true mass of $9.4 M_{\oplus}$) produces slightly worse measurements than the higher end, with the RMS values for these two sections being 38% and 22%, respectively. As expected, the higher mass systems with their larger semi-amplitudes are easier to measure accurately.

6.6.3 Detecting long period companions

Of the five stars that had Jupiter analogs inserted into their planetary systems in §6.3, three of them are observed during our 36 month simulation. The other two stars were skipped by the scheduler, likely due to the fact that both stars are faint (V magnitudes of 11.09 and 11.97) and located at relatively low declinations (δ of 23nd 15. This combination precludes the stars from spending the time needed at low airmass to obtain observations at the desired precision listed in the observing database.

The three stars with Jupiter analogs that did get observed were all tagged by the assessment algorithm as needing human review due to the large offsets in their RV values. Two of the systems displayed a linear trend in their RV data, implying the presence of a massive, long period companion. Without observing one of the quadrature transitions for the planet, however, we are unable to place limits on its mass or period. These stars were added to the list of systems that should continue to be monitored at every assessment phase.

The Jupiter analog in the third system did pass through quadrature during our 3 years of simulations (Figure 6.11), allowing us to compute a mass and period estimate for it, in addition to the fit we derive for the 16d planet that TESS detected in this system (Table 6.1). Our fit to the Jupiter analog's mass is correct to within 0.6%, however the period estimate is off from the true period of 3366 days by 4%. With further monitoring, the period would like be more closely constrained, which would help us to achieve a better mass estimate for the short-period super-Earth, whose measured mass in this fit differs from the true mass of 12.08 $M_{\oplus}$ by 26%.

Parameter	Planet b	Planet c
Period [days]	16.49	3505 ± 314
Mass [M_{jup}]	0.028 ± 0.005	1.66 ± 0.03
Mean anomaly [deg]	238.84	312 ± 49
Eccentricity	0	0
Longitude of pericenter [deg]	0	167 ± 54
Semiamplitude [m/s]	2.2 ± 0.4	21.6 ± 0.6
Semi-major axis [AU]	0.1285461 ± 0.0000002	4.6 ± 0.3
Periastron passage time [JD]	2458351.56	2455465 ± 605
Stellar mass [M_{sun}]	1.04	
RMS [m/s]	1.93	
Stellar jitter [m/s]	1.48	
Epoch [JD]	2458362.50	
Data points	26	
Span of observations [JD]	2458492.00 - 2459313.82	

Table 6.1: Fit parameters for the two planets orbiting TESSAPF54

6.7 Discussion

The results presented in the above pages are the first assessments of the impact that the APF can have in the post-TESS era of exoplanet science. After 36 months of simulated observations, during which we attained roughly a year (356 nights) of data, our survey produced 65 3σ and 50 $5+\sigma$ planetary mass estimates for planets originally detected by the TESS mission. It is immediately clear that the telescope can provide a valuable set of mass measurements for planets with masses, M >4$M_{\oplus}$, many of which will fall in the 1-4$R_{\oplus}$ range of the diagram where the M-R relation is not yet well understood. Indeed, we increase the number of planets with $5+\sigma$ mass measurements in the M < 30 $M_{\oplus}$and R <4 $R_{\oplus}$ region of the M-R diagram from 15 to 80, a 400% boost.

With its ability to perform consistent, high cadence observations over a number of years, the APF is sensitive both to low-mass short period planets and to massive, outer com-

panion planets like our own Jupiter. This ability to probe both regions of a planetary system is crucial for developing a clear picture of the overall system architecture and for constraining our theories on planet formation.

One of the shortcomings of the methodology described in this work is the lack of detections of the non-transiting planets orbiting the target stars that we know are there and contributing to the RV data thanks to the TESS simulation. Of the 27 non-transiting companions with semi-amplitudes, K >1.5 we recover only 1-2. This suggests that the conventional RV approach of aiming first and foremost for a planet's quadrature points when trying to measure its mass may in fact hide the existence of additional Keplerian signatures. Additionally, when observing only at the quadrature phases, we lost the ability to try and discern the exoplanets' eccentricities, which have measurable effects for translating from semi-amplitudes to actual mass values. Studies into optimizing RV survey strategies have suggested that observing almost exactly off quadrature, when the planets RV phase curve exhibits the steepest slope, may make for a better planet detection approach (Ford, 2008; Loredo *et al.*, 2011).

One of the largest takeaways from this work will be the ability to test and evolve our observation strategy for TESS followup over the next year before the satellite launches. Having now developed our second generation dynamic scheduler and the simulation software necessary to implement long-term survey simulations, we can determine the effects of different prioritization schemes (e.g. focusing on the steepest sections of a planet's phase curve instead of the quadrature points) or different survey approaches (e.g. focusing on one small group of stars at a time and observing them multiple times per night to beat down the RV noise levels) on the mass estimates we are able to generate. By looking at the planets that the telescope is able to

detect/characterize we can also attempt to identify if there is a systematic bias produced by our selection function and prioritization scheme, and determine what steps can be used to quantify and/or negate that bias. And by inserting *different* mass-radius relations in the beginning of the process, when we first calculate our true and estimated masses, we can investigate whether or not a facility like the APF can enable us to discern the difference in the underlying relationship between the two parameters based on the mass measurements it produces.

On a broader scale, this simulator can help to improve general RV survey planning and data assessment. In the current approach to RV science, target selection, data acquisition, and science results on the detected planet demographics are all tightly tied together and hugely influential on one another. By implementing a consistent and well defined algorithmic process for each of these steps and restricting that feedback loop, we can look into whether a non-human biased survey can gain a better understanding of nature's underlying distributions and therefore the physics that shapes these planets. In particular, experiments looking at how changing the prioritization scheme or target selection process part way through the survey affects the M-R diagram and the resulting M-R relation inference, or how using an incorrect assumption for what the target selection was can affect the M-R relation inference could shed much needed light on the best ways to move forward with RV followup efforts across many telescopes, not just the APF.

In short, the results of this project, at the time of the thesis writing process, are exciting and promising - both for the APF's immediate effectiveness at TESS-based followup efforts, and for the potential improvements that careful, longer term analysis of our results and methodology might provide to the radial velocity field as a whole.

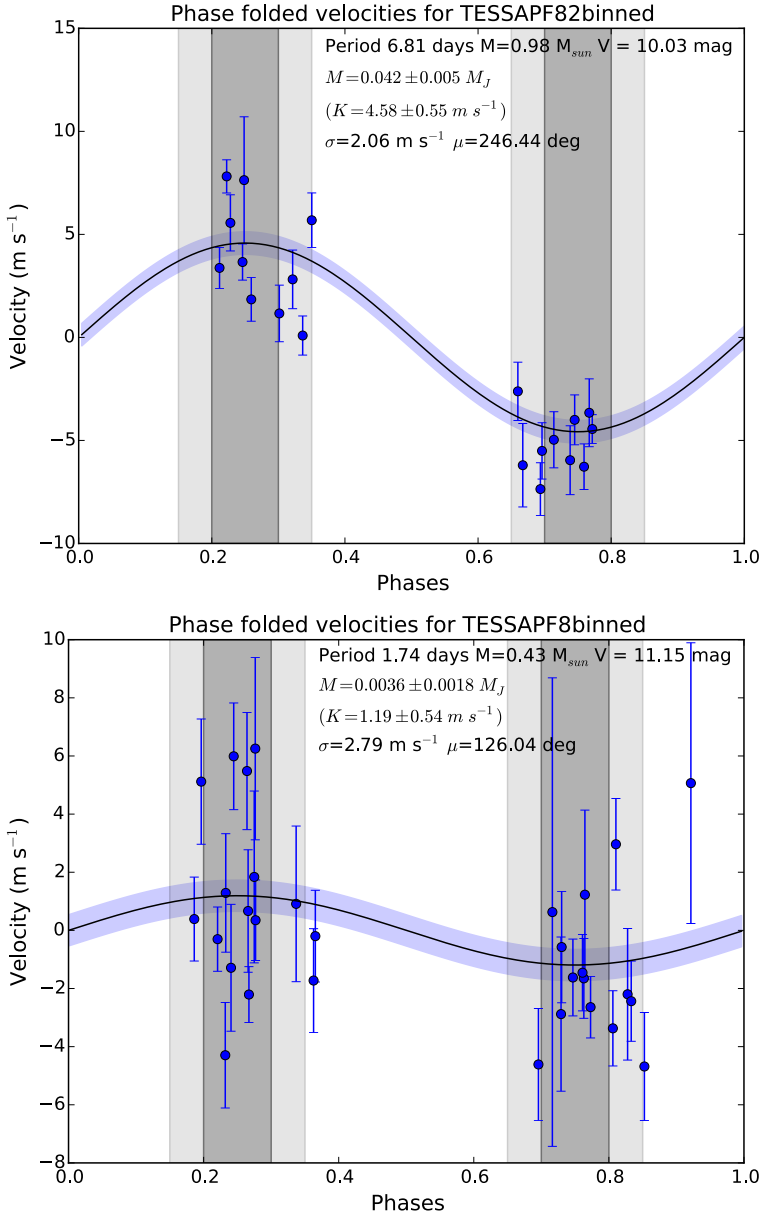

Figure 6.7: Two fits to planetary systems at the end of our observing simulation. Blue points are the binned RV data, while the black curve is the fit to the data from Systemic and the light blue span around the curve denotes the 1σ range. The scheduler's prioritization of the quadrature bins is clear in both examples, and while the focus helps to determine the mass of TESSAPF82 to within 0.7% of its true mass (top), it is not sufficient to produce a credible estimate of the mass for TESSAPF8 (bottom).

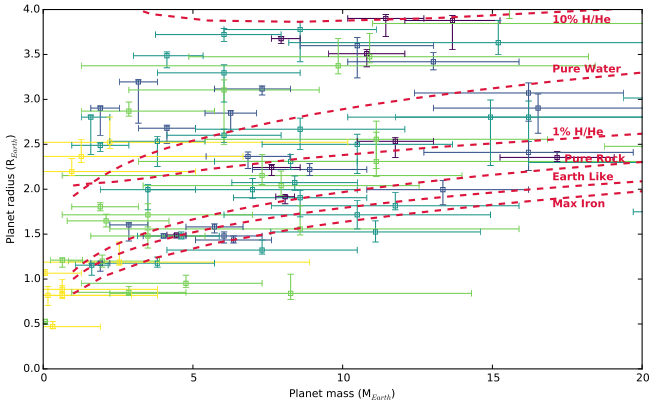

Figure 6.8: Example of the current state of exoplanet mass-radius diagrams. The data was obtained from the exoplanet archive on April 11, 2016 and the composition curves come from Lopez *et al.* (2012) except for the "max iron" curve which is taken from Marcus *et al.* (2010). Planets colors represent their fractional mass uncertainties, with blue being <25%, while those with mass uncertainties from 25-50% of their measured mass are shown in teal, 50-100% are pink, 100-300% are green and those with uncertainties > 300% are yellow.

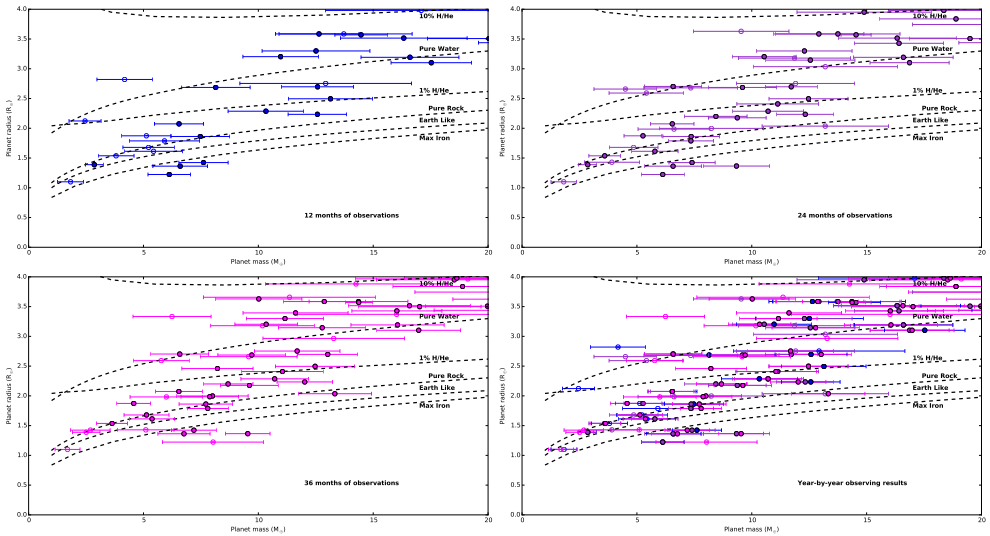

Figure 6.9: Updates of the APF's contributions to the M-R diagram after one (top left), two (top right) and three (bottom left) years of TESS followup observing. Open circles represent 3 σ detections and filled circles represent 5+ σ detections. The bottom right plot shows the evolution of the M-R diagram over time, using the same color scheme as the rest of the figure. Both the shrinking of our mass measurement error bars and the increase in the number of 3 and 5 σ observations are visible.

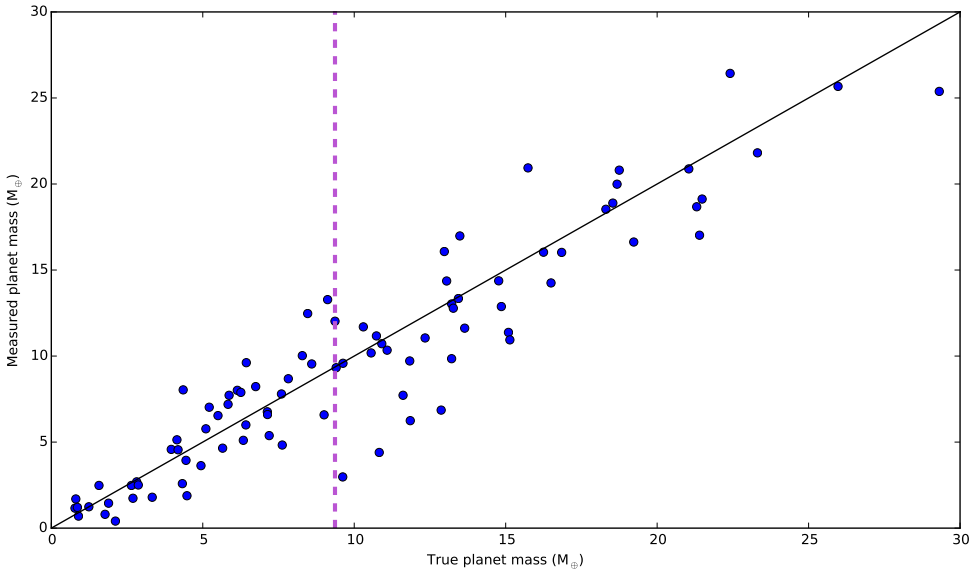

Figure 6.10: Measured masses from our simulated observations and the resulting planet fit models compared to the planets' true masses, which are used to generate the RV data. The scatter is smaller for low mass planets (M <the median true mass value, shown in purple), which we attribute to the combination of our non-varying stellar noise approach and the higher number of observations that these planets get due to their prioritization in the scheduler for having small radii.

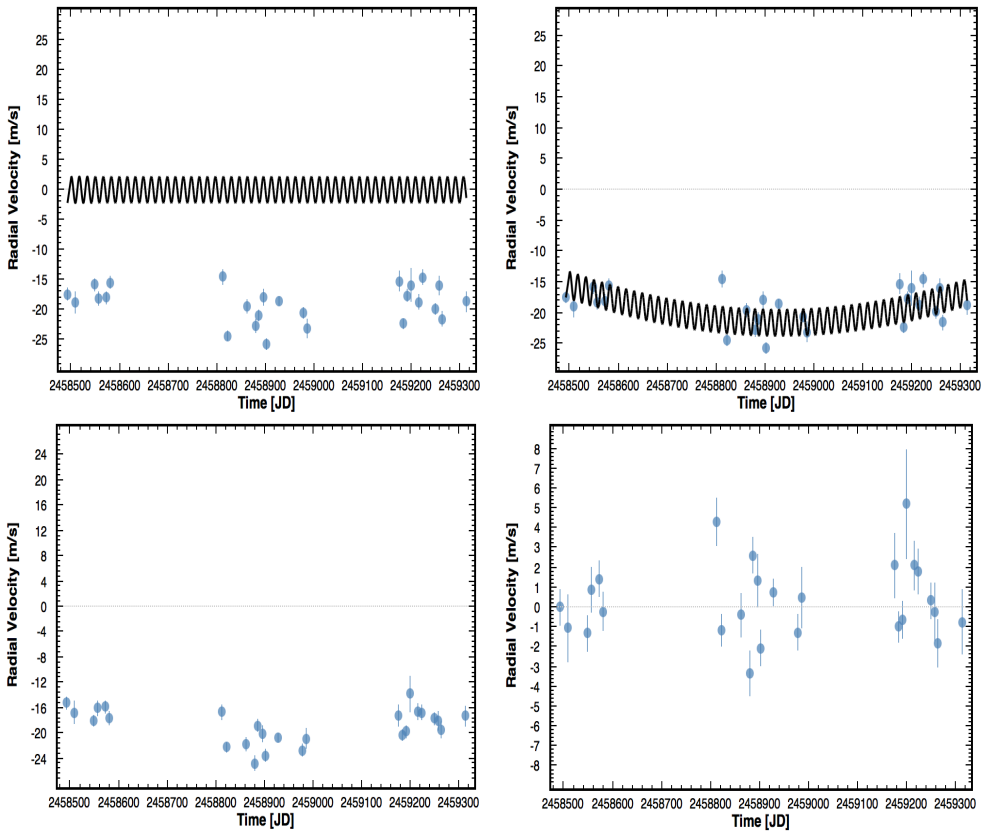

Figure 6.11: Planetary fits and the resulting residuals (top and bottom, respectively) for TES-SAPF54. The large offset in the RV residuals to the one planet fit (left) show a large offset, suggesting the presence of a massive, long period companion. After the inclusion of a 1.66 M_{Jup} planet on a 3505 day orbit (right) the residuals become much more normally distributed about 0 m s^{-1}.

Chapter 7

Future Directions

Two decades of work have proven that low-mass exoplanets are common. Planets with $R < 3R_{\oplus}$ are ubiquitous, with stars hosting 1.6 such worlds on average (Howard *et al.*, 2012; Petigura *et al.*, 2013b; Cassan *et al.*, 2012). The current exoplanet census occupies a broad range of parameter space, and has consistently defied theoretical expectations. When one looks at the mass-period distribution of the known exoplanets, three broad, but well separated, groups are apparent, all of which lack solar System counterparts: (1) hot Jupiters with periods, $P < 10$ days, (2) super-Earth/sub-Neptunes with orbits smaller than Mercury's and (3) exo-Jupiters with periods, $P > 100$ days.

This menagerie raises urgent questions regarding solar system formation. Where and how do hot Jupiters form: *in situ*, or beyond the snow line followed by inwards migration, either dynamic or quiescent? What are the super-Earths in short-period orbits made of: rocky cores with substantial, irradiated, atmospheres or more exotic water worlds? And how does the activity of the host star affect the detection thresholds and characterization precision of the

orbiting planets?

With a host of new questions to answer, exoplanetary science is shifting from detection to characterization. To successfully affect this change, we must develop a nuanced understanding not just of the planets and planetary systems themselves, but also of the host stars' stellar activity.

7.0.1 Measuring exoplanet densities and locating difficult to detect planets

Kepler, its successes notwithstanding, has demonstrated several reasons why transit photometry alone is insufficient to fulfill the exoplanet characterization charge. The planet-multiplicity findings from the mission make it clear that most planet-hosting stars have more than one planet in orbit (Rowe *et al.*, 2014). Such systems are likely to have members that do not transit at all due to orbital inclination, or that do not transit during the lifetime of a spacecraft. These limitations point to a significant population of planets, varying widely in size and composition, that are completely invisible to the transit detection method (Figure 7.1). These unseen companions, however, can have large effects on the overall structure of the planetary system. For example, the presence of exo-Jupiters is predicted to be anti-correlated with the presence of tightly-packed super-Earth inner systems (Batygin and Laughlin, 2015b), and mean-motion resonance crossings of exo-Jupiters are expected to influence the formation of terrestrial planets with semi-major axes, $a < 2$AU (Lykawka and Ito, 2013). Therefore, to guide our theoretical understanding of planet formation and evolution, it is important that we detect *all* of the planetary members of these extrasolar systems so that they can be properly compared with theory.

Transit photometry provides planetary radii and orbital distances, but only rarely gives

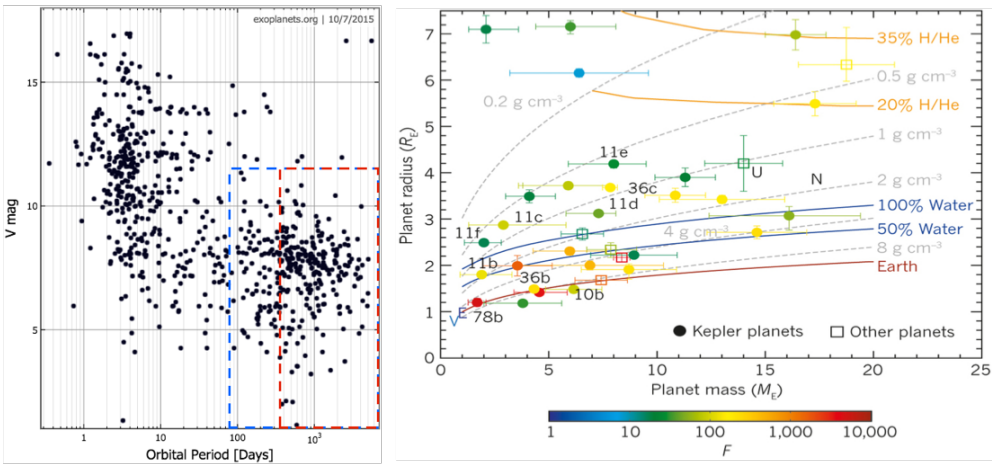

Figure 7.1: Left: The regions of parameter space among already confirmed exoplanets that would be unreachable by K2 (in blue: 423 stars) and TESS (in red: 268 stars) due to their relatively short mission lifetimes, but that are fully accessible to the APF. Right: The degeneracy between planet mass and radius, making it clear that there is no direct way to go from one parameter to the other (figure from Lissauer *et al.* (2014)). RV's ability to directly measure masses and find long period systems that K2 and TESS cannot, makes it a perfect complement to transit photometry.

direct information on planetary masses. This especially plagues the search for Earth-like planets, as combining Kepler data with ground-based observations shows a strong mass-radius degeneracy for the exceedingly common, low-mass planets in the 1-4$R_\oplus$ range (see, e.g., the Rogers (2015) paper titled "Most 1.6 $R_\oplus$ planets are not rocky"). Planets in this range form a class *wholly alien* to our own Solar System, and demonstrate that Earth-sized planets need not have Earth-like compositions. Thus, while we can use transits to determine the sizes of planets, without mass measurements we have no handle on compositions (Figure 7.1).

Combining transit detections with Doppler follow-up observations on ground-based telescopes like the APF solves both of these issues. The RV-determined lower limit to planetary mass estimates ($M \sin i$) can be turned into an absolute mass value by obtaining the planet's orbital inclination from transit observations. An absolute mass and a radius give a bulk density,

which then points towards the likely composition of an exoplanet (Figure 2b). Additionally, RV detections are substantially unaffected by orbital geometry, so a vast-aggregate of non-transiting planets are visible to RV facilities. Unlike transit observations, which detect planets during their fleeting inferior conjunctions, RV observations permit the planetary signal to build in the data over time. Thus, the signals of long-period planets, like our own Jupiter and Saturn, become apparent over only a quarter of their orbital periods - the time necessary to see an inflection in the RV curve. RV telescopes, which have much longer lifetimes, and much lower costs than transit satellites, present our best chance of determining the full architecture of exoplanetary systems and the compositions of those planets that do transit.

RV observations require bright stars, at least 1-2 orders of magnitude brighter than the typical Kepler target, which is why only a small number of stars have been studied using both methods (see §6.1). *Kepler*'s second phase mission, known as K2, is already addressing this lack of overlap, observing bright stars in at least ten campaign fields across the sky through 2016. And NASA's next transit photometry mission, the Transiting Exoplanet Survey Satellite (TESS), will improve things even further - observing the closest and brightest stars across the night sky for evidence of transiting planets. Unlike the original *Kepler* mission, there is no exclusive use period for the K2 and TESS data, which creates the opportunity for immediate RV follow-up.

7.1 K2 follow up efforts

Each of K2's 10 planned campaign pointings lasts approximately 80 days, and seven of the ten approved fields are in regions of the sky easily accessible by the APF. The mission's operations team estimates 10,000-20,000 targets per campaign, all collected with 30-min cadence. Based on *Kepler* statistics and the expected photometric performance, K2 is predicted to detect $\sim$50 planet candidates per year with orbital periods, P < 8 days and radii, R < $2R_{\oplus}$ (Howell *et al.*, 2014).

Work is already underway within the UCSC APF team to identify K2 planetary systems candidates that are well-suited to RV follow-up. We have obtained the public data from K2 campaigns 0 and 4-6, visible to the APF, and we are removing the systematic low-frequency variations that permeate the photometry due to K2's decreased pointing ability. We have applied a Box-fitting Least Squares algorithm to identify transit-like signals in the de-trended data and are culling the candidates so obtained. Because the *Kepler* reduction pipeline is being repurposed to handle K2's photometry analyses, the data products from K2 will look exceedingly similar to the original *Kepler* light curves. The same photometry pipeline will be modified to reduce future TESS data, so our work on the K2 target stars will serve as an excellent testbed for developing planetary transit detection software compatible with TESS in the remaining year leading up to the satellite's launch.

With the results of our newly operational pipeline in hand, we have selected potential planet-hosting stars best suited for APF follow-up, namely bright (V <13), G/K/M dwarfs located in the Northern part of the sky. We are currently using the APF's first generation dy-

namic scheduler to obtain I_2 cell observations of the most promising candidates, and will soon be upgrading to the new scheduler described in Chapter 6, which will match these targets with precision requirements (based on the semi-amplitude calculated from their K2 radii estimates and the probabilistic mass-radius relations of Wolfgang and Lopez (2015)) and cadence requirements designed to efficiently fill out the phase curves of any transiting planets. Our observing cadences will be shift-tuned to minimize the build-up of aliases that can masquerade as additional planets, or block signals due to real, non-transiting companions.

7.1.1 Expected Results & Applications

7.1.1.1 K2 planet characterization project

The APF will provide RV confirmation and planetary masses for the most interesting K2 transiting planets - those that have at least 2-3 transits during the duration of photometric observations. The short periods of these planets mean that even those with $R < 2\ R_\oplus$ will have RV semi-amplitude values, $K \gtrsim 1$ m s^{-1} , levels easily detectable by the APF in stars with well characterized noise properties. Even planets with RV signals below 1 m s^{-1}, whose presence would be hard to validate with APF data alone, are potentially extractable because the transit data will allow us to confirm their signals in the RV periodogram. For bright stars, this would increase the APF's sensitivity to well below the 1 m s^{-1} level cited in Vogt *et al.* (2014b), and based on Doppler monitoring alone.

Identifying transiting planet candidates in the K2 data is a relatively simple endeavor, thanks to the high quality of systematic-corrected and publicly available light curve data. Raw K2 photometry is contaminated by systematic effects related to the drift of the spacecraft from

solar radiation pressure. Every 6 hours, thrusters are fired to correct the position. Because a target star's position drifts across the CCD pixels, which vary in sensitivity, the spacecraft's motion manifests itself as a 6 hour period "saw-tooth" shape in the light curves. Fortunately, several research groups have developed techniques to account for this. For example, Vanderburg and Johnson (2014) monitor the positions of the target centroids and remove the dependence of the flux on the centroid position. These corrected light curves are publicly available as K2SFF high level science products (HLSP) on the Mikulski Archive for Space Telescopes (MAST). We downloaded these light curves for the K2 fields of interest. We then removed low frequency variability from the time series using the *kepflatten* routine in the publicly available *PyKE Kepler* data reduction software (Still and Barclay, 2012).

Once the light curves were flattened, they were ready to be searched for transit signals. We used the Box-Least-Squares (BLS) algorithm to search for transit-like events. The algorithm phase-folds the light curve for a range of periods and, at each period, attempts to fit a box of a variable width and depth to the folded light curve. It produces a BLS periodogram, which quantifies the strength of the fit as a function of the period. After producing the periodograms for all targets, we considered all peaks for which the periodogram power was greater than 6 standard deviations above the median. Furthermore, the box depth and the ratio of the box width to the period provide a constraint on the search space given the observed range of these parameters for the collection of confirmed transiting planets. We phase-folded the light curves at the significant peaks with physically plausible box depths and durations and visually examined the resulting light curves. False positives like eclipsing binaries are usually easy to filter out given their "V-shaped" transits and the presence of significant secondary eclipses.

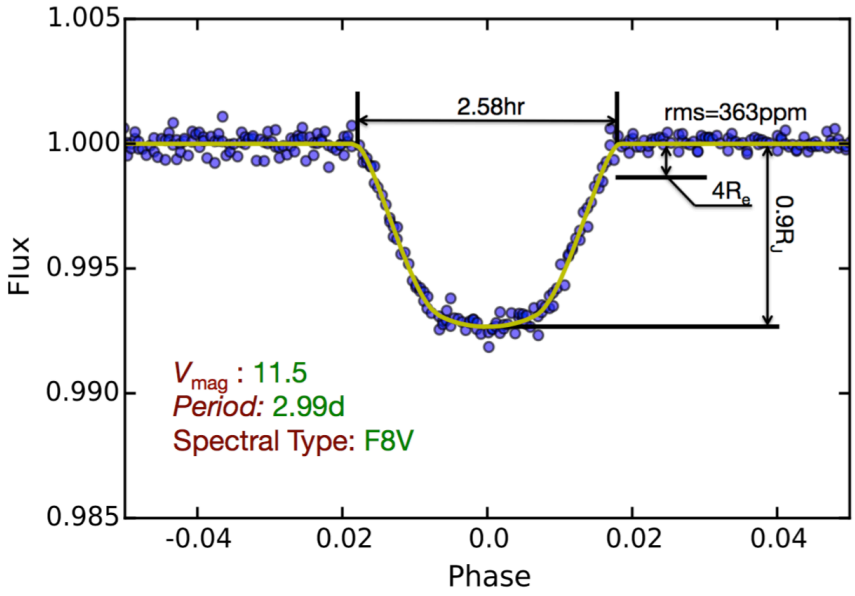

Figure 7.2: Transit signature of the inflated hot Jupiter EPIC212110888b as detected in the K2 data using our transit search pipeline.

The first K2 APF target observations are already underway. An example of photometric light curve for one of our first-round targets, a hot Jupiter (HJ) in orbit around an F8V star designated K2APF2, is shown in Figure 7.2. The planet was detected in the K2 photometry by both our APF team, and a team based at Harvard leading to a collaborative effort on the APF and the TRES spectrograph on the Tillinghast telescope at Mt. Hopkins (Figure 7.3). The planet was published by another team (Lillo-Box *et al.*, 2016) before our write up was complete, but still serves as an excellent proof of concept for the APF's ability to perform a competitive K2 follow-up survey. The APF velocities do seem to give a higher semi-amplitude than the TRES velocities, and the combined best-fit is 221 $\pm$ 40 m s^{-1} which is in agreement with Lillo-Box *et al.* (2016) which claims 209 m s^{-1}.

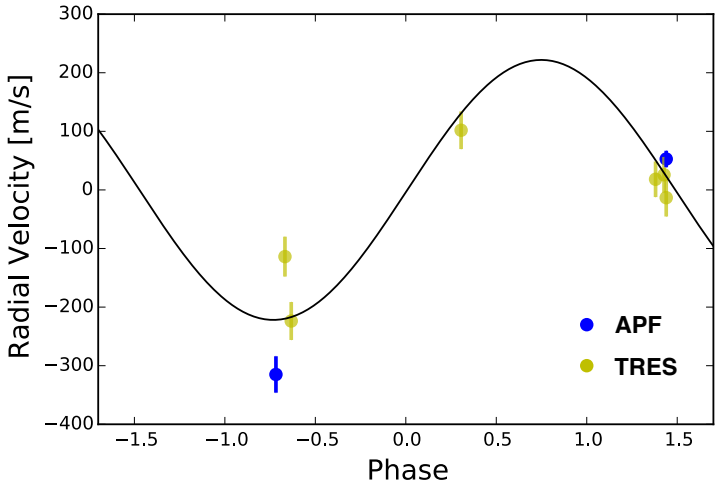

Figure 7.3: The RV data obtained by our team on the APF and the Harvard team using the TRES spectrograph on the Tillinghast telescope.

7.1.1.2 The search for Hot Jupiter progenitors project

Falling well within the APF's detection capabilities is the population of super-Earth planets on 1-10 day orbits suggested as progenitors for the *in situ* formation of hot Jupiters. This theory (presented recently in work such as that by Batygin and Laughlin (2015a) and Boley *et al.* (2015)) suggests that 10-15$M_{\oplus}$ planets located at $\sim$0.05 AU can undergo runaway accretion, resulting in the formation of HJs and negating the need for Jovian planets to migrate inward from beyond the snow line (thereby disrupting their smaller, terrestrial companions). Assessing the validity of this claim can be done via a variety of observational efforts, which can be accomplished with a combination of K2 and APF data. A key first project is to determine the masses of the upper envelope of the super-Earth population and see if they predominantly match the M < 20$M_{\oplus}$ cores that are expected to be sub-critical for HJ formation.

Secondly, because the planet-metallicity relation for HJs has been thoroughly documented (Fischer and Valenti, 2005b; Sousa *et al.*, 2011b, e.g.), and only the most massive super-Earths are expected to become HJs, a substantial, positive, mass-metallicity correlation should exist among most super-Earths with periods, P < 10 days. To test for this relationship we will use the high resolution (R $\sim$ 150,000) template spectra that we acquire for every star in our RV surveys to determine heavy element abundances. This work will go beyond first order [Fe/H] values, using instead an updated, automated version of the LTE spectral analysis code MOOG to determine individual element abundances via equivalent widths (Magrini *et al.*, 2014).

The quantification of these individual abundances enables a third check on the inward

migration theory. If the population of short-period, high-mass super-Earths that the APF can detect and characterize form according to the conventional inward migration paradigm, then the most massive super Earths will have formed from disks that were preferentially abundant in oxygen, and by extension, silicon (Robinson *et al.*, 2006). If they are forming *in situ*, however, the iron abundance will be quite substantial, because hot Jupiters require metal rich disks to form, and roughly equal to the silicate concentration. Therefore, if *in situ* formation is responsible for the HJs, we expect to see high metallicity values, but *not* a favoring of oxygen/silicon over iron in the host stars.

7.2 Using TESS and the APF to Find Targets for JWST

Using the transit search software that we prototype on K2 observations and the time-varying prioritization scheme described in the previous section, we will launch an RV follow-up campaign for the transiting planets detected by TESS. As previously mentioned, TESS will survey the entire Northern sky in one-month strips, focusing on the closest and brightest stars. Simulations of the TESS planet yield, predict over 100 planets transiting stars brighter than V = 12 and with declinations visible to the APF (Sullivan *et al.*, 2015). The short periods of these planets mean that even those with R < 2 $R_{\oplus}$could have RV semi-amplitudes, K $\gtrsim$ 1 m s^{-1} , signals detectable by the APF in stars with well-characterized noise properties.

The next large advance in exoplanet characterization will be the James Webb Space Telescope (JWST) which is designed (in part) to study the atmospheres of exoplanets via transmission spectroscopy and to search for the building blocks of alien life. Observing time on

this next-generation flagship mission will be severely limited, however, and the short timeline between the TESS and JWST launches ($\sim$1 year) creates an *immediate* need to characterize as many TESS systems as possible within the limited time span and then identify those stars worth observing with JWST. Because of TESS's anti-Sun orientation, the stars observed in each month's strip of the sky will move behind the sun (making them unavailable for ground-based follow up) only 4 months after TESS observes them. This means that to gain the highest impact data, RV follow up must happen immediately after the light curves are processed so as not to be put on hold until the next observing season, some 9-10 months later which would thwart JWST target selection efforts. We have designed the APF's new version of the dynamic scheduler to support *exactly* this kind of rapidly evolving observing plan by allowing flexible, immediate adjustments to the telescope's nightly target selection process.

JWST's CVZ is smaller than TESS's, expanding just 10° from the North Ecliptic Pole. However, there are still orders of magnitude more stars in the CVZ than JWST can observe for exoplanet science during its nominal 5 year mission. Down-selecting from thousands of targets to a mere handful of the most interesting stars will require high-cadence, high-precision RV follow-up on a sizable number of stellar targets. By providing weekly, high-precision RV observations of the most interesting stars in the CVZ, along with stellar activity levels and individual elemental abundances, we will develop a much needed resource for the selection of the best targets for JWST - stars with low levels of jitter and flicker, that have confirmed planets with precision mass estimates.

Bibliography

Akeson, R. L.; Chen, X.; Ciardi, D.; Crane, M.; Good, J.; Harbut, M.; Jackson, E.; Kane, S. R.; Laity, A. C.; Leifer, S.; Lynn, M.; McElroy, D. L.; Papin, M.; Plavchan, P.; Ramírez, S. V.; Rey, R.; von Braun, K.; Wittman, M.; Abajian, M.; Ali, B.; Beichman, C.; Beekley, A.; Berriman, G. B.; Berukoff, S.; Bryden, G.; Chan, B.; Groom, S.; Lau, C.; Payne, A. N.; Regelson, M.; Saucedo, M.; Schmitz, M.; Stauffer, J.; Wyatt, P. and Zhang, A. The NASA Exoplanet Archive: Data and Tools for Exoplanet Research. PASP **125**, 989 (2013).

Allende Prieto, C.; Barklem, P. S.; Lambert, D. L. and Cunha, K. S^4N: A spectroscopic survey of stars in the solar neighborhood. The Nearest 15 pc. A&A **420**, 183 (2004).

Ammons, S. M.; Robinson, S. E.; Strader, J.; Laughlin, G.; Fischer, D. and Wolf, A. The N2K Consortium. IV. New Temperatures and Metallicities for More than 100,000 FGK Dwarfs. ApJ **638**, 1004 (2006).

Anglada-Escudé, G.; Arriagada, P.; Tuomi, M.; Zechmeister, M.; Jenkins, J. S.; Ofir, A.; Dreizler, S.; Gerlach, E.; Marvin, C. J.; Reiners, A.; Jeffers, S. V.; Butler, R. P.; Vogt, S. S.; Amado, P. J.; Rodríguez-López, C.; Berdiñas, Z. M.; Morin, J.; Crane, J. D.; Shectman, S. A.; Thompson, I. B.; Díaz, M.; Rivera, E.; Sarmiento, L. F. and Jones, H. R. A. Two

planets around Kapteyn's star: a cold and a temperate super-Earth orbiting the nearest halo red dwarf. MNRAS **443**, L89 (2014).

Anglada-Escudé, G.; Arriagada, P.; Vogt, S. S.; Rivera, E. J.; Butler, R. P.; Crane, J. D.; Shectman, S. A.; Thompson, I. B.; Minniti, D.; Haghighipour, N.; Carter, B. D.; Tinney, C. G.; Wittenmyer, R. A.; Bailey, J. A.; O'Toole, S. J.; Jones, H. R. A. and Jenkins, J. S. A Planetary System around the nearby M Dwarf GJ 667C with At Least One Super-Earth in Its Habitable Zone. ApJ **751**, L16 (2012).

Balan, S. T. and Lahav, O. EXOFIT: orbital parameters of extrasolar planets from radial velocities. MNRAS **394**, 1936 (2009).

Baluev, R. V. Distinguishing between a true period and its alias, and other tasks of model discrimination. MNRAS **422**, 2372 (2012).

Baraffe, I.; Chabrier, G.; Allard, F. and Hauschildt, P. H. Evolutionary models for solar metallicity low-mass stars: mass-magnitude relationships and color-magnitude diagrams. A&A **337**, 403 (1998).

Batalha, N. M.; Rowe, J. F.; Bryson, S. T.; Barclay, T.; Burke, C. J.; Caldwell, D. A.; Christiansen, J. L.; Mullally, F.; Thompson, S. E.; Brown, T. M.; Dupree, A. K.; Fabrycky, D. C.; Ford, E. B.; Fortney, J. J.; Gilliland, R. L.; Isaacson, H.; Latham, D. W.; Marcy, G. W.; Quinn, S. N.; Ragozzine, D.; Shporer, A.; Borucki, W. J.; Ciardi, D. R.; Gautier, III, T. N.; Haas, M. R.; Jenkins, J. M.; Koch, D. G.; Lissauer, J. J.; Rapin, W.; Basri, G. S.; Boss, A. P.; Buchhave, L. A.; Carter, J. A.; Charbonneau, D.; Christensen-Dalsgaard, J.; Clarke, B. D.;

Cochran, W. D.; Demory, B.-O.; Desert, J.-M.; Devore, E.; Doyle, L. R.; Esquerdo, G. A.; Everett, M.; Fressin, F.; Geary, J. C.; Girouard, F. R.; Gould, A.; Hall, J. R.; Holman, M. J.; Howard, A. W.; Howell, S. B.; Ibrahim, K. A.; Kinemuchi, K.; Kjeldsen, H.; Klaus, T. C.; Li, J.; Lucas, P. W.; Meibom, S.; Morris, R. L.; Prša, A.; Quintana, E.; Sanderfer, D. T.; Sasselov, D.; Seader, S. E.; Smith, J. C.; Steffen, J. H.; Still, M.; Stumpe, M. C.; Tarter, J. C.; Tenenbaum, P.; Torres, G.; Twicken, J. D.; Uddin, K.; Van Cleve, J.; Walkowicz, L. and Welsh, W. F. Planetary Candidates Observed by Kepler. III. Analysis of the First 16 Months of Data. ApJS **204**, 24 (2013a).

Batalha, N. M.; Rowe, J. F.; Bryson, S. T.; Barclay, T.; Burke, C. J.; Caldwell, D. A.; Christiansen, J. L.; Mullally, F.; Thompson, S. E.; Brown, T. M.; Dupree, A. K.; Fabrycky, D. C.; Ford, E. B.; Fortney, J. J.; Gilliland, R. L.; Isaacson, H.; Latham, D. W.; Marcy, G. W.; Quinn, S. N.; Ragozzine, D.; Shporer, A.; Borucki, W. J.; Ciardi, D. R.; Gautier, III, T. N.; Haas, M. R.; Jenkins, J. M.; Koch, D. G.; Lissauer, J. J.; Rapin, W.; Basri, G. S.; Boss, A. P.; Buchhave, L. A.; Carter, J. A.; Charbonneau, D.; Christensen-Dalsgaard, J.; Clarke, B. D.; Cochran, W. D.; Demory, B.-O.; Desert, J.-M.; Devore, E.; Doyle, L. R.; Esquerdo, G. A.; Everett, M.; Fressin, F.; Geary, J. C.; Girouard, F. R.; Gould, A.; Hall, J. R.; Holman, M. J.; Howard, A. W.; Howell, S. B.; Ibrahim, K. A.; Kinemuchi, K.; Kjeldsen, H.; Klaus, T. C.; Li, J.; Lucas, P. W.; Meibom, S.; Morris, R. L.; Prša, A.; Quintana, E.; Sanderfer, D. T.; Sasselov, D.; Seader, S. E.; Smith, J. C.; Steffen, J. H.; Still, M.; Stumpe, M. C.; Tarter, J. C.; Tenenbaum, P.; Torres, G.; Twicken, J. D.; Uddin, K.; Van Cleve, J.; Walkowicz, L. and Welsh, W. F. Planetary Candidates Observed by Kepler. III. Analysis of the First 16 Months

of Data. ApJS **204**, 24 (2013b).

Batygin, K. and Laughlin, G. Jupiter's decisive role in the inner Solar System's early evolution. *Proceedings of the National Academy of Science* **112**, 4214 (2015a).

Batygin, K. and Laughlin, G. Jupiter's decisive role in the inner Solar System's early evolution. *Proceedings of the National Academy of Science* **112**, 4214 (2015b).

Batygin, K. and Morbidelli, A. Dissipative Divergence of Resonant Orbits. AJ **145**, 1 (2013).

Beal, T. NASA needs Kitt Peak telescope for exoplanet duty (2014). Online; accessed 2015-02-09.

Beers, T. C.; Flynn, K. and Gebhardt, K. Measures of location and scale for velocities in clusters of galaxies - A robust approach. *Astronomical Journal* **100**, 32 (1990).

Bertin, E. and Arnouts, S. SExtractor: Software for source extraction. *Astronomy and Astrophysics* **117**, 393 (1996).

Boisse, I.; Bonfils, X. and Santos, N. C. SOAP. A tool for the fast computation of photometry and radial velocity induced by stellar spots. A&A **545**, A109 (2012).

Boley, A. C.; Morris, M. A. and Ford, E. B. The In Situ Formation of Systems with Tightly-packed Inner Planets. In *American Astronomical Society Meeting Abstracts* (2015), vol. 225 of *American Astronomical Society Meeting Abstracts*, p. 257.22.

Bonfils, X.; Mayor, M.; Delfosse, X.; Forveille, T.; Gillon, M.; Perrier, C.; Udry, S.; Bouchy, F.; Lovis, C.; Pepe, F.; Queloz, D.; Santos, N. C. and Bertaux, J.-L. The HARPS search for

southern extra-solar planets. X. A msin(i) = 11 Earth mass planet around the nearby spotted M dwarf GJ 674. A&A **474**, 293 (2007).

Bouchy, F.; Pepe, F. and Queloz, D. Fundamental photon noise limit to radial velocity measurements. *Astronomy & Astrophysics* **374**, 733 (2001).

Boyajian, T. S.; von Braun, K.; van Belle, G.; McAlister, H. A.; ten Brummelaar, T. A.; Kane, S. R.; Muirhead, P. S.; Jones, J.; White, R.; Schaefer, G.; Ciardi, D.; Henry, T.; López-Morales, M.; Ridgway, S.; Gies, D.; Jao, W.-C.; Rojas-Ayala, B.; Parks, J. R.; Sturmann, L.; Sturmann, J.; Turner, N. H.; Farrington, C.; Goldfinger, P. J. and Berger, D. H. Stellar Diameters and Temperatures. II. Main-sequence K- and M-stars. ApJ **757**, 112 (2012).

Burt, J.; Holden, B.; Hanson, R.; Laughlin, G.; Vogt, S. S.; Butler, R. P.; Keiser, S. and Deich, W. The capabilities and performance of the Automated Planet Finder Telescope with the implementation of a dynamic scheduler. *Journal of Astronomical Telescopes, Instruments, and Systems* (2015).

Burt, J.; Vogt, S. S.; Butler, R. P.; Hanson, R.; Meschiari, S.; Rivera, E. J.; Henry, G. W. and Laughlin, G. The Lick-Carnegie Exoplanet Survey: Gliese 687 - A Neptune-mass Planet Orbiting a Nearby Red Dwarf. *The Astrophysical Journal* **789**, 114 (2014).

Butler, R. P. The HIRES/Keck Precision Radial Velocity Exoplanet Survey (in prep). *Astrophysical Journal* (2016).

Butler, R. P.; Marcy, G. W.; Fischer, D. A.; Brown, T. M.; Contos, A. R.; Korzennik, S. G.; Nisenson, P. and Noyes, R. W. Evidence for Multiple Companions to Upsilon Andromedae.

ApJ **526**, 916 (1999).

Butler, R. P.; Marcy, G. W.; Williams, E.; McCarthy, C.; Dosanjh, P. and Vogt, S. S. Attaining Doppler Precision of 3 m s^{-1}. *Publications of the ASP* **108**, 500 (1996a).

Butler, R. P.; Marcy, G. W.; Williams, E.; McCarthy, C.; Dosanjh, P. and Vogt, S. S. Attaining Doppler Precision of 3 M s-1. PASP **108**, 500 (1996b).

Butler, R. P.; Marcy, G. W.; Williams, E.; McCarthy, C.; Dosanjh, P. and Vogt, S. S. Attaining Doppler Precision of 3 M s-1. PASP **108**, 500 (1996c).

Butler, R. P.; Vogt, S. S.; Marcy, G. W.; Fischer, D. A.; Wright, J. T.; Henry, G. W.; Laughlin, G. and Lissauer, J. J. A Neptune-Mass Planet Orbiting the Nearby M Dwarf GJ 436. ApJ **617**, 580 (2004).

Cassan, A.; Kubas, D.; Beaulieu, J.-P.; Dominik, M.; Horne, K.; Greenhill, J.; Wambsganss, J.; Menzies, J.; Williams, A.; Jørgensen, U. G.; Udalski, A.; Bennett, D. P.; Albrow, M. D.; Batista, V.; Brillant, S.; Caldwell, J. A. R.; Cole, A.; Coutures, C.; Cook, K. H.; Dieters, S.; Prester, D. D.; Donatowicz, J.; Fouqué, P.; Hill, K.; Kains, N.; Kane, S.; Marquette, J.-B.; Martin, R.; Pollard, K. R.; Sahu, K. C.; Vinter, C.; Warren, D.; Watson, B.; Zub, M.; Sumi, T.; Szymański, M. K.; Kubiak, M.; Poleski, R.; Soszynski, I.; Ulaczyk, K.; Pietrzyński, G. and Wyrzykowski, Ł. One or more bound planets per Milky Way star from microlensing observations. Nature **481**, 167 (2012).

Charbonneau, D.; Brown, T. M.; Latham, D. W. and Mayor, M. Detection of planetary transits across a sun-like star. ApJ **529**, L45 (2000).

Charbonneau, P. Dynamo Models of the Solar Cycle. *Living Reviews in Solar Physics* **7**, 3 (2010).

Chiang, E. and Laughlin, G. The minimum-mass extrasolar nebula: in situ formation of close-in super-Earths. MNRAS **431**, 3444 (2013).

Connes, P. Absolute astronomical accelerometry. *Astrophysics and Space Science* **110**, 211 (1985).

Cosentino, R.; Lovis, C.; Pepe, F.; Collier Cameron, A.; Latham, D. W.; Molinari, E.; Udry, S.; Bezawada, N.; Black, M.; Born, A.; Buchschacher, N.; Charbonneau, D.; Figueira, P.; Fleury, M.; Galli, A.; Gallie, A.; Gao, X.; Ghedina, A.; Gonzalez, C.; Gonzalez, M.; Guerra, J.; Henry, D.; Horne, K.; Hughes, I.; Kelly, D.; Lodi, M.; Lunney, D.; Maire, C.; Mayor, M.; Micela, G.; Ordway, M. P.; Peacock, J.; Phillips, D.; Piotto, G.; Pollacco, D.; Queloz, D.; Rice, K.; Riverol, C.; Riverol, L.; San Juan, J.; Sasselov, D.; Segransan, D.; Sozzetti, A.; Sosnowska, D.; Stobie, B.; Szentgyorgyi, A.; Vick, A. and Weber, L. Harps-N: the new planet hunter at TNG. In *Society of Photo-Optical Instrumentation Engineers (SPIE) Conference Series* (2012), vol. 8446 of *Society of Photo-Optical Instrumentation Engineers (SPIE) Conference Series*, p. 1.

Coughlin, J. L.; Mullally, F.; Thompson, S. E.; Rowe, J. F.; Burke, C. J.; Latham, D. W.; Batalha, N. M.; Ofir, A.; Quarles, B. L.; Henze, C. E.; Wolfgang, A.; Caldwell, D. A.; Bryson, S. T.; Shporer, A.; Catanzarite, J.; Akeson, R.; Barclay, T.; Borucki, W. J.; Boyajian, T. S.; Campbell, J. R.; Christiansen, J. L.; Girouard, F. R.; Haas, M. R.; Howell, S. B.; Huber, D.; Jenkins, J. M.; Li, J.; Patil-Sabale, A.; Quintana, E. V.; Ramirez, S.; Seader, S.; Smith,

J. C.; Tenenbaum, P.; Twicken, J. D. and Zamudio, K. A. Planetary Candidates Observed by Kepler. VII. The First Fully Uniform Catalog Based on The Entire 48 Month Dataset (Q1-Q17 DR24). *ArXiv e-prints* (2015).

Crane, J. D.; Shectman, S. A. and Butler, R. P. The Carnegie Planet Finder Spectrograph. In *Society of Photo-Optical Instrumentation Engineers (SPIE) Conference Series* (2006), vol. 6269 of Proc. SPIE, p. 626931.

Cutri, R. M.; Skrutskie, M. F.; van Dyk, S.; Beichman, C. A.; Carpenter, J. M.; Chester, T.; Cambresy, L.; Evans, T.; Fowler, J.; Gizis, J.; Howard, E.; Huchra, J.; Jarrett, T.; Kopan, E. L.; Kirkpatrick, J. D.; Light, R. M.; Marsh, K. A.; McCallon, H.; Schneider, S.; Stiening, R.; Sykes, M.; Weinberg, M.; Wheaton, W. A.; Wheelock, S. and Zacarias, N. VizieR Online Data Catalog: 2MASS All-Sky Catalog of Point Sources (Cutri+ 2003). *VizieR Online Data Catalog* **2246** (2003).

Dawson, R. I. and Fabrycky, D. C. Radial Velocity Planets De-aliased: A New, Short Period for Super-Earth 55 Cnc e. ApJ **722**, 937 (2010).

Dressing, C. D. and Charbonneau, D. The Occurrence Rate of Small Planets around Small Stars. ApJ **767**, 95 (2013).

Dumusque, X.; Pepe, F.; Lovis, C.; Ségransan, D.; Sahlmann, J.; Benz, W.; Bouchy, F.; Mayor, M.; Queloz, D.; Santos, N. and Udry, S. An Earth-mass planet orbiting α Centauri B. Nature **491**, 207 (2012).

Dumusque, X.; Santos, N. C.; Udry, S.; Lovis, C. and Bonfils, X. Planetary detection limits tak-

ing into account stellar noise. II. Effect of stellar spot groups on radial-velocities. *Astronomy & Astrophysics* **527**, A82 (2011).

Eastman, J. D.; Brown, T. M.; Hygelund, J.; van Eyken, J.; Tufts, J. R. and Barnes, S. NRES: the network of robotic Echelle spectrographs. In *Society of Photo-Optical Instrumentation Engineers (SPIE) Conference Series* (2014), vol. 9147 of *Society of Photo-Optical Instrumentation Engineers (SPIE) Conference Series*, p. 16.

Eaton, J. A.; Henry, G. W. and Fekel, F. C. Advantages of Automated Observing with Small Telescopes. In Oswalt, T. D., ed., *Astrophysics and Space Science Library* (2003), vol. 288 of *Astrophysics and Space Science Library*, p. 189.

Efron, B. Bootstrap methods: Another look at the jackknife. *Ann. Statistics* **7**, 1 (1979).

Eggenberger, A. and Udry, S. Detection and Characterization of Extrasolar Planets through Doppler Spectroscopy. In Montmerle, T.; Ehrenreich, D. and Lagrange, A.-M., eds., *EAS Publications Series* (2010), vol. 41 of *EAS Publications Series*, pp. 27–75.

Endl, M.; Cochran, W. D.; Tull, R. G. and MacQueen, P. J. A Dedicated M Dwarf Planet Search Using The Hobby-Eberly Telescope. AJ **126**, 3099 (2003).

Fabrycky, D. C.; Lissauer, J. J.; Ragozzine, D.; Rowe, J. F.; Steffen, J. H.; Agol, E.; Barclay, T.; Batalha, N.; Borucki, W.; Ciardi, D. R.; Ford, E. B.; Gautier, T. N.; Geary, J. C.; Holman, M. J.; Jenkins, J. M.; Li, J.; Morehead, R. C.; Morris, R. L.; Shporer, A.; Smith, J. C.; Still, M. and Van Cleve, J. Architecture of Kepler's Multi-transiting Systems. II. New Investigations with Twice as Many Candidates. ApJ **790**, 146 (2014).

Fischer, D.; Anglada-Escude, G.; Arriagada, P.; Baluev, R. V.; Bean, J. L.; Bouchy, F.; Buchhave, L. A.; Carroll, T.; Chakraborty, A.; Crepp, J. R.; Dawson, R. I.; Diddams, S. A.; Dumusque, X.; Eastman, J. D.; Endl, M.; Figueira, P.; Ford, E. B.; Foreman-Mackey, D.; Fournier, P.; Furesz, G.; Gaudi, B. S.; Gregory, P. C.; Grundahl, F.; Hatzes, A. P.; Hebrard, G.; Herrero, E.; Hogg, D. W.; Howard, A. W.; Johnson, J. A.; Jorden, P.; Jurgenson, C. A.; Latham, D. W.; Laughlin, G.; Loredo, T. J.; Lovis, C.; Mahadevan, S.; McCracken, T. M.; Pepe, F.; Perez, M.; Phillips, D. F.; Plavchan, P. P.; Prato, L.; Quirrenbach, A.; Reiners, A.; Robertson, P.; Santos, N. C.; Sawyer, D.; Segransan, D.; Sozzetti, A.; Steinmetz, T.; Szentgyorgyi, A.; Udry, S.; Valenti, J. A.; Wang, S. X.; Wittenmyer, R. A. and Wright, J. T. State of the Field: Extreme Precision Radial Velocities. *ArXiv e-prints* (2016).

Fischer, D. A. and Valenti, J. The Planet-Metallicity Correlation. ApJ **622**, 1102 (2005a).

Fischer, D. A. and Valenti, J. The Planet-Metallicity Correlation. ApJ **622**, 1102 (2005b).

Ford, E. B. Quantifying the Uncertainty in the Orbits of Extrasolar Planets. AJ **129**, 1706 (2005).

Ford, E. B. Improving the Efficiency of Markov Chain Monte Carlo for Analyzing the Orbits of Extrasolar Planets. ApJ **642**, 505 (2006).

Ford, E. B. Adaptive scheduling algorithms for planet searches. *The Astronomical Journal* **135**, 1008 (2008).

Fressin, F.; Torres, G.; Charbonneau, D.; Bryson, S. T.; Christiansen, J.; Dressing, C. D.;

Jenkins, J. M.; Walkowicz, L. M. and Batalha, N. M. The False Positive Rate of Kepler and the Occurrence of Planets. ApJ **766**, 81 (2013).

Fulton, B. J.; Weiss, L. M.; Sinukoff, E.; Isaacson, H.; Howard, A. W.; Marcy, G. W.; Henry, G. W.; Holden, B. P. and Kibrick, R. I. Three Super-Earths Orbiting HD 7924. *Astrophysical Journal* **805**, 175 (2015).

Garcia-Piquer, A.; Guàrdia, J.; Colomé, J.; Ribas, I.; Gesa, L.; Morales, J. C.; Pérez-Calpena, A.; Seifert, W.; Quirrenbach, A.; Amado, P. J.; Caballero, J. A. and Reiners, A. CARMENES instrument control system and operational scheduler. In *Society of Photo-Optical Instrumentation Engineers (SPIE) Conference Series* (2014), vol. 9152 of *Society of Photo-Optical Instrumentation Engineers (SPIE) Conference Series*, p. 21.

Girardi, L.; Groenewegen, M. A. T.; Hatziminaoglou, E. and da Costa, L. Star counts in the Galaxy. Simulating from very deep to very shallow photometric surveys with the TRILEGAL code. A&A **436**, 895 (2005).

Gonzalez, G. The stellar metallicity-giant planet connection. MNRAS **285**, 403 (1997).

Gregory, P. C. Bayesian re-analysis of the Gliese 581 exoplanet system. MNRAS **415**, 2523 (2011).

Han, E.; Wang, S. X.; Wright, J. T.; Feng, Y. K.; Zhao, M.; Fakhouri, O.; Brown, J. I. and Hancock, C. Exoplanet Orbit Database. II. Updates to Exoplanets.org. PASP **126**, 827 (2014).

Hansen, B. M. S. and Murray, N. Migration Then Assembly: Formation of Neptune-mass Planets inside 1 AU. ApJ **751**, 158 (2012).

Hayes, D. S. and Latham, D. W. A rediscussion of the atmospheric extinction and the absolute spectral-energy distribution of VEGA. ApJ **197**, 593 (1975).

Henry, G. W. Techniques for Automated High-Precision Photometry of Sun-like Stars. PASP **111**, 845 (1999a).

Henry, G. W. Techniques for Automated High-Precision Photometry of Sun-like Stars. PASP **111**, 845 (1999b).

Henry, G. W.; Fekel, F. C. and Hall, D. S. An Automated Search for Variability in Chromospherically Active Stars. AJ **110**, 2926 (1995).

Henry, G. W.; Fekel, F. C.; Kaye, A. B. and Kaul, A. 10 New γ Doradus and δ Scuti Stars. AJ **122**, 3383 (2001).

Henry, G. W.; Marcy, G. W.; Butler, R. P. and Vogt, S. S. A Transiting "51 Peg-like" Planet. ApJ **529**, L41 (2000).

Henry, T. J. and McCarthy, Jr., D. W. The mass-luminosity relation for stars of mass 1.0 to 0.08 solar mass. AJ **106**, 773 (1993).

Howard, A. W.; Johnson, J. A.; Marcy, G. W.; Fischer, D. A.; Wright, J. T.; Bernat, D.; Henry, G. W.; Peek, K. M. G.; Isaacson, H.; Apps, K.; Endl, M.; Cochran, W. D.; Valenti, J. A.; Anderson, J. and Piskunov, N. E. The California Planet Survey. I. Four New Giant Exoplanets. ApJ **721**, 1467 (2010).

Howard, A. W.; Marcy, G. W.; Bryson, S. T.; Jenkins, J. M.; Rowe, J. F.; Batalha, N. M.; Borucki, W. J.; Koch, D. G.; Dunham, E. W.; Gautier, III, T. N.; Van Cleve, J.; Cochran,

W. D.; Latham, D. W.; Lissauer, J. J.; Torres, G.; Brown, T. M.; Gilliland, R. L.; Buchhave, L. A.; Caldwell, D. A.; Christensen-Dalsgaard, J.; Ciardi, D.; Fressin, F.; Haas, M. R.; Howell, S. B.; Kjeldsen, H.; Seager, S.; Rogers, L.; Sasselov, D. D.; Steffen, J. H.; Basri, G. S.; Charbonneau, D.; Christiansen, J.; Clarke, B.; Dupree, A.; Fabrycky, D. C.; Fischer, D. A.; Ford, E. B.; Fortney, J. J.; Tarter, J.; Girouard, F. R.; Holman, M. J.; Johnson, J. A.; Klaus, T. C.; Machalek, P.; Moorhead, A. V.; Morehead, R. C.; Ragozzine, D.; Tenenbaum, P.; Twicken, J. D.; Quinn, S. N.; Isaacson, H.; Shporer, A.; Lucas, P. W.; Walkowicz, L. M.; Welsh, W. F.; Boss, A.; Devore, E.; Gould, A.; Smith, J. C.; Morris, R. L.; Prsa, A.; Morton, T. D.; Still, M.; Thompson, S. E.; Mullally, F.; Endl, M. and MacQueen, P. J. Planet Occurrence within 0.25 AU of Solar-type Stars from Kepler. ApJS **201**, 15 (2012).

Howell, S. B.; Sobeck, C.; Haas, M.; Still, M.; Barclay, T.; Mullally, F.; Troeltzsch, J.; Aigrain, S.; Bryson, S. T.; Caldwell, D.; Chaplin, W. J.; Cochran, W. D.; Huber, D.; Marcy, G. W.; Miglio, A.; Najita, J. R.; Smith, M.; Twicken, J. D. and Fortney, J. J. The K2 Mission: Characterization and Early Results. PASP **126**, 398 (2014).

Isaacson, H. and Fischer, D. Chromospheric Activity and Jitter Measurements for 2630 Stars on the California Planet Search. ApJ **725**, 875 (2010a).

Isaacson, H. and Fischer, D. Chromospheric Activity and Jitter Measurements for 2630 Stars on the California Planet Search. ApJ **725**, 875 (2010b).

Johnson, J. A. and Apps, K. On the Metal Richness of M Dwarfs with Planets. ApJ **699**, 933 (2009).

Kukla, A. *Extraterrestrials: a philosophical perspective*. Extraterrestrials: A Philosophical Perspective. Lexington Books (2010).

Lanclos, K.; Peck, M.; Saylor, M.; Kibrick, R. I. and Allen, S. L. Tuning a 2.4-meter telescope... blindfolded. In *Society of Photo-Optical Instrumentation Engineers (SPIE) Conference Series* (2014), vol. 9145 of *Society of Photo-Optical Instrumentation Engineers (SPIE) Conference Series*, p. 4.

Lillo-Box, J.; Demangeon, O.; Santerne, A.; Barros, S. C. C.; Barrado, D.; Hébrard, G.; Osborn, H. P.; Armstrong, D. J.; Almenara, J.-M.; Boisse, I.; Bouchy, F.; Brown, D. J. A.; Courcol, B.; Deleuil, M.; Delgado Mena, E.; Díaz, R. F.; Kirk, J.; Lam, K. W. F.; McCormac, J.; Pollacco, D.; Rajpurohit, A.; Rey, J.; Santos, N. C.; Sousa, S. G.; Tsantaki, M. and Wilson, P. A. EPIC210957318b and EPIC212110888b: two inflated hot-Jupiters around Solar-type stars. *ArXiv e-prints* (2016).

Lissauer, J. J.; Dawson, R. I. and Tremaine, S. Advances in exoplanet science from Kepler. Nature **513**, 336 (2014).

Lissauer, J. J.; Ragozzine, D.; Fabrycky, D. C.; Steffen, J. H.; Ford, E. B.; Jenkins, J. M.; Shporer, A.; Holman, M. J.; Rowe, J. F.; Quintana, E. V.; Batalha, N. M.; Borucki, W. J.; Bryson, S. T.; Caldwell, D. A.; Carter, J. A.; Ciardi, D.; Dunham, E. W.; Fortney, J. J.; Gautier, III, T. N.; Howell, S. B.; Koch, D. G.; Latham, D. W.; Marcy, G. W.; Morehead, R. C. and Sasselov, D. Architecture and Dynamics of Kepler's Candidate Multiple Transiting Planet Systems. ApJS **197**, 8 (2011a).

Lissauer, J. J.; Ragozzine, D.; Fabrycky, D. C.; Steffen, J. H.; Ford, E. B.; Jenkins, J. M.; Shporer, A.; Holman, M. J.; Rowe, J. F.; Quintana, E. V.; Batalha, N. M.; Borucki, W. J.; Bryson, S. T.; Caldwell, D. A.; Carter, J. A.; Ciardi, D.; Dunham, E. W.; Fortney, J. J.; Gautier, III, T. N.; Howell, S. B.; Koch, D. G.; Latham, D. W.; Marcy, G. W.; Morehead, R. C. and Sasselov, D. Architecture and Dynamics of Kepler's Candidate Multiple Transiting Planet Systems. ApJS **197**, 8 (2011b).

Lithwick, Y. and Wu, Y. Resonant Repulsion of Kepler Planet Pairs. ApJ **756**, L11 (2012).

Lopez, E. D.; Fortney, J. J. and Miller, N. How Thermal Evolution and Mass-loss Sculpt Populations of Super-Earths and Sub-Neptunes: Application to the Kepler-11 System and Beyond. ApJ **761**, 59 (2012).

Loredo, T. J.; Berger, J. O.; Chernoff, D. F.; Clyde, M. A. and Liu, B. Bayesian Methods for Analysis and Adaptive Scheduling of Exoplanet Observations. *ArXiv e-prints* (2011).

Lovis, C.; Dumusque, X.; Santos, N. C.; Bouchy, F.; Mayor, M.; Pepe, F.; Queloz, D.; Ségransan, D. and Udry, S. The HARPS search for southern extra-solar planets. XXXI. Magnetic activity cycles in solar-type stars: statistics and impact on precise radial velocities. *ArXiv e-prints* (2011).

Lovis, C.; Mayor, M.; Pepe, F.; Alibert, Y.; Benz, W.; Bouchy, F.; Correia, A. C. M.; Laskar, J.; Mordasini, C.; Queloz, D.; Santos, N. C.; Udry, S.; Bertaux, J.-L. and Sivan, J.-P. An extrasolar planetary system with three Neptune-mass planets. Nature **441**, 305 (2006).

Lykawka, P. S. and Ito, T. Terrestrial Planet Formation during the Migration and Resonance Crossings of the Giant Planets. ApJ **773**, 65 (2013).

Magrini, L.; Randich, S.; Friel, E.; Spina, L.; Jacobson, H.; Cantat-Gaudin, T.; Donati, P.; Baglioni, R.; Maiorca, E.; Bragaglia, A.; Sordo, R. and Vallenari, A. FAMA: Fast Automatic MOOG Analysis. Astrophysics Source Code Library (2014).

Marcus, R. A.; Sasselov, D.; Hernquist, L. and Stewart, S. T. Minimum Radii of Super-Earths: Constraints from Giant Impacts. ApJ **712**, L73 (2010).

Marcy, G. W. and Butler, R. P. A Planetary Companion to 70 Virginis. ApJ **464**, L147 (1996).

Marcy, G. W.; Butler, R. P.; Vogt, S. S.; Fischer, D. A.; Henry, G. W.; Laughlin, G.; Wright, J. T. and Johnson, J. A. Five New Extrasolar Planets. ApJ **619**, 570 (2005).

Massey, P.; Strobel, K.; Barnes, J. V. and Anderson, E. Spectrophotometric standards. ApJ **328**, 315 (1988).

Mayor, M.; Marmier, M.; Lovis, C.; Udry, S.; Ségransan, D.; Pepe, F.; Benz, W.; Bertaux, J. .; Bouchy, F.; Dumusque, X.; Lo Curto, G.; Mordasini, C.; Queloz, D. and Santos, N. C. The HARPS search for southern extra-solar planets XXXIV. Occurrence, mass distribution and orbital properties of super-Earths and Neptune-mass planets. *ArXiv e-prints* (2011).

Mayor, M. and Quelos, D. A search for substellar companions to solar-type stars via precise Doppler measurements: a first Jupiter mass companion detected. In Pallavicini, R. and Dupree, A. K., eds., *Cool Stars, Stellar Systems, and the Sun* (1996), vol. 109 of *Astronomical Society of the Pacific Conference Series*, p. 35.

Mayor, M.; Udry, S.; Lovis, C.; Pepe, F.; Queloz, D.; Benz, W.; Bertaux, J.-L.; Bouchy, F.; Mordasini, C. and Segransan, D. The harps search for southern extra-solar planets. xiii. a planetary system with 3 super-earths (4.2, 6.9, and 9.2 m earth). A&A **493**, 639 (2009a).

Mayor, M.; Udry, S.; Lovis, C.; Pepe, F.; Queloz, D.; Benz, W.; Bertaux, J.-L.; Bouchy, F.; Mordasini, C. and Segransan, D. The HARPS search for southern extra-solar planets. XIII. A planetary system with 3 super-Earths (4.2, 6.9, and 9.2 M Earth). A&A **493**, 639 (2009b).

Meschiari, S.; Wolf, A. S.; Rivera, E.; Laughlin, G.; Vogt, S. and Butler, P. Systemic: A Testbed for Characterizing the Detection of Extrasolar Planets. I. The Systemic Console Package. *Publications of the ASP* **121**, 1016 (2009a).

Meschiari, S.; Wolf, A. S.; Rivera, E.; Laughlin, G.; Vogt, S. and Butler, P. Systemic: A Testbed for Characterizing the Detection of Extrasolar Planets. I. The Systemic Console Package. PASP **121**, 1016 (2009b).

Meschiari, S.; Wolf, A. S.; Rivera, E.; Laughlin, G.; Vogt, S. and Butler, P. Systemic Console: Advanced analysis of exoplanetary data (2012). Astrophysics Source Code Library.

Montgomery, R. and Laughlin, G. Formation and detection of Earth mass planets around low mass stars. *Icarus* **202**, 1 (2009).

Motalebi, F.; Udry, S.; Gillon, M.; Lovis, C.; Ségransan, D.; Buchhave, L. A.; Demory, B. O.; Malavolta, L.; Dressing, C. D.; Sasselov, D.; Rice, K.; Charbonneau, D.; Collier Cameron, A.; Latham, D.; Molinari, E.; Pepe, F.; Affer, L.; Bonomo, A. S.; Cosentino, R.; Dumusque, X.; Figueira, P.; Fiorenzano, A. F. M.; Gettel, S.; Harutyunyan, A.; Haywood, R. D.; Johnson,

J.; Lopez, E.; Lopez-Morales, M.; Mayor, M.; Micela, G.; Mortier, A.; Nascimbeni, V.; Philips, D.; Piotto, G.; Pollacco, D.; Queloz, D.; Sozzetti, A.; Vanderburg, A. and Watson, C. A. The HARPS-N Rocky Planet Search. I. HD 219134 b: A transiting rocky planet in a multi-planet system at 6.5 pc from the Sun. A&A **584**, A72 (2015).

Neves, V.; Bonfils, X.; Santos, N. C.; Delfosse, X.; Forveille, T.; Allard, F. and Udry, S. Metallicity of M dwarfs. III. Planet-metallicity and planet-stellar mass correlations of the HARPS GTO M dwarf sample. A&A **551**, A36 (2013).

Noyes, R. W.; Hartmann, L. W.; Baliunas, S. L.; Duncan, D. K. and Vaughan, A. H. Rotation, convection, and magnetic activity in lower main-sequence stars. *Astrophysical Journal* **279**, 763 (1984).

Oja, T. UBV photometry of stars whose positions are accurately known. VII. A&AS **100**, 591 (1993).

Paulson, D. B.; Saar, S. H.; Cochran, W. D. and Henry, G. W. Searching for Planets in the Hyades. III. The Quest for Short-Period Planets. AJ **127**, 1644 (2004).

Pepe, F.; Lovis, C.; Ségransan, D.; Benz, W.; Bouchy, F.; Dumusque, X.; Mayor, M.; Queloz, D.; Santos, N. C. and Udry, S. The HARPS search for Earth-like planets in the habitable zone. I. Very low-mass planets around <ASTROBJ>HD 20794</ASTROBJ>, <ASTROBJ>HD 85512</ASTROBJ>, and <ASTROBJ>HD 192310</ASTROBJ>. A&A **534**, A58 (2011).

Petigura, E. A.; Howard, A. W. and Marcy, G. W. Prevalence of Earth-size planets orbiting Sun-like stars. *Proceedings of the National Academy of Science* **110**, 19273 (2013a).

Petigura, E. A.; Howard, A. W. and Marcy, G. W. Prevalence of Earth-size planets orbiting Sun-like stars. *Proceedings of the National Academy of Science* **110**, 19273 (2013b).

Podgorski, W.; Bean, J.; Bergner, H.; Chun, M.-Y.; Crane, J.; Evans, I.; Evans, J.; Furesz, G.; Guzman, D.; Kim, K.-M.; McCracken, K.; Mueller, M.; Norton, T.; Park, C.; Park, S.; Plummer, D.; Szentgyorgyi, A.; Uomoto, A. and Yuk, I.-S. A novel systems engineering approach to the design of a precision radial velocity spectrograph: the GMT-Consortium Large Earth Finder (G-CLEF). In *Ground-based and Airborne Instrumentation for Astronomy V* (2014), vol. 9147 of Proc. SPIE, p. 91478W.

Press, W. H.; Teukolsky, S. A.; Vetterling, W. T. and Flannery, B. P. *Numerical recipes in C. The art of scientific computing*. Cambridge: University Press, |c1992, 2nd ed. (1992).

Queloz, D.; Henry, G. W.; Sivan, J. P.; Baliunas, S. L.; Beuzit, J. L.; Donahue, R. A.; Mayor, M.; Naef, D.; Perrier, C. and Udry, S. No planet for HD 166435. A&A **379**, 279 (2001).

Radovan, M. V.; Cabak, G. F.; Laiterman, L. H.; Lockwood, C. T. and Vogt, S. S. A radial velocity spectrometer for the Automated Planet Finder Telescope at Lick Observatory. In *Society of Photo-Optical Instrumentation Engineers (SPIE) Conference Series* (2010), vol. 7735 of *Society of Photo-Optical Instrumentation Engineers (SPIE) Conference Series*, p. 4.

Rajpaul, V.; Aigrain, S.; Osborne, M. A.; Reece, S. and Roberts, S. A Gaussian process framework for modelling stellar activity signals in radial velocity data. MNRAS **452**, 2269 (2015).

Ramírez, I.; Allende Prieto, C. and Lambert, D. L. Oxygen Abundances in Nearby FGK Stars and the Galactic Chemical Evolution of the Local Disk and Halo. ApJ **764**, 78 (2013).

Ricker, G. R.; Winn, J. N.; Vanderspek, R.; Latham, D. W.; Bakos, G. Á.; Bean, J. L.; Berta-Thompson, Z. K.; Brown, T. M.; Buchhave, L.; Butler, N. R.; Butler, R. P.; Chaplin, W. J.; Charbonneau, D.; Christensen-Dalsgaard, J.; Clampin, M.; Deming, D.; Doty, J.; De Lee, N.; Dressing, C.; Dunham, E. W.; Endl, M.; Fressin, F.; Ge, J.; Henning, T.; Holman, M. J.; Howard, A. W.; Ida, S.; Jenkins, J.; Jernigan, G.; Johnson, J. A.; Kaltenegger, L.; Kawai, N.; Kjeldsen, H.; Laughlin, G.; Levine, A. M.; Lin, D.; Lissauer, J. J.; MacQueen, P.; Marcy, G.; McCullough, P. R.; Morton, T. D.; Narita, N.; Paegert, M.; Palle, E.; Pepe, F.; Pepper, J.; Quirrenbach, A.; Rinehart, S. A.; Sasselov, D.; Sato, B.; Seager, S.; Sozzetti, A.; Stassun, K. G.; Sullivan, P.; Szentgyorgyi, A.; Torres, G.; Udry, S. and Villasenor, J. Transiting Exoplanet Survey Satellite (TESS). In *Society of Photo-Optical Instrumentation Engineers (SPIE) Conference Series* (2014), vol. 9143 of *Society of Photo-Optical Instrumentation Engineers (SPIE) Conference Series*, p. 20.

Riddle, R. L.; Hogstrom, K.; Papadopoulos, A.; Baranec, C. and Law, N. M. The Robo-AO automated intelligent queue system. In *Society of Photo-Optical Instrumentation Engineers (SPIE) Conference Series* (2014), vol. 9152 of *Society of Photo-Optical Instrumentation Engineers (SPIE) Conference Series*, p. 1.

Rivera, E. J.; Laughlin, G.; Butler, R. P.; Vogt, S. S.; Haghighipour, N. and Meschiari, S. The Lick-Carnegie Exoplanet Survey: a Uranus-Mass Fourth Planet for GJ 876 in an Extrasolar Laplace Configuration. ApJ **719**, 890 (2010).

Roberts, D. H.; Lehar, J. and Dreher, J. W. Time Series Analysis with Clean - Part One - Derivation of a Spectrum. AJ **93**, 968 (1987).

Robertson, P. and Mahadevan, S. Disentangling Planets and Stellar Activity for Gliese 667C. ApJ **793**, L24 (2014).

Robinson, S. E.; Laughlin, G.; Bodenheimer, P. and Fischer, D. Silicon and Nickel Enrichment in Planet Host Stars: Observations and Implications for the Core Accretion Theory of Planet Formation. ApJ **643**, 484 (2006).

Rogers, L. A. Most 1.6 Earth-radius Planets are Not Rocky. ApJ **801**, 41 (2015).

Rojas-Ayala, B.; Covey, K. R.; Muirhead, P. S. and Lloyd, J. P. Metallicity and Temperature Indicators in M Dwarf K-band Spectra: Testing New and Updated Calibrations with Observations of 133 Solar Neighborhood M Dwarfs. ApJ **748**, 93 (2012).

Rowan, D.; Meschiari, S.; Laughlin, G.; Vogt, S. S.; Butler, R. P.; Burt, J.; Wang, S.; Holden, B.; Hanson, R.; Arriagada, P.; Keiser, S.; Teske, J. and Diaz, M. The Lick-Carnegie Exoplanet Survey: HD 32963 – A New Jupiter Analog Orbiting a Sun-like Star. ApJ **817**, 104 (2016).

Rowe, J. F.; Bryson, S. T.; Marcy, G. W.; Lissauer, J. J.; Jontof-Hutter, D.; Mullally, F.; Gilliland, R. L.; Issacson, H.; Ford, E.; Howell, S. B.; Borucki, W. J.; Haas, M.; Huber, D.; Steffen, J. H.; Thompson, S. E.; Quintana, E.; Barclay, T.; Still, M.; Fortney, J.; Gautier, III, T. N.; Hunter, R.; Caldwell, D. A.; Ciardi, D. R.; Devore, E.; Cochran, W.; Jenkins, J.; Agol, E.; Carter, J. A. and Geary, J. Validation of Kepler's Multiple Planet Candidates. III. Light Curve Analysis and Announcement of Hundreds of New Multi-planet Systems. ApJ **784**, 45 (2014).

Rupprecht, G.; Pepe, F.; Mayor, M.; Queloz, D.; Bouchy, F.; Avila, G.; Benz, W.; Bertaux,

J.-L.; Bonfils, X.; Dall, T.; Delabre, B.; Dekker, H.; Eckert, W.; Fleury, M.; Gilliotte, A.; Gojak, D.; Guzman, J. C.; Kohler, D.; Lizon, J.-L.; Lo Curto, G.; Longinotti, A.; Lovis, C.; Megevand, D.; Pasquini, L.; Reyes, J.; Sivan, J.-P.; Sosnowska, D.; Soto, R.; Udry, S.; Van Kesteren, A.; Weber, L. and Weilenmann, U. The exoplanet hunter HARPS: performance and first results. In Moorwood, A. F. M. and Iye, M., eds., *Ground-based Instrumentation for Astronomy* (2004), vol. 5492 of Proc. SPIE, pp. 148–159.

Saar, S. H.; Butler, R. P. and Marcy, G. W. Magnetic Activity-related Radial Velocity Variations in Cool Stars: First Results from the Lick Extrasolar Planet Survey. ApJ **498**, L153 (1998).

Saar, S. H. and Donahue, R. A. Activity-Related Radial Velocity Variation in Cool Stars. ApJ **485**, 319 (1997).

Santos, N. C.; Bouchy, F.; Mayor, M.; Pepe, F.; Queloz, D.; Udry, S.; Lovis, C.; Bazot, M.; Benz, W.; Bertaux, J.-L.; Lo Curto, G.; Delfosse, X.; Mordasini, C.; Naef, D.; Sivan, J.-P. and Vauclair, S. The HARPS survey for southern extra-solar planets. II. A 14 Earth-masses exoplanet around μ Arae. *Astronomy & Astrophysics* **426**, L19 (2004).

Santos, N. C.; Mayor, M.; Naef, D.; Pepe, F.; Queloz, D.; Udry, S. and Blecha, A. The CORALIE survey for Southern extra-solar planets. IV. Intrinsic stellar limitations to planet searches with radial-velocity techniques. A&A **361**, 265 (2000).

Sato, B.; Fischer, D. A.; Henry, G. W.; Laughlin, G.; Butler, R. P.; Marcy, G. W.; Vogt, S. S.; Bodenheimer, P.; Ida, S.; Toyota, E.; Wolf, A.; Valenti, J. A.; Boyd, L. J.; Johnson, J. A.; Wright, J. T.; Ammons, M.; Robinson, S.; Strader, J.; McCarthy, C.; Tah, K. L. and Minniti,

D. The N2K Consortium. II. A Transiting Hot Saturn around HD 149026 with a Large Dense Core. ApJ **633**, 465 (2005).

Scargle, J. D. Studies in astronomical time series analysis. II - Statistical aspects of spectral analysis of unevenly spaced data. ApJ **263**, 835 (1982).

Schlaufman, K. C. and Laughlin, G. A physically-motivated photometric calibration of M dwarf metallicity. A&A **519**, A105 (2010).

Seager, S., ed. *Planet Migration*, University of Arizona Press, pp. 347–371 (2011).

Sinukoff, E. Optimization of Planet Finder Observing Strategy. In Apai, D. and Gabor, P., eds., *Search for Life Beyond the Solar System. Exoplanets, Biosignatures & Instruments* (2014), p. 4P.

Soubiran, C.; Bienayme, O.; Mishenina, T. V. and Kovtyukh, V. V. VizieR Online Data Catalog: Galactic disk stars vertical distribution. IV. (Soubiran+, 2008). *VizieR Online Data Catalog* **348**, 91 (2008).

Sousa, S. G.; Santos, N. C.; Israelian, G.; Mayor, M. and Udry, S. Spectroscopic stellar parameters for 582 FGK stars in the HARPS volume-limited sample. Revising the metallicity-planet correlation. A&A **533**, A141 (2011a).

Sousa, S. G.; Santos, N. C.; Israelian, G.; Mayor, M. and Udry, S. Spectroscopic stellar parameters for 582 FGK stars in the HARPS volume-limited sample. Revising the metallicity-planet correlation. A&A **533**, A141 (2011b).

Still, M. and Barclay, T. PyKE: Reduction and analysis of Kepler Simple Aperture Photometry data. Astrophysics Source Code Library (2012).

Stone, R. P. S. Spectrophotometry of Flux Calibration Stars for Hubble Space Telescope. ApJS **107**, 423 (1996).

Sullivan, P. W.; Winn, J. N.; Berta-Thompson, Z. K.; Charbonneau, D.; Deming, D.; Dressing, C. D.; Latham, D. W.; Levine, A. M.; McCullough, P. R.; Morton, T.; Ricker, G. R.; Vanderspek, R. and Woods, D. The Transiting Exoplanet Survey Satellite: Simulations of Planet Detections and Astrophysical False Positives. ApJ **809**, 77 (2015).

Takeda, G.; Ford, E. B.; Sills, A.; Rasio, F. A.; Fischer, D. A. and Valenti, J. A. Structure and Evolution of Nearby Stars with Planets. II. Physical Properties of ˜1000 Cool Stars from the SPOCS Catalog. ApJS **168**, 297 (2007).

Tanner, A.; Beichman, C.; Bryden, G.; Lisse, C. and Lawler, S. Survey of Nearby FGK Stars at 160 μm with Spitzer. ApJ **704**, 109 (2009).

Torres, G. On the Use of Empirical Bolometric Corrections for Stars. AJ **140**, 1158 (2010).

Tremaine, S. and Dong, S. The Statistics of Multi-planet Systems. AJ **143**, 94 (2012).

Triaud, A. H. M. J.; Anderson, D. R.; Collier Cameron, A.; Doyle, A. P.; Fumel, A.; Gillon, M.; Hellier, C.; Jehin, E.; Lendl, M.; Lovis, C.; Maxted, P. F. L.; Pepe, F.; Pollacco, D.; Queloz, D.; Ségransan, D.; Smalley, B.; Smith, A. M. S.; Udry, S.; West, R. G. and Wheatley, P. J. WASP-80b: a gas giant transiting a cool dwarf. A&A **551**, A80 (2013).

van Leeuwen, F. Validation of the new Hipparcos reduction. A&A **474**, 653 (2007).

Vanderburg, A. and Johnson, J. A. A Technique for Extracting Highly Precise Photometry for the Two-Wheeled Kepler Mission. PASP **126**, 948 (2014).

Vogt, S. S.; Allen, S. L.; Bigelow, B. C.; Bresee, L.; Brown, B.; Cantrall, T.; Conrad, A.; Couture, M.; Delaney, C.; Epps, H. W.; Hilyard, D.; Hilyard, D. F.; Horn, E.; Jern, N.; Kanto, D.; Keane, M. J.; Kibrick, R. I.; Lewis, J. W.; Osborne, J.; Pardeilhan, G. H.; Pfister, T.; Ricketts, T.; Robinson, L. B.; Stover, R. J.; Tucker, D.; Ward, J. and Wei, M. Z. HIRES: the high-resolution echelle spectrometer on the Keck 10-m Telescope. In Crawford, D. L. and Craine, E. R., eds., *Instrumentation in Astronomy VIII* (1994a), vol. 2198 of *Society of Photo-Optical Instrumentation Engineers (SPIE) Conference Series*, p. 362.

Vogt, S. S.; Allen, S. L.; Bigelow, B. C.; Bresee, L.; Brown, B.; Cantrall, T.; Conrad, A.; Couture, M.; Delaney, C.; Epps, H. W.; Hilyard, D.; Hilyard, D. F.; Horn, E.; Jern, N.; Kanto, D.; Keane, M. J.; Kibrick, R. I.; Lewis, J. W.; Osborne, J.; Pardeilhan, G. H.; Pfister, T.; Ricketts, T.; Robinson, L. B.; Stover, R. J.; Tucker, D.; Ward, J. and Wei, M. Z. HIRES: the high-resolution echelle spectrometer on the Keck 10-m Telescope. In Crawford, D. L. and Craine, E. R., eds., *Society of Photo-Optical Instrumentation Engineers (SPIE) Conference Series* (1994b), vol. 2198 of *Society of Photo-Optical Instrumentation Engineers (SPIE) Conference Series*, pp. 362–+.

Vogt, S. S.; Burt, J.; Meschiari, S.; Butler, R. P.; Henry, G. W.; Wang, S.; Holden, B.; Gapp, C.; Hanson, R.; Arriagada, P.; Keiser, S.; Teske, J. and Laughlin, G. Six Planets Orbiting HD 219134. ApJ **814**, 12 (2015).

Vogt, S. S.; Butler, R. P.; Rivera, E. J.; Kibrick, R.; Burt, J.; Hanson, R.; Meschiari, S.; Henry,

G. W. and Laughlin, G. A Four-planet System Orbiting The K0V Star HD 141399. ApJ **787**, 97 (2014a).

Vogt, S. S.; Radovan, M.; Kibrick, R.; Butler, R. P.; Alcott, B.; Allen, S.; Arriagada, P.; Bolte, M.; Burt, J.; Cabak, J.; Chloros, K.; Cowley, D.; Deich, W.; Dupraw, B.; Earthman, W.; Epps, H.; Faber, S.; Fischer, D.; Gates, E.; Hilyard, D.; Holden, B.; Johnston, K.; Keiser, S.; Kanto, D.; Katsuki, M.; Laiterman, L.; Lanclos, K.; Laughlin, G.; Lewis, J.; Lockwood, C.; Lynam, P.; Marcy, G.; McLean, M.; Miller, J.; Misch, T.; Peck, M.; Pfister, T.; Phillips, A.; Rivera, E.; Sandford, D.; Saylor, M.; Stover, R.; Thompson, M.; Walp, B.; Ward, J.; Wareham, J.; Wei, M. and Wright, C. APF-The Lick Observatory Automated Planet Finder. *Publications of the ASP* **126**, 359 (2014b).

Vogt, S.S. et al. Apf – the lick observatory automated planet finder (2014). PASP, In Press.

Walker, G. A. H. The first high-precision radial velocity search for extra-solar planets. *New Astronomy* **56**, 9 (2012).

Walker, G. A. H.; Walker, A. R.; Irwin, A. W.; Larson, A. M.; Yang, S. L. S. and Richardson, D. C. A search for Jupiter-mass companions to nearby stars. *Icarus* **116**, 359 (1995).

Wenger, M.; Ochsenbein, F.; Egret, D.; Dubois, P.; Bonnarel, F.; Borde, S.; Genova, F.; Jasniewicz, G.; Laloë, S.; Lesteven, S. and Monier, R. The SIMBAD astronomical database. The CDS reference database for astronomical objects. *Astronomy and Astrophysics* **143**, 9 (2000).

Wolfgang, A. and Lopez, E. How Rocky Are They? The Composition Distribution of Kepler's Sub-Neptune Planet Candidates within 0.15 AU. ApJ **806**, 183 (2015).

Wolfgang, A.; Rogers, L. A. and Ford, E. B. Probabilistic Mass-Radius Relationship for Sub-Neptune-Sized Planets. *ArXiv e-prints* (2015).

Wright, J. T. Radial Velocity Jitter in Stars from the California and Carnegie Planet Search at Keck Observatory. *Publications of the ASP* **117**, 657 (2005).

Wright, J. T. Radial velocity jitter in stars from the california and carnegie planet search at keck observatory. *Publications of the Astronomical Society of the Pacific* **117**, pp. 657 (2005).

Wright, J. T.; Fakhouri, O.; Marcy, G. W.; Han, E.; Feng, Y.; Johnson, J. A.; Howard, A. W.; Fischer, D. A.; Valenti, J. A.; Anderson, J. and Piskunov, N. The Exoplanet Orbit Database. PASP **123**, 412 (2011).

Zechmeister, M. and Kürster, M. The generalised Lomb-Scargle periodogram. A new formalism for the floating-mean and Keplerian periodograms. A&A **496**, 577 (2009).

Zolotuhkin, I. The Extrasolar Planets Encyclopaedia (1995). [Online; accessed 2015-02-09].